INCORPORATION OF LUNAR PASSAGES INTO SECONDARY PAYLOAD TRANSFER DESIGN

by

Josiah Badiali

A Thesis

Submitted to the Faculty of Purdue University

In Partial Fulfillment of the Requirements for the degree of

Master of Science in Aeronautics and Astronautics

School of Aeronautics and Astronautics

West Lafayette, Indiana

December 2024

THE PURDUE UNIVERSITY GRADUATE SCHOOL
STATEMENT OF COMMITTEE APPROVAL

Dr. Kathleen C. Howell, Chair

School of Aeronautics and Astronautics

Dr. Kenshiro Oguri

School of Aeronautics and Astronautics

Dr. Carolin Frueh

School of Aeronautics and Astronautics

Approved by:

Dr. Dengfeng Sun

To my grandfather

Edward J. Badiali

November 18, 1934 - November 30, 2016

ACKNOWLEDGMENTS

First, I would like to give gratitude to my family. To the father who raised me, despite all of the circumstances. To the sister who guided me and pushed me to venture outside of my comfort zone. To the brother who inspired me and showed that there is more to life than work. To the mother who supported me throughout my collegiate career. To the grandmother who coddled me, and provided a warm home to escape my troubles. Lastly, to the grandfather who believed in my education, I know he would be proud of this.

I'd also like to acknowledge my friends and colleagues in the research group, your collective insight and feedback has been invaluable to my maturation as a researcher since the day I joined. I would be remiss if I didn't give thanks to the peers who acted as my mentors, Stephen Scheuerle and Beom Park. I can't forget my close friends who not only aided me as a researcher, but also gave me so much happiness here at Purdue. So, a big shout-out to Liam Fahey, Ricardo Gómez Cano, Antony "Chef Tony" Fleming, and of course, Cody and Kasi Waldecker.

I cannot go through and acknowledge the research group without giving my sincere gratitude to its head and my advisor, Dr. Kathleen Howell. Thank you for all of the guidance throughout my time here, for granting me all of the opportunities I've had to develop and for your patience in keeping me from getting sidetracked. Furthermore, I would like to thank my committee, Dr. Carolin Frueh and Dr. Kenshiro Oguri for taking the time to give me excellent feedback and to review this (rather lengthy) document.

Lastly, I would like to extend my gratitude to both Purdue's School of Aeronautics and Astronautics and Intuitive Machines LLC (Award 21123283) for providing me with the funding necessary to pursue this degree. Without the insight from the folks at Intuitive Machines, this project would not have come together as it has.

TABLE OF CONTENTS

LIST OF TABLES

LIST OF FIGURES

ABSTRACT

A dramatic increase in the number of missions for inserting both large satellites as well as rideshare spacecraft into cislunar trajectories has been noted as of recently. While ballistic lunar transfers (BLTs) have proven a reliable means for sending primary missions to their destination orbits, the inflexible jettison conditions imposed upon secondary payloads may significantly limit viable pathways. This investigation is centered about designing a framework to construct lunar transfers for secondary payloads from various commissioning maneuver (CM) states to select periodic orbits near the Moon. These continuous passageways are modelled in the Bi-Circular Restricted 4-Body Problem (BCR4BP), while necessary dynamical insights are recovered from the application of dynamical systems theory to both the BCR4BP and the Circular Restricted 3-Body Problem (CR3BP). To understand the impact of a Moon encounter on an outbound lunar transfer, families of BLTs are generated for primary payloads, where select members that have close flybys are isolated an examined. A modular, multi-phase framework is then developed, stemming from the lunar encounter. With this, transfers from a variety of sample CM states to Halo, Butterfly and Lyapunov orbits are presented. The versatility of the design framework is highlighted through a case study for a double-flyby transfer to a select Lyapunov orbit. The presented analysis provides an intuitive strategy for diversifying the otherwise limited pool of viable transfers that send secondary payloads to cislunar orbits.

1. INTRODUCTION

Recent years have witnessed a stark increase in both interest and execution of endeavors seeking to push a sustained presence further into the reaches of space. Perhaps most famous of which are NASA's Artemis and Gateway missions, which employ orbits centered about the Moon, a great distance beyond the majority of existing missions residing near the Earth [1]. Lunar operations are an interest not exclusive to missions featuring larger spacecraft, with Intuitive Machines' Khon-1 [2] and well as the Lunar IceCube [3], Lunar Flashlight [4], Cislunar Explorers [5], LunaH-Map [6] and EQUULEUS [7] missions all serve to exemplify both previous and future intent in orbiting smaller, unmanned satellites about the Moon. A characteristic each of the previous undertakings share is the stringent fuel-consumption restrictions inherent to small spacecraft. Moreover, rideshare missions also face another obstacle in having to conform to the primary payload's location, speed and date at jettison from the launch vehicle, further limiting the available trajectories befitting mission specifications. Lunar flybys present a primary means of mitigating these hindrances, as they have proven to be a cost-effective method for altering a spacecraft's energy and trajectory orientation.

Due to their low-altitude passages, lunar flybys are particularly sensitive to simulate using higher-fidelity modelling. In response to this, lower-fidelity multi-body dynamical models, such as the Circular Restricted Three-Body Problem (CR3BP) and the Bi-Circular Restricted Four-Body Problem (BCR4BP) are employed in the investigation. Within these models, initial guesses are dynamically informed and optimized in order to meet various sample state and epoch constraints imposed upon the secondary payload. Ultimately, a strategy for rapidly constructing a flexible and modular framework utilizing lunar flybys to discern viable lunar transfers for secondary payloads is examined.

1.1 Previous Contributions

The history of lunar transfers is extensive and diverse. In 1960, Mickelwait and Booton outlined strategies for Earth-to-Moon transfers, while Schwaniger focuses on free-return trajectories three years later in 1963 [8] [9]. The free-return trajectory would become standard practice in the early era of lunar missions, with it first being executed by the then Soviet

Union's Luna 3 in 1959, then becoming the modus operandi of the Apollo missions in the 1960s. The Soviet Union's Luna 10 would become the first mission to insert into a Lunar orbit in 1966, using a direct transfer which would be emulated by many missions following. NASA's Lunar Prospector would commission such a flight path in 1998, using three apolune-lowering maneuvers in order to arrive in its science orbit [10]. About a decade following this, the Indian Space Research Organization (ISRO) would undergo their first lunar excursion in 2008 with Chandrayaan-1, similarly exercising four maneuvers to settle in a polar lunar orbit [11]. The Lunar Reconnaissance Orbiter (LRO) would launch from Cape Canaveral in 2009 also to use a direct transfer, eventually inserting into a frozen orbit about the Moon where it remains to this day [12]. During this time, Earth-to-Moon mission organizers would begin implementing an alternative to the more traditional direct transfer, one which would utilize solar gravitational effects to minimize necessary fuel expenditure.

Lunar transfers which leverage solar perturbations date back to the Hiten mission, launched in 1990, where several lunar flybys and extended solar-perturbed trajectory segments were leveraged [13]. Koon et al. would later analyze the four-body dynamics present in the Hiten mission by coupling two sets of three-body systems [14]. Further analysis into the instantaneous solar tidal effects is carried out in the CR3BP by Davis in 2011 [15]. Later that year, NASA's GRAIL mission would support the previous studies by directly guiding twin satellites into a low-altitude lunar orbit using separate BLTs [16]. Boudad et al. later incorporate insights from Davis' dissertation into the BCR4BP within the scope of heliocentric escape dynamics [17]. This four-body model would then become central in the mission design of the Lunar IceCube mission in 2018, one which would travel along a multi-lobed solar-perturbed lunar transfer toward its destination science orbit about the Moon [18] [3]. Scheuerle expands upon this approach with an analysis on the Sun's perturbing effect on spacecraft hamiltonian as well as the development of families of BLT solutions in the BCR4BP [19]. He would later provide a framework for intuitively introducing low-thrust into solar-perturbed lunar transfers, giving rise to Cislunar Low-Energy Flight paths (CLEFs) [20]. The recent CAPSTONE mission also utilizes a BLT in order to insert into a 9:2 Near-Rectilinear Halo Orbit (NRHO), the proposed host trajectory for NASA's upcoming Gateway mission [21] [22]. For an upcoming example, the Houston-based Intuitive Machines

intends to employ a BLT centered about a lunar flyby for transferring their Khon-1 satellite into a frozen orbit about the Moon [2]. Hoffman further analyzes the implementation of lunar swingbys in the scope of the Khon-1 mission [23]. Moon passages are common in general BLT design, though exceptionally so for missions of secondary payloads, as evidenced by Lunar IceCube and Khon-1. The correlation is no coincidence, as the tighter propellant constraints often attributed to secondary payloads may benefit from the Moon's attractive force.

Gravity assists are a key tool in the construction of interplanetary trajectories, and as such have a rich history in missions looking to venture beyond the Earth-Moon region. Of course, their usage is not exclusive to deep-space missions, as any flight path non-negligibly affected by the Moon's gravity may be constructed to be assisted by it. A keystone to Schwaniger's free-return trajectories is the gravitational pull of the approaching body, though additional works have been produced expanding the utility of the Moon's influence. Egorov explores the applications of precise passages to alter a spacecraft's departing orientation, addressed in the context of the spatial three-body problem [24]. In 1981, Farquhar and Dunham expand upon Egorov's method in their pursuit of a path to observe Earth's geomagnetic tail, utilizing a secondary lunar flyby to design arrival arcs into various Sun-synchronous periodic orbits [25]. Alternative heliocentric escape sequences featuring multiple lunar flybys were explored for the ISEE-3 mission in 1984 [26]. Flybys have aided in insertion into cislunar periodic orbits as well, as a passage over the Moon's surface re-oriented NASA's LCROSS satellite to a highly-inclined orbit about the Earth [27]. Additionally, the 2018 TESS operation inserted into a 2:1 resonant periodic orbit with the aid of a lunar swingby [28]. More recently, the first mission in the Artemis campaign performed flybys to both insert and depart a distant retrograde orbit (DRO) about the Moon [1]. These past missions, as well as those upcoming such as Khon-1, serve to inform and guide the research direction investigated in this document.

1.2 Document Objective and Overview

The investigation seeks to design a flexible process by which viable lunar transfers are constructed with a constrained initial state and epoch. To this end, lunar flybys are leveraged to alter the state and orientation of the transfer path, as well as potentially reduce the necessary propellant. The relative 2-body problem, CR3BP and BCR4BP models are all used within the candidate trajectory design, while B-Plane targeting informs the passages by the Moon. While the method put forth is intended to be of use for any destination orbit in the cislunar regime, specific focus is placed on inserting into Halo, Butterfly and Lyapunov orbits. The remainder of the document is organized into the following chapters:

- **Chapter 2**: Newton's laws of gravitation admit an $\mathcal{N}$-body model which does not provide an analytical solution for systems of more than two bodies. Assumptions are presented in this section enabling the derivation of the equations of motion for the lower-fidelity CR3BP and BCR4BP models from the formulation of the $\mathcal{N}$-body model. Following the introduction of the CR3BP and BCR4BP, their respective Hamiltonians are produced alongside the equilibrium solutions admitted by these dynamical models. Analysis into rate of change for the Hamiltonians as a functions position is provided, followed by transformations between pertinent rotating reference frames.

- **Chapter 3**: In response to the lower-fidelity models providing no analytical solution, linearization methods are employed to gleam information from the underlying dynamics. Using these methods, a state transition matrix (STM) is introduced, which alongside differential corrections methods is a key tool for both periodic orbit and lunar transfer construction alike. A technique for uncovering manifolds into and out of periodic orbits is also discussed, as well as a flexible alternative in pseudo-manifolds. Lastly, natural parameter continuation (NPC) and pseudo-arclength continuation (PALC) are addressed as means of stepping through families of solutions.

- **Chapter 4**: To preface the development of lunar transfers for rideshare missions, traditional techniques of determining passageways for primary payloads are explored. The solar tidal effects on instantaneous orbital elements are outlined, followed by the

definition and application of perigee mapping strategies for discerning lunar transfer initial guesses. Using these, BLTs and their host families are converged, mapping routes from an initial low-Earth orbit (LEO) to destination cislunar trajectories, all within the scope of the BCR4BP. Lastly, transfers to circular lunar orbits are also explored, from which trajectories that encounter the Moon on their outbound leg are isolated and examined.

- **Chapter 5**: In this section, an epoch-independent method for mapping a departing apoapsis location given the state of a lunar flyby is presented. With this, initial guess loci may be generated and, with insights presented by patterns in solar perturbing effects, filtered to uncover loci of candidate transfers. Individual phases of the transfer are then separated and independently provided sets of initial guesses, employing a K-D tree algorithm to determine transfers likely to converge. A multiple-shooting approach is then used to correct for a continuous BLT arc to destination Halo, Butterfly and Lyapunov orbits.

- **Chapter 6**: The modularity of the framework developed in Chapter 5 is highlighted with a case study for the transfer between a specified jettison condition to a desired Lyapunov orbit. Along the way, two lunar flybys are leveraged to correctly alter the spacecraft energy and orientation such that insertion into the Manifold is made more viable.

- **Chapter 7**: This final remarks of the document summarize the results presented as well as outline the benefits and considerations relevant to the established design process. Following this, potential avenues for expansion upon the investigation are presented to further improve upon present shortcomings.

2. DYNAMICAL MODELS

In order to evaluate the motion of an object as affected by its environment, a set of dynamical equations must be employed to understand the latent physics at play. Within the context of trajectory design, this pursuit is largely dedicated toward emulating the dominant gravitational forces acting upon a spacecraft. A body's motion while accelerated by $\mathcal{N}$ bodies may be modeled by Newton's laws of gravitation, though modern mathematics has only found enough integrals of motion to admit a closed-form solution for the scenario of the relative motion of one object orbiting another, unperturbed by external forces. Since gravitational effects extend indefinitely into space, a *perfect* model of a spacecraft's motion would contain gravitational influences from a seemingly infinite amount of sources, both known and unknown. A more realistic approach is to focus on simulating the motion of a negligible-mass body under the pull of only the dominant gravitational accelerations within the context of the problem. As an example, missions within the cislunar region and beyond are significantly influenced by both the Moon's and Sun's gravities, and as such require dynamical models which incorporate them. To this end, assumptions and rotating reference frames are employed to mold Newton's $\mathcal{N}$-body model into equations that provide dynamical insights into the motion of a spacecraft within a three or four-body regime.

2.1 The $\mathcal{N}$-Body Model

Regardless of where one is, they are constantly acted upon by the forces of gravity from an innumerable amount of objects. In the 17th century, Sir Isaac Newton described the force of gravity acting upon a center of mass due to the presence of another mass with what would become known as Newton's Law of Universal Gravitation [29]:

$$M_a R_a'' = \tilde{G}\frac{M_b M_a}{R_{ab}^2} \tag{2.1}$$

Where the gravity of mass M_b is acting upon mass M_a. Variables R_a and R_b are the distances of masses M_a and M_b from an inertially fixed location. R_{ab} is the relative distance between both of the masses, and $\tilde{G}$ is the universal gravitational constant with value $G \approx 6.674 \cdot$

$10^{-11}\frac{N\cdot m^2}{kg^2}$. Since the primes indicate a derivative with respect to dimensional time, it is noted that (2.1) represents the force, and subsequently acceleration, imparted upon mass M_a by the gravity of M_b.

This scalar expression may also be expressed in vector notation to represent the individual components of the acceleration vector. First, note that an over-arrow, such as $\vec{R}$ is used to denote a vector quantity. Secondly, the subscript for a vector indicates the direction of the vector; for instance, $\vec{R}_{ab}$ is the position vector *from* point a *to* point b, or $\vec{R}_{ab} = \vec{R}_b - \vec{R}_a$. Lastly, we may note that gravity is an *attractive* force, thus the gravitational force acting upon mass M_a is directed away from it. With these in mind, (2.1) may be expressed in vector form, as shown in (2.2).

$$M_a\vec{R}''_a = \tilde{G}\frac{M_bM_a}{\vec{R}^3_{ab}}\vec{R}_{ab} \tag{2.2}$$

Where the lack of an over-arrow indicates the magnitude of the associated vector. Examining the equation, the vector component on the right-hand-side indicates that the gravitational force is directed from M_a to M_b.

As noted before, any body is acted upon by an infinite number of gravitational forces at a given moment. For instance, a person standing on Earth's surface is, of course, being pulled towards the ground by Earth's gravity, though they are also being pulled by the Moon, Sun, Jupiter, Mercury, Pluto, etc. Naturally, the gravitational effects of those listed are relatively insignificant compared to that of the Earth, though this does not dismiss their existence. In a similar vein, if the gravitational forces acting upon a mass M_a by N bodies were to be modelled, (2.2) may be applied to each attractive source, as shown in (2.3).

$$M_a\vec{R}''_a = \tilde{G}\frac{M_1M_a}{R^3_{a1}}\vec{R}_{a1} + \tilde{G}\frac{M_2M_a}{R^3_{a2}}\vec{R}_{a2} + \cdots + \tilde{G}\frac{M_NM_a}{R^3_{aN}}\vec{R}_{aN} = \sum_{\substack{\mathrm{i}=1\\ \mathrm{i}\neq a}}^{N}\tilde{G}\frac{M_\mathrm{i}M_a}{R^3_{a\mathrm{i}}}\vec{R}_{a\mathrm{i}} \tag{2.3}$$

It is with (2.3) that the $\mathcal{N}$-body problem is best described, though while the forces of infinite gravitational sources can be expressed mathematically, the above equation only admits a closed-form solution in one specific scenario. Equation (2.3) outlines a second-order differential equation for three-dimensional vector. Moreover, each relative position vector is

dependent upon the location of the gravitational sources with respect to the inertial point of reference. These positions must also be solved for, adding $N-1$ three-dimensional vector equations of motion to be integrated. Since these are second-order vector differential equations, each component of the vector, of which there are three, requires two integrals (one for the position component, and one for its corresponding first derivative). As a result, each body requires six integrals and thus six constants of integration. Coupled with the fact that this is required for each of the N bodies, this means that $6N$ integrals of motion are required for a closed-form solution.

Currently, only ten constants of integration have been discovered, with one from conservation of energy, three from conservation of angular momentum, and six from conservation of linear momentum. If the simplest case of $N = 2$ is examined, 12 integrals of motion are needed, exceeding modern capabilities by two. One approach is to discard the inertially-fixed basepoint in favor of one attached to one of the gravitational bodies' center of mass, an equation to summarize this new formulation is presented by (2.4).

$$\vec{R}''_{ba} + \tilde{G}\frac{M_a + M_b}{R^3_{ba}}\vec{R}_{ba} = \sum_{\substack{\mathrm{i}=1 \\ \mathrm{i}\neq a,b}}^{N} \tilde{G}M_{\mathrm{i}}\left(\frac{\vec{R}_{a\mathrm{i}}}{R^3_{a\mathrm{i}}} - \frac{\vec{R}_{b\mathrm{i}}}{R^3_{b\mathrm{i}}}\right) \tag{2.4}$$

This manipulation eliminates the need for information about the state of one of the bodies and the necessary constants of integrations then becomes $6(N-1)$, which in the case of the relative two-body problem now only needs six constants, allowing for a closed-form solution. The equations of motion for the relative two-body problem are based upon (2.4), where the right-hand-side becomes the three-dimensional zero vector.

In the scenario of $N > 2$, the relative formulation still does not admit a closed-form solution and thus alternative measures would need to be taken. By using appropriate assumptions as well as shifting from inertial to rotating reference frames, various equations of motion for $N = 3, 4$ have been uncovered, though analytical solutions to these are still prohibited by the lack of additional integrals of motion. Regardless, various approximative measures are taken in order to gleam insights from the three and four-body problems.

A high-fidelity model has been constructed by implementing celestial ephemerides and various other external forces into (2.3) to accurately represent the motion of a spacecraft. The complexity of the model increases with its accuracy, and as a result it becomes difficult to extrapolate information from this higher-fidelity model (often referred to as "Ephemeris"). While numerical methods may be employed to converge onto solutions within Ephemeris, determining the initial guess within such an unintuitive and sensitive dynamical system is a difficult task. In response to this, initial guess determination is often relegated to lower-fidelity models where dynamical systems theory can uncover insights into the dynamics. Since the construction of a lunar transfer within this framework is non-negligibly impacted by the gravities of the Earth, Moon and Sun, the lower-fidelity models to be employed in this investigation are both the Circular Restricted 3-Body Problem (CR3BP) and the Bi-Circular Restricted 4-Body Problem (BCR4BP).

2.2 The Circular Restricted 3-Body Problem

As implied by its name, the CR3BP is a dynamical model centered about the notion that $N = 3$. Of course, there exist far more than three bodies in reality, but this model is used in scenarios where only two gravitational sources disproportionately affect the spacecraft. Within this section, the relevant assumptions and reference frames are introduced in order to craft the CR3BP equations of motion. Following this, a relevant constant of integration, as well as equilibrium solutions and the latent symmetry within the dynamics are explored.

2.2.1 Assumptions

To simplify the dynamics of the general three-body problem, specific assumptions may be leveraged. As a conceptual keystone for the three-body problem, an assumption must be made such that there are no external gravitational sources acting upon the system of three bodies. First, note that general convention assigns the order of the primaries to their respective masses; the largest being referred to as the first body, while the least massive is the third. With this in mind, the Circular Restricted 3-Body Problem, as well as several other three and four-body models, is centered about the supposition that the third body is

of negligible mass as compared to the other two, or $M_1 \geq M_2 \gg M_3$. As a consequence of this, the presence of M_3 does not impact the motion of the larger two bodies (which are referred to as the "primary bodies", or "primaries" for short). Since the larger bodies are now dynamically isolated, they effectively exist within a two-body scenario where their motion with respect to one another is a closed conic. The CR3BP attributes a circular trajectory to this conic, formally stating that the primaries move in circular orbits about their shared center of mass, or barycenter. The assumption of circular orbits is not consistent through all restricted three-body formulations, for example, the Elliptic Restricted 3-Body Problem (ER3BP) holds that the primaries move in elongated orbits about their barycenter. A benefit of the assumptions made by the CR3BP is the lack of time-dependence within the dynamics of the primaries, as their circular tracks would be traveled at both a constant rate and radius. These assumptions work in conjunction with the implementation of a rotating reference frame in order to formulate the equations of motion for the CR3BP.

It should be noted that the fidelity of a simplified model lies heavily on the scenarios to which it is being applied. For instance, the assumption of circular orbits is applicable when attempting to model three-body systems such as the Earth about the Sun, or the Moon about the Earth, as they have orbital eccentricities of approximately 0.02 and 0.06, respectively. In the case of Mercury's orbit about the Sun (an eccentricity of about 0.21), more significant differences will form between the CR3BP-modeled dynamics and higher-fidelity simulations. The implementation of a lower-fidelity model may only be applicable if the underlying assumptions reasonably adhere with nature, as the opposite case would see little coherence between simulation and reality, and thus little merit in the pursuit.

2.2.2 Kinematics

Before deriving the equations of motion, relevant parameters must first be defined. The position vectors of the first and second primaries are represented with $\vec{R}_1$ and $\vec{R}_2$ respectively. Moreover, since the center of mass of the primaries will always lie along the line between them, their motion with respect to the barycenter will always appear to be circles with the two bodies on either end of a line which pierces the origin. A top-down representation of

this motion is given in Figure 2.1. An arbitrary inertial coordinate system may be defined such that $\hat{X}$ lies along the vector from M_1 to M_2 at a given moment in time, $\hat{Z}$ is along the angular momentum vector of either primary, and $\hat{Y} = \hat{Z} \times \hat{X}$. The angle θ is formed between $\hat{X}$ and the line formed between the two primaries as it rotates over time.

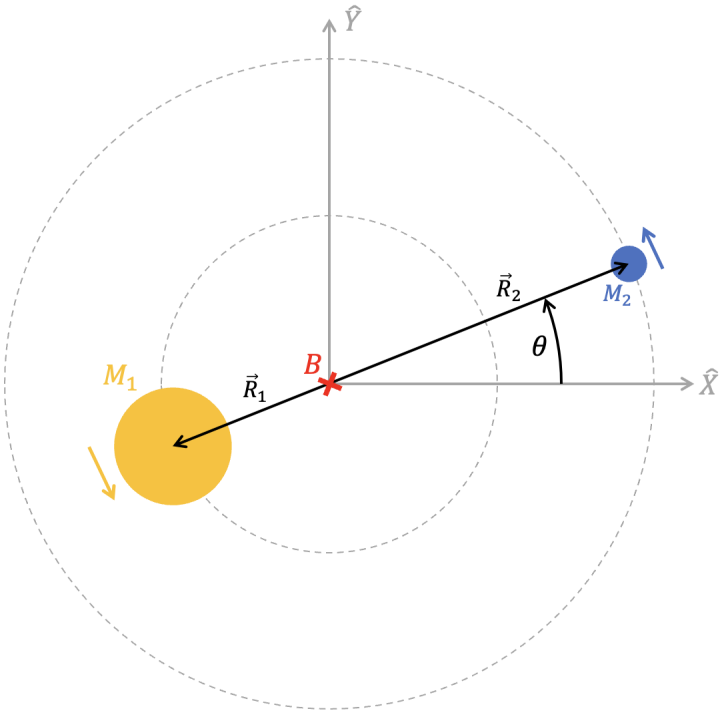

Figure 2.1. The circular motion of the primaries about their common barycenter

The motion of M_3, while guided by the gravitational forces of the larger masses, is unconstrained by assumptions made in the model. A result of this is that the smallest body, with sufficient energy, is capable of traversing anywhere within three-dimensional space. This behavior is depicted in Figure 2.2, along with the position vector of the third mass with respect to the barycenter, $\vec{R}_3$. Furthermore, relative position vectors from M_1 and M_2 to M_3 are given as $\vec{R}_{13}$ and $\vec{R}_{23}$ respectively.

A rotating reference frame is constructed such that $\hat{x}$ is along the direction from M_1 to M_2 at any given moment. The direction $\hat{z}$ is defined to be consistently alongside its inertial counterpart, $\hat{Z}$. Lastly, $\hat{y}$ completes the orthonormal triad such that $\hat{y} = \hat{z} \times \hat{x}$. The inertial and rotating reference frames are related be a single rotation of angle θ about their respective

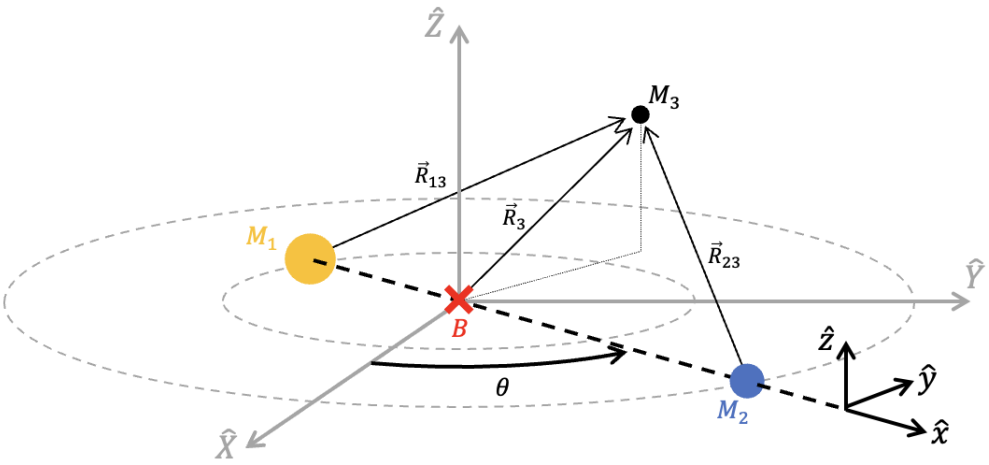

Figure 2.2. Motion of M_3 with respect to inertial and rotating reference frames

z-axes. For ease in describing the motion of the smallest body with respect to the primaries, the position vector $\vec{R}_3$ is expressed in terms of the rotating coordinate system such that:

$$\vec{R}_3 = X\hat{x} + Y\hat{y} + Z\hat{z} \tag{2.5}$$

Also within the rotating reference frame, the positions of the primaries are fixed as the frame is centered about their motion and their distances with respect to the barycenter are constant. Their motion within the rotating frame may be expressed with equations (2.6) and (2.7).

$$\vec{R}_1 = -R_1\ \hat{x} \tag{2.6}$$

$$\vec{R}_2 = R_2\ \hat{x} \tag{2.7}$$

The position vectors of M_3 with respect to the primaries are thus the differences between the position vectors of M_3 and either primary with respect to the barycenter.

$$\vec{R}_{13} = \vec{R}_3 - \vec{R}_1 = (X + R_1)\,\hat{x} + Y\hat{y} + Z\hat{z} \tag{2.8}$$

$$\vec{R}_{23} = \vec{R}_3 - \vec{R}_2 = (X - R_2)\,\hat{x} + Y\hat{y} + Z\hat{z} \tag{2.9}$$

With the motion of each of the bodies described in terms of the rotating reference frame, the equations of motion for the CR3BP may be derived.

2.2.3 Equations of Motion

Returning to Newton's Law of Gravitation as expressed by equation (2.3), the net acceleration acting upon M_3 due to the gravities of M_1 and M_2 may be represented as:

$$\vec{R}_3'' = -\tilde{G}\frac{M_1}{R_{13}^3}\vec{R}_{13} - \tilde{G}\frac{M_2}{R_{23}^3}\vec{R}_{23} \tag{2.10}$$

Since $\vec{R}_3$ is defined in a rotating coordinate system and Newton's Law of Gravitation requires time derivatives as viewed in an inertial frame, the Transport Theorem is necessary. For an arbitrary position vector $\vec{x}$ expressed in a rotating reference frame $\mathcal{R}$, its time derivative with respect to the inertial frame $\mathcal{I}$ is provided in equation (2.11).

$$\frac{^{\mathcal{I}}d\vec{x}}{d\tau} = \frac{^{\mathcal{R}}d\vec{x}}{d\tau} + {}^{\mathcal{I}}\vec{\omega}^{\mathcal{R}} \times \vec{x} \tag{2.11}$$

Where ${}^{\mathcal{I}}\vec{\omega}^{\mathcal{R}}$ is the angular velocity of $\mathcal{R}$ with respect to $\mathcal{I}$, which in the case of the CR3BP kinematics is the time rate of change of θ, represented as $N\hat{z}$. Moreover, τ is used to represent dimensional time. Since the motion of the primaries about their barycenter is represented using circular orbits, the angular velocity of the rotating frame is constant. With this, the Transport Theorem may be applied to take the first and second derivatives of the position vector, as shown in (2.12).

$$\begin{aligned} {}^{\mathcal{I}}\vec{R}_3' &= (X' - NY)\hat{x} + (Y' + NX)\hat{y} + Z'\hat{z} \\ {}^{\mathcal{I}}\vec{R}_3'' &= (X'' - 2NY' - N^2X)\hat{x} + (Y'' + 2NX' - N^2Y)\hat{y} + Z''\hat{z} \end{aligned} \tag{2.12}$$

Inserting the second derivative into equation (2.10) and separating the scalar components into three separate equations, equation (2.13) is created.

$$
\begin{aligned}
X'' - 2NY' - N^2X &= -\tilde{G}\frac{M_1}{R_{13}^3}(X + R_1) - \tilde{G}\frac{M_2}{R_{23}^3}(X - R_2) \\
Y'' + 2NX' - N^2Y &= -\tilde{G}\frac{M_1}{R_{13}^3}Y - \tilde{G}\frac{M_2}{R_{23}^3}Y \\
Z'' &= -\tilde{G}\frac{M_1}{R_{13}^3}Z - \tilde{G}\frac{M_2}{R_{23}^3}Z
\end{aligned}
\tag{2.13}
$$

Expressing the motion in terms of dimensionless quantities allows for an intuitive interpretation of the behavior with respect to relevant distances and times of the analyzed system. For example, 1 AU is a non-dimensional representation of the average distance between the Earth and Sun, and is far more intuitive than its equivalent 149597898 km. A similar principal is at play when non-dimensionalizing the equations of motion, though the concept is also applied to units of time and mass as well. In order to normalize the dimensional quantities, characteristic quantities of length (ℓ^*) and mass (m^*) are chosen such that:

$$
\begin{aligned}
\ell^* &= R_1 + R_2 \\
m^* &= M_1 + M_2
\end{aligned}
$$

In other words, the characteristic length is the constant distance between the two primaries, and the characteristic mass is the total mass of the system. The characteristic time is defined as the reciprocal of the dimensional mean motion of the primaries.

$$
t^* = \frac{1}{N} = \sqrt{\frac{\ell^{*3}}{\tilde{G}m^*}}
$$

Since the characteristic time quantity is the inverse of the mean motion, normalizing the mean motion would require dividing the quantity by itself, resulting in the non-dimensional mean motion (n) being unity. Furthermore, due to the choices of characteristic quantities, the non-dimensional universal gravitational constant (G) also results in a value of one.

$$
G = \tilde{G}\frac{m^*t^{*2}}{\ell^{*3}} = 1 \tag{2.14}
$$

With the characteristic quantities defined, the governing position vector of the third body ($\vec{r}$) may be normalized.

$$\vec{r} = \frac{R_3}{\ell^*} = x\hat{x} + y\hat{y} + z\hat{z} \tag{2.15}$$

Considering that the two primaries exist at consistent distances from their barycenter, their position vectors within the rotating frame may be represented as a proportion of the characteristic length. This proportion may be represented as a function of the two masses. Defining a non-dimensional mass parameter, μ:

$$\mu = \frac{M_2}{m^*} = 1 - \frac{M_1}{m^*} \tag{2.16}$$

This mass parameter may be used to describe the distances of either primary from their center of mass, as presented in (2.17) and (2.18).

$$\vec{r}_1 = -\mu\hat{x} \tag{2.17}$$

$$\vec{r}_2 = (1-\mu)\,\hat{x} \tag{2.18}$$

The normalized positions of M_3 with respect to either M_1 or M_2 may be evaluated as well.

$$\vec{r}_{13} = (x+\mu)\hat{x} + y\hat{y} + z\hat{z} = \frac{\vec{R}_{13}}{\ell^*} \tag{2.19}$$

$$\vec{r}_{23} = (x+\mu-1)\hat{x} + y\hat{y} + z\hat{z} = \frac{\vec{R}_{23}}{\ell^*} \tag{2.20}$$

First noting that $n = Nt^* = 1$, equations (2.14) through (2.20) may be rearranged and inserted into (2.13) such that:

$$\begin{aligned}
(x'' - \frac{2ny'}{t^*} - \frac{n^2x}{t^{*2}})\ell^* &= -\left(\frac{1-\mu}{r_{13}^3}(x+\mu) + \frac{\mu}{r_{23}^3}(x-1+\mu)\right)\frac{\ell^*}{t^{*2}} \\
(y'' + \frac{2nx'}{t^*} - \frac{n^2y}{t^{*2}})\ell^* &= -\left(\frac{1-\mu}{r_{13}^3}y + \frac{\mu}{r_{23}^3}y\right)\frac{\ell^*}{t^{*2}} \\
(z'')\ell^* &= -\left(\frac{1-\mu}{r_{13}^3}z + \frac{\mu}{r_{23}^3}z\right)\frac{\ell^*}{t^{*2}}
\end{aligned} \tag{2.21}$$

Recall that dimensional time, τ, is related to non-dimensional time, t, via $\tau = t^* t$. For an arbitrary function (f) which is differentiable with respect to both dimensional and non-dimensional time, the following is true via the derivative chain rule:

$$f' = \frac{\partial f}{\partial \tau} = \frac{\partial f}{\partial t}\frac{\partial t}{\partial \tau} = \dot{f}\frac{1}{t^*} \tag{2.22}$$

Where over-dots indicate a derivative with respect to non-dimensional time, and primes indicate a derivative with respect to dimensional time. The result in (2.22) may be expanded to the second derivative.

$$f'' = \frac{\partial f'}{\partial \tau} = \frac{\partial}{\partial \tau}\left(\frac{\partial f}{\partial t}\frac{\partial t}{\partial \tau}\right) = \frac{\partial}{\partial \tau}\left(\frac{\partial f}{\partial t}\right)\frac{\partial t}{\partial \tau} + \frac{\partial f}{\partial t}\frac{\partial^2 t}{\partial \tau^2}$$

Since $\frac{\partial^2 t}{\partial \tau^2} = 0$, further simplification proceeds as follows:

$$f'' = \frac{\partial}{\partial \tau}\left(\frac{\partial f}{\partial t}\right)\frac{\partial t}{\partial \tau} = \frac{\partial}{\partial t}\left(\frac{\partial f}{\partial t}\right)\left(\frac{\partial t}{\partial \tau}\right)^2 = \ddot{f}\frac{1}{t^{*2}} \tag{2.23}$$

Applying (2.22) and (2.23) to the dimensional-time derivatives in equation (2.21):

$$\begin{aligned}
(\ddot{x} - 2n\dot{y} - n^2 x)\frac{\ell^*}{t^{*2}} &= -\left(\frac{1-\mu}{r_{13}^3}(x+\mu) + \frac{\mu}{r_{23}^3}(x-1+\mu)\right)\frac{\ell^*}{t^{*2}} \\
(\ddot{y} + 2n\dot{x} - n^2 y)\frac{\ell^*}{t^{*2}} &= -\left(\frac{1-\mu}{r_{13}^3}y + \frac{\mu}{r_{23}^3}y\right)\frac{\ell^*}{t^{*2}} \\
(\ddot{z})\frac{\ell^*}{t^{*2}} &= -\left(\frac{1-\mu}{r_{13}^3}z + \frac{\mu}{r_{23}^3}z\right)\frac{\ell^*}{t^{*2}}
\end{aligned}$$

Simplification leads to the non-dimensional equations of motion for the CR3BP, given in equation (2.24). Recall that a byproduct of the non-dimensionalization is that $n = 1$.

$$\begin{aligned}
\ddot{x} &= 2n\dot{y} + n^2 x - \frac{1-\mu}{r_{13}^3}(x+\mu) - \frac{\mu}{r_{23}^3}(x-1+\mu) \\
\ddot{y} &= n^2 y - 2n\dot{x} - \frac{1-\mu}{r_{13}^3}y - \frac{\mu}{r_{23}^3}y \\
\ddot{z} &= -\frac{1-\mu}{r_{13}^3}z - \frac{\mu}{r_{23}^3}z
\end{aligned} \tag{2.24}$$

A pseudo-potential function, Ω, may be employed to further condense the equations of motion, as demonstrated by (2.25) and (2.26)

$$\Omega = \frac{1}{2}\left(x^2 + y^2\right) + \frac{1-\mu}{r_{13}} + \frac{\mu}{r_{23}} \tag{2.25}$$

$$\begin{aligned} \ddot{x} &= \frac{\partial \Omega}{\partial x} + 2\dot{y} \\ \ddot{y} &= \frac{\partial \Omega}{\partial y} - 2\dot{x} \\ \ddot{z} &= \frac{\partial \Omega}{\partial z} \end{aligned} \tag{2.26}$$

The function Ω differs from a standard potential function in that its gradient does not equal the gravitational force field acting upon the third body, neither in the rotating nor inertial reference frames. Despite this, its gradient largely covers the gravitational effects acting upon the third body within the rotating frame, and has a similar composition to the standard definition of specific gravitational potential energy, thus it is referred to as a "pseudo-potential" function.

2.2.4 Jacobi Constant

Due to the time-independent formulation of the attracting bodies' motion, the Hamiltonian describing the acceleration of M_3 within the context of the CR3BP is not a function of time. To formulate this quantity, first consider the dot product between the rotating velocity of M_3 with its associated acceleration, given in (2.27).

$$\dot{\vec{r}} \bullet \ddot{\vec{r}} = \dot{x}\ddot{x} + \dot{y}\ddot{y} + \dot{z}\ddot{z} = \dot{\vec{r}} \bullet \nabla\Omega \tag{2.27}$$

Furthermore, if:

$$\dot{\vec{r}} \bullet \ddot{\vec{r}} = \frac{1}{2}\frac{d}{dt}\left(\dot{\vec{r}} \bullet \dot{\vec{r}}\right) \tag{2.28}$$

and

$$\dot{\vec{r}} \bullet \nabla\Omega = \frac{\partial \Omega}{\partial x}\frac{\partial x}{\partial t} + \frac{\partial \Omega}{\partial y}\frac{\partial y}{\partial t} + \frac{\partial \Omega}{\partial z}\frac{\partial z}{\partial t} = \frac{d\Omega}{dt} \tag{2.29}$$

then via (2.27), equations (2.28) and (2.29) may be equated. By integrating the resulting expression with respect to non-dimensional time

$$\frac{1}{2}\int\left(\frac{d}{dt}\left(\dot{\vec{r}}\bullet\dot{\vec{r}}\right)\right)dt=\int\left(\frac{d\Omega}{dt}\right)dt$$

the result may be solved for the constant of integration, a quantity which is termed the Jacobi Constant (JC).

$$JC=2\Omega-v^2 \tag{2.30}$$

Where $v=||\dot{\vec{r}}||$. While only having a single integral of motion, analysis of the CR3BP still benefits greatly from the existence of this solution. The Jacobi Constant represents an "energy-like" quantity attributed to the state of M_3 which, due to the pseudo-potential function being conservative, may only change with alterations in velocity. This fact may be leveraged for comparison of relative energy levels between periodic orbits or ballistically propagated transfer arcs. Equation (2.30) demonstrates that an increase in speed of M_3 results in a *decrease* in Jacobi Constant value. Since the energy-like quantity is constant, its value cannot be altered unless an external stimulus acts upon M_3. Some celestial objects represented as the third body may alter their Jacobi Constant via outgassing, though an application relevant to the investigation is a spacecraft expending propellant. In response to this, M_3 will be referred to as a spacecraft throughout the document.

2.2.5 Equilibrium Solutions

In the CR3BP, there exist locations at which the summation of the accelerations acting upon the spacecraft, including both gravitational and centripetal, equals zero. These locations are known as "equilibrium", "Lagrange" or "libration" points, and serve as spots where non-moving objects indefinitely remain still, as depicted in the rotating frame. To find these positions, first revisit the CR3BP equations of motion (equation (2.24)) under the assumption that $\dot{\vec{r}}=\ddot{\vec{r}}=\vec{0}$.

$$x_{eq} = \frac{1-\mu}{r_{13}^3}(x_{eq}+\mu) + \frac{\mu}{r_{23}^3}(x_{eq}-1+\mu)$$
$$y_{eq} = \left(\frac{(1-\mu)}{r_{13}^3} + \frac{\mu}{r_{23}^3}\right) y_{eq}$$
$$0 = \left(\frac{1-\mu}{r_{13}^3} + \frac{\mu}{r_{23}^3}\right) z_{eq}$$

It is evident that the only solution for z_{eq} is zero, and $y_{eq} = 0$ satisfies its own expression as well. In the case of $y_{eq} = z_{eq} = 0$, all solutions lie along the rotating x-axis, though the precise locations may be determined using the following:

$$x_{eq} - \frac{(1-\mu)(x_{eq}+\mu)}{|x_{eq}+\mu|^3} - \frac{\mu(x_{eq}-1+\mu)}{|x_{eq}-1+\mu|^3} = 0$$

Since the presence of absolute value functions introduces a sign-dependency in the expression, each of the possible versions may be written out. In doing so, note that:

$$\frac{x_{eq}+\mu}{|x_{eq}+\mu|^3} = \begin{cases} \frac{1}{(x_{eq}+\mu)^2} & \text{if } (x_{eq}+\mu) > 0 \\ -\frac{1}{(x_{eq}+\mu)^2} & \text{if } (x_{eq}+\mu) < 0 \end{cases} \tag{2.31}$$

The case of $(x_{eq}+\mu) < 0$ automatically establishes $(x_{eq}-1+\mu) < 0$, resulting in three equations to solve, as shown by (2.32) through (2.34). The expressions for these collinear equilibrium solutions cannot be evaluated analytically, thus numerical root-finding methods are employed. The collinear point locations vary depending on the system; those pertaining to three-body systems relevant to the investigation are listed in Tables 2.1 and 2.2.

$$x_{eq} = \frac{1-\mu}{(x_{eq}+\mu)^2} + \frac{\mu}{(x_{eq}-1+\mu)^2} \tag{2.32}$$
$$x_{eq} = \frac{1-\mu}{(x_{eq}+\mu)^2} - \frac{\mu}{(x_{eq}-1+\mu)^2} \tag{2.33}$$
$$x_{eq} = -\frac{1-\mu}{(x_{eq}+\mu)^2} - \frac{\mu}{(x_{eq}-1+\mu)^2} \tag{2.34}$$

Lagrange himself uncovered the expressions for the remaining two equilibrium solutions, doing so by focusing on the non-zero solutions pertaining to y_{eq} [30].

$$\left(1 - \frac{1-\mu}{r_{13}^3} + \frac{\mu}{r_{23}^3}\right) y_{eq} = 0$$

Certainly $y_{eq} = 0$ is a standout solution, though the term within the parentheses equals zero when both r_{13} and r_{23} are equal to unity. Recalling that the distance between the two primaries is also equal to one in dimensionless units, the only location which can connect a distance to either primary as far as they are apart is the vertex of an equilateral triangle with two vertices coincident with M_1 and M_2. Since r_{13} and r_{23} are positive, the equilateral triangle may flip about the $\hat{x}$ axis to identify the location of the other equilateral Lagrange point. Expressions for these may be formed analytically, as given by (2.35).

$$\begin{aligned} x_{eq} &= 0.5 - \mu \\ y_{eq} &= \pm\frac{\sqrt{3}}{2} \end{aligned} \tag{2.35}$$

The Lagrange points are labelled from one to five, with the first three belonging to the collinear equilibrium points, the fourth being the equilateral point in the positive $\hat{y}$-direction, and the one mirrored about $\hat{x}$ is the fifth. Figure 2.3 illustrates the locations of each of the equilibrium solutions for an arbitrary M_1-M_2 system.

The method presented may determine the locations of the five equilibrium solutions for any pair of celestial bodies, though of particular interest to the investigation are the Earth-Moon and Sun-Barycenter systems. The "barycenter" in the Sun-Barycenter system is a fictitious body of mass equal to the combined Earth-Moon system, located at the Earth-Moon barycenter as it orbits the Sun. Such a model is useful in transitioning between the CR3BP and BCR4BP.

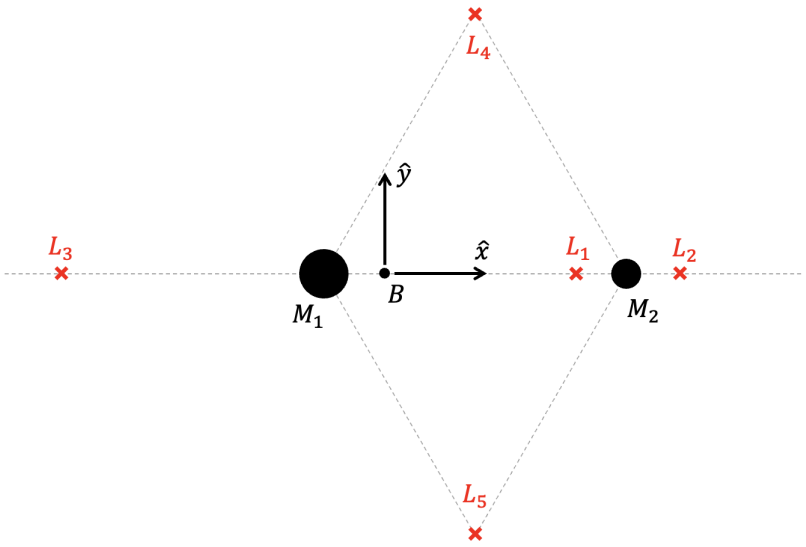

Figure 2.3. Lagrange points for an arbitrary system, viewed in the rotating reference frame

Table 2.1. Lagrange Point Positions for Earth-Moon System

Position Component	$L_1(ND)$	$L_2(ND)$	$L_3(ND)$	$L_4(ND)$	$L_5(ND)$
x_{eq}	0.836915	1.155682	-1.005063	0.487849	0.487849
y_{eq}	0	0	0	0.866025	-0.866025
z_{eq}	0	0	0	0	0

Table 2.2. Lagrange Point Positions for Sun-Barycenter System

Position Component	$L_1(ND)$	$L_2(ND)$	$L_3(ND)$	$L_4(ND)$	$L_5(ND)$
x_{eq}	0.989986	1.010075	-1.000001	0.499997	0.499997
y_{eq}	0	0	0	0.866025	-0.866025
z_{eq}	0	0	0	0	0

2.2.6 Symmetry

A beneficial feature of the N-body problem is the existence of symmetric properties, which are often crucial for periodic orbit construction. In the CR3BP, there exist two primary forms of symmetry: one resultant from the Mirror Theorem, and another from the independence of spatial and planar dynamics within the equations of motion. Focusing on the former, the Mirror theorem was first published by Roy and Ovenden in 1955 and is applicable to gravitational models of any value of N so long as other external forces are not present. A synopsis of the Mirror Theorem is that for any position ($\vec{R}_{\mathrm{i}}$) and velocity vector ($\dot{\vec{R}}_{\mathrm{j}}$), where $\mathrm{i,j} = 1, 2, \cdots, N$, a mirrored configuration exists if either scenario is true [31]:

1. If all position vectors $\vec{R}_{\mathrm{i}}$ are aligned (parallel or anti-parallel), and if all velocity vectors $\dot{\vec{R}}_{\mathrm{j}}$ are perpendicular with each position vector.

2. If all velocity vectors $\dot{\vec{R}}_{\mathrm{j}}$ are aligned, and if all position vectors $\vec{R}_{\mathrm{i}}$ are perpendicular with each velocity vector.

While the position and velocity vectors described were analyzed in the context of an inertial reference frame, the same results still hold true within the rotating frame. Since the motion of the primaries is assumed to be circular and on opposite ends of their barycenter, the angle between both their own and each others position and velocity vectors will always be 90 degrees. Additionally, when viewed within the lens of the rotating reference frame, the position and velocity vectors of either primary are permanently collinear with the $\hat{x}$ and $\hat{y}$ directions respectively. As a result, the Mirror Theorem within the context of the CR3BP rotating frame is solely focused on the position and velocity of the spacecraft. The previous axioms may be simplified to accommodate this new perspective:

1. If the spacecraft is located along the $\hat{x}$ axis, and its velocity is either parallel or anti-parallel to the $\hat{y}$ axis.

2. If the spacecraft is located within the $\hat{x}$-$\hat{z}$ plane, and its velocity is normal to the plane.

Since the second item encompasses the first, it becomes the working rule for applying the Mirror Theorem to a spacecraft trajectory within the CR3BP rotating frame. Within the

CR3BP, a "mirrored configuration" is one that has a beginning state satisfying the above condition and a subsequent trajectory $\hat{x}$-$\hat{z}$ symmetric to that produced by propagating the initial state in reverse time. For example, consider the non-dimensional initial state in the Earth-Moon rotating frame, $\vec{x}$ where $\vec{x} = \begin{bmatrix} 0.5 & 0 & 0.2 & 0 & 0.1 & 0 \end{bmatrix}^T$. Propagating $\vec{x}$ for 0.2 (as shown in blue) and -0.2 (orange) non-dimensional time units in the CR3BP, the resulting mirrored trajectories may be viewed in Figure 2.4

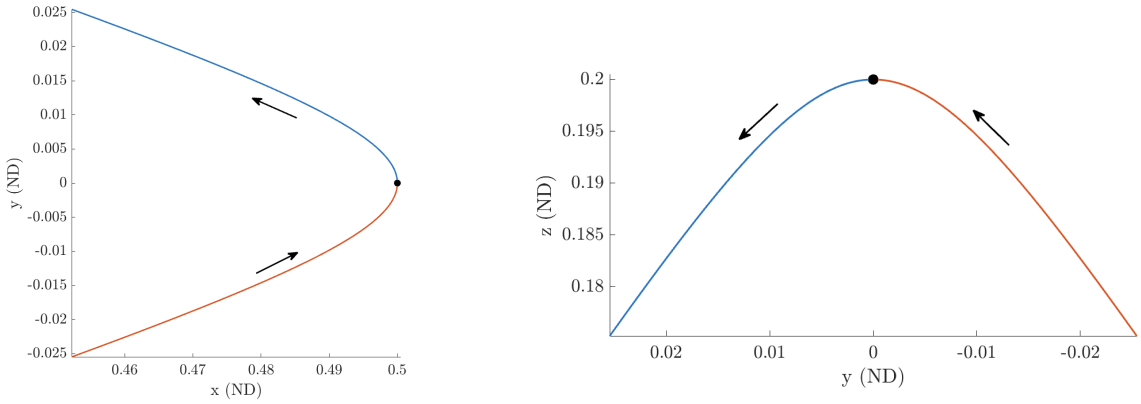

(a) $\hat{x}$-$\hat{y}$ projection

(b) $\hat{y}$-$\hat{z}$ projection

Figure 2.4. Propagation of $\vec{x}$ forward and backward in time. Position of $\vec{x}$ marked with black dot, arrows outline path taken by spacecraft.

Should a trajectory ballistically propagated from an initial state satisfying the terms of the Mirror Theorem again have a perpendicular crossing with the $\hat{x}$-$\hat{z}$ plane, this motion would be considered periodic in the rotating reference frame. This is because the reverse-time propagation would meet the second perpendicular crossing, matching its state, and thus enclosing the path in a continuous loop.

Symmetry about the $\hat{x}$-$\hat{z}$ plane may be determined using the Mirror Theorem, though the CR3BP equations of motion also admit latent symmetry about the $\hat{x}$-$\hat{z}$ plane as well. Again considering the CR3BP equations of motion in (2.24), the dynamics for the in-plane motion are co-dependent upon each other's motion. In other words, $\ddot{x}$ is an explicit function of $\dot{y}$ and visa versa, but neither $\ddot{x}$ nor $\ddot{y}$ are explicit functions of $\dot{z}$. Moreover, $\ddot{x}$ and $\ddot{y}$ are only explicit functions of z^2, meaning that changes in the sign of z do not affect the in-plane dynamics. Should an initial spatial state have its z component mirrored across the $\hat{x}$-$\hat{y}$ plane,

and subsequently its $\dot{z}$ value reflected as well, the planar dynamics of the resultant trajectory would remain unaffected. An example of this is demonstrated in Figure 2.5 where an initial state (in blue), $\vec{x} = \begin{bmatrix} 0.3 & 0.2 & 0.1 & -0.1 & -0.5 & 0.4 \end{bmatrix}^T$ and its spatial reflection (in orange) are both propagated for $+0.3$ non-dimensional time units.

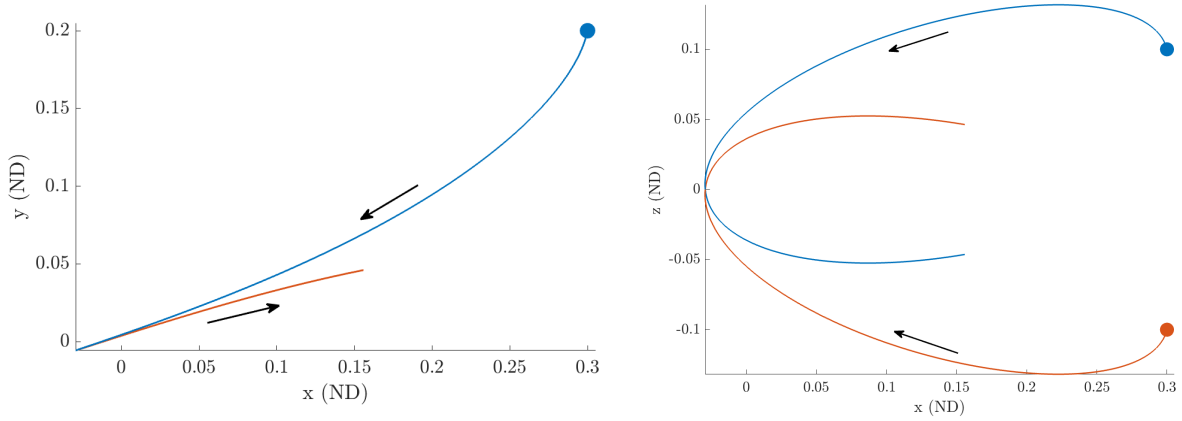

(a) $\hat{x}$-$\hat{y}$ projection

(b) $\hat{x}$-$\hat{z}$ projection

Figure 2.5. Comparison of spatially mirrored trajectories. Arrows indicate direction of motion, dots show the initial positions for their respective arcs.

Both forms of symmetry weigh heavily on the construction of transfers to cislunar orbits, as the Mirror Theorem and its corollary are instrumental for the convergence of periodic orbits, and spatial symmetry implies that all non-planar transit legs exist in symmetrical pairs.

2.3 The Bi-Circular Restricted 4-Body Problem

The BCR4BP is a dynamical model which, through reasonable assumptions, models the motion of a spacecraft in an $N = 4$ environment, with particular attention paid to the Sun-Earth-Moon system for this investigation. This section establishes the assumptions and kinematics necessary for the construction of the equations of motion, as well as analysis into the system Hamiltonian, and instantaneous equilibrium solutions. Moreover, all relevant information will be introduced in terms of the two separate rotating reference frames em-

ployed by the BCR4BP. Lastly, a method for transforming between the two rotating reference frames is presented.

2.3.1 Assumptions

Much like the CR3BP, the BCR4BP assumes that the smallest of the four bodies is of negligible mass as compared to the other three, and as such, does not affect their motion. In keeping with the convention laid out by the CR3BP, the smallest mass is denoted M_3. Moreover, masses M_1 and M_2 orbit about their shared barycenter, B_1. The motion of this center of mass is then modeled as a closed circular orbit about the largest mass in the system, M_4. As a result, both M_4 and B_1 may be modeled to traverse circular paths about their shared barycenter, B_2.

Regarding the Sun-Earth-Moon system, the two planes of motion (Sun-B_1 and Earth-Moon) are skewed by an average angle of about 5.15 degrees [32]. There is no restriction on the inclination between the two planes of motion in the general BCR4BP, though for cases where the two planes are sufficiently close in inclination, it may be assumed that the angle between the two planes is zero. With the skew-planar configuration, an evolving ascending node variable will need to be introduced in order to track the paths of both bodies in one plane with respect to another. By assuming co-planar motion, the dimensionality of the analysis is lessened by one. Moreover, the periodicity of the dynamics is made more consistent, as in the case of the Sun-Earth-Moon system, the three attracting bodies would realign each synodic month, rather than the time period between solar eclipses. Due to its simplicity and relatively small deviation from nature, a co-planar configuration of the Sun-Earth-Moon BCR4BP will be utilized by this investigation. A depiction of the co-planar BCR4BP is provided in Figure 2.6.

A drawback of the assumptions made is that the BCR4BP is a dynamically incoherent system, as the gravitational forces of each of the three larger bodies may all influence the motion of the spacecraft, but the gravitational force of M_4 does not individually act upon M_1 or M_2. As a result, the Bi-Circular 4-Body Problem overestimates the net solar force acting upon the body by neglecting the indirect acceleration caused by the Sun pulling

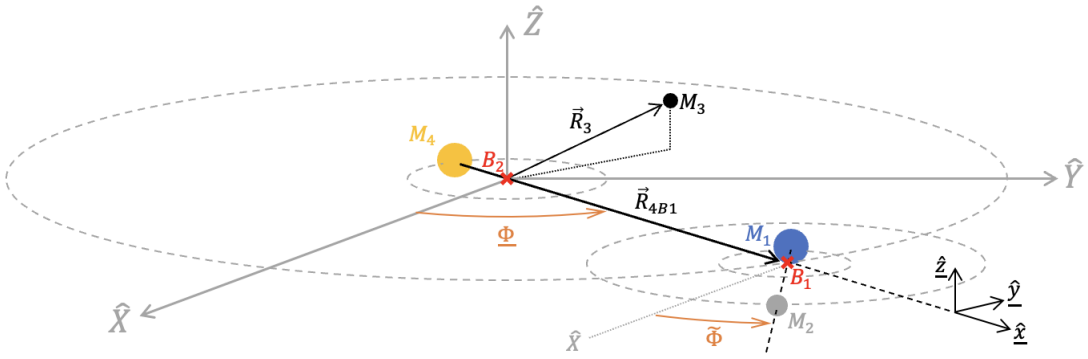

Figure 2.6. Motion of primaries as modeled in the Co-planar Bi-Circular Restricted 4-Body Problem

on the other attracting bodies. This has demonstrated challenges in transitioning select long-term cislunar periodic trajectories from the BCR4BP to a higher-fidelity ephemeris model [33]. Fortunately, the construction of transfer trajectories with transient passages by either the Earth or Moon is minimally affected by this shortcoming, and the simulation of three simultaneous gravitational sources creates a convenient method for propagating lunar transfers in a single model.

2.3.2 Kinematics: Earth-Moon Frame

While the motion of M_3 in the BCR4BP may be modeled in an inertial reference frame, the usage of rotating coordinate systems has the benefit of illustrating the spacecraft's path with respect to relevant gravitational bodies. Appropriate choices in reference frames may also lead to a simplified implementation of the Mirror Theorem. Much like in the CR3BP, the rotating reference frame matching the Moon's motion about the Earth, or the Earth-Moon frame, may be utilized in the BCR4BP. Due to the existence of two relevant rotating frames within the Bi-Circular Restricted 4-Body Problem, directions and quantities evaluated in the Earth-Moon frame are distinguished with a tilde. For instance, the direction of the Moon's position vector with respect to the Earth is represented with $\tilde{\hat{x}}$, while $\tilde{\hat{z}}$ is along the Moon's angular momentum about the Earth, and $\tilde{\hat{y}} = \tilde{\hat{y}} \times \tilde{\hat{x}}$. A diagram of the motion of a spacecraft, M_3 within the Earth-Moon frame is provided by Figure 2.7.

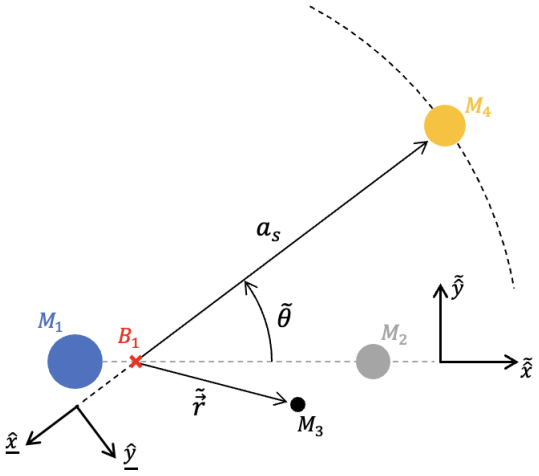

Figure 2.7. Motion of M_3 and M_4 as viewed in the Earth-Moon frame

The direction from the Sun to the Earth-Moon barycenter, B_1 is shown in Figure 2.6 to be $\hat{\underline{x}}$, and its dimensional distance is represented with R_4. Since the rotation rates of the Sun-B_1 and Earth-Moon reference frames differ, the position of the Sun in the Earth-Moon reference frame evolves over time. This motion is related to the $\tilde{\hat{x}}$-$\tilde{\hat{y}}$-$\tilde{\hat{z}}$ coordinate frame via the sun angle, $\tilde{\theta}$, measured from $\tilde{\hat{x}}$ to $-\hat{\underline{x}}$. A benefit of the circular paths assumption is that the rotation rates of both reference frames are constant, thus $\tilde{\theta}$ evolves linearly with time. The dimensional position of the spacecraft relative to B_1 in the Earth-Moon rotating frame is given by $\tilde{\vec{R}}$, which may be defined in terms of Earth-Moon rotating coordinates as shown in (2.36).

$$\tilde{\vec{R}} = \tilde{X}\tilde{\hat{x}} + \tilde{Y}\tilde{\hat{y}} + \tilde{Z}\tilde{\hat{z}} \tag{2.36}$$

Moreover, the positions of the Earth and Moon may be expressed along the $\tilde{\hat{x}}$ axis to be:

$$\tilde{\vec{R}}_1 = -R_1\tilde{\hat{x}} \tag{2.37}$$

$$\tilde{\vec{R}}_2 = R_2\tilde{\hat{x}} \tag{2.38}$$

The x-axis of the other rotating reference frame, that from the Sun to B_1, may be leveraged to formulate the position vector of the Sun, $\tilde{\vec{R}}_4$. The unit vector associated with this axis,

$\underline{\hat{x}}$ may be represented in terms of Earth-Moon coordinates as $\underline{\hat{x}} = -\cos\tilde{\theta}\tilde{\hat{x}} - \sin\tilde{\theta}\tilde{\hat{y}}$. This substitution is performed in (2.39).

$$\tilde{\vec{R}}_4 = -R_4\underline{\hat{x}} = R_4\left(\cos\tilde{\theta}\tilde{\hat{x}} + \sin\tilde{\theta}\tilde{\hat{y}}\right) \tag{2.39}$$

Using equations (2.36) through (2.39), the relative positions of the spacecraft with respect to each of the attracting bodies may be expressed in the Earth-Moon rotating frame.

$$\tilde{\vec{R}}_{13} = \tilde{\vec{R}} - \tilde{\vec{R}}_1 = \left(\tilde{X} + R_1\right)\tilde{\hat{x}} + \tilde{Y}\tilde{\hat{y}} + \tilde{Z}\tilde{\hat{z}} \tag{2.40}$$

$$\tilde{\vec{R}}_{23} = \tilde{\vec{R}} - \tilde{\vec{R}}_2 = \left(\tilde{X} - R_2\right)\tilde{\hat{x}} + \tilde{Y}\tilde{\hat{y}} + \tilde{Z}\tilde{\hat{z}} \tag{2.41}$$

$$\tilde{\vec{R}}_{43} = \tilde{\vec{R}} - \tilde{\vec{R}}_4 = \left(\tilde{X} - R_4\cos\tilde{\theta}\right)\tilde{\hat{x}} + (\tilde{Y} - R_4\sin\tilde{\theta})\tilde{\hat{y}} + \tilde{Z}\tilde{\hat{z}} \tag{2.42}$$

The governing equation for the development of the BCR4BP equations of motion is, similar to the case of the CR3BP, Newton's law of universal gravitation. This equation requires the position vector $\tilde{\vec{R}}$ to be measured with respect to an inertial location. With the assumption of no external forces acting upon the four-body system, this spot would be the system center of mass, or B_2. The position of the spacecraft with respect to B_2 may be formulated in the Earth-Moon rotating coordinate frame, as shown in equation (2.43).

$$\begin{aligned}\tilde{\vec{R}}_{B_23} &= \tilde{\vec{R}} + \tilde{\vec{R}}_{B_2B_1} \\ &= \tilde{X}\tilde{\hat{x}} + \tilde{Y}\tilde{\hat{y}} + \tilde{Z}\tilde{\hat{z}} + R_{B_2B_1}\underline{\hat{x}} \\ &= (\tilde{X} - R_{B_2B_1}\cos\tilde{\theta})\tilde{\hat{x}} + (\tilde{Y} - R_{B_2B_1}\sin\tilde{\theta})\tilde{\hat{y}} + \tilde{Z}\tilde{\hat{z}}\end{aligned} \tag{2.43}$$

Using equations (2.40) through (2.43), Section 2.3.4 constructs the BCR4BP equations of motion within the context of the Earth-Moon rotating frame.

2.3.3 Kinematics: Sun-Barycenter Frame

Modelling the motion of an arbitrary spacecraft through the lens of the Sun-Barycenter, or Sun-B_1 rotating reference frame follows a similar process to that shown in Section 2.3.2. The Sun-Barycenter rotating coordinate system may be formally defined as the $\underline{\hat{x}}$-$\underline{\hat{y}}$-$\underline{\hat{z}}$ or-

thonormal triad where $\hat{x}$ is the unit vector along the direction from the Sun to B_1, $\hat{z}$ is the unit vector along the angular momentum vector of B_1 about B_2, and $\hat{y} = \hat{z} \times \hat{x}$. It may be noted that the Earth-Moon rotating frame tracks two of the three attracting bodies by the nature of its definition. In contrast, these two bodies are in motion about their fixed-position center of mass within the Sun-Barycenter coordinate system. This behavior is visualized in Figure 2.8.

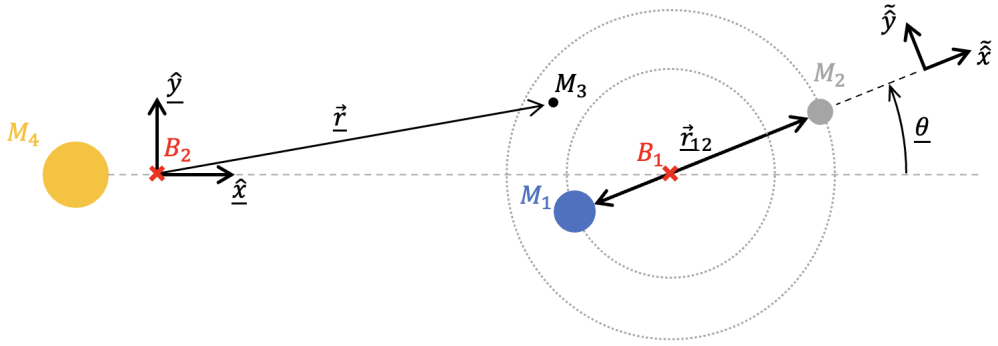

Figure 2.8. Motion of M_1, M_2 and M_3 as viewed in the Sun-B_1 frame

The lowercase position vectors in Figure 2.8 refer to the non-dimensional counterparts for the position vectors constructed in this section. Within the context of the Sun-Barycenter frame, the two sets of rotating coordinates may be related using the Moon angle, θ. From visual inspection, it is concluded that $\tilde{\hat{x}} = \cos\theta\, \hat{x} + \sin\theta\, \hat{y}$. Moreover, it may be noted that the Moon angle is zero when the Sun and Moon are on opposite sides of the Earth, though this orientation corresponds to a Sun angle of 180 degrees. The evolution of the Moon and Sun angles is one-to-one, a relationship demonstrated by (2.44) (when measured in radians).

$$\theta = \pi - \tilde{\theta} \tag{2.44}$$

The position vector of the spacecraft relative to B_2 may be expressed in Sun-Barycenter coordinates, as given in (2.45).

$$\vec{R} = X\, \hat{x} + Y\, \hat{y} + Z\, \hat{z} \tag{2.45}$$

The dimensional position vectors of the attracting bodies may be formulated as shown by equations (2.46) through (2.48).

$$\underline{\vec{R}}_1 = \underline{\vec{R}}_{B_2B_1} + \underline{\vec{R}}_{B_11} = R_{B_2B_1}\underline{\hat{x}} - R_1\tilde{\hat{x}} = (R_{B_2B_1} - R_1\cos\underline{\theta})\,\underline{\hat{x}} - R_1\sin\underline{\theta}\;\underline{\hat{y}} + \underline{Z}\;\underline{\hat{z}} \tag{2.46}$$

$$\underline{\vec{R}}_2 = \underline{\vec{R}}_{B_2B_1} + \underline{\vec{R}}_{B_12} = R_{B_2B_1}\underline{\hat{x}} + R_2\tilde{\hat{x}} = (R_{B_2B_1} + R_2\cos\underline{\theta})\,\underline{\hat{x}} + R_2\sin\underline{\theta}\;\underline{\hat{y}} + \underline{Z}\;\underline{\hat{z}} \tag{2.47}$$

$$\underline{\vec{R}}_4 = -R_4\underline{\hat{x}} \tag{2.48}$$

Relating (2.45) with (2.46) through (2.48), the location of the spacecraft relative to each of the attracting bodies may be introduced.

$$\underline{\vec{R}}_{13} = \underline{\vec{R}} - \underline{\vec{R}}_1 = (\underline{X} + R_1\cos\underline{\theta} - R_{B_2B_1})\,\underline{\hat{x}} + (\underline{Y} + R_1\sin\underline{\theta})\,\underline{\hat{y}} + \underline{Z}\;\underline{\hat{z}} \tag{2.49}$$

$$\underline{\vec{R}}_{23} = \underline{\vec{R}} - \underline{\vec{R}}_2 = (\underline{X} - R_2\cos\underline{\theta} - R_{B_2B_1})\,\underline{\hat{x}} + (\underline{Y} - R_2\sin\underline{\theta})\,\underline{\hat{y}} + \underline{Z}\;\underline{\hat{z}} \tag{2.50}$$

$$\underline{\vec{R}}_{43} = \underline{\vec{R}} - \underline{\vec{R}}_4 = (\underline{X} + R_4)\,\underline{\hat{x}} + \underline{Y}\;\underline{\hat{y}} + \underline{Z}\;\underline{\hat{z}} \tag{2.51}$$

Since the origin of the Sun-Barycenter frame is also the inertially-fixed centerpoint of the BCR4BP, the derivation of the Sun-B_1 equations of motion can be sufficiently performed with $\underline{\vec{R}}$ as it is defined in (2.45). This process is more thoroughly detailed in Section 2.3.5.

2.3.4 Equations of Motion: Earth-Moon Frame

The derivation for the equations of motion for the BCR4BP, regardless of reference frame, begins with the expansion of Newton's law of universal gravitation. Applying equation (2.3) to the case of $N = 4$ and simplifying:

$$\vec{R}_3'' = -\tilde{G}\frac{M_1}{R_{13}^3}\vec{R}_{13} - \tilde{G}\frac{M_2}{R_{23}^3}\vec{R}_{23} - \tilde{G}\frac{M_4}{R_{43}^3}\vec{R}_{43} \tag{2.52}$$

Recall that the derivative of the position vector $\vec{R}_3$ is with respect to an inertial reference frame. In order to represent the dynamics within the scope of the Earth-Moon rotating frame, each position vector in (2.52) is expressed in $\tilde{\hat{x}}$-$\tilde{\hat{y}}$-$\tilde{\hat{z}}$ coordinates. Similar to the case of the CR3BP, the Transport Theorem will be required to take the second time-derivative

of the Sun-B_1 counterpart for $\vec{R}_3$. Using equations (2.40) through (2.43) for substituting in $\tilde{\vec{R}}_{B_2 3}$ for $\vec{R}_3$ as well as the Earth-Moon rotating counterparts for $\vec{R}_{13}$, $\vec{R}_{23}$ and $\vec{R}_{43}$:

$$\mathcal{I}\tilde{\vec{R}}''_{B_2 3} = -\tilde{G}\frac{M_1}{\tilde{R}_{13}^3}\tilde{\vec{R}}_{13} - \tilde{G}\frac{M_2}{\tilde{R}_{23}^3}\tilde{\vec{R}}_{23} - \tilde{G}\frac{M_4}{\tilde{R}_{43}^3}\tilde{\vec{R}}_{43} \tag{2.53}$$

The representation of the universal gravitational constant with a tilde, $\tilde{G}$ still indicates it is a dimensional quantity for consistency with the CR3BP derivation. Its Earth-Moon non-dimensional counterpart, G, is formulated by equation (2.14).

Before proceeding, relevant non-dimensionalization parameters may be defined. Since the normalization should be with regard to the Earth-Moon rotating frame, the characteristic length, mass and time are all based upon the Earth-Moon system, similar to those used in the CR3BP. The characteristic length, $\tilde{\ell}^*$ is defined to be the average length between the Earth and Moon. The total mass of the Earth-Moon system is the characteristic mass in the Earth-Moon frame, $\tilde{m}^*$. Lastly, the characteristic time is defined to be the reciprocal of the rotating frame's mean motion, N_{EM}. Formal definitions for each of these quantities are provided in (2.54), while their values are given in Table 2.3

$$\begin{aligned} \tilde{\ell}^* &= R_1 + R_2 \\ \tilde{m}^* &= M_1 + M_2 \\ \tilde{t}^* &= \sqrt{\frac{\tilde{\ell}^{*3}}{\tilde{G}\tilde{m}^*}} = \frac{1}{N_{EM}} \end{aligned} \tag{2.54}$$

The angles associated with rotations of the Sun-Barycenter and Earth-Moon coordinate systems with respect to the inertial frame are $\underline{\Phi}$ and $\tilde{\Phi}$ respectively, as depicted in Figure 2.6. A result of the model's Bi-Circular path assumption is that both $\underline{\Phi}$ and $\tilde{\Phi}$ have constant rates of change, N_{SB} and N_{EM}, respectively. The rate of change of the Earth-Moon frame, similar to the case in the CR3BP, becomes unity when non-dimensionalized with respect to its own frame (i.e. $\tilde{n}_{EM} = 1$).

Table 2.3. Values for Characteristic Quantities of the Earth-Moon System

	$\tilde{\ell}^*$ (km)	$\tilde{m}^*$ (kg)	$\tilde{t}^*$ (seconds)	$\tilde{t}^*$ (days)
Value	384748	403503	375700	4.3484

The Earth-Moon normalized rate of change of the Sun-Barycenter frame with respect to the inertial coordinate system, $\tilde{n}_{SB}$ may be related to its dimensional counterpart as follows:

$$\tilde{n}_{SB} = N_{SB}\tilde{t}^* = \sqrt{\frac{\tilde{G}(M_4 + \tilde{m}^*)}{\tilde{R}_4^3}}\sqrt{\frac{\tilde{\ell}^{*3}}{\tilde{G}\tilde{m}^*}} \tag{2.55}$$

The non-dimensional time rate of change of the Sun angle as viewed in the Earth-Moon rotating frame is the normalized rate of change of the Earth-Moon frame subtracted from that of the Sun-Barycenter frame, or $\dot{\tilde{\theta}} = \tilde{n}_{SB} - \tilde{n}_{EM}$. Intuitively, the rate of rotation of the Moon about the Earth is far greater than that of the Earth about the Sun, thus the value of $\dot{\tilde{\theta}}$ is negative. As a result, while the Sun angle is measured counter-clockwise within the Earth-Moon frame, its natural evolution is in the opposite direction. Quantities pertaining to the Sun may also be non-dimensionalized with respect to the Earth-Moon system.

$$a_s = \frac{R_4}{\tilde{\ell}^*} \tag{2.56}$$

$$\tilde{m}_s = \frac{M_4}{\tilde{m}^*} \tag{2.57}$$

Using equations (2.56) and (2.57), $\tilde{n}_{SB}$ may be expressed using dimensionless parameters.

$$\tilde{n}_{SB} = \sqrt{\frac{\tilde{G}(M_4 + \tilde{m}^*)}{\tilde{R}_4^3}}\sqrt{\frac{\tilde{\ell}^{*3}}{\tilde{G}\tilde{m}^*}} = \sqrt{\frac{\tilde{m}_s + 1}{a_s^3}} \tag{2.58}$$

A non-dimensional mass parameter, $\tilde{\mu}$, may be introduced to normalize the individual masses of the Earth and Moon.

$$\tilde{\mu} = \frac{M_2}{\tilde{m}^*} = 1 - \frac{M_1}{\tilde{m}^*} \tag{2.59}$$

Since the distances of the Earth and Moon are inversely related to the proportions of their masses with regard to $\tilde{m}^*$, the mass parameter may also be used to describe the positions of M_1 and M_2, as shown in (2.60) and (2.61).

$$\tilde{\vec{r}}_1 = \frac{\tilde{\vec{R}}_1}{\tilde{\ell}^*} = -\tilde{\mu}\hat{\tilde{x}} \tag{2.60}$$

$$\tilde{\vec{r}}_2 = \frac{\tilde{\vec{R}}_2}{\tilde{\ell}^*} = (1-\tilde{\mu})\,\hat{\tilde{x}} \tag{2.61}$$

The non-dimensionalized position of the Sun with respect to B_1 is:

$$\tilde{\vec{r}}_4 = \frac{\tilde{\vec{R}}_4}{\tilde{\ell}^*} = a_s\left(\cos\tilde{\theta}\hat{\tilde{x}} + \sin\tilde{\theta}\hat{\tilde{y}}\right) \tag{2.62}$$

The position vector of the spacecraft with respect to the Earth-Moon barycenter may be normalized as well:

$$\tilde{\vec{r}} = \frac{\tilde{\vec{R}}}{\tilde{\ell}^*} = \tilde{x}\hat{\tilde{x}} + \tilde{y}\hat{\tilde{y}} + \tilde{z}\hat{\tilde{z}} \tag{2.63}$$

With the normalized locations of each body defined, the dimensionless relative position vectors may be constructed.

$$\begin{aligned}
\tilde{\vec{r}}_{13} &= \frac{\tilde{\vec{R}}_{13}}{\tilde{\ell}^*} = (\tilde{x}+\tilde{\mu})\hat{\tilde{x}} + \tilde{y}\hat{\tilde{y}} + \tilde{z}\hat{\tilde{z}} \\
\tilde{\vec{r}}_{23} &= \frac{\tilde{\vec{R}}_{23}}{\tilde{\ell}^*} = (\tilde{x}-(1-\tilde{\mu}))\hat{\tilde{x}} + \tilde{y}\hat{\tilde{y}} + \tilde{z}\hat{\tilde{z}} \\
\tilde{\vec{r}}_{43} &= \frac{\tilde{\vec{R}}_{43}}{\tilde{\ell}^*} = (\tilde{x}-a_s\cos\tilde{\theta})\hat{\tilde{x}} + (\tilde{y}-a_s\sin\tilde{\theta})\hat{\tilde{y}} + \tilde{z}\hat{\tilde{z}}
\end{aligned} \tag{2.64}$$

Returning to equation (2.53), the second dimensional time derivative of $\tilde{\vec{R}}_{B_23}$ viewed in the inertial frame is evaluated as follows:

$${}^{\mathcal{I}}\tilde{\vec{R}}''_{B_23} = {}^{\mathcal{I}}\tilde{\vec{R}}'' + {}^{\mathcal{I}}\tilde{\vec{R}}''_{B_2B_1} \tag{2.65}$$

Where expressions for the two position vectors on the right-hand side are provided in terms of Earth-Moon rotating coordinates via (2.36) and (2.43). Since neither quantity is in terms of inertial coordinates, the Transport Theorem will be necessary for deriving both. Recalling that the angular velocity of the Earth-Moon frame with respect to the inertial frame, ${}^{\mathcal{I}}\vec{\omega}^{\mathcal{E}}$ is equal to $N_{EM}\tilde{\hat{z}}$, the first and second inertial derivatives of $\tilde{\vec{R}}$ are outlined in (2.66).

$$\begin{aligned} {}^{\mathcal{I}}\tilde{\vec{R}}' &= (\tilde{X}' - N_{EM}\tilde{Y})\tilde{\hat{x}} + (\tilde{Y}' + N_{EM}\tilde{X})\tilde{\hat{y}} + \tilde{Z}'\tilde{\hat{z}} \\ {}^{\mathcal{I}}\tilde{\vec{R}}'' &= (\tilde{X}'' - 2N_{EM}\tilde{Y}' - N_{EM}^2\tilde{X})\tilde{\hat{x}} + (\tilde{Y}'' + 2N_{EM}\tilde{X}' - N_{EM}^2\tilde{Y})\tilde{\hat{y}} + \tilde{Z}''\tilde{\hat{z}} \end{aligned} \tag{2.66}$$

The acceleration vector may be represented in terms of non-dimensional variables, recalling that the primes may be converted to dots via (2.22) and (2.23):

$${}^{\mathcal{I}}\tilde{\vec{R}}'' = \ddot{\tilde{r}}\frac{\tilde{\ell}^*}{\tilde{t}^{*2}} = \frac{\tilde{\ell}^*}{\tilde{t}^{*2}}(\ddot{\tilde{x}} - 2\tilde{n}_{EM}\dot{\tilde{y}} - \tilde{n}_{EM}^2\tilde{x})\tilde{\hat{x}} + (\ddot{\tilde{y}} + 2\tilde{n}_{EM}\dot{\tilde{x}} - \tilde{n}_{EM}^2\tilde{y})\tilde{\hat{y}} + \ddot{\tilde{z}}\tilde{\hat{z}} \tag{2.67}$$

Since $\tilde{\vec{R}}_{B_2B_1}$ is a function of the sun angle, $\tilde{\theta}$, its time rate of change as viewed in $\mathcal{E}$ is the rotation rate of the Sun-Barycenter frame with respect to the Earth-Moon system, or $\tilde{\theta}' = (N_{SB} - N_{EM})$. With this, the Transport Theorem may be applied to $\tilde{\vec{R}}_{B_2B_1}$:

$$\begin{aligned} {}^{\mathcal{I}}\tilde{\vec{R}}'_{B_2B_1} &= N_{SB}R_{B_2B_1}\left(\sin\tilde{\theta}\tilde{\hat{x}} - \cos\tilde{\theta}\tilde{\hat{y}}\right) \\ {}^{\mathcal{I}}\tilde{\vec{R}}''_{B_2B_1} &= N_{SB}^2R_{B_2B_1}\left(\cos\tilde{\theta}\tilde{\hat{x}} + \sin\tilde{\theta}\tilde{\hat{y}}\right) = -N_{SB}^2\tilde{\vec{R}}_{B_2B_1} \end{aligned} \tag{2.68}$$

Since the distance between the two barycenters is directly related to the proportional mass of the Sun with respect to the entire system, $R_{B_2B_1}$ may be alternatively expressed as:

$$R_{B_2B_1} = R_4\left(\frac{\tilde{m}_s}{\tilde{m}_s + 1}\right) \tag{2.69}$$

Since the directions of vectors $\tilde{\vec{R}}_{B_2B_1}$ and $\tilde{\vec{R}}_4$ are anti-parallel:

$${}^{\mathcal{I}}\tilde{\vec{R}}''_{B_2B_1} = N_{SB}^2\left(\frac{\tilde{m}_s}{\tilde{m}_s + 1}\right)\tilde{\vec{R}}_4 \tag{2.70}$$

By using equations (2.55), (2.58) and (2.62), the acceleration may be related to non-dimensional quantities:

$$^{\mathcal{I}}\tilde{\vec{R}}''_{B_2B_1} = \left(\ddot{\tilde{r}}_{B_2B_1}\right)\frac{\tilde{\ell}^*}{\tilde{t}^{*2}} = \frac{\tilde{\ell}^*}{\tilde{t}^{*2}}\left(\frac{\tilde{m}_s}{a_s^3}\right)\tilde{\vec{r}}_4 \tag{2.71}$$

Replacing variables on the right-hand side of (2.53) with their non-dimensional counterparts and simplifying:

$$\begin{aligned} ^{\mathcal{I}}\tilde{\vec{R}}''_{B_23} &= \left(\frac{\tilde{\ell}^{*3}}{\tilde{m}^*\tilde{t}^{*2}}\right)\left(-\frac{\tilde{m}^*(1-\tilde{\mu})}{\tilde{\ell}^{*3}\tilde{r}_{13}^3}\tilde{\vec{r}}_{13}\tilde{\ell}^* - \frac{\tilde{m}^*(\tilde{\mu})}{\tilde{\ell}^{*3}\tilde{r}_{23}^3}\tilde{\vec{r}}_{23}\tilde{\ell}^* - \frac{\tilde{m}^*\tilde{m}_s}{\tilde{\ell}^{*3}\tilde{r}_{43}^3}\tilde{\ell}^*\tilde{\vec{r}}_{43}\right) \\ ^{\mathcal{I}}\tilde{\vec{R}}''_{B_23} &= \left(-\frac{(1-\tilde{\mu})}{\tilde{r}_{13}^3}\tilde{\vec{r}}_{13} - \frac{\tilde{\mu}}{\tilde{r}_{23}^3}\tilde{\vec{r}}_{23} - \frac{\tilde{m}_s}{\tilde{r}_{43}^3}\tilde{\vec{r}}_{43}\right)\frac{\tilde{\ell}^*}{\tilde{t}^{*2}} \end{aligned} \tag{2.72}$$

By inserting equations (2.65), (2.66) and (2.71) into (2.72) and simplifying, the vector form of the Earth-Moon BCR4BP equations of motion is defined.

$$\ddot{\tilde{\vec{r}}} = -\frac{1-\tilde{\mu}}{\tilde{r}_{13}^3}\tilde{\vec{r}}_{13} - \frac{\tilde{\mu}}{\tilde{r}_{23}^3}\tilde{\vec{r}}_{23} - \frac{\tilde{m}_s}{\tilde{r}_{43}^3}\tilde{\vec{r}}_{43} - \frac{\tilde{m}_s}{a_s^3}\tilde{\vec{r}}_4 \tag{2.73}$$

Recalling that $\tilde{n}_{EM} = 1$, the scalar second-order differential equations may be represented as such:

$$\begin{aligned} \ddot{\tilde{x}} &= 2\dot{\tilde{y}} + \tilde{x} - \frac{(1-\tilde{\mu})(\tilde{x}+\tilde{\mu})}{\tilde{r}_{13}^3} - \frac{\tilde{\mu}(\tilde{x}+\tilde{\mu}-1)}{\tilde{r}_{23}^3} - \frac{\tilde{m}_s(\tilde{x}-a_s\cos\tilde{\theta})}{\tilde{r}_{43}^3} - \frac{\tilde{m}_s}{a_s^2}\cos\tilde{\theta} \\ \ddot{\tilde{y}} &= \tilde{y} - 2\dot{\tilde{x}} - \frac{(1-\tilde{\mu})\tilde{y}}{\tilde{r}_{13}^3} - \frac{\tilde{\mu}\tilde{y}}{\tilde{r}_{23}^3} - \frac{\tilde{m}_s(\tilde{y}-a_s\sin\tilde{\theta})}{\tilde{r}_{43}^3} - \frac{\tilde{m}_s}{a_s^2}\sin\tilde{\theta} \\ \ddot{\tilde{z}} &= -\frac{(1-\tilde{\mu})\tilde{z}}{\tilde{r}_{13}^3} - \frac{\tilde{\mu}\tilde{z}}{\tilde{r}_{23}^3} - \frac{\tilde{m}_s\tilde{z}}{\tilde{r}_{43}^3} \end{aligned} \tag{2.74}$$

Similar to the CR3BP, a scalar pseudo-potential function, $\tilde{\Omega}$, may be defined to simplify the equations of motion.

$$\tilde{\Omega} = \frac{1}{2}\left(\tilde{x}^2+\tilde{y}^2\right) + \frac{1-\tilde{\mu}}{\tilde{r}_{13}} + \frac{\tilde{\mu}}{\tilde{r}_{23}} + \frac{\tilde{m}_s}{\tilde{r}_{43}} - \frac{\tilde{m}_s}{a_s^2}\left(\tilde{x}\cos\tilde{\theta}+\tilde{y}\sin\tilde{\theta}\right) \tag{2.75}$$

While the gradient of the pseudo-potential is not the inertial vector force field acting upon the spacecraft, it can be used to largely describe the scalar equations of motion.

$$\begin{aligned} \ddot{\tilde{x}} &= \frac{\partial \tilde{\Omega}}{\partial \tilde{x}} + 2\dot{\tilde{y}} \\ \ddot{\tilde{y}} &= \frac{\partial \tilde{\Omega}}{\partial \tilde{y}} - 2\dot{\tilde{x}} \\ \ddot{\tilde{z}} &= \frac{\partial \tilde{\Omega}}{\partial \tilde{z}} \end{aligned} \tag{2.76}$$

2.3.5 Equations of Motion: Sun-Barycenter Frame

Similar to the case of the Earth-Moon frame, the derivation of the equations of motion for the Sun-Barycenter frame begin with the expansion of Newton's law of gravitation, previously done in equation (2.52). In this coordinate system, the origin doubles as the system's inertial centerpoint. As a result, the derivation of the equations of motion does not need to account for a shift in anchor-point of the spacecraft's position vector. Populating equation (2.52) with relevant position vectors defined in Section 2.3.3:

$$\underline{\vec{R}}'' = -\tilde{G}\frac{M_1}{\underline{R}_{13}^3}\underline{\vec{R}}_{13} - \tilde{G}\frac{M_2}{\underline{R}_{23}^3}\underline{\vec{R}}_{23} - \tilde{G}\frac{M_4}{\underline{R}_{43}^3}\underline{\vec{R}}_{43} \tag{2.77}$$

Since the spacecraft position vector is given by (2.45) in terms of Sun-B_1 rotating coordinates, the Transport Theorem is necessary for taking its first and second derivatives with respect to an inertial coordinate frame. The angular velocity from the inertial to the Sun-Barycenter frame, ${}^{\mathcal{I}}\vec{\omega}^{\mathcal{S}}$ is $N_{SB}\hat{\underline{z}}$.

$$\begin{aligned} {}^{\mathcal{I}}\underline{\vec{R}}' &= (\underline{X}' - N_{SB}\underline{Y})\hat{\underline{x}} + (\underline{Y}' + N_{SB}\underline{X})\hat{\underline{y}} + \underline{Z}'\hat{\underline{z}} \\ {}^{\mathcal{I}}\underline{\vec{R}}'' &= (\underline{X}'' - 2N_{SB}\underline{Y}' - N_{SB}^2\underline{X})\hat{\underline{x}} + (\underline{Y}'' + 2N_{SB}\underline{X}' - N_{SB}^2\underline{Y})\hat{\underline{y}} + \underline{Z}''\hat{\underline{z}} \end{aligned} \tag{2.78}$$

Non-dimensionalization with respect to the Sun-Barycenter frame follows a pattern similar to that done in Section 2.3.4, though now focused on parameters relevant to the Sun and the fictitious B_1 particle.

$$\underline{\ell}^* = \underline{R}_4 + R_{B_2B_1} = \tilde{\ell}^* a_s \tag{2.79}$$

$$\underline{m}^* = M_1 + M_2 + M_4 = M_4 + \tilde{m}^* \tag{2.80}$$

$$\underline{t}^* = \frac{1}{N_{SB}} = \sqrt{\frac{\underline{\ell}^{*3}}{\tilde{G}\underline{m}^*}} \tag{2.81}$$

Where $\tilde{G}$ is the dimensional universal gravitational constant. Expanding upon (2.81), the dimensional mean motions, N_{SB} and N_{EM} may be related with their normalized counterparts via the characteristic time quantity, as shown by (2.82) and (2.83).

$$\underline{n}_{SB} = N_{SB}\underline{t}^* = 1 \tag{2.82}$$

$$\underline{n}_{EM} = N_{EM}\underline{t}^* = \frac{\underline{t}^*}{\tilde{t}^*} = \frac{1}{\tilde{n}_{SB}} \tag{2.83}$$

The dimensionless spacecraft position vector may be formulated using the characteristic length.

$$\vec{\underline{r}} = \frac{\vec{\underline{R}}}{\underline{\ell}^*} \tag{2.84}$$

A mass fraction, $\underline{\mu}$ is defined as the proportion of the total system mass occupied by the Earth-Moon pair.

$$\underline{\mu} = \frac{M_1 + M_2}{\underline{m}^*} = 1 - \frac{M_4}{\underline{m}^*} \tag{2.85}$$

Since the proportion of total mass occupied by a single particle along a line is inversely related to its distance from the total center of mass, the positions of the Sun and B_1 may be expressed in terms of $\underline{\mu}$, as demonstrated in (2.86).

$$\begin{aligned} \underline{r}_4 &= -\underline{\mu} \\ \underline{r}_{B_1} &= 1 - \underline{\mu} \end{aligned} \tag{2.86}$$

Where the position of B_1 is along $\hat{\underline{x}}$, and that to the Sun is anti-parallel. The non-dimensional universal gravitational constant, G is also defined using the characteristic parameters.

$$G = \tilde{G}\frac{\underline{m}^*\underline{t}^{*2}}{\underline{\ell}^{*3}} = 1 \tag{2.87}$$

Lastly, non-dimensionalization of the relative position vectors given by equations (2.49) through (2.51) is provided by (2.88) through (2.90).

$$\vec{\underline{r}}_{13} = \frac{\vec{\underline{R}}_{13}}{\underline{\ell}^*} = \left(\underline{x} + \frac{\tilde{\mu}}{a_s}\cos\underline{\theta} - (1-\underline{\mu})\right)\hat{\underline{x}} + \left(\underline{y} + \frac{\tilde{\mu}}{a_s}\sin\underline{\theta}\right)\hat{\underline{y}} + \underline{z}\,\hat{\underline{z}} \tag{2.88}$$

$$\vec{\underline{r}}_{23} = \frac{\vec{\underline{R}}_{23}}{\underline{\ell}^*} = \left(\underline{x} - \frac{1-\tilde{\mu}}{a_s}\cos\underline{\theta} - (1-\underline{\mu})\right)\hat{\underline{x}} + \left(\underline{y} - \frac{1-\tilde{\mu}}{a_s}\sin\underline{\theta}\right)\hat{\underline{y}} + \underline{z}\,\hat{\underline{z}} \tag{2.89}$$

$$\vec{\underline{r}}_{43} = \frac{\vec{\underline{R}}_{43}}{\underline{\ell}^*} = \left(\underline{x} + \underline{\mu}\right)\hat{\underline{x}} + \underline{y}\,\hat{\underline{y}} + \underline{z}\,\hat{\underline{z}} \tag{2.90}$$

For simplicity, the scalar components of $\vec{\underline{r}}_1$ and $\vec{\underline{r}}_2$ are assigned variables:

$$\begin{aligned}
\underline{x}_E &= (1-\underline{\mu}) - \frac{\tilde{\mu}}{a_s}\cos\underline{\theta} \\
\underline{y}_E &= -\frac{\tilde{\mu}}{a_s}\sin\underline{\theta} \\
\underline{x}_M &= (1-\underline{\mu}) + \frac{1-\tilde{\mu}}{a_s}\cos\underline{\theta} \\
\underline{y}_M &= \frac{1-\tilde{\mu}}{a_s}\sin\underline{\theta}
\end{aligned} \tag{2.91}$$

The normalized masses of the Earth and Moon may also be represented by functions of $\underline{\mu}$ and $\tilde{\mu}$:

$$\begin{aligned}
\frac{M_1}{\underline{m}^*} &= \frac{M_1}{M_1+M_2+M_4} = \frac{M_1}{M_1+M_2}\frac{M_1+M_2}{M_1+M_2+M_3} = (1-\tilde{\mu})\underline{\mu} \\
\frac{M_2}{\underline{m}^*} &= \frac{M_2}{M_1+M_2+M_4} = \frac{M_2}{M_1+M_2}\frac{M_1+M_2}{M_1+M_2+M_3} = \tilde{\mu}\underline{\mu}
\end{aligned} \tag{2.92}$$

Returning to the right-hand side of the current equation of motion provided in (2.77), various relations may be substituted in to create an equation governed by dimensionless variables.

$$\underline{\vec{R}}'' = -\left(\frac{\underline{\mu}(1-\tilde{\mu})}{\underline{r}_{13}^3}\underline{\vec{r}}_{13} + \frac{\underline{\mu}\tilde{\mu}}{\underline{r}_{23}^3}\underline{\vec{r}}_{23} + \frac{1-\underline{\mu}}{\underline{r}_{43}^3}\underline{\vec{r}}_{43}\right)\frac{\underline{\ell}^*}{\underline{t}^{*2}} \tag{2.93}$$

Focusing on the left-hand side, by inserting expressions for normalized parameters into (2.78) and converting to be with respect to dimensionless time:

$$\underline{\vec{R}}'' = \underline{\ddot{\vec{r}}}\frac{\underline{\ell}^*}{\underline{t}^{*2}} = \left((\underline{\ddot{x}} - 2\underline{n}_{SB}\underline{\dot{y}} - \underline{n}_{SB}^2\underline{x})\hat{\underline{x}} + (\underline{\ddot{y}} + 2\underline{n}_{SB}\underline{\dot{x}} - \underline{n}_{SB}^2\underline{y})\hat{\underline{y}} + \underline{\ddot{z}}\ \hat{\underline{z}}\right) \tag{2.94}$$

Where $\underline{n}_{SB} = 1$. Equating (2.92) and (2.94), then simplifying and breaking into scalar expressions, the Sun-Barycenter formulation for the BCR4BP is displayed in (2.95).

$$\begin{aligned}
\underline{\ddot{x}} &= 2\underline{\dot{y}} + \underline{x} - \frac{\underline{\mu}(1-\tilde{\mu})}{\underline{r}_{13}^3}(\underline{x} - \underline{x}_E) - \frac{\underline{\mu}\tilde{\mu}}{\underline{r}_{23}^3}(\underline{x} - \underline{x}_M) - \frac{1-\underline{\mu}}{\underline{r}_{43}^3}(\underline{x} + \underline{\mu}) \\
\underline{\ddot{y}} &= \underline{y} - 2\underline{\dot{x}} - \frac{\underline{\mu}(1-\tilde{\mu})}{\underline{r}_{13}^3}(\underline{y} - \underline{y}_E) - \frac{\underline{\mu}\tilde{\mu}}{\underline{r}_{23}^3}(\underline{y} - \underline{y}_M) - \frac{1-\underline{\mu}}{\underline{r}_{43}^3}\underline{y} \\
\underline{\ddot{z}} &= -\frac{\underline{\mu}(1-\tilde{\mu})}{\underline{r}_{13}^3}\underline{z} - \frac{\underline{\mu}\tilde{\mu}}{\underline{r}_{23}^3}\underline{z} - \frac{1-\underline{\mu}}{\underline{r}_{43}^3}\underline{z}
\end{aligned} \tag{2.95}$$

A pseudo-potential function for the equations of motion in the Sun-B_1 frame, $\underline{\Omega}$ may be defined such that its gradient may be used to largely describe the rotating acceleration acting upon a spacecraft in the BCR4BP.

$$\underline{\Omega} = \frac{1}{2}\left(\underline{x}^2 + \underline{y}^2\right) + \frac{\underline{\mu}(1-\tilde{\mu})}{\underline{r}_{13}} + \frac{\underline{\mu}\tilde{\mu}}{\underline{r}_{23}} + \frac{1-\tilde{\mu}}{\underline{r}_{43}} \tag{2.96}$$

This formulation was chosen such that its derivatives with respect to the position components may fit into the equations of motion as shown in equation (2.97).

$$\begin{aligned}
\underline{\ddot{x}} &= \frac{\partial\underline{\Omega}}{\partial\underline{x}} + 2\underline{\dot{y}} \\
\underline{\ddot{y}} &= \frac{\partial\underline{\Omega}}{\partial\underline{y}} - 2\underline{\dot{x}} \\
\underline{\ddot{z}} &= \frac{\partial\underline{\Omega}}{\partial\underline{z}}
\end{aligned} \tag{2.97}$$

2.3.6 Hamiltonian: Earth-Moon Frame

In the Circular Restricted 3-Body Problem, a benefit of excluding time as an explicit variable in the equations of motion is that an integral of motion, the Jacobi Constant, was derived from the system Hamiltonian. Since the Bi-Circular Restricted 4-Body Problem is explicitly time-dependent in either of its formulations (via the Sun and Moon angles), its system Hamiltonian is non-constant. As a result, the BCR4BP does not possess a single constant of integration. Regardless, a time-variant quantity of similar formulation to the CR3BP's Jacobi Constant may be leveraged to gain insight into the instantaneous energy of a spacecraft. In an effort to maintain consistency with the Jacobi Constant, previous authors [20] [34] have defined a scaled Hamiltonian for the Earth-Moon BCR4BP as:

$$\tilde{H} = 2\tilde{\Omega} - (\dot{\tilde{x}}^2 + \dot{\tilde{y}}^2 + \dot{\tilde{z}}^2) \tag{2.98}$$

Scheuerle presents a thorough derivation of the true system Hamiltonian as well as a comparison with the scaled version [20]. The manipulation of the Hamiltonian is done such that a change in its value is roughly mirrored by the instantaneous change in Jacobi Constant, or $\Delta\tilde{H} \approx \Delta JC$. Previous authors have added a term $\rho = -1690$ to $\tilde{H}$ such that individual values of the Hamiltonian are on a similar scale to their Jacobi Constant counterparts [35]. Since the investigation is more concerned with the relative change in Hamiltonian rather than its particular value, the scaling factor ρ is disregarded. It should also be noted that if the quantities in the pseudo-potential function pertaining to the Sun were to be removed, the Jacobi Constant and Hamiltonian values would align perfectly. A sample trajectory is provided in Figure 2.9 alongside the evolution of its corresponding Hamiltonian and instantaneous Jacobi Constant values. While the shapes of the curves differ, their secular behaviors are similar.

Within the context of a lunar transfer investigation, the time derivative of the Hamiltonian is particularly useful. A preliminary expression may be obtained by applying the derivative chain rule:

$$\dot{\tilde{H}} = \frac{\partial \tilde{H}}{\partial \tilde{\theta}} \frac{\partial \tilde{\theta}}{\partial t} = \frac{\partial \tilde{H}}{\partial \tilde{\theta}} \dot{\tilde{\theta}} \tag{2.99}$$

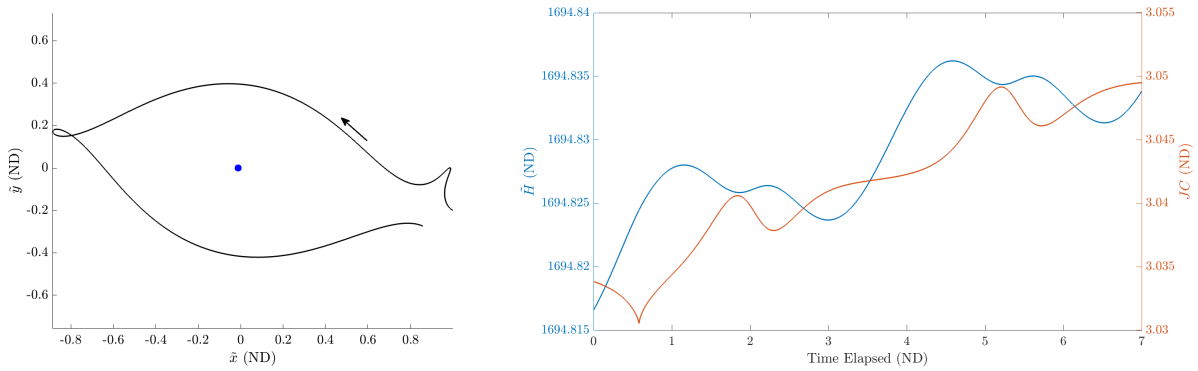

(a) Trajectory in Earth-Moon frame

(b) Values of $\tilde{H}$ and instantaneous JC

Figure 2.9. Evolution of energy-like quantities over propagation time of sample trajectory.

Since the velocity components are not tied to epoch, the derivative applies to the pseudo-potential function:

$$\frac{\partial \tilde{H}}{\partial \tilde{\theta}} = 2\frac{\partial \tilde{\Omega}}{\partial \tilde{\theta}}$$

Recalling that:

$$\tilde{r}_{43} = \sqrt{(\tilde{x} - a_s \cos\tilde{\theta})^2 + (\tilde{y} - a_s \sin\tilde{\theta})^2 + \tilde{z}^2} \tag{2.100}$$

the derivative is evaluated.

$$\frac{\partial \tilde{\Omega}}{\partial \tilde{\theta}} = \tilde{m}_s \frac{\tilde{y} a_s \cos\tilde{\theta} - \tilde{x} a_s \sin\tilde{\theta}}{\tilde{r}_{43}^3} - \frac{\tilde{m}_s}{a_s^2}\left(\tilde{y}\cos\tilde{\theta} - \tilde{x}\sin\tilde{\theta}\right) \tag{2.101}$$

Substituting (2.101) into (2.99) and simplifying, the time rate of change of the Earth-Moon Hamiltonian is presented in (2.102).

$$\dot{\tilde{H}} = 2\dot{\tilde{\theta}}\tilde{m}_s\left(\tilde{y}\cos\tilde{\theta} - \tilde{x}\sin\tilde{\theta}\right)\left[\frac{a_s}{\tilde{r}_{43}^3} - \frac{1}{a_s^2}\right] \tag{2.102}$$

Since $\dot{\tilde{\theta}}$ is a constant value, local extrema for $\tilde{H}$ exist when either $\tilde{y}\cos\tilde{\theta} - \tilde{x}\sin\tilde{\theta} = 0$ or $\frac{a_s}{\tilde{r}_{43}^3} = \frac{1}{a_s^2}$. In the first case, the relation for $\underline{y}$ may be substituted such that the condition becomes $\underline{y} = 0$. The second may only be satisfied when $\tilde{r}_{43} = a_s$, or when the spaceship is of an equal distance from the Sun as B_1. Near the Earth-Moon region in the Sun-Barycenter

rotating frame, the second condition (which spans a spherical shell about B_2 of radius $\underline{\ell}^*$) may be approximated as a vertical plane normal to $\hat{\underline{x}}$. As such, changes to the Earth-Moon Hamiltonian can be subdivided into four quadrants as viewed in the Sun-B_1 frame, where the diagonal pairs share similar energy-alteration properties. This phenomenon is visualized in Figure 2.10, which is a re-creation of Figure 2.19 from page 80 of [20].

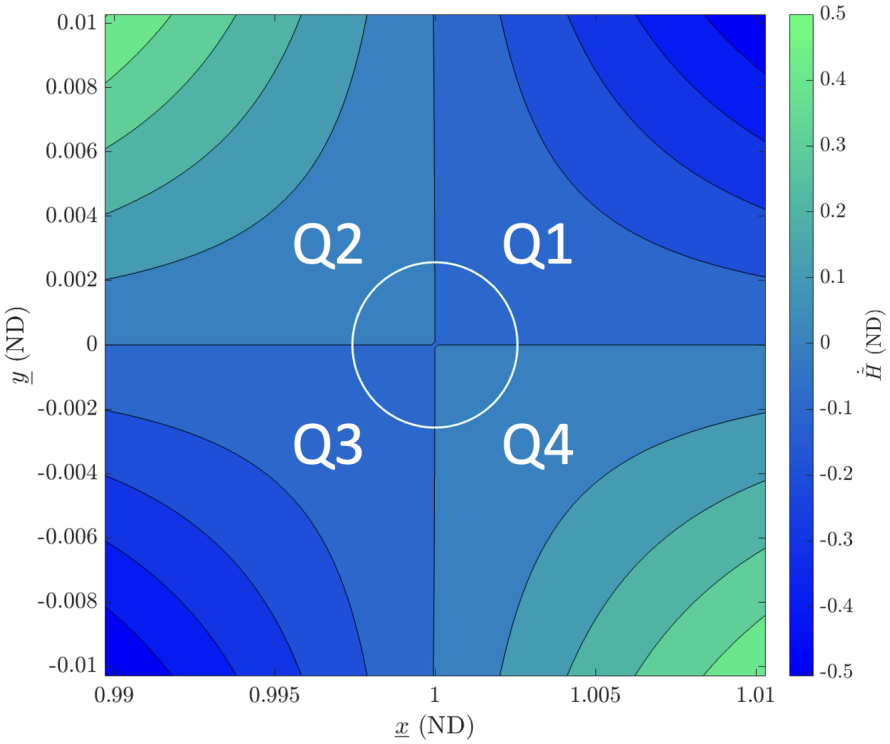

Figure 2.10. $\dot{\tilde{H}}$ as viewed in the Sun-B_1 reference frame, white circle is the Moon's orbit about the Earth.

Since the expression for $\dot{\tilde{H}}$ includes the Sun angle which evolves alongside propagation time, switching to the Sun-Barycenter frame provides a convenient means of visualizing the changes to the Earth-Moon Hamiltonian. As the new frame rotates along with the Sun angle, the time-dependency of (2.102) is removed, allowing for it to become solely a function of position. Since changes in Hamiltonian and kinetic energy are negatively related, the Sun's perturbation reduces the spacecraft energy in quadrants 2 and 4, while the opposite occurs in quadrants 1 and 3. A previous investigation found that changes in instantaneous orbital

elements are also tied to quadrants in the Sun-Barycenter frame [15], though in contrast to $\dot{\tilde{H}}$, these changes are also dependent upon the motion of the spacecraft.

2.3.7 Hamiltonian: Sun-Barycenter Frame

The energy-like quantity attributed to the motion of a spacecraft as viewed in the Sun-$B1$ frame is defined such that it mirrors the Earth-Moon Hamiltonian defined in Section 2.3.6. As such, this quantity is also referred to as the "Hamiltonian", though for the Sun-Barycenter frame, denoted $\underline{H}$. To mirror the general structure of the Jacobi Constant, $\underline{H}$ is scaled such that:

$$\underline{H} = 2\underline{\Omega} - (\dot{\underline{x}}^2 + \dot{\underline{y}}^2 + \dot{\underline{z}}^2) \tag{2.103}$$

While the Sun acts as a perturbation within the context of the Earth-Moon formulation, both the Earth and Moon cause variations to $\underline{H}$. For spacecraft located distant from the Earth-Moon region, these perturbations are often negligible, and the value of $\underline{H}$ evolves relatively constantly. When close to the sphere of influence of the Earth-Moon system, this near-constant behavior is no longer upheld. This relationship is captured by the expression for the time rate of change of the Sun-Barycenter Hamiltonian, provided by (2.104).

$$\dot{\underline{H}} = \frac{\partial \underline{H}}{\partial \tilde{\theta}} \frac{\partial \tilde{\theta}}{\partial t} = 2\dot{\tilde{\theta}} \frac{\underline{\mu}(1-\tilde{\mu})\tilde{\mu}}{a_s} \left((\underline{x} - (1-\underline{\mu})) \sin\tilde{\theta} - \underline{y}\cos\tilde{\theta} \right) \left(\frac{1}{\underline{r}_{13}^3} - \frac{1}{\underline{r}_{23}^3} \right) \tag{2.104}$$

When analyzing (2.104), it may be noted that local extrema may occur in either the case of $\underline{x} - (1-\underline{\mu})\sin\tilde{\theta} - \underline{y}\cos\tilde{\theta} = 0$ or when $\frac{1}{\underline{r}_{13}^3} = \frac{1}{\underline{r}_{23}^3}$. These two scenarios may be reduced to $\tilde{y} = 0$ and $\underline{r}_{13} = \underline{r}_{23}$. The first condition is straightforward, as changes to the spacecraft $\underline{H}$ occur whenever it crosses $\tilde{\hat{x}}$. The other states that extrema occur when the spacecraft is equidistant from both the Earth and Moon. This is satisfied by positions spanning a vertical plane normal to $\tilde{\hat{x}}$ situated at the location between the two primaries, or where $\tilde{x} = 0.5 - \tilde{\mu}$. Much like $\dot{\tilde{H}}$, the time rate of change of $\underline{H}$ is a position-dependent function when viewed in the alternative reference frame, that being the Earth-Moon coordinate system for $\dot{\underline{H}}$. Moreover, quadrants within the Earth-Moon frame outline the growth and decay of $\underline{H}$, a behavior shown in Figure 2.11, recreated from figure 2.39 on page 112 of [20].

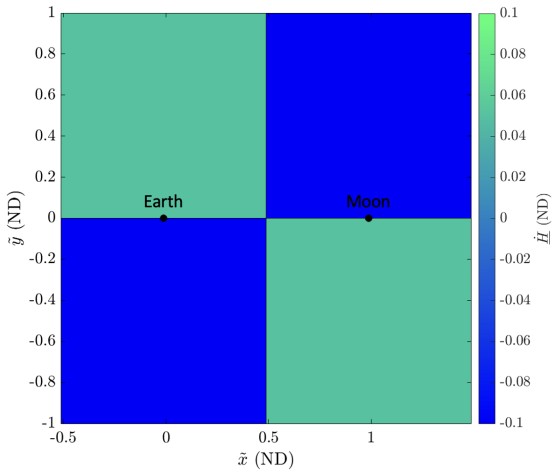

Figure 2.11. $\underline{\dot{H}}$ as viewed in the Sun-B_1 reference frame.

While seemingly consistent within each quadrant, the magnitude of $\underline{\dot{H}}$ exponentially increases as distance with respect to either the Earth or Moon is minimized. This is demonstrated by Figure 2.12, where the perspective is shifted to focus on either the Earth or Moon, and the color scale is shifted to a logarithmic representation of $\underline{\dot{H}}$.

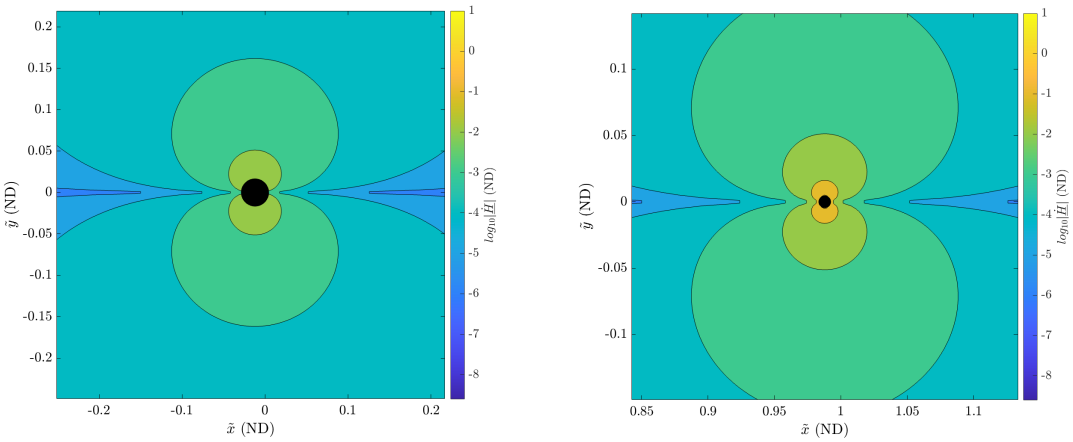

(a) Earth to scale in black

(b) Moon to scale in black

Figure 2.12. Changes in Sun-Barycenter Hamiltonian near the Earth and Moon. Color scale modified to show $\log_{10}\left|\underline{\dot{H}}\right|$.

Since the absolute value must be taken to use a logarithmic scale, the behavior shown in Figure 2.12 only represents the magnitude of the Hamiltonian time rate of change. Meanwhile,

the signs of $\underline{\dot{H}}$ follow the same quadrant behavior as visualized in Figure 2.11. As a result, relatively large changes in the Sun-Barycenter Hamiltonian will occur during relatively close passages of either the Earth or Moon.

2.3.8 Instantaneous Equilibrium Solutions: Earth-Moon Frame

An effect of introducing epoch-dependence into the dynamics is that the equilibrium solutions, or the locations where the net acceleration is zero, are time-variant. Since the Sun's location is constantly changing, its gravitational acceleration re-orients alongside it, causing the equilibrium solution positions to shift in response. The determination of these locations is consequently a completely numerical endeavor, as no analytical expression has been provided to determine each instantaneous equilibrium solution for any given Sun angle. To begin, first consider the Earth-Moon equations of motion for the BCR4BP, as given in (2.74), where each of the acceleration and velocity components are set to zero:

$$\begin{aligned} \tilde{x} - \frac{(1-\tilde{\mu})(\tilde{x}+\tilde{\mu})}{|\tilde{r}_{13}|^3} - \frac{\tilde{\mu}(\tilde{x}+\tilde{\mu}-1)}{|\tilde{r}_{23}|^3} - \frac{\tilde{m}_s(\tilde{x}-a_s\cos\tilde{\theta})}{|\tilde{r}_{43}|^3} - \frac{\tilde{m}_s}{a_s^2}\cos\tilde{\theta} = 0 \\ \tilde{y} - \frac{(1-\tilde{\mu})\tilde{y}}{|\tilde{r}_{13}|^3} - \frac{\tilde{\mu}\tilde{y}}{|\tilde{r}_{23}|^3} - \frac{\tilde{m}_s(\tilde{y}-a_s\sin\tilde{\theta})}{|\tilde{r}_{43}|^3} - \frac{\tilde{m}_s}{a_s^2}\sin\tilde{\theta} = 0 \\ \frac{(1-\tilde{\mu})\tilde{z}}{|\tilde{r}_{13}|^3} + \frac{\tilde{\mu}\tilde{z}}{|\tilde{r}_{23}|^3} + \frac{\tilde{m}_s\tilde{z}}{|\tilde{r}_{43}|^3} = 0 \end{aligned} \tag{2.105}$$

Much like the case in the CR3BP, the third equation is only solved with $\tilde{z} = 0$. Aside from this simplification, only numerical methods can be employed to find the remaining zeroes for (2.105). Since $\tilde{y} = 0$ is no longer a consistent solution for all values of $\dot{\tilde{\theta}}$, the root-finding strategy is required to simultaneously locate the $\tilde{x}$ and $\tilde{y}$-components of the equilibrium point position. To accomplish this, a two-dimensional Newton-Raphson algorithm is constructed using (2.106) for a target vector $\vec{F} = \begin{bmatrix} F_1 & F_2 \end{bmatrix}^T$ and free-variable vector $\vec{X} = \begin{bmatrix} \tilde{x} & \tilde{y} \end{bmatrix}^T$. In this case, F_1 and F_2 are the top two equations of (2.105).

$$\vec{X}_{i+1} = \vec{X}_i - J^{-1}\vec{F} \tag{2.106}$$

Where $\vec{X}_1$ is the initial guess vector, index i is the update iteration counter for the initial guess vector, and J is the Jacobian matrix, as defined by (2.107).

$$J = \frac{\partial \vec{F}}{\partial \vec{X}} = \begin{bmatrix} \frac{\partial F_1}{\partial \tilde{x}} & \frac{\partial F_1}{\partial \tilde{y}} \\ \frac{\partial F_2}{\partial \tilde{x}} & \frac{\partial F_2}{\partial \tilde{y}} \end{bmatrix} \tag{2.107}$$

The Lagrange points for the CR3BP serve as initial guesses for their BCR4BP counterparts. Following this, the positions of the Earth-Moon BCR4BP equilibrium points (denoted $\tilde{E}_\text{i}$, numbered in the same convention as L_i) are converged using the iterative Newton-Raphson algorithm for discrete Sun angles from 0 to 360°. Doing so produces continuous tracks traveled by $\tilde{E}_\text{i}$, as shown by Figure 2.13 and Figure 2.14. To analyze a single example curve, focus on the track of $\tilde{E}_1$, isolated in Figure 2.13. The corresponding CR3BP Lagrange points are plotted for comparison.

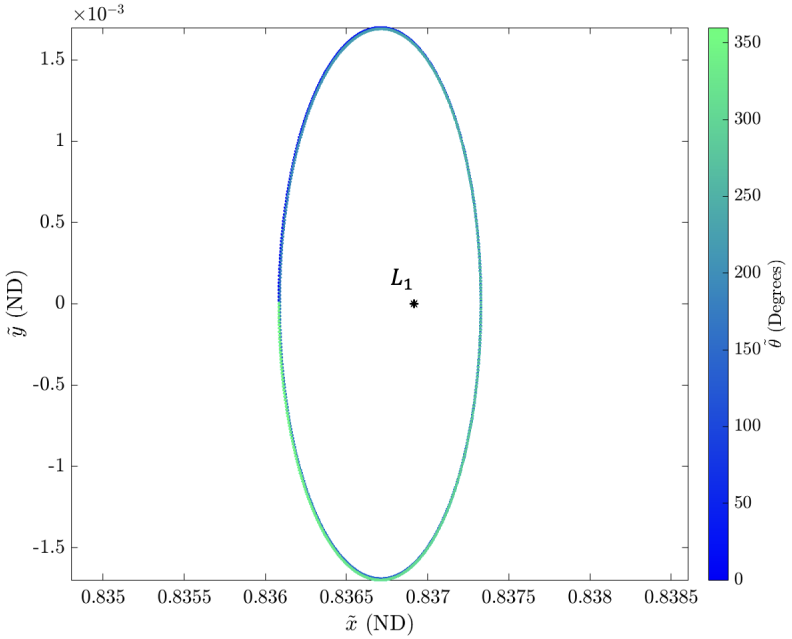

Figure 2.13. Position of $\tilde{E}_1$ (in the Earth-Moon frame) as a function of Sun angle.

The path shown above is actually two loops, where the second near-perfectly traces the first. This looping behavior is shared by the other instantaneous equilibrium points as well, though special consideration is to be made for $\tilde{E}_3$.

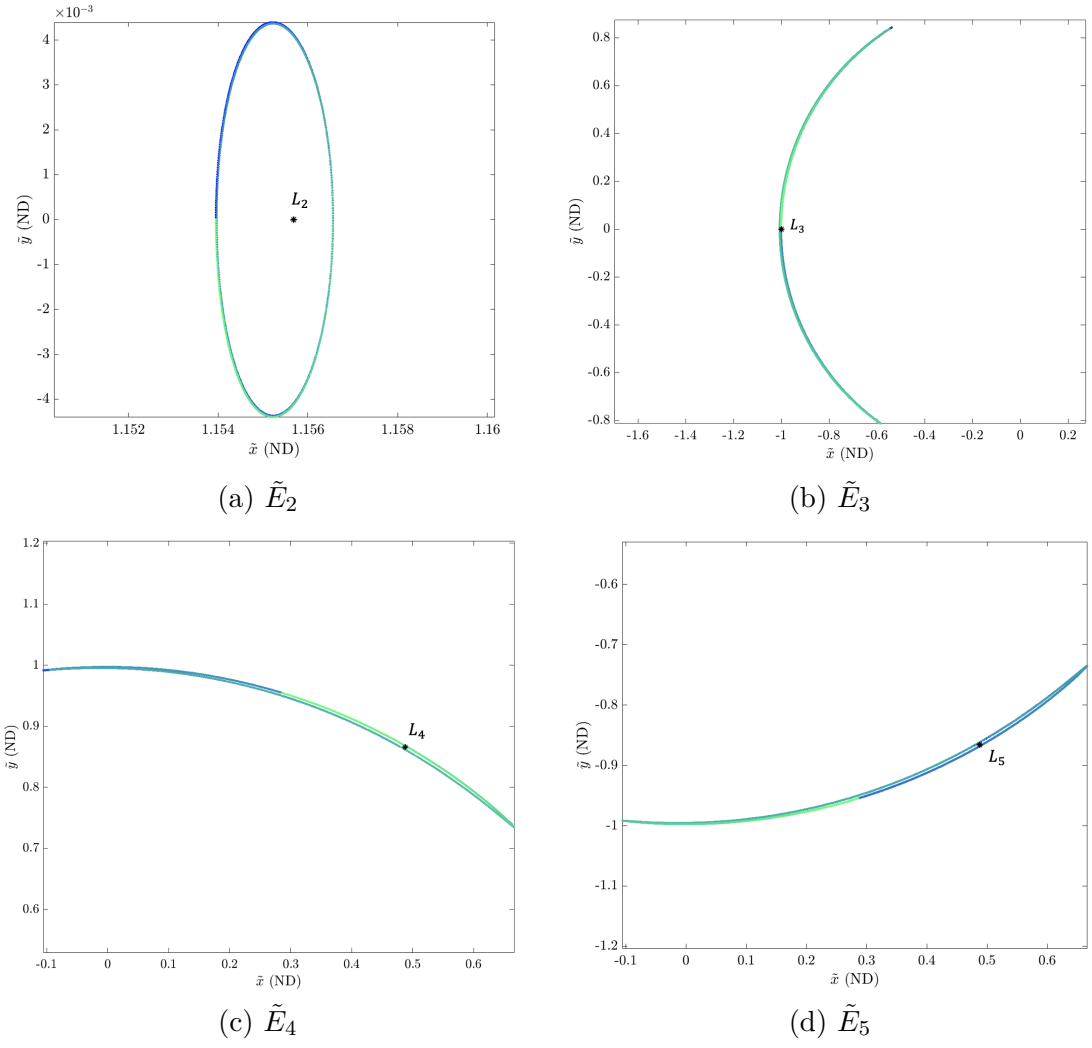

(a) $\tilde{E}_2$ (b) $\tilde{E}_3$

(c) $\tilde{E}_4$ (d) $\tilde{E}_5$

Figure 2.14. Paths traveled by the remaining equilibrium points. Color scale matches that in Figure 2.13.

While the arc shown for $\tilde{E}_3$ is continuous, it is not consistently traversed by a single point. Over the course of a synodic month, there are periods of time where there simultaneously exist between one to three $\tilde{E}_3$ points. Previous authors have used $\tilde{E}_3^{\mathrm{j}}$, where $\mathrm{j} = 1, 2, 3$ to distinguish between the simultaneous solutions [35]. The complete behavior of $\tilde{E}_3$ may be best viewed when looking at its $\tilde{x}$ and $\tilde{y}$-components as individual functions of $\tilde{\theta}$, demonstrated by Figure 2.15. The Sun angle ranges in which there are multiple equilibrium points are the regions where a vertical line may be traced on the plot to intersect the curve multiple times.

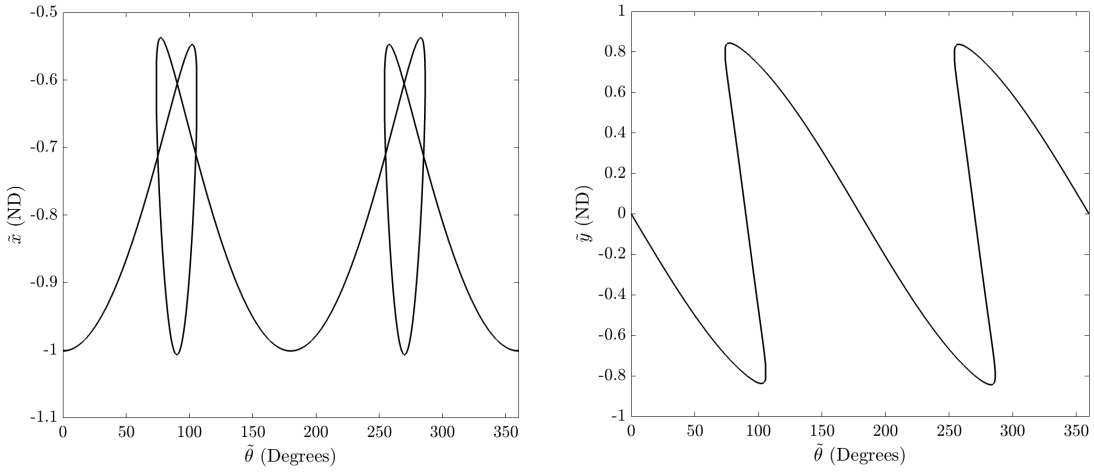

(a) (b)

Figure 2.15. Evolution of $\tilde{x}$ (a) and $\tilde{y}$ (b) components of $\tilde{E}_3$

The tracks for all of the instantaneous Earth-Moon equilibrium solutions are compared to one another in Figure 2.16. Lastly, the associated Hamiltonian values for each of the equilibrium solutions also vary with $\tilde{\theta}$, as depicted in Figure 2.17.

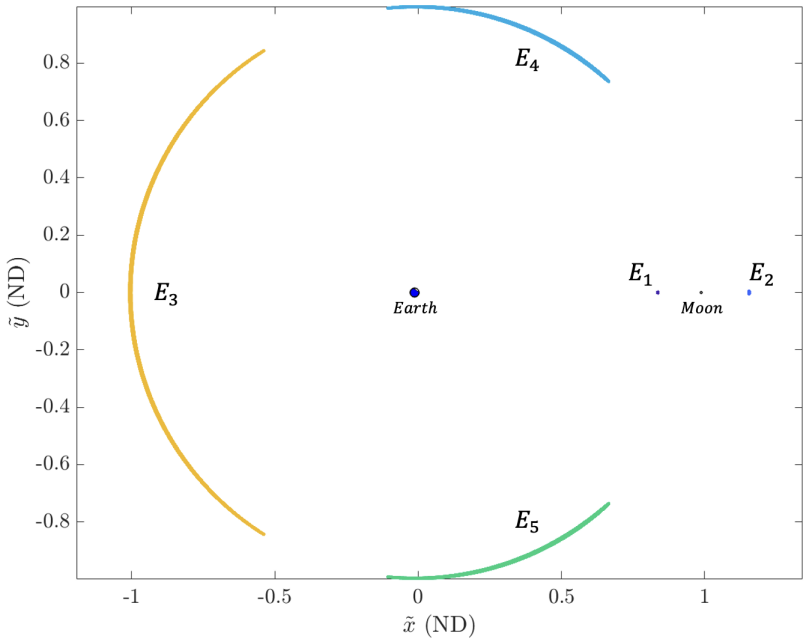

Figure 2.16. Arcs for each equilibrium solution in the Earth-Moon frame.

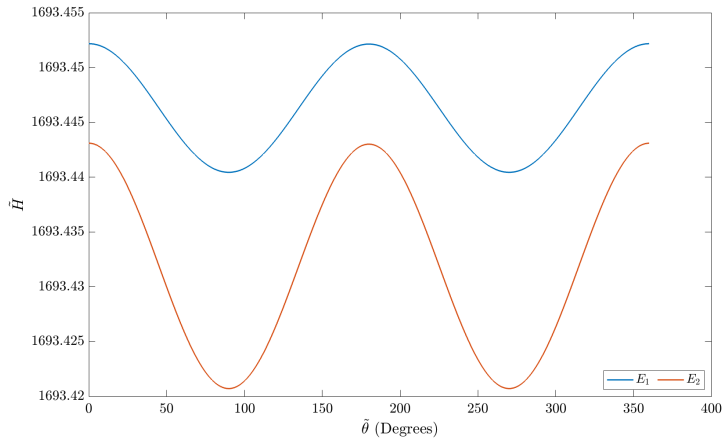

(a) $\tilde{E}_1$ and $\tilde{E}_2$

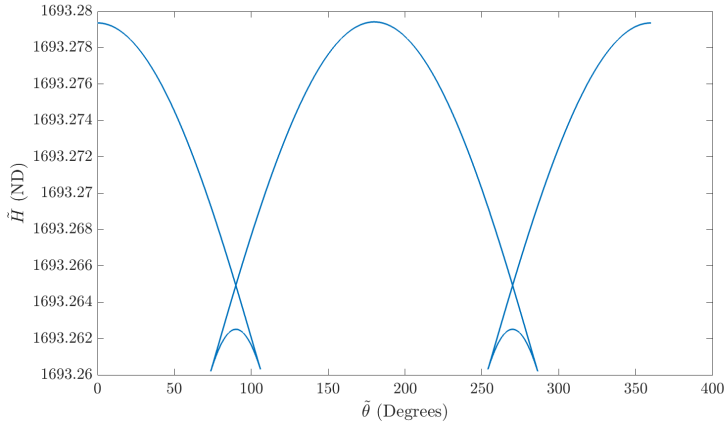

(b) $\tilde{E}_3$

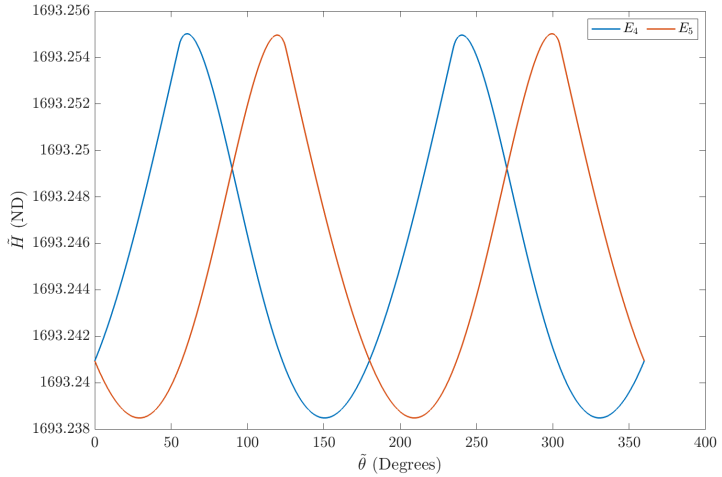

(c) $\tilde{E}_4$ and $\tilde{E}_5$

Figure 2.17. Earth-Moon Hamiltonian associated with each equilibrium solution, as a function of Sun angle.

2.3.9 Instantaneous Equilibrium Solutions: Sun-Barycenter Frame

The process for deriving the instantaneous equilibrium solutions in the Sun-Barycenter frame parallels that outlined in Section 2.3.8. Since both the Earth and Moon are moving in the Sun-B_1 reference frame, the equilibrium solutions must also change position to accommodate. Beginning with the governing equations of motion (from (2.95)) and setting acceleration and velocity terms to zero:

$$\begin{aligned} \underline{x} - \frac{\underline{\mu}(1-\tilde{\mu})}{|\underline{r}_{13}|^3}(\underline{x}-\underline{x}_E) - \frac{\underline{\mu}\tilde{\mu}}{|\underline{r}_{23}|^3}(\underline{x}-\underline{x}_M) - \frac{1-\underline{\mu}}{|\underline{r}_{43}|^3}(\underline{x}+\underline{\mu}) = 0 \\ \underline{y} - \frac{\underline{\mu}(1-\tilde{\mu})}{|\underline{r}_{13}|^3}(\underline{y}-\underline{y}_E) - \frac{\underline{\mu}\tilde{\mu}}{|\underline{r}_{23}|^3}(\underline{y}-\underline{y}_M) - \frac{1-\underline{\mu}}{|\underline{r}_{43}|^3}\underline{y} = 0 \\ \frac{\underline{\mu}(1-\tilde{\mu})}{|\underline{r}_{13}|^3}\underline{z} + \frac{\underline{\mu}\tilde{\mu}}{|\underline{r}_{23}|^3}\underline{z} + \frac{1-\underline{\mu}}{|\underline{r}_{43}|^3}\underline{z} = 0 \end{aligned} \tag{2.108}$$

Similar to the equilibrium solutions in the Earth-Moon frame, the z-component equation may only be solved by $\underline{z} = 0$. This is due to the assumption that the Earth-Moon and Sun-Barycenter planes of motion are co-planar, as there is no gravitational force nor centripetal acceleration acting out of this plane, thus no spatial equilibrium solution. If the co-planar simplification is not made, then these locations would deviate from either plane of motion.

Returning to the problem, the top two equations may only be solved using numerical root-finding techniques. In the investigation, a two-dimensional Newton-Raphson algorithm is used, highlighted by (2.106) where in this case $\vec{F} = \begin{bmatrix} F_1 & F_2 \end{bmatrix}^T$ and $\vec{X} = \begin{bmatrix} \underline{x} & \underline{y} \end{bmatrix}^T$. The components F_1 and F_2 correspond to the top two equations in (2.108). For initial guesses, the Lagrange points for the Sun-B_1 CR3BP (where B_1 is a single body of mass equal to that of the Earth-Moon system) are used. The resulting paths taken by each of the Sun-Barycenter equilibrium solutions (denoted $\underline{E}_\text{i}$) as a function of Moon angle are shown in Figures 2.18 and 2.19. Since $\underline{E}_1$ and $\underline{E}_2$ are relatively close to the Earth-Moon system, their variations are significant compared to the remaining equilibrium points.

The weak perturbations by the Earth and Moon cause the more distant equilibrium points ($\underline{E}_3$ through $\underline{E}_5$) to deviate from their libration point counterparts by little more

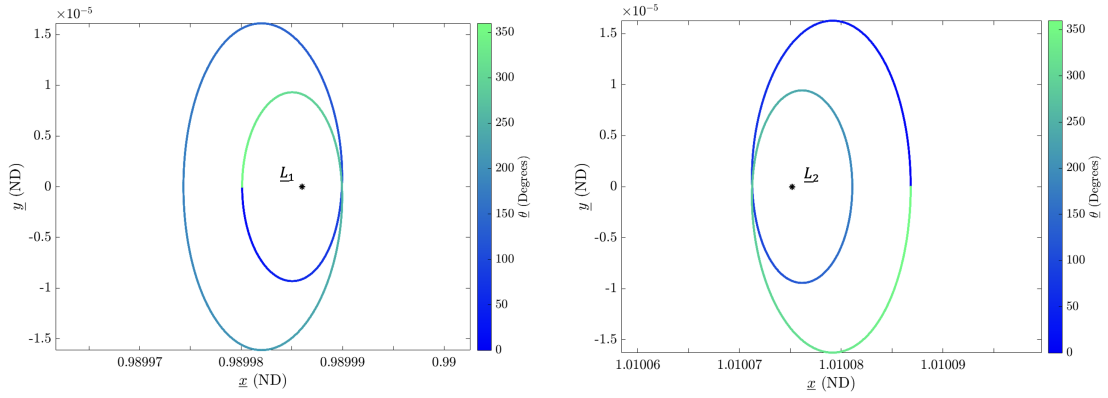

(a) (b)

Figure 2.18. Positions of $\underline{E}_1$ (a) and $\underline{E}_2$ (b) as functions of $\underline{\theta}$. Corresponding Sun-B_1 Lagrange points provided for comparison.

than several kilometers. Moreover, in contrast to $\tilde{E}_3$ in the Earth-Moon frame, none of $\underline{E}_\mathrm{i}$ ever simultaneously exist as multiple points at a given time.

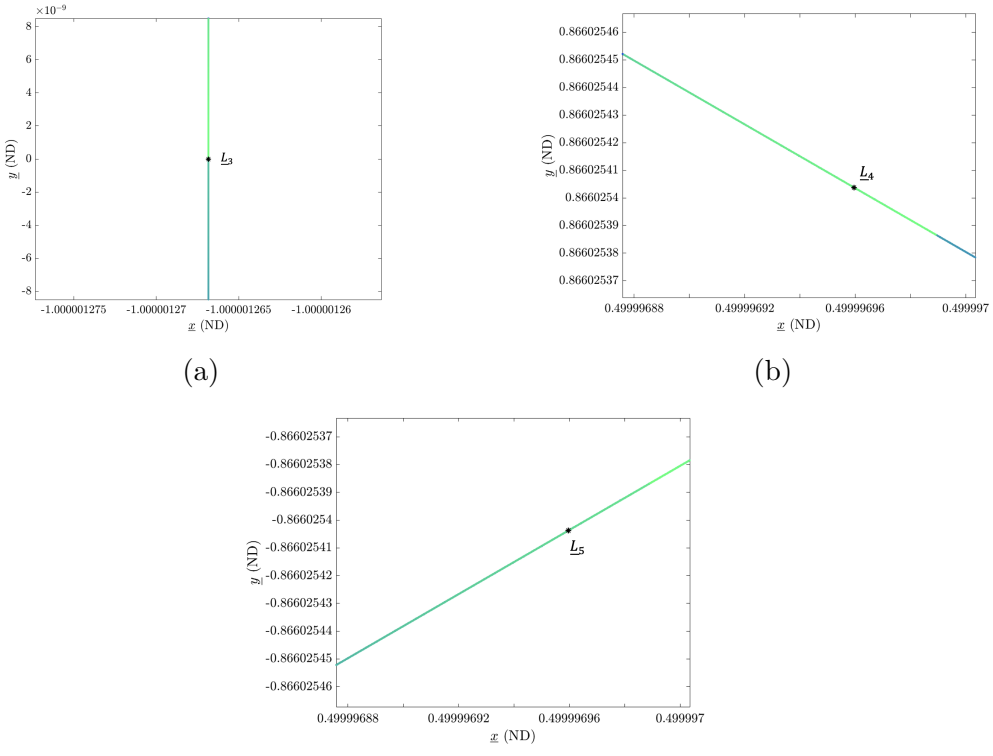

(c)

Figure 2.19. Positions of $\underline{E}_1$ (a) and $\underline{E}_2$ (b) as functions of $\underline{\theta}$. Corresponding Sun-B_1 Lagrange points provided for comparison.

The Hamiltonian variation for $\underline{E}_{\text{i}}$ across all Moon angle values is minimal. Their mean values across the span of a synodic month are provided in Table 2.4, while the associated variation for each quantity is generally negligible.

Table 2.4. Average $\underline{H}$ values for each of the Sun-Barycenter equilibrium solutions

	$\underline{E}_1$	$\underline{E}_2$	$\underline{E}_3$	$\underline{E}_4$	$\underline{E}_5$
$mean(\underline{H})$ (ND)	3.000898	3.000894	3.000003	2.999997	2.999997

The most variable equilibrium points, $\underline{E}_1$ and $\underline{E}_2$, have a maximum deviation from their respective Lagrange points on the order of 10^{-7} non-dimensional units. While changes are present, the majority of applications in the Sun-Barycenter frame may reasonably approximate the BCR4BP equilibrium points with their corresponding CR3BP solutions.

2.3.10 Symmetry within the BCR4BP

Much like the CR3BP, symmetry exists within the BCR4BP about two surfaces: the x-z and x-y planes. It may be noted that this property is equally present in either rotating frame, thus a generalization between the two is presented using accent-less variables (i.e. x, y and z).

For the first mode, recall the axioms for the Mirror Theorem state that x-z symmetry exists if either: all position vectors are aligned among themselves and normal to all velocity vectors or all velocity vectors are collinear among themselves and perpendicular with all position vectors. For the CR3BP, this is simplified in the rotating frame as the two primaries have fixed positions and velocities. In the case of the BCR4BP, complexity is still reduced when examining the Mirror Theorem in a rotating frame, though not as significantly as in the three-body problem due to the remaining motion of at least one gravitational mass. Within the Earth-Moon rotating frame, the motion of the Sun is circular about B_1, and thus its velocity is always perpendicular with its own position vector. In order for either rule of the Mirror Theorem to be satisfied, the Sun would have to be aligned with the Earth and Moon, or when $\tilde{\theta} = k\boldsymbol{\pi}$ for $k = 0, \pm 1, \pm 2, \cdots$ is satisfied. When this is true, the Mirror

Theorem may apply if the position of the spacecraft is along the $\tilde{x}$-$\tilde{z}$ plane, with a velocity purely along the $\pm\tilde{\hat{y}}$ direction.

The conditions for the Mirror Theorem still apply for motion within the Sun-B_1 frame, though now the Earth and Moon both move. Luckily, the alignment of the Sun, Earth and Moon still serves as a keystone for applying the Mirror Theorem in the Sun-B_1 frame. Similar to the other rotating frame, $\underline{x}$-$\underline{z}$ symmetry occurs when the position of the spacecraft is located along this plane, with a velocity perpendicular to it. Moreover, the aligning of the three bodies simultaneously occurs in either rotating frame, meaning that a spacecraft which satisfies the conditions for one frame will have a Mirrored trajectory in the other as well.

The implementation of the Mirror Theorem is rather simple. Once an initial spacecraft state and epoch is found such that the rules for a mirror configuration are satisfied, then the reflection may be achieved by propagating backwards in time. By doing so, the resultant arc will be symmetric with its forward-propagated counterpart about the x-z plane. An example scenario is provided in Figure 2.20 where the initial non-dimensional state $\tilde{\vec{x}} = \begin{bmatrix} 0.9 & 0 & 0.1 & 0 & 0.05 & 0 & \pi \end{bmatrix}^T$ is propagated both forward and backward for a time of 2 ND.

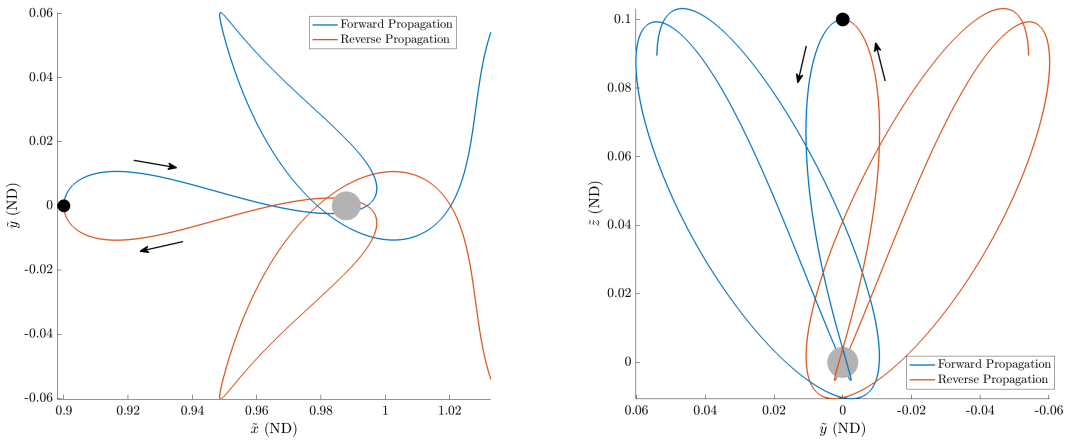

(a) $\tilde{x}$-$\tilde{y}$ projection (b) $\tilde{y}$-$\tilde{z}$ projection

Figure 2.20. Trajectories from $\tilde{\vec{x}}$ propagation, where the arrows indicate motion in forward time and the black dot is the location of $\tilde{\vec{x}}$. Motion in Earth-Moon frame. Moon to scale.

The same trajectory transformed to the Sun-Barycenter reference frame is also symmetric, as shown in Figure 2.21.

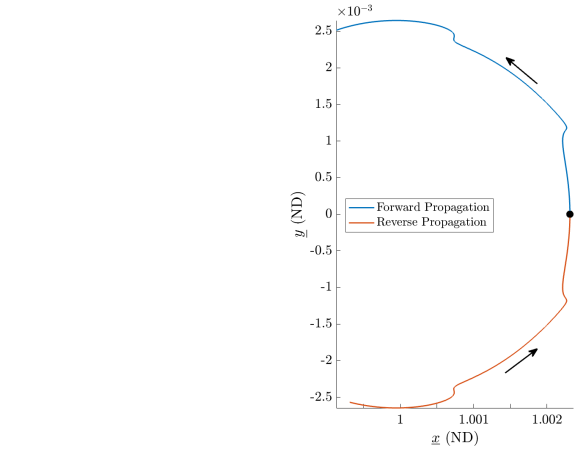

(a) $\underline{x}$-$\underline{y}$ projection

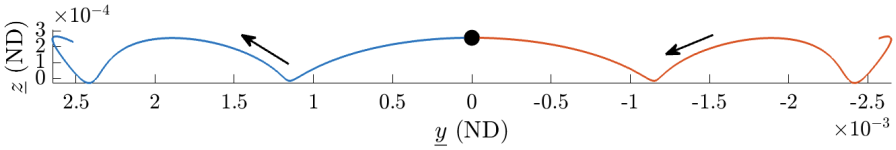

(b) $\underline{y}$-$\underline{z}$ projection

Figure 2.21. Motion from Figure 2.20 rotated to the Sun-B_1 frame. Arrows indicate motion in forward time and the black dot is the transformed location of $\tilde{\tilde{x}}$.

The other mode of symmetry, or that across the x-y plane may be explained using the same logic applied to the CR3BP in Section 2.2.6. Since the dynamical equations for either rotating frame of the BCR4BP have two paired second-order equations of motion with $\ddot{x}$ and $\ddot{y}$, the remaining spatial component is isolated. In other words, the functions of $\ddot{x}$ and $\ddot{y}$ are not influenced by $\dot{z}$, and as a result of the co-planar assumption, this is always true for either representation of the BCR4BP. Moreover, the in-plane equations are only dependent upon the magnitude of the spatial position component, meaning that changes in its sign do not affect the x and y-accelerations acting upon the spacecraft. As a result, any initial condition is reflected about the x-y plane when its initial conditions are flipped about the z-axis. An example trajectory is given in both the Earth-Moon and Sun-Barycenter frames, as shown in Figures 2.22 and 2.23.

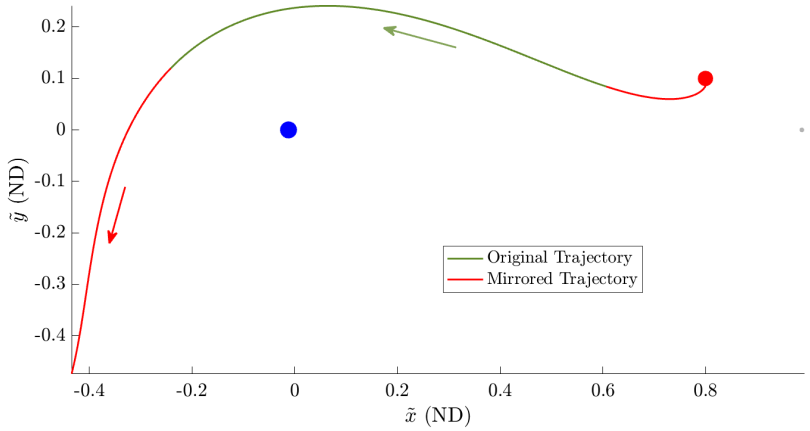

(a) $\tilde{x}$-$\tilde{y}$ projection

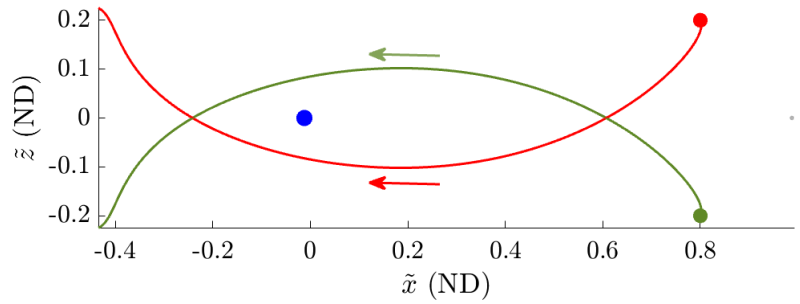

(b) $\tilde{x}$-$\tilde{z}$ projection

Figure 2.22. Spatially reflected trajectories in Earth-Moon frame. Dots indicate starting locations and arrows show direction of propagation.

A natural extension is that should the propagation of an initial state abiding by the rules of the Mirror Theorem have a point which again perpendicularly intersects the x-z plane at a Sun (or Moon) angle of an integer multiple of pi, then the resulting trajectory is periodic. The frequency of the Sun, Earth and Moon realigning is a key factor in the determination of periodic structures in the BCR4BP, an event which occurs far more frequently in the co-planar model than a Sun-inclined BCR4BP representation.

2.3.11 Transformations Between BCR4BP Rotating Frames

While either rotating reference frame in the BCR4BP has its own distinct set of governing equations, the state and epoch with regard to one rotating frame may be transformed

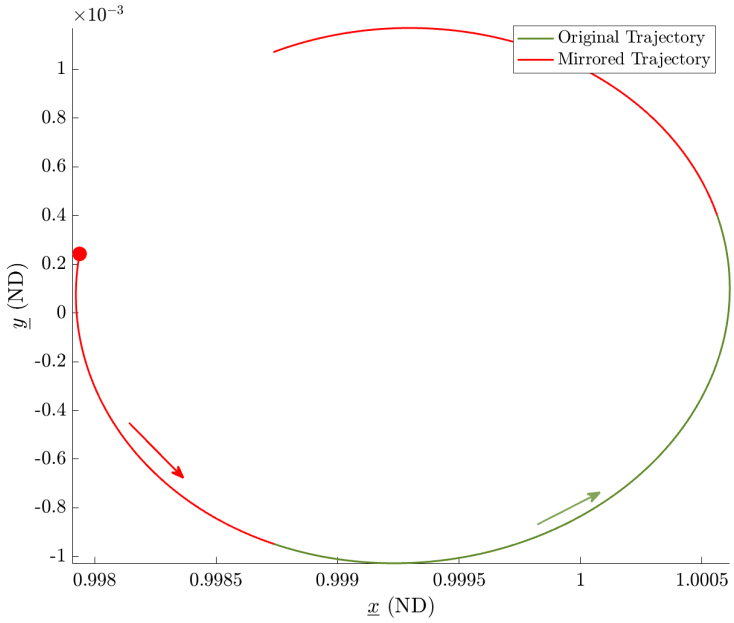

(a) $\underline{x}$-$\underline{y}$ projection

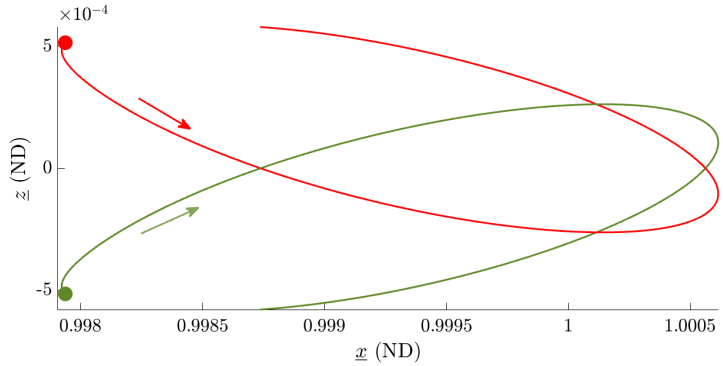

(b) $\underline{x}$-$\underline{z}$ projection

Figure 2.23. Transformation of reflected trajectories from Figure 2.22 to the Sun-Barycenter Frame.

to be in terms of the other. Since both sets of equations of motion are derived from a common inertial expression, the dynamics are consistent between reference frames. As a result, expressions may be constructed to rotate a seven-dimensional state (position, velocity and epoch) between the Earth-Moon and Sun-B_1 frames without a dynamical discontinuity. The transformation between the two frames must accommodate changes in coordinate frames,

scaling to appropriate non-dimensional values and shifts in reference frame origin. To begin, consider the relationship between the two sets of axes, as summarized in Figure 2.24.

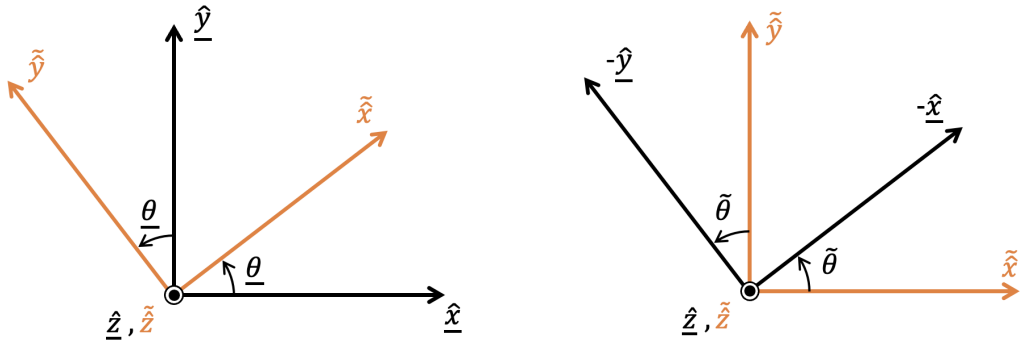

Figure 2.24. Relation between the rotating coordinate frames in terms of Moon angle (a) and Sun angle (b)

Recalling the correspondence between Sun and Moon angles in (2.44), a direction cosine matrix (DCM) may be constructed to rotate from the Sun-B_1 to the Earth-Moon frame.

$$\begin{bmatrix} \tilde{\hat{x}} \\ \tilde{\hat{y}} \\ \tilde{\hat{z}} \end{bmatrix} = \begin{bmatrix} \cos\underline{\theta} & \sin\underline{\theta} & 0 \\ -\sin\underline{\theta} & \cos\underline{\theta} & 0 \\ 0 & 0 & 1 \end{bmatrix} \begin{bmatrix} \underline{\hat{x}} \\ \underline{\hat{y}} \\ \underline{\hat{z}} \end{bmatrix} = {}^{\mathcal{S}}C^{\mathcal{E}} \begin{bmatrix} \underline{\hat{x}} \\ \underline{\hat{y}} \\ \underline{\hat{z}} \end{bmatrix} \tag{2.109}$$

Since the DCM is an orthogonal matrix, its inverse is equal to its transpose, thus the opposite rotation may be defined in (2.3.11).

$$\begin{bmatrix} \underline{\hat{x}} \\ \underline{\hat{y}} \\ \underline{\hat{z}} \end{bmatrix} = \begin{bmatrix} \cos\underline{\theta} & -\sin\underline{\theta} & 0 \\ \sin\underline{\theta} & \cos\underline{\theta} & 0 \\ 0 & 0 & 1 \end{bmatrix} \begin{bmatrix} \tilde{\hat{x}} \\ \tilde{\hat{y}} \\ \tilde{\hat{z}} \end{bmatrix} = \begin{bmatrix} -\cos\tilde{\theta} & -\sin\tilde{\theta} & 0 \\ \sin\tilde{\theta} & -\cos\tilde{\theta} & 0 \\ 0 & 0 & 1 \end{bmatrix} \begin{bmatrix} \tilde{\hat{x}} \\ \tilde{\hat{y}} \\ \tilde{\hat{z}} \end{bmatrix} = {}^{\mathcal{E}}C^{\mathcal{S}} \begin{bmatrix} \tilde{\hat{x}} \\ \tilde{\hat{y}} \\ \tilde{\hat{z}} \end{bmatrix} \tag{2.110}$$

The matrices ${}^{\mathcal{E}}C^{\mathcal{S}}$ and ${}^{\mathcal{S}}C^{\mathcal{E}}$ may be multiplied with position vectors in the Earth-Moon and Sun-Barycenter frames (respectively) to rotate to the alternative reference frame. This transformation accounts for neither the appropriate scaling of the position vectors nor the

differing origins, so additional measures are required. To appropriately accommodate these considerations, the position components are dimensionalized by multiplying by their respective characteristic length, then normalized by the other. In the case of transforming from Earth-Moon to Sun-Barycenter, this re-scaling is done by dividing by a_s, while the inverse transformation requires a multiplication by a_s. Lastly, a shift in origin is only required for the x-component of either vector, and is demonstrated for translating from B_1 to B_2 by (2.111) and vice versa with (2.112).

$$\underline{\vec{r}} = \frac{1}{a_s}{}^{\mathcal{E}}C^{\mathcal{S}}\tilde{\vec{r}} + \begin{bmatrix} 1-\underline{\mu} \\ 0 \\ 0 \end{bmatrix} \tag{2.111}$$

$$\tilde{\vec{r}} = a_s{}^{\mathcal{S}}C^{\mathcal{E}}\left(\underline{\vec{r}} - \begin{bmatrix} 1-\underline{\mu} \\ 0 \\ 0 \end{bmatrix}\right) \tag{2.112}$$

As an aside, the quantity $1-\underline{\mu}$ is equivalent to $\frac{\tilde{m}_s}{\tilde{m}_s+1}$. The conversion for position vectors of either reference frame to the other are covered by equations (2.111) and (2.112), though they are not applicable toward velocity vectors. To transform the motion of the spacecraft, accommodation for both motion within the reference frame as well as the rotational rates of the coordinate axes is required. First, to establish an intuitive nomenclature, dimensional time is denoted τ, while non-dimensional time with respect to the Earth-Moon and Sun-Barycenter frames are $\tilde{t}$ and $\underline{t}$ respectively. These may all be related using their respective characteristic times, as shown in (2.113).

$$\tau = \tilde{t}^*\tilde{t} = \underline{t}^*\underline{t} \tag{2.113}$$

The velocity vector for the Sun-B_1 frame is the derivative of $\underline{\vec{r}}$ with respect to $\underline{t}$. Applying this derivative to (2.111) and expanding via the product rule:

$$\dot{\underline{\vec{r}}} = \frac{1}{a_s}\frac{\partial}{\partial \underline{t}}\left({}^{\mathcal{E}}C^{\mathcal{S}}\right)\tilde{\vec{r}} + \frac{1}{a_s}{}^{\mathcal{E}}C^{\mathcal{S}}\frac{\partial \tilde{\vec{r}}}{\partial \underline{t}} \tag{2.114}$$

Leveraging the relationship between the time variables, as shown in (2.113), the derivatives may be converted to be in terms of $\tilde{t}$.

$$\frac{\partial}{\partial \underline{t}} = \frac{\partial}{\partial \tilde{t}} \cdot \frac{\partial \tilde{t}}{\partial \underline{t}} = \frac{\partial}{\partial \tilde{t}} \cdot \frac{\underline{t}}{\tilde{t}} = \frac{\partial}{\partial \tilde{t}} \cdot \frac{1}{\tilde{n}_{SB}} \tag{2.115}$$

Changing the partial derivative to be with respect to Earth-Moon dimensionless time allows for a simplification of (2.114), as demonstrated in (2.116).

$$\dot{\underline{\vec{r}}} = \frac{1}{\tilde{n}_{SB} a_s} \left({}^{\mathcal{E}}\dot{C}^{\mathcal{S}} \tilde{\vec{r}} + {}^{\mathcal{E}}C^{\mathcal{S}} \dot{\tilde{\vec{r}}} \right) \tag{2.116}$$

Equation (2.116) is the final form of the rotation of an Earth-Moon velocity vector, $\dot{\tilde{\vec{r}}}$ to its Sun-B_1 counterpart, $\dot{\underline{\vec{r}}}$. The time derivative for the direction cosine matrix, as provided in (2.117), is found using the chain rule and $\dot{\tilde{\theta}} = \tilde{n}_{SB} - 1$.

$${}^{\mathcal{E}}\dot{C}^{\mathcal{S}} = \dot{\tilde{\theta}} \begin{bmatrix} \sin\tilde{\theta} & -\cos\tilde{\theta} & 0 \\ \cos\tilde{\theta} & \sin\tilde{\theta} & 0 \\ 0 & 0 & 0 \end{bmatrix} \tag{2.117}$$

Using a similar process outlined by equations (2.114) through (2.117), the rotation of a velocity vector in the Sun-B_1 frame to the Earth-Moon coordinate system is given by (2.118).

$$\dot{\tilde{\vec{r}}} = a_s \tilde{n}_{SB} \left({}^{\mathcal{S}}\dot{C}^{\mathcal{E}} \underline{\vec{r}} + {}^{\mathcal{S}}C^{\mathcal{E}} \dot{\underline{\vec{r}}} \right) \tag{2.118}$$

Where:

$${}^{\mathcal{S}}\dot{C}^{\mathcal{E}} = \dot{\underline{\theta}} \begin{bmatrix} -\sin\underline{\theta} & \cos\underline{\theta} & 0 \\ -\cos\underline{\theta} & -\sin\underline{\theta} & 0 \\ 0 & 0 & 0 \end{bmatrix} \tag{2.119}$$

The rotation of a complete Earth-Moon seven-dimensional state vector to its Sun-Barycenter counterpart may be expressed in a single equation, as shown by (2.120), while the inverse rotation is given in (2.121).

$$\begin{bmatrix} \underline{\vec{r}} \\ \underline{\dot{\vec{r}}} \\ \underline{\theta} \end{bmatrix} = \begin{bmatrix} \frac{1}{a_s}\underline{\underline{\mathcal{E}}}\underline{\underline{C}}^{\mathcal{S}} & 0_{3\times 3} & 0 \\ \frac{1}{a_s\tilde{n}_{SB}}\underline{\underline{\mathcal{E}}}\underline{\underline{\dot{C}}}^{\mathcal{S}} & \frac{1}{a_s\tilde{n}_{SB}}\underline{\underline{\mathcal{E}}}\underline{\underline{C}}^{\mathcal{S}} & 0 \\ 0_{3\times 3} & 0_{3\times 3} & -1 \end{bmatrix} \begin{bmatrix} \tilde{\vec{r}} \\ \dot{\tilde{\vec{r}}} \\ \tilde{\theta} \end{bmatrix} + \begin{bmatrix} 1-\underline{\mu} & 0 & 0 & 0 & 0 & 0 & \boldsymbol{\pi} \end{bmatrix}^T \tag{2.120}$$

$$\begin{bmatrix} \tilde{\vec{r}} \\ \dot{\tilde{\vec{r}}} \\ \tilde{\theta} \end{bmatrix} = \begin{bmatrix} a_s\underline{\underline{\mathcal{S}}}\underline{\underline{C}}^{\mathcal{E}} & 0_{3\times 3} & 0 \\ a_s\tilde{n}_{SB}\underline{\underline{\mathcal{S}}}\underline{\underline{\dot{C}}}^{\mathcal{E}} & a_s\tilde{n}_{SB}\underline{\underline{\mathcal{S}}}\underline{\underline{C}}^{\mathcal{E}} & 0 \\ 0_{3\times 3} & 0_{3\times 3} & -1 \end{bmatrix} \begin{bmatrix} \underline{\vec{r}} + \left(1-\underline{\mu}\right)\underline{\hat{x}} \\ \underline{\dot{\vec{r}}} \\ \underline{\theta} \end{bmatrix} + \begin{bmatrix} 0 & 0 & 0 & 0 & 0 & 0 & \boldsymbol{\pi} \end{bmatrix}^T \tag{2.121}$$

For example trajectories rotated between the two frames, compare Figures 2.20 and 2.21, or for an alternate example, Figures 2.22 and 2.23.

3. DYNAMICAL SYSTEMS THEORY & NUMERICAL METHODS

A consequence of the CR3BP and BCR4BP equations of motion not admitting an analytical solution is that a combination of dynamical systems theory and numerical techniques must be used to gain insights into the dynamics. Dynamical systems theory (DST) within the context of trajectory design is the informed application of linearized dynamics to the non-linear equations of motion to approximate the future behavior of the spacecraft. Numerical methods are the means by which the linearization is performed. In this section, the first-order Taylor series approximations of the CR3BP and BCR4BP equations of motion are used to construct variational equations of the state dynamics. With these, a State Transition Matrix is formulated and utilized to determine state conditions for periodic orbits and transfer arcs. Continuation techniques are then defined to leverage converged states as initial guesses for subsequent targeting procedures. Lastly, dynamical systems theory may be applied to discrete states in order to construct natural passages into and out of periodic orbits, known as manifolds.

3.1 Linear Variational Equations

Using the dynamical equations of motion developed in the previous chapter, the motion of a spacecraft relative to the origin of its reference frame may be propagated. Linear variational equations give insight into the behavior of a spacecraft relative to another reference state within the rotating frame. The reference motion may be a lagrange point, the isochronous point on a perturbed flight path or even along an independent trajectory, to name some examples. For the development of the equations, consider two isochronous states along adjacent, independent arcs, as demonstrated by Figure 3.1. The goal of the linear variational equations is to relate the change in the relative difference between the two states to the difference vector itself. This difference vector is denoted $\delta\vec{x}(t)$, while its change is the corresponding time derivative, $\delta\dot{\vec{x}}(t)$.

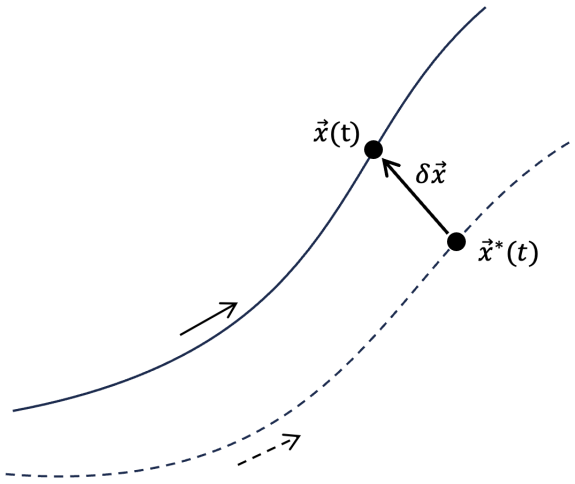

Figure 3.1. Relationship between target state $\vec{x}(t)$ and its isochronous reference, $\vec{x}^*(t)$.

From visual inspection of Figure 3.1, the target and reference states may be related using the difference vector as such:

$$\vec{x}(t) = \vec{x}^*(t) + \delta\vec{x}(t) \tag{3.1}$$

The changes of either state as propagation continues may also be related by deriving both sides of (3.1) with respect to time, as shown in equation (3.2).

$$\dot{\vec{x}}(t) = \dot{\vec{x}}^*(t) + \delta\dot{\vec{x}}(t) \tag{3.2}$$

For simplicity, an alternative representation of the time derivative may be defined: $F(\vec{x}, t) = \dot{\vec{x}}(t)$. This function may be linearized by performing a first-order Taylor series expansion about the reference solution, given in (3.3)

$$F(\vec{x}, t) \approx F(\vec{x}^*(t), t) + \left.\frac{\partial F}{\partial \vec{x}}\right|_{(\vec{x}=\vec{x}^*)} (\vec{x}(t) - \vec{x}^*(t)) + \cdots \tag{3.3}$$

The dots represent higher order terms of the Taylor expansion which are assumed to be negligible. By expanding $F(\vec{x}, t)$ via (3.2) and noting $F(\vec{x}^*(t), t) = \dot{\vec{x}}^*(t)$ the resultant expressions may be substituted into (3.3), then simplified.

$$\dot{\vec{x}}^*(t) + \delta\dot{\vec{x}}(t) \approx \dot{\vec{x}}^*(t) + \left.\frac{\partial F}{\partial \vec{x}}\right|_{(\vec{x}=\vec{x}^*)} (\vec{x}(t) - \vec{x}^*(t))$$

$$\delta\dot{\vec{x}}(t) \approx \left.\frac{\partial F}{\partial \vec{x}}\right|_{(\vec{x}=\vec{x}^*)} \delta\vec{x} \tag{3.4}$$

The Jacobian $\frac{\partial F}{\partial \vec{x}}$ may be represented as matrix $A(t)$, where if $\vec{x}(t) = \left[x, y, z, \dot{x}, \dot{y}, \dot{z}\right]^T$:

$$A(t) = \begin{bmatrix} \frac{\partial \dot{x}}{\partial x} & \frac{\partial \dot{x}}{\partial y} & \frac{\partial \dot{x}}{\partial z} & \frac{\partial \dot{x}}{\partial \dot{x}} & \frac{\partial \dot{x}}{\partial \dot{y}} & \frac{\partial \dot{x}}{\partial \dot{z}} \\ \frac{\partial \dot{y}}{\partial x} & \frac{\partial \dot{y}}{\partial y} & \frac{\partial \dot{y}}{\partial z} & \frac{\partial \dot{y}}{\partial \dot{x}} & \frac{\partial \dot{y}}{\partial \dot{y}} & \frac{\partial \dot{y}}{\partial \dot{z}} \\ \frac{\partial \dot{z}}{\partial x} & \frac{\partial \dot{z}}{\partial y} & \frac{\partial \dot{z}}{\partial z} & \frac{\partial \dot{z}}{\partial \dot{x}} & \frac{\partial \dot{z}}{\partial \dot{y}} & \frac{\partial \dot{z}}{\partial \dot{z}} \\ \frac{\partial \ddot{x}}{\partial x} & \frac{\partial \ddot{x}}{\partial y} & \frac{\partial \ddot{x}}{\partial z} & \frac{\partial \ddot{x}}{\partial \dot{x}} & \frac{\partial \ddot{x}}{\partial \dot{y}} & \frac{\partial \ddot{x}}{\partial \dot{z}} \\ \frac{\partial \ddot{y}}{\partial x} & \frac{\partial \ddot{y}}{\partial y} & \frac{\partial \ddot{y}}{\partial z} & \frac{\partial \ddot{y}}{\partial \dot{x}} & \frac{\partial \ddot{y}}{\partial \dot{y}} & \frac{\partial \ddot{y}}{\partial \dot{z}} \\ \frac{\partial \ddot{z}}{\partial x} & \frac{\partial \ddot{z}}{\partial y} & \frac{\partial \ddot{z}}{\partial z} & \frac{\partial \ddot{z}}{\partial \dot{x}} & \frac{\partial \ddot{z}}{\partial \dot{y}} & \frac{\partial \ddot{z}}{\partial \dot{z}} \end{bmatrix} \tag{3.5}$$

Since each of the state components are independent of one another, many elements of $A(t)$ are equal to zero. Moreover, $\ddot{x}$, $\ddot{y}$ and $\ddot{z}$ all reflect the dynamical equations of motion, thus the corresponding pseudo-potential functions may be leveraged to condense the expression for $A(t)$. The (6×6) representation of the Jacobian is more suitable for the CR3BP, while state vectors in the BCR4BP often append an epoch variable as a seventh component. The $A(t)$ Jacobian for the CR3BP is provided by expression (3.6), while its (7×7) BCR4BP version is represented in terms of the Earth-Moon frame in (3.7) and Sun-Barycenter frame by (3.8).

$$A(t) = \begin{bmatrix} 0 & 0 & 0 & 1 & 0 & 0 \\ 0 & 0 & 0 & 0 & 1 & 0 \\ 0 & 0 & 0 & 0 & 0 & 1 \\ \Omega_{xx} & \Omega_{xy} & \Omega_{xz} & 0 & 2 & 0 \\ \Omega_{yx} & \Omega_{yy} & \Omega_{yz} & -2 & 0 & 0 \\ \Omega_{zx} & \Omega_{zy} & \Omega_{zz} & 0 & 0 & 0 \end{bmatrix} \tag{3.6}$$

Both the Sun and Moon angles are independent of the other state parameters, though the pseudo-potential functions do rely on their respective epoch variables. Additionally, the time derivative of either $\tilde{\theta}$ or $\underline{\theta}$ is constant, meaning that its derivative with respect to anything also leads to zero. As a result, the last row of either BCR4BP Jacobian matrix is entirely comprised of zeros, while the last column is not.

$$\tilde{A}(t) = \begin{bmatrix} 0 & 0 & 0 & 1 & 0 & 0 & 0 \\ 0 & 0 & 0 & 0 & 1 & 0 & 0 \\ 0 & 0 & 0 & 0 & 0 & 1 & 0 \\ \tilde{\Omega}_{\tilde{x}\tilde{x}} & \tilde{\Omega}_{\tilde{x}\tilde{y}} & \tilde{\Omega}_{\tilde{x}\tilde{z}} & 0 & 2 & 0 & \tilde{\Omega}_{\tilde{x}\tilde{\theta}} \\ \tilde{\Omega}_{\tilde{y}\tilde{x}} & \tilde{\Omega}_{\tilde{y}\tilde{y}} & \tilde{\Omega}_{\tilde{y}\tilde{z}} & -2 & 0 & 0 & \tilde{\Omega}_{\tilde{y}\tilde{\theta}} \\ \tilde{\Omega}_{\tilde{z}\tilde{x}} & \tilde{\Omega}_{\tilde{z}\tilde{y}} & \tilde{\Omega}_{\tilde{z}\tilde{z}} & 0 & 0 & 0 & \tilde{\Omega}_{\tilde{z}\tilde{\theta}} \\ 0 & 0 & 0 & 0 & 0 & 0 & 0 \end{bmatrix} \tag{3.7}$$

$$\underline{A}(t) = \begin{bmatrix} 0 & 0 & 0 & 1 & 0 & 0 & 0 \\ 0 & 0 & 0 & 0 & 1 & 0 & 0 \\ 0 & 0 & 0 & 0 & 0 & 1 & 0 \\ \underline{\Omega}_{\underline{x}\underline{x}} & \underline{\Omega}_{\underline{x}\underline{y}} & \underline{\Omega}_{\underline{x}\underline{z}} & 0 & 2 & 0 & \underline{\Omega}_{\underline{x}\underline{\theta}} \\ \underline{\Omega}_{\underline{y}\underline{x}} & \underline{\Omega}_{\underline{y}\underline{y}} & \underline{\Omega}_{\underline{y}\underline{z}} & -2 & 0 & 0 & \underline{\Omega}_{\underline{y}\underline{\theta}} \\ \underline{\Omega}_{\underline{z}\underline{x}} & \underline{\Omega}_{\underline{z}\underline{y}} & \underline{\Omega}_{\underline{z}\underline{z}} & 0 & 0 & 0 & \underline{\Omega}_{\underline{z}\underline{\theta}} \\ 0 & 0 & 0 & 0 & 0 & 0 & 0 \end{bmatrix} \tag{3.8}$$

This linearization opens up several applications, such as gaining insight to motion relative to libration points or forecasting the isochronous correspondence between adjacently-flying spacecraft. A particularly interesting use for the linearized behavior is the estimation of changes to downstream behavior as a result of a perturbation to an initial state. To perform this task, any of the $A(t)$ matrices developed in this section may be extrapolated to evaluate relative behavior at a different instance in time; the primary mechanism for doing so is the state transition matrix.

3.2 State Transition Matrix

As seen in Section 3.1, the change of a state relative to an isochronous reference condition may be approximated by using the difference vector itself and derivatives of the equations of motion evaluated about the reference motion. This relationship can be extrapolated such that the downstream condition of a perturbed state may be approximated using a sensitivity matrix, known as the state transition matrix (STM). To construct the STM, first consider a trajectory where along it are three states evaluated at times t_o, t_1 and t_2. An example illustration of this trajectory is provided in Figure 3.2. Alterations to $\vec{x}(t_o)$ will shift the course of the downstream trajectory, changing $\vec{x}(t_1)$, which in turn also causes $\vec{x}(t_2)$ to deviate. The alteration experienced by $\vec{x}(t_1)$ as a result of a preceding perturbation at t_o may be represented as shown in (3.9).

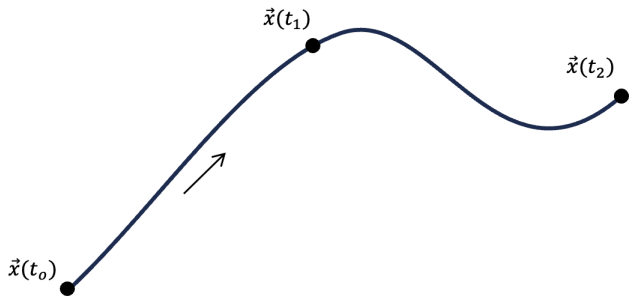

Figure 3.2. Example trajectory with three discrete states along its path.

$$\delta\vec{x}(t_1) = \frac{\partial\vec{x}(t_1)}{\partial\vec{x}(t_o)}\delta\vec{x}(t_o) \tag{3.9}$$

The matrix quantity in (3.9) is the state transition matrix of $\vec{x}(t_1)$ as a result of perturbations at $\vec{x}(t_o)$, alternatively represented with $\Phi(t_1, t_o)$. Extrapolating further, it stands to reason that alterations experienced by $\vec{x}(t_1)$ will propagate downward to deviate $\vec{x}(t_2)$ as well. This phenomena may be expressed mathematically using the derivative chain rule:

$$\delta\vec{x}(t_2) = \frac{\partial\vec{x}(t_2)}{\partial\vec{x}(t_1)}\frac{\partial\vec{x}(t_1)}{\partial\vec{x}(t_o)}\delta\vec{x}(t_o) = \frac{\partial\vec{x}(t_2)}{\partial\vec{x}(t_o)}\delta\vec{x}(t_o) \tag{3.10}$$

This chaining may be repeated for any number of following points, highlighting a core property of the STM:

$$\Phi(t_n, t_o) = \Phi(t_n, t_{n-1})\Phi(t_{n-1}, t_{n-2}) \cdots \Phi(t_2, t_1)\Phi(t_1, t_o) \tag{3.11}$$

The general structure of the STM for the state at an arbitrary time t, $\Phi(t, t_o)$ is presented in (3.12).

$$\Phi(t, t_o) = \begin{bmatrix} \frac{\partial x}{\partial x_o} & \frac{\partial x}{\partial y_o} & \frac{\partial x}{\partial z_o} & \frac{\partial x}{\partial \dot{x}_o} & \frac{\partial x}{\partial \dot{y}_o} & \frac{\partial x}{\partial \dot{z}_o} \\ \frac{\partial y}{\partial x_o} & \frac{\partial y}{\partial y_o} & \frac{\partial y}{\partial z_o} & \frac{\partial y}{\partial \dot{x}_o} & \frac{\partial y}{\partial \dot{y}_o} & \frac{\partial y}{\partial \dot{z}_o} \\ \frac{\partial z}{\partial x_o} & \frac{\partial z}{\partial y_o} & \frac{\partial z}{\partial z_o} & \frac{\partial z}{\partial \dot{x}_o} & \frac{\partial z}{\partial \dot{y}_o} & \frac{\partial z}{\partial \dot{z}_o} \\ \frac{\partial \dot{x}}{\partial x_o} & \frac{\partial \dot{x}}{\partial y_o} & \frac{\partial \dot{x}}{\partial z_o} & \frac{\partial \dot{x}}{\partial \dot{x}_o} & \frac{\partial \dot{x}}{\partial \dot{y}_o} & \frac{\partial \dot{x}}{\partial \dot{z}_o} \\ \frac{\partial \dot{y}}{\partial x_o} & \frac{\partial \dot{y}}{\partial y_o} & \frac{\partial \dot{y}}{\partial z_o} & \frac{\partial \dot{y}}{\partial \dot{x}_o} & \frac{\partial \dot{y}}{\partial \dot{y}_o} & \frac{\partial \dot{y}}{\partial \dot{z}_o} \\ \frac{\partial \dot{z}}{\partial x_o} & \frac{\partial \dot{z}}{\partial y_o} & \frac{\partial \dot{z}}{\partial z_o} & \frac{\partial \dot{z}}{\partial \dot{x}_o} & \frac{\partial \dot{z}}{\partial \dot{y}_o} & \frac{\partial \dot{z}}{\partial \dot{z}_o} \end{bmatrix} \tag{3.12}$$

Another characteristic of the STM may be discovered when examining the change of the initial state with respect to itself.

$$\Phi(t_o, t_o) = \frac{\partial \vec{x}(t_o)}{\partial \vec{x}(t_o)} = \mathbb{I}_n \tag{3.13}$$

Where $\mathbb{I}_n$ is the identity matrix of size $n \times n$, and n is the dimension of the state vector $\vec{x}$. Returning to (3.9), it is noted that the change in the initial state resulting from an alteration to the final state is determined by inverting the STM.

$$\delta\vec{x}(t_o) = \Phi(t_1, t_o)^{-1}\delta\vec{x}(t_1) \tag{3.14}$$

In other words, $\Phi(t_o, t_1) = \Phi(t_1, t_o)^{-1}$. Next, consider the time rate of change of the state at an arbitrary downstream time t, as initialized in equation (3.15).

$$\frac{\partial}{\partial t}\left(\delta\vec{x}(t)\right) = \frac{\partial}{\partial t}\left(\Phi(t, t_o)\right)\delta\vec{x}(t_o) + \Phi(t, t_o)\frac{\partial}{\partial t}\left(\delta\vec{x}(t_o)\right) \tag{3.15}$$

The deviation of the initial state is unaffected by a change in the subsequent propagation time, t. Additionally, an approximation relating the time rate of change of $\delta\vec{x}$ is done using

linear variational equations, given by (3.5). With this, a first-order approximation may be applied such that:

$$A(t)\delta\vec{x}(t) = A(t)\Phi(t,t_o)\delta\vec{x}(t_o) \approx \dot{\Phi}(t,t_o)\delta\vec{x}(t_o) \tag{3.16}$$

By simplifying, the final property of the STM is derived:

$$\dot{\Phi}(t,t_o) \approx A(t)\Phi(t,t_o) \tag{3.17}$$

The STM follows the same properties when applied in either the CR3BP or BCR4BP. The only difference between the two is the structure of the matrix itself. Since the Jacobian from the CR3BP variational equations is constructed from the 6-dimensional state vector, the corresponding STM is consequently (6×6). The BCR4BP counterpart accounts for variations due to change in the epoch variable as well, meaning that the STM in the BCR4BP includes an appended row to reflect $\frac{\partial\theta}{\partial\vec{x}_o}$ and a column for $\frac{\partial\vec{x}}{\partial\theta_o}$. The variable θ is a placeholder for either the Sun or Moon angle, depending on the reference frame being used. As the epoch variable propagates independently from the spacecraft state, the following is true:

$$\frac{\partial\theta}{\partial x_o} = \frac{\partial\theta}{\partial y_o} = \frac{\partial\theta}{\partial z_o} = \frac{\partial\theta}{\partial \dot{x}_o} = \frac{\partial\theta}{\partial \dot{y}_o} = \frac{\partial\theta}{\partial \dot{z}_o} = 0 \tag{3.18}$$

$$\frac{\partial\theta}{\partial\theta_o} = 1 \tag{3.19}$$

In practice, determination of the state transition matrix for an arbitrary time t may be performed by numerically integrating both the equations of motion and the isochronous $\dot{\Phi}(t,t_o)$ expressions simultaneously. Both the initial state $\vec{x}(t_o)$ as well as $\Phi(t_o,t_o)$ are used as starting conditions for the integrator. Once the STM is produced, differential corrections may be employed to perform a variety of tasks, such as constructing periodic orbits or stitching together separate arcs into a trajectory continuous in all state components.

3.3 Differential Corrections

Differential corrections is the process by which an initial guess vector $\vec{X}^*$ is iteratively updated to become $\vec{X}$ which satisfies $||\vec{F}(\vec{X})|| \leq \xi$, where $\vec{F}$ is the constraint vector and ξ is

a desired tolerance. The investigation utilizes a multi-dimensional Newton-Raphson method for constructing the corrector, where each update to the free-variable vector $\vec{X}$ is governed by expression (3.20).

$$\vec{X}_{i+1} = \vec{X}_i - \left(\left. \frac{\partial \vec{F}}{\partial \vec{X}} \right|_{(\vec{X}=\vec{X}_i)} \right)^{-1} \vec{F}(\vec{X}_i) = \vec{X}_i - DF^{-1}\vec{F}(\vec{X}_i) \tag{3.20}$$

While the nomenclature used for the derivative matrix lacks an index, DF updates iteratively as well. For the matrix inversion to be possible, DF must be square, or in other words, the dimensions of the $\vec{X}$ and $\vec{F}(\vec{X})$ vectors must be the same. Should this not be the case, approximate matrix inversion for a non-square matrix is possible using either a least-squares or minimum-norm solution. If $\vec{F}(\vec{X}) \in \mathbb{R}^m$ and $\vec{X} \in \mathbb{R}^n$, then a system is overdetermined when $m > n$ and underdetermined when $n > m$. Matrix inversion may be accomplished for an over-constrained system by using a least-squares approach, as shown in (3.21), while that for the under-constrained case is performed using a minimum-norm approach via (3.22).

$$\vec{X}_i = (DF^T DF)^{-1} DF^T \cdot \vec{F}(\vec{X}_i) \tag{3.21}$$

$$\vec{X}_i = DF^T (DF \cdot DF^T)^{-1} \vec{F}(\vec{X}_i) \tag{3.22}$$

While any set of requirements can be imposed by the $\vec{F}$ vector, typical entries for Lunar transfer design include state continuity, altitude, apse and maneuver cost constraints. Within the investigation, state continuity constraints are commonly used to stitch together multiple arcs for continuous transfer construction, while perpendicular-crossing conditions are often sought out for determining periodic solutions. The differential corrections process may be sub-divided into two categories, single shooting and multiple shooting, where the former focuses on correcting the initial conditions for a single trajectory, and the latter for several. Regardless of which sub-division is being employed, targeting may always be summarized by the process detailed in equation (3.20).

3.3.1 Single Shooting

A single set of initial conditions may be iteratively altered to provide a variety of results, though one of particular relevance is periodic motion. Recalling from Sections 2.2.6 and 2.3.10, if two states along a single path satisfy the axioms of the Mirror Theorem, then repeated motion will result. To investigate this, first consider an initial guess for the free-variable vector, $\vec{X}^* = \begin{bmatrix} 1.1386 & 0 & 0 & 0.001 & 0.8990 & 0 \end{bmatrix}^T$. This initial guess is propagated in the CR3BP for a time of flight of 3.3838 non-dimensional units. If periodicity were desired, both ends of the trajectory should be coincident with the $\hat{x}$-$\hat{z}$ plane with velocities perfectly aligned with the $\pm\hat{y}$ direction. The correction scheme for these conditions is referred to as a "perpendicular-crossing targeter", and may be constructed using various methods. The satisfaction of the Mirror Theorem by the initial state is maintained by omitting the initial y, $\dot{x}$ and $\dot{z}$ components. Moreover, the desired end-state is a second perpendicular crossing, thus the same three components for the final state comprise the target vector, $\vec{F}$. For this example, the time of flight (T) is also a free-variable, though it does not need to be targeted and may instead be replaced with an event function that triggers when $y = 0$. The target and free-variable vectors are thus defined as:

$$\vec{F}(\vec{X}) = \begin{bmatrix} y_f \\ \dot{x}_f \end{bmatrix} \qquad \vec{X} = \begin{bmatrix} x_{\mathrm{i}} \\ \dot{y}_{\mathrm{i}} \\ T \end{bmatrix} \tag{3.23}$$

Noting that spatial velocities may be omitted from $\vec{F}(\vec{X})$ and $\vec{X}$ since the initial state indicates the motion will always be planar, though they are included in a more generalized perpendicular crossing targeter. Equation (3.23) also highlights that this problem is under-constrained, thus the update algorithm utilizes (3.22). The DF matrix is formulated using a combination of elements from the STM as well as end-state conditions.

$$DF = \frac{\partial \vec{F}(\vec{X})}{\partial \vec{X}} = \begin{bmatrix} \phi_{21} & \phi_{25} & \dot{y}_f \\ \phi_{41} & \phi_{45} & \ddot{x}_f \end{bmatrix} \tag{3.24}$$

Where ϕ_{ij} is the element from the i-th row and j-th column of the STM. The initial condition for a periodic orbit is found by recursively updating the free-variable vector until the magnitude of $\vec{F}(\vec{X})$ is less than a sample tolerance of $\xi = 1 \times 10^{-10}$. The converged solution is compared with the initial guess trajectory in Figure 3.3.

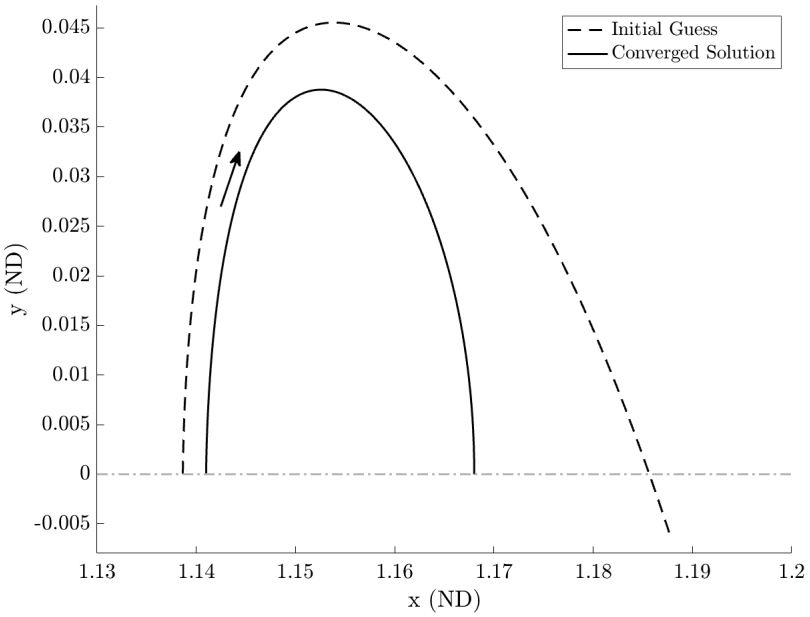

Figure 3.3. Comparison between initial and converged trajectories. The grey line is along $y = 0$. Motion shown in the Earth-Moon rotating frame.

Another approach is to fix the initial x position, which may be accomplished by eliminating the first entry in $\vec{X}$ and consequently the first column in DF. The resulting converged trajectory is compared with the same initial condition in Figure 3.4.

Lastly, the purpose of a perpendicular crossing targeter is to leverage the Mirror Theorem to construct a repeating trajectory. Should the ending condition of either converged trajectory continue to be propagated for double the time of flight, the end of the resultant arc matches its own initial state. This is demonstrated for the fixed-initial position converged solution in Figure 3.5.

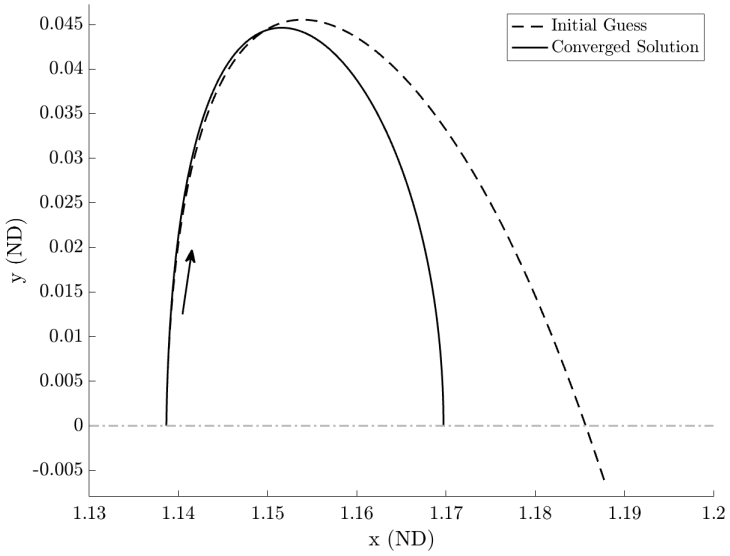

Figure 3.4. Comparison between initial and converged trajectories for a fixed initial position. The grey line is along $y = 0$. Motion shown in the Earth-Moon rotating frame.

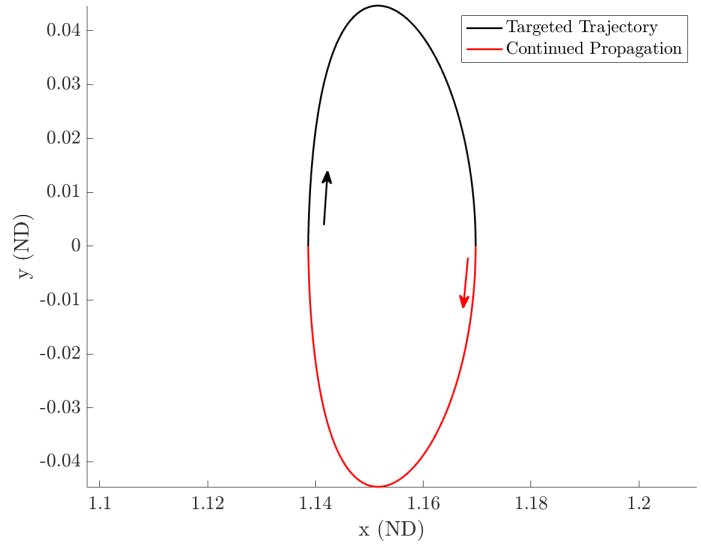

Figure 3.5. Subsequent propagation of ending condition from Figure 3.4, forming a periodic orbit.

As noted in Section 2.3.10, periodic orbits in the BCR4BP have an additional condition of the epoch variable being an integer multiple of π at the perpendicular crossing. Single-shooting for a BCR4BP periodic solution using this method would require an additional constraint in order to enforce this. A result is that the initial epoch as well as time of flight are both more restricted. For example, an Earth-Moon periodic orbit would need $\tilde{\theta}_{\mathrm{i}} = k_1\pi$ for an integer value of k_1, and the time of flight must correspond to a change in sun angle of $\Delta\tilde{\theta} = k_2 2\pi$, where k_2 is also an integer. With a sufficiently lenient tolerance, periodicity can be targeted in terms of position and velocity, though if the epoch considerations are not met, the Mirror Theorem does not apply and the downstream trajectory will deviate. Since the durations of periodic orbits in the BCR4BP must be integer ratios of the time for the rotating frames to realign, dynamically repeating motion in this model solely exists as discrete resonant trajectories. In contrast to this, the lack of time-variance within the dynamics of the CR3BP (as viewed in the rotating frame) means that periodic orbits exist within continuous families rather than individual solutions.

3.3.2 Multiple Shooting

Scenarios which challenge a single-shooting algorithm are various and abundant. Difficulties commonly arise when propagating through a dynamically sensitive region, or correcting a trajectory with a lengthy flight duration. One practice for minimizing potential difficulties is the incorporation of multiple independent segments in the targeting scheme, or multiple shooting. A generalized illustration for this is provided in Figure 3.6.

By segmenting portions of a reference trajectory, negative perturbations to one segment do not necessarily cascade throughout the rest of the propagation, creating an inherent bias towards the desired reference. This is particularly effective for long-duration trajectories, as minute changes to the initial condition in a single shooter may lead to significant over-correcting at the tail end. Some scenarios also look to propagate a single leg forward in time to meet another being propagated in reverse, another situation requiring a multiple shooter. To demonstrate the construction of a multi-segment algorithm, consider the scenario of four segments which deviate from a reference trajectory, all propagated forward in time.

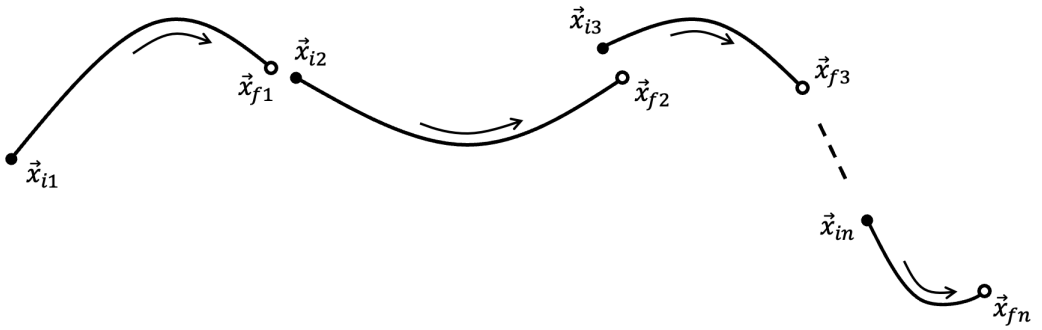

Figure 3.6. Illustration of n independent segments.

Moreover, the initial location of the first arc is fixed and a target location for the end of the fourth arc is defined. A sample set of trajectories fitting this scenario are propagated in the Earth-Moon BCR4BP, as shown in Figure 3.7.

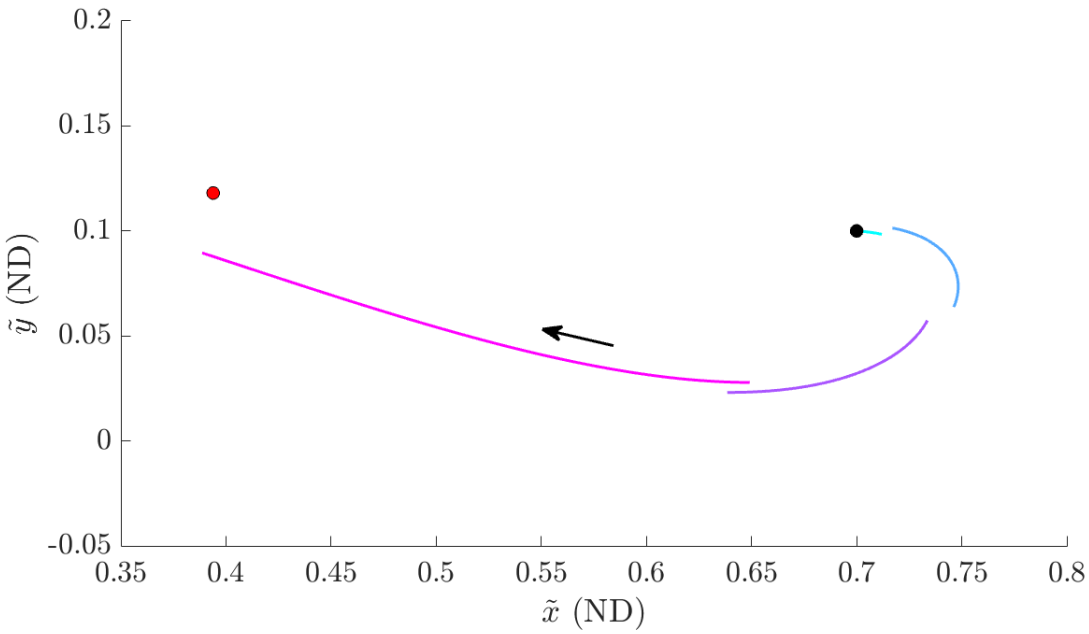

Figure 3.7. Propagation of each set of initial conditions in the BCR4BP. Black dot is the fixed initial position, red dot is the desired final location. Motion shown in the Earth-Moon frame.

The colors of the arcs are to distinguish each independent trajectory. To create a continuous trajectory from the black dot to the red, the $\vec{F}(\vec{X})$ vector must accommodate for both the target location and the full-state continuity between each end state and the following initial condition vector. Since this scenario is in the BCR4BP, each set of initial conditions has an associated epoch, thus the continuity constraints must also ensure the epochs align. Explicitly listing each requirement, there must be: no change position of $\vec{x}_{\text{i}1}$, continuity between $\vec{x}_{f1}$ and $\vec{x}_{\text{i}2}$, $\vec{x}_{f2}$ and $\vec{x}_{\text{i}3}$, $\vec{x}_{f3}$ and $\vec{x}_{\text{i}4}$, as well as position continuity between the target destination and the end of the fourth segment. With these, the free-variable and constraint vectors may be defined for this scenario:

$$\vec{F}(\vec{X}) = \begin{bmatrix} \vec{x}_{f1} - \vec{x}_{\text{i}2} \\ \vec{x}_{f2} - \vec{x}_{\text{i}3} \\ \vec{x}_{f3} - \vec{x}_{\text{i}4} \\ \vec{r}_{f4} - \vec{r}_{T} \end{bmatrix} \qquad \vec{X} = \begin{bmatrix} \vec{v}_{\text{i}1} \\ \vec{x}_{\text{i}2} \\ \vec{x}_{\text{i}3} \\ \vec{x}_{\text{i}4} \\ T_1 \\ T_2 \\ T_3 \\ T_4 \end{bmatrix} \tag{3.25}$$

Where $\vec{v}_{\text{i}1}$ is the initial velocity of the first segment, and $\vec{r}_{f4}$ is the ending position of the last arc. Since the length of $\vec{X}$ is greater than $\vec{F}(\vec{X})$, this targeter is also under-determined. To demonstrate how the DF matrix is constructed, consider the derivative of the first continuity constraint with respect to $\vec{X}$. Alterations to $\vec{v}_{\text{i}1}$ change its downstream state $\vec{x}_{f1}$ as modeled by the third through sixth columns of the STM for the first trajectory. This matrix will be denoted as $\tilde{\Phi}_1^{v\text{i}}$, where the subscript is the corresponding segment index and the superscript indicates an isolation of the elements corresponding to the initial velocity. The continuity constraint also includes the initial state of the second arc, which is unaffected by perturbations of $\vec{v}_{\text{i}1}$ as the two segments are independent. Deriving this constraint with respect to $\vec{x}_{\text{i}2}$ leads to the negative (7×7) identity matrix. The vector $\vec{x}_{f1} - \vec{x}_{\text{i}2}$ is independent of the other two initial conditions, thus their derivatives are (7×7) zero matrices. A change in time of

flight for the first arc will also shift the final state, thus the derivative is the time derivative of $\vec{x}_{f1}$. Since T_2 only affects the states downstream of $\vec{x}_{i2}$, the constraint is independent of the second time of flight, as well as those for the third and fourth segments. Repeating a similar procedure for the other constraints, the DF matrix may be constructed as shown in equation (3.26).

$$DF = \begin{bmatrix} \tilde{\Phi}_1^{vi} & -\mathbb{I}_{7\times7} & 0_{7\times7} & 0_{7\times7} & \dot{\vec{x}}_{f1} & 0_{7\times1} & 0_{7\times1} & 0_{7\times1} \\ 0_{7\times7} & \tilde{\Phi}_2 & -\mathbb{I}_{7\times7} & 0_{7\times7} & 0_{7\times1} & \dot{\vec{x}}_{f2} & 0_{7\times1} & 0_{7\times1} \\ 0_{7\times7} & 0_{7\times7} & \tilde{\Phi}_3 & -\mathbb{I}_{7\times7} & 0_{7\times1} & 0_{7\times1} & \dot{\vec{x}}_{f3} & 0_{7\times1} \\ 0_{3\times7} & 0_{3\times7} & 0_{3\times7} & \tilde{\Phi}_4^{rf} & 0_{3\times1} & 0_{3\times1} & 0_{3\times1} & \dot{\vec{r}}_{f4} \end{bmatrix} \tag{3.26}$$

When applied to the targeting algorithm, the solution converges as shown in Figure 3.8.

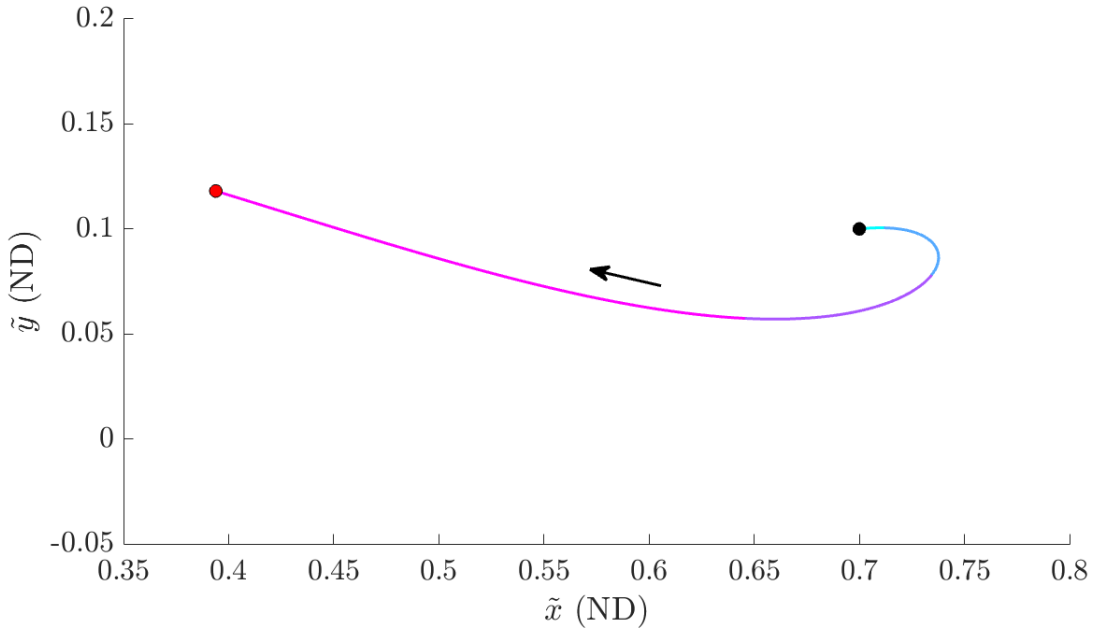

Figure 3.8. Converged trajectory from Figure 3.7. Black dot is the fixed initial position, red dot is the desired final location. Motion shown in the Earth-Moon frame.

Epoch continuity is less obvious when viewing a converged arc in configuration space, though Figure 3.9 better illustrates its preservation.

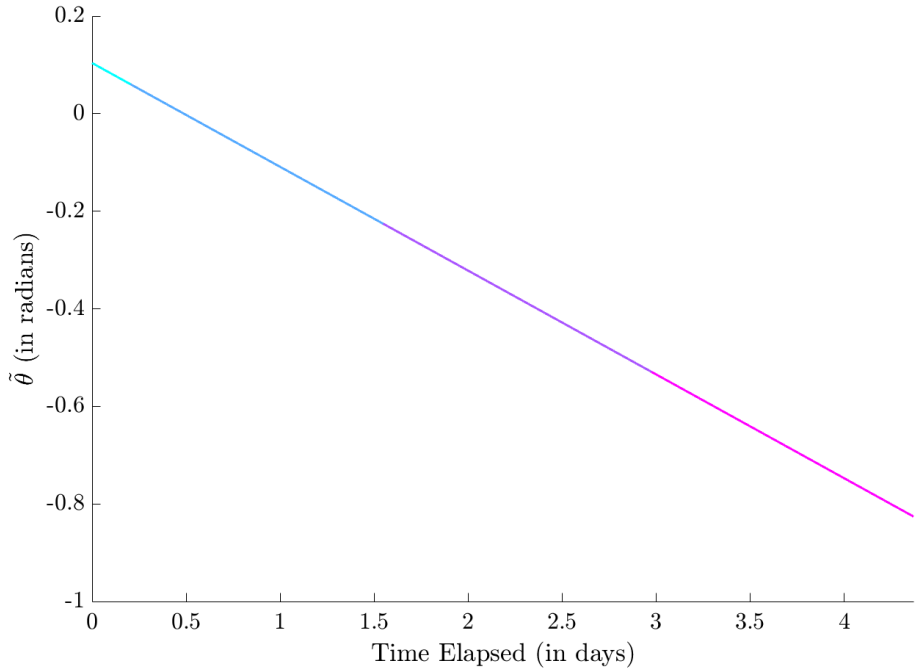

Figure 3.9. Sun angle values for correspondingly colored segments in Figure 3.8.

While the inclusion of additional segments does aid in mitigating dynamical sensitivity, the increased size of the DF matrix has the potential to increase numerical error in its inversion, as well as a greater likelihood of user error. Due to this, an increase in the number of arcs does not necessarily lead to a decrease in targeting difficulty, and single shooting should be utilized when applicable. This investigation frequently features long propagation periods, passages within dynamically sensitive regions, as well as forward and backward propagated segments, thus the inclusion of multiple shooting is justified. While differential corrections is the process for converging an initial guess onto a desired solution, continuation is a method which allows for a diversification of the initial states available.

3.4 Continuation Methods

As noted at the end of Section 3.3.1, periodic orbits within the CR3BP exist within continuous families of solutions, while counterparts in the BCR4BP are only feasible when they are resonant with a synodic month. Following the convergence of a single CR3BP periodic orbit, it is possible to utilize a continuation method to subsequently determine

the initial conditions for another. Doing so, the solution space for repeating libration point trajectories is diversified, creating a pool of candidate destination orbits for a Lunar transfer. In this section, methods for translating through a continuous family of solutions in the CR3BP are examined in the form of natural parameter and pseudo-arclength continuation. Following these, a strategy for dynamically continuing from a converged synodic-resonant CR3BP to its BCR4BP counterpart is introduced with Solar Gravity Continuation.

3.4.1 Natural Parameter Continuation

In the context of CR3BP periodic orbits, the term "continuous family" refers to the set of periodic orbits which generally share similar physical attributes between adjacent members. These groups are continuous in that there exist an infinite number of members spanning a finite track through the family. As a result, there exist no discontinuities in physical attributes when continuing through the solution set. This fact may be leveraged when attempting to determine a periodic solution using converged initial conditions belonging to another family member. Consider an arbitrary state component, c_{i} of a converged initial state vector. Next, define a continuation parameter, p such that traversal through the family results from a variation in its value. For the value of the continuation parameter corresponding to the initial state, p_{i}, the un-converged initial guess for a neighboring solution ($c^*_{\mathrm{i+1}}$) may be produced by evaluating c_{i} at $p_{\mathrm{i+1}}$, where:

$$p_{\mathrm{i+1}} = p_{\mathrm{i}} + \delta p_{\mathrm{i}} \tag{3.27}$$

In other words, following the convergence of a solution using a corrections algorithm, that same state may be used as an initial guess for targeting another periodic orbit where some parameter has been altered by a chosen step-size of δp_{i}. The process of manually stepping along a physical attribute in order to target neighboring solutions is known as natural parameter continuation (NPC). A visualization of this is provided in Figure 3.10(a), where $\delta c_{\mathrm{i+1}}$ is the difference between the converged and initial components, c. Furthermore, should convergence of upon the adjacent solution $c_{\mathrm{i+1}}$ occur, this state may in turn be used for an-

other subsequent shift in p. Repeating this ultimately traces out the behavior of component c across the solution family, as demonstrated by the orange curve in Figure 3.10(b).

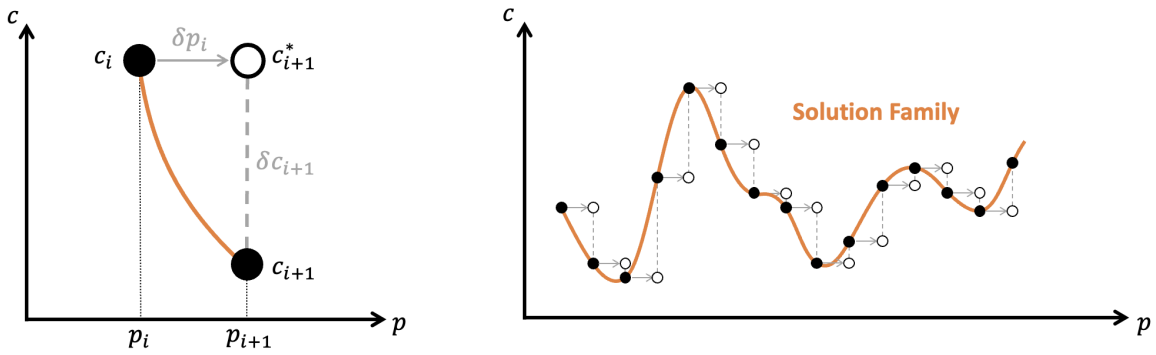

Figure 3.10. Visualization of a single NPC step (a) compared with multiple steps forming a solution family curve (b).

A continuous solution family curve exists for any attribute c, though not all are guaranteed to have variations. For instance, the Lyapunov family in the CR3BP is solely comprised of planar trajectories (an example member of which is provided in Figure 3.5), thus the curves for initial conditions z and $\dot{z}$ are consistently zero. Furthermore, Figure 3.10(b) demonstrates that in regions where $\left|\frac{\partial c}{\partial p}\right|$ is large, NPC may provide an initial guess which deviates significantly from its converged counterpart, or where δc_{i+1} is relatively substantial. Should this deviation be so great that divergence occurs within the corrections algorithm, a smaller step size is required.

Natural parameter continuation may be used to continue through an L_2 Lyapunov periodic orbit family, as demonstrated by Figure 3.11. In this case, traversal through the family is stopped when the perilune radius equals that of the Moon's radius. This does not signify the end of the family, as the trajectory continuation may still continue within the body of the Moon, though this portion of the set is not feasible for real-world application. Continuation for the Lyapunov family features uniform steps of the initial state's x-component toward the Moon, though stepping along any monotonically changing parameter will also suffice. For instance, the period of each individual orbit also increases during this continuation (as

demonstrated in Figure 3.12), though convergence becomes increasingly challenging as the vertical asymptote is approached.

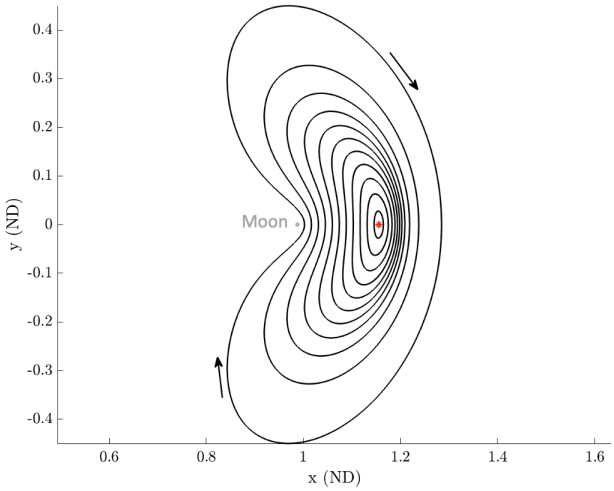

Figure 3.11. L_2 CR3BP Lyapunov orbit family. Red asterisk marks L_2. Motion shown in the Earth-Moon frame.

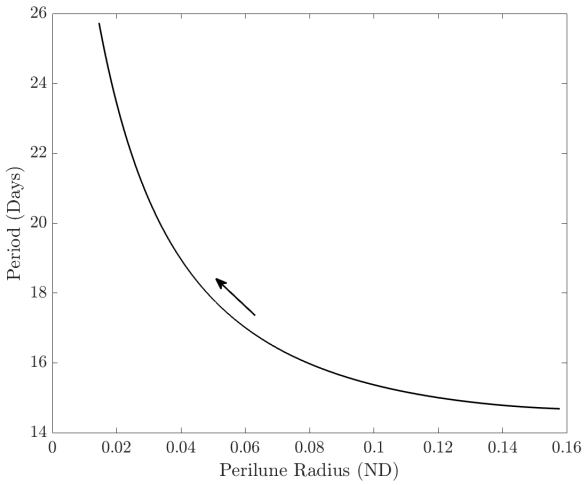

Figure 3.12. L_2 CR3BP Lyapunov orbit family periods as a function of perilune distance. Arrow indicates direction of continuation.

While NPC provides an intuitive means for determining families of solutions, there are situations where it struggles. Scenarios where monotonic change is not present in any characteristic of the family or when it is unclear how the continuation should persist both challenge

an ordinary NPC algorithm. For cases such as these, a more adaptive continuation procedure, such as pseudo-arclength, may be favorable.

3.4.2 Pseudo-arclength Continuation

In contrast to its intuitive natural parameter counterpart, pseudo-arclength continuation (PALC) proceeds along a non-physical track. By forming the next initial guess along the line tangent to the solution space curve, PALC can more adaptively produce families of trajectories. As a result, for scenarios where no continuation parameter changes monotonically or intuitively, pseudo-arclength continuation grants a greater likelihood to generate solution sets. To define this process, first consider an already converged free-variable vector, $\vec{X}_{\mathrm{i}}$, the scenario constraint vector $\vec{F}(\vec{X})$, and the Jacobian matrix corresponding to $\vec{X}_{\mathrm{i}}$, $DF(\vec{X}_{\mathrm{i}})$. The solution space spans n-dimensions, where n is the length of $\vec{X}$. Because of this, visualization is often difficult when n is greater than 3. For an under-constrained system, the null space of the DF matrix is the $((n-m)\times n)$-dimensional solution for $DF\cdot\vec{X}=\vec{0}$, where m is the length of $\vec{F}(\vec{X})$.

Stepping along the null space provides an initial guess which more closely adheres to the general behavior of the $\vec{X}_{\mathrm{i}}$ as it progresses through the family. In order to apply this to the initial conditions vector, the null space must be a vector as well, meaning that $(n-m)$ must be equal to one. Defining $\vec{N}(\vec{X}_{\mathrm{i}})=\mathrm{Null}(DF(\vec{X}_{\mathrm{i}}))$, the governing equation for PALC is defined in (3.28). The vector $\vec{X}^{*}_{\mathrm{i+1}}$ is the subsequent un-converged set of free variables, and Δs is the enforced step size along the solution curve.

$$\vec{X}^{*}_{\mathrm{i+1}}=\vec{X}_{\mathrm{i}}+\Delta s\cdot\vec{N}(\vec{X}_{\mathrm{i}}) \tag{3.28}$$

To maintain consistency in stepping along the solution space curve, the following condition is defined:

$$(\vec{X}^{*}_{\mathrm{i+1}}-\vec{X}_{\mathrm{i}})\bullet\vec{N}(\vec{X}_{\mathrm{i}})=\Delta s \tag{3.29}$$

Equation (3.29) states that the un-converged new initial condition must lie a distance of Δs away from the previous family member's state along the null space. This expression is

equated to zero and appended into the constraint vector (now denoted $\vec{G}(\vec{X}_{i+1})$) in order to enforce this requirement.

$$\vec{G}(\vec{X}_{i+1}) = \begin{bmatrix} \vec{F}(\vec{X}_{i+1}) \\ (\vec{X}_{i+1} - \vec{X}_i) \bullet \vec{N}(\vec{X}_i) - \Delta s \end{bmatrix} \tag{3.30}$$

The derivative of the appended constraint with respect to $\vec{X}_{i+1}$ is the null vector itself, thus:

$$DG(\vec{X}_{i+1}) = \begin{bmatrix} DF(\vec{X}_{i+1}) \\ \vec{N}(\vec{X}_i)^T \end{bmatrix} \tag{3.31}$$

Leading to the equation $\vec{G}(\vec{X}_{i+1}) = DG(\vec{X}_{i+1}) \cdot \vec{X}_{i+1}$ to be iteratively solved. Now, the appended condition creates a square matrix which does not require a pseudo-inversion during the corrections process. As an example, the L_2 Southern Halo family may be found using PALC, as shown in Figure 3.13.

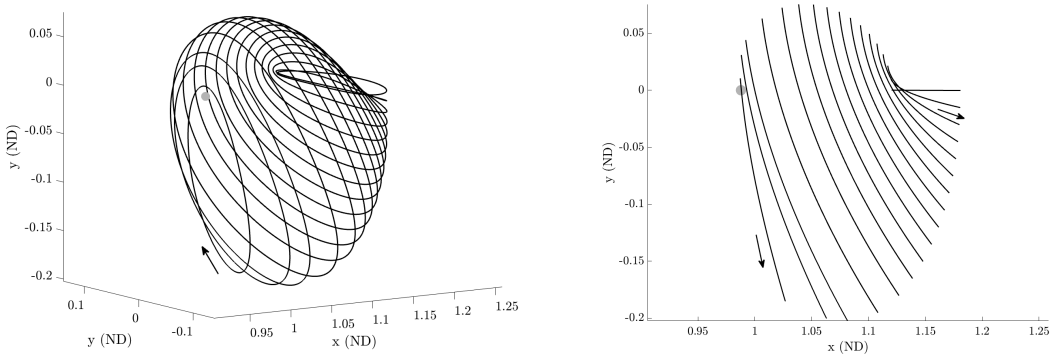

(a) (b)

Figure 3.13. CR3BP L_2 Southern Halo Family shown in an isometric view (a) and as an x-z projection (b). Motion shown in the Earth-Moon frame.

Another set of CR3BP periodic trajectories relevant to the investigation is the period-doubling Halo orbits, or the Butterfly family (also denoted "P2HO$_1$"). Stemming from a period-doubling bifurcation within the highly-inclined subset of L_2 Halo family, a two-lobe orbit may be targeted for periodicity and continued also using PALC. In doing so, the butterfly family is uncovered and plotted in Figure 3.14.

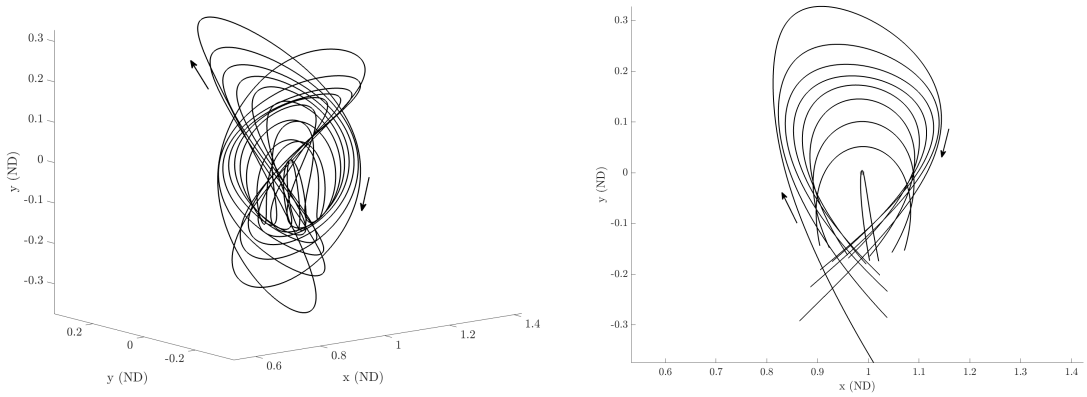

(a) (b)

Figure 3.14. CR3BP L_2 Southern Butterfly Family shown in an isometric view (a) and as an x-z projection (b). Behavior depicted in the Earth-Moon frame.

Earlier investigations in the BCR4BP use pseudo-arclength continuation to track the unintuitive behavior of the Earth-Moon $\tilde{E}_3$ equilibrium solution(s) [35]. While both natural parameter and pseudo-arclength continuation schemes may successfully step onto adjacent periodic trajectories in the CR3BP, the inexistence of orbit families in the BCR4BP nullifies their utility. Instead, a continuation method between the three-body and four-body models is defined in Section 3.4.3.

3.4.3 Solar Gravity Continuation

Due to the time-variant nature of the BCR4BP dynamics, periodic solutions in this model only exist as discrete synodic-resonant trajectories. This means that families are reduced to collections of individual solutions rather than continuous sets. To visualize this, select resonant orbits within the southern L_2 Halo family are plotted against the surface created by the family in Figure 3.15.

In the CR3BP, a Halo orbit such as the 9:2 NRHO is determined by first linearizing the motion about L_2, continuing through the Lyapunov family to the Halo bifurcation, then traversing the Halos until the 9:2 is converged. To find BCR4BP counterpart, the CR3BP result is to be directly continued to the BCR4BP using a method called solar gravity

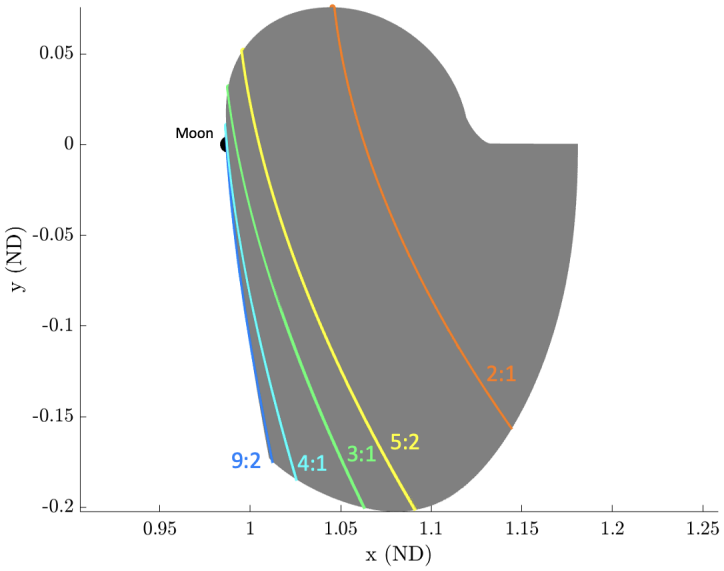

Figure 3.15. Select sidereal-resonant orbits within the CR3BP L_2 halo family. Motion presented in the Earth-Moon frame.

continuation (SGC). A homotopy parameter ϵ is defined and implemented into the Earth-Moon BCR4BP equations of motion.

$$\begin{aligned}
\ddot{\tilde{x}} &= 2\dot{\tilde{y}} + \tilde{x} - \frac{(1-\tilde{\mu})(\tilde{x}+\tilde{\mu})}{\tilde{r}_{13}^3} - \frac{\tilde{\mu}(\tilde{x}+\tilde{\mu}-1)}{\tilde{r}_{23}^3} - \epsilon\left(\frac{\tilde{m}_s(\tilde{x}-a_s\cos\tilde{\theta})}{\tilde{r}_{43}^3} + \frac{\tilde{m}_s}{a_s^2}\cos\tilde{\theta}\right) \\
\ddot{\tilde{y}} &= \tilde{y} - 2\dot{\tilde{x}} - \frac{(1-\tilde{\mu})\tilde{y}}{\tilde{r}_{13}^3} - \frac{\tilde{\mu}\tilde{y}}{\tilde{r}_{23}^3} + \epsilon\left(\frac{\tilde{m}_s(\tilde{y}-a_s\sin\tilde{\theta})}{\tilde{r}_{43}^3} - \frac{\tilde{m}_s}{a_s^2}\sin\tilde{\theta}\right) \\
\ddot{\tilde{z}} &= -\frac{(1-\tilde{\mu})\tilde{z}}{\tilde{r}_{13}^3} - \frac{\tilde{\mu}\tilde{z}}{\tilde{r}_{23}^3} - \epsilon\frac{\tilde{m}_s\tilde{z}}{\tilde{r}_{43}^3}
\end{aligned} \tag{3.32}$$

Where if $\epsilon = 1$, the equations of motion are unchanged, and when $\epsilon = 0$, they become reduced to the Earth-Moon CR3BP equations of motion. Intuitively, shifting the SGC parameter from one to zero is effectively "turning off" the solar gravity, thus continuing along changing dynamics rather than a select characteristic. It should be noted that this effect is only present in the acceleration terms, and that the definitions for the characteristic mass and time quantities are to remain unchanged by variations of the solar influence. As a result, the motion of the Sun in the Earth-Moon frame remains constant while its mass is variable. It may be noted that trajectories in the Sun-B_1 CR3BP may also be continued to their

corresponding BCR4BP representation by scaling the distances of the Earth and Moon from their barycenter, though this is unnecessary for the investigation.

Consider the 3:1 NRHO, one of the members isolated in Figure 3.13. The trajectories shown in that figure are sidereal-resonant Halo orbits, though it often serves as a better initial guess to locate their synodic-resonant counterparts for SGC. To do this, locate the member of the family which has a non-dimensional period of $2\pi \cdot R_{ss} \cdot b/a$, where a and b are integers from the resonance ratio a:b, and $R_{ss} \approx 1.08$ is the duration of a synodic month normalized by that of a sidereal month. Afterwards, this trajectory is used as the initial guess corresponding to $\epsilon = 0$, where the solar gravity continuation from $\epsilon = 0$ to $\epsilon = 1$ is performed. The resulting set of solutions is provided in Figure 3.16(a), where the CR3BP and BCR4BP solutions are isolated in Figure 3.16(b). Using the same method, the L_2 2:1 synodic-resonant Lyapunov may be produced in the BCR4BP, as depicted in Figure 3.17.

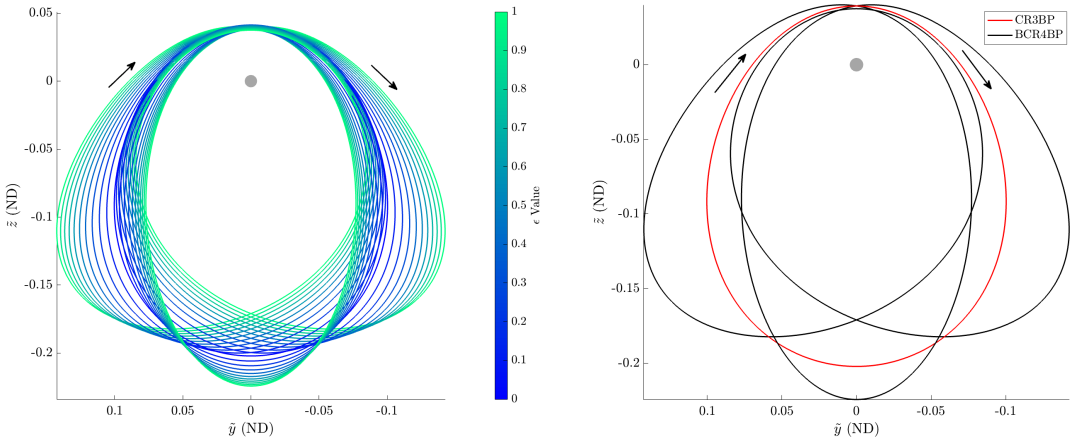

(a) (b)

Figure 3.16. Solar gravity continuation of the L_2 3:1 synodic-resonant NRHO. Motion shown in the Earth-Moon frame.

While a continuous set of solutions may be produced, the intermediate solutions between $\epsilon = 0$ and 1 belong to fictitious intermediate dynamics, thus are largely inapplicable to realistic trajectory design.

Solar gravity continuation is a convenient approach utilizing homotopy to more reliably converge periodic orbits in the BCR4BP. It should be noted that not all synodic-resonant trajectories require SGC in order to be uncovered within four-body dynamics, as some sets

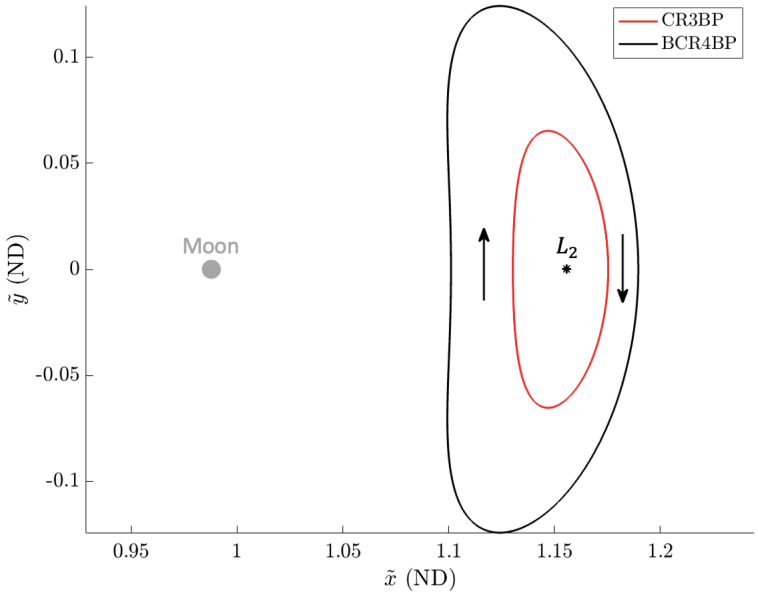

Figure 3.17. L_2 2:1 synodic-resonant Lyapunov orbit in the CR3BP and BCR4BP. Motion in the Earth-Moon reference frame.

of initial conditions between the CR3BP and BCR4BP are similar enough to be targeted without continuation. Many of these cases exist for members of the L_1 Lyapunov, as well as even the 9:2 synodic-resonant NRHO, though a different approach such as multiple-shooting $\hat{x}$-$\hat{z}$ plane crossings for individual lobes may be necessary.

3.5 Invariant Manifold Construction

While perturbation analysis may be applied to an arbitrary point in order to predict downstream changes and correct accordingly, it may also be used to map pathways to and from a given state. Should a small alteration occur to a spacecraft's motion along a repeating trajectory, there are particular manners by which it is predisposed to deviate. The arc traced out by traveling along this perturbed path is known as a manifold, and is often used for creating minimal-cost passages either into or out of periodic orbits. Invariant manifold theory seeks to linearize these pathways by expanding upon the Jacobian matrices defined in previous sections. This section will cover the determination of hyperbolic manifolds associated with both equilibrium solutions and periodic orbits.

3.5.1 Manifolds for Equilibrium Solutions

While perfect placement of a particle on any of the libration points would lead to stillness in the CR3BP rotating frame, these locations are unstable. This means that for even the smallest deviation from the host location will lead to a disparity that will only continue to grow if uncorrected. The manner by which this tends to occur is along one the Lagrange point's associated unstable manifold paths. Manifolds are naturally non-linear, though their initial behavior may be approximated using a first-order reduction. If the deviation from a CR3BP libration point is modeled as $\delta\vec{x}(t)$, then its evolution is the time rate of change of this quantity. Recalling from equation (3.4) that this change in deviation may be related to $\delta\vec{x}(t)$ itself using the Jacobian $A(t)$. As a result, an eigen-decomposition may be performed on this matrix in order to understand the latent tendencies of $\delta\vec{x}$. For the square matrix $A(t)$ of dimension $(n \times n)$, there exist both an eigenvalue and eigenvector matrix (Λ and $V(t)$, respectively) which satisfy the relation (3.33).

$$A(t)V(t) = \Lambda V(t) \tag{3.33}$$

While the nomenclature in (3.33) implies time-variance for the Jacobian and eigenvector matrices, this is only true for the general formulation. In the case of deviation measured at a single instance in time relative to a still libration point, both $A(t)$ and $V(t)$ are time-constant. The eigen-matrices $V(t)$ and Λ are comprised of the individual eigenvectors and eigenvalues respectively, as demonstrated by (3.34).

$$\Lambda = \begin{bmatrix} \lambda_1 & 0 & 0 & \cdots & 0 \\ 0 & \lambda_2 & 0 & \cdots & 0 \\ \vdots & & \ddots & & \vdots \\ 0 & \cdots & 0 & \lambda_{n-1} & 0 \\ 0 & \cdots & 0 & 0 & \lambda_n \end{bmatrix} \qquad V(t) = \begin{bmatrix} \vec{v}_1(t) & \vec{v}_2(t) & \cdots & \vec{v}_{n-1}(t) & \vec{v}_n(t) \end{bmatrix} \tag{3.34}$$

Where λ_j is the eigenvalue corresponding to eigenvector $\vec{v}_j$. Eigenvalues of the Jacobian indicate the behavior of the associated manifold, where $\text{Real}(\lambda_j) > 0$ indicates progressive

departure from the initial location, and $\text{Real}(\lambda_j) < 0$ is associated with asymptotic arrival. Purely imaginary eigenvalues indicate locally-bounded oscillatory behavior, though complex values of λ_j which possess non-zero real and imaginary components represent a spiralling pattern, though this is not found with any of the CR3BP libration points. Since the CR3BP describes a Hamiltonian system, the eigenvalues of $A(t)$ exist in oppositely-signed pairs [36]. Moreover, since complex eigenvalues of a real matrix exist in conjugate pairs, all oscillatory motion is also represented as differently-signed sets. As a result, should an unstable mode exist for an equilibrium solution, then there must exist an equally stable, symmetric manifold.

To model these passageways, the initial state coincident with the equilibrium solution is perturbed by a non-dimensional value d along one of the eigenvectors. By defining an unstable eigenvector $\vec{v}_u$ corresponding to $\text{Real}(\lambda_u) > 0$ as well as a stable eigenvector $\vec{v}_s$ where $\text{Real}(\lambda_s) < 0$, an initial condition $(\vec{x}^*)$ for a Lagrange point hyperbolic manifold may be found using (3.35).

$$\begin{aligned} \vec{x}_u^* &= \vec{x}_{L_i} \pm d\frac{\vec{v}_u}{||\vec{v}_u^r||} \\ \vec{x}_s^* &= \vec{x}_{L_i} \pm d\frac{\vec{v}_s}{||\vec{v}_s^r||} \end{aligned} \tag{3.35}$$

Where $\vec{x}_{L_i}$ is the state associated with libration point L_i, and the superscript "r" above $\vec{v}$ indicates the isolation of the position-components of the associated eigenvector. The value of d is chosen by the user, though it behaves as the scaling parameter for the perturbation along the eigenvector. Since manifolds asymptotically depart and approach, a small choice of d may not bypass the relatively slow asymptotically-departing section of the manifold, and numerical error may aggregate. Inversely, too large of a step creates a disparity between the non-linear manifold dynamics and the linearized approximation using the eigenvector. A step size corresponding to 40 kilometers is used for finding the hyperbolic manifolds as shown in Figure 3.18. Where unstable manifolds are given in red, and their stable counterparts in blue. The directions of the eigenvalues are also provided by the dashed lines, where the superscript "+" indicates the version of (3.35) which adds the perturbation, and "−" for that which subtracts it.

The BCR4BP analog for Figure 3.18 may be created by repeating this process for $\tilde{A}(t)$ at various sun angles. The result is two sets of planar manifold tubes that behave similarly

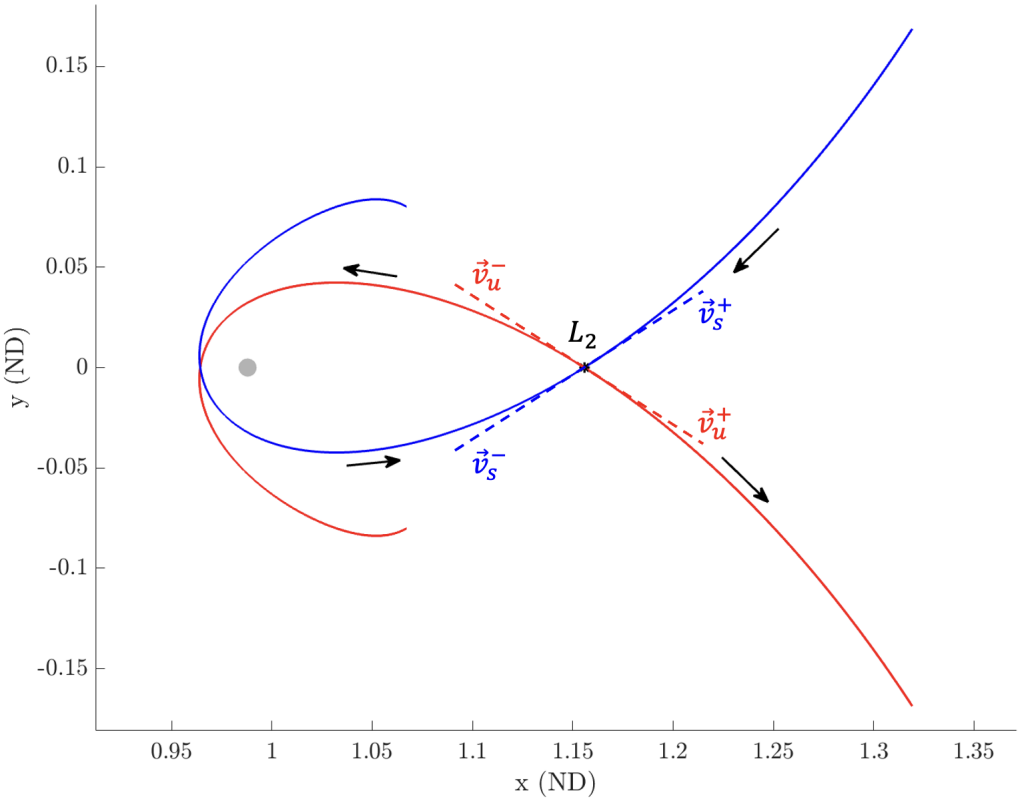

Figure 3.18. Hyperbolic manifolds for the CR3BP L_2 Lagrange point. Arrows indicate motion in forward time. Motion in the Earth-Moon frame.

to their CR3BP counterparts, as shown in Figure 3.19. Determining manifold states at discrete points along a track is not exclusive to the BCR4BP equilibrium solutions, as this is also the general process by which manifold tubes for periodic orbits are created. The major difference is the matrix by which the eigen-decomposition is performed, as elaborated further in Section 3.5.2.

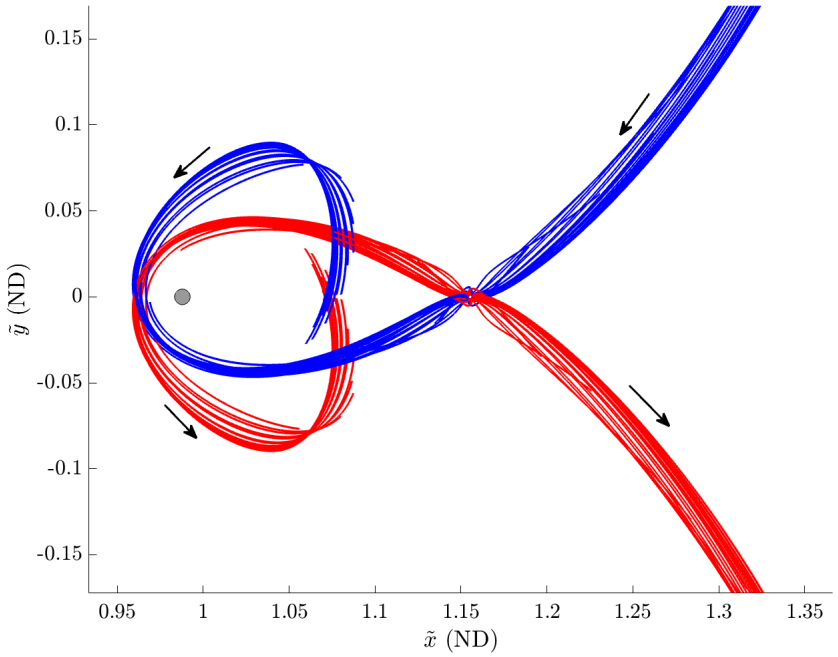

Figure 3.19. Hyperbolic manifolds for the $\tilde{E}_2$ equilibrium point at various sun angles. Arrows indicate motion in forward time, while unstable manifolds are in red, stable in blue. Motion shown in the Earth-Moon frame.

3.5.2 Manifolds for Periodic Orbits

Applying invariant manifold theory to a discrete state along a periodic orbit creates natural pathways into and out of the trajectory. As a result, a spacecraft that lies along one of these passages (in phase space) may either depart or arrive into the periodic orbit by expending little to no propellant. Furthermore, forming hyperbolic manifolds at numerous discrete points along the periodic orbit creates a more variable catalog of departure and arrival pathways. In order to construct a manifold arc for a single state along a periodic orbit, first consider an arbitrary state $\vec{x}(t_o)$ that lies along a trajectory which repeats in time intervals of $\mathbb{P}$ non-dimensional units. By propagating the STM for a single period of the orbit, the state returns to its initial value, but $\Phi(t_o + \mathbb{P}, t_o) \neq \Phi(t_o, t_o)$. The propagated state transition matrix, $\Phi(t_o + \mathbb{P}, t_o)$ is referred to as the "monodromy matrix", and serves as the information center for motion relating to the periodic orbit. For determining the

stability characteristics of periodic orbits, an eigen-decomposition of the monodromy matrix is performed such that:

$$\vec{V}(t)\Phi(t_o + \mathbb{P}, t_o) = \Lambda\vec{V}(t) \tag{3.36}$$

Where $t = t_o + \mathbb{P}$, and matrices $\vec{V}$ and Λ are defined as previously shown in equation (3.34). According to Lyapunov's Theorem, should an eigenvalue λ_j satisfy (3.33), then so too shall its inverse λ_j^{-1} [37]. Moreover, since $\Phi(t_o + \mathbb{P}, t_o)$ is comprised of real entries, any complex members of its eigenvalue matrix are accompanied by their conjugate. In the case of periodic orbits, real eigenvalues with magnitude greater than one are associated with unstable manifolds which depart the location in forward time, while those less than unity are their stable counterparts, returning from a distance in reverse time. Since eigenvalues comprised of real numbers come as inverted pairs, the existence of an unstable eigenvalue ensures that there is also a stable mode. The center subspace is formed about eigenvalues of magnitude equal to one, though not all values within this space imply the same behavior. In the CR3BP, the existence of two unitary eigenvalues is guaranteed for periodic orbit states, as the model is a Hamiltonian system with a single integral of motion [38]. Of these two unity eigenvalues, one has an eigenvector which points in the direction of the periodic orbit itself, while the other is along the continuation pattern of the orbit's family. The BCR4BP has only one unitary eigenvector which is associated with the linear progression of its epoch variable. Complex eigenvalues pairs exist for both models, where those of magnitude one indicate the presence of local quasi-periodic motion. McCarthy provides insightful discussions on the complex subspace [39], while Williams thoroughly outlines the relationship between eigen-decomposition and trajectory design as a whole [36].

As the initial location within the orbit is altered, represented by a change in t_o, the subsequent values of the both $\Phi(t_o + \mathbb{P}, t_o)$ and $V(t)$ change as well. This indicates that the eigen-decomposition must be performed for each discrete point evaluated for a manifold, as the eigenvectors for one location are not applicable at another. On the other hand, the stability characteristics of the orbit remain the same throughout its propagation, a property which is reflected by the un-changing eigenvalues within Λ. Various stability indices exist to describe the tendency of a perturbed spacecraft to depart its host orbit, though in general,

the instability of a periodic orbit is measured by the magnitude of its largest eigenvalue. Since $\lambda > 1$ indicates departing behavior, as an eigenvalue grows increasingly larger than one, this likelihood for deviation becomes more pronounced.

A periodic orbit hyperbolic manifold may be constructed by applying (3.35) to the eigenvectors corresponding to the stable/unstable eigenvalues of the monodromy matrix, then propagating in forward time for the unstable arc, and reverse time for the stable mode. By repeating this procedure for the monodromy matrix and its decomposition at various locations in the orbit, a "manifold tube" may be constructed. An example manifold tube for the L_2 2:1 synodic-resonant Lyapunov orbit is propagated in the CR3BP as shown in Figure 3.20(a), while its BCR4BP counterpart is depicted in Figure 3.20(b). Both plots exhibit motion in the Earth-Moon rotating reference frame. Recall from Figure 3.17 that the size of this trajectory varies significantly between from the CR3BP to the BCR4BP, thus the geometry of the manifold tubes has been correspondingly altered.

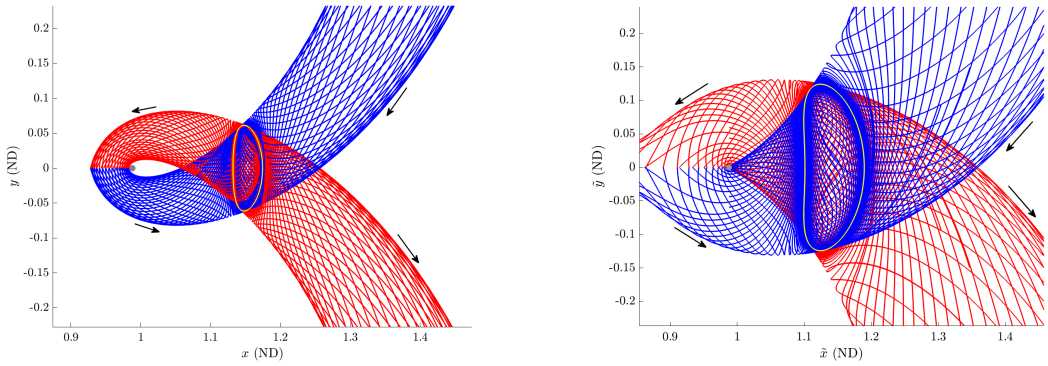

(a) CR3BP (b) BCR4BP

Figure 3.20. Stable (blue) and unstable (red) manifold tubes for the L_2 2:1 synodic-resonant Lyapunov. Arrows indicate behavior in positive time, and baseline orbits are outlined in yellow. Moon-side tubes truncated at $y = 0$.

The choice in step-off distance d may be informed by the relative stability of the orbit, as more unstable trajectories need less perturbation (and thus a smaller value for d) for a manifold to quickly leave the vicinity. Particularly stable orbits, such as the 9:2 NRHO, may require a value of d corresponding to several-hundred kilometers, as the manifolds have

a tendency to continuously wrap around the host orbit and accrue numerical error before departing.

The absence of a unitary eigenvalue corresponding to the along-family direction for BCR4BP periodic orbits contributes to the notion that continuous periodic orbit families do not exist within the model. Due to this, there is little flexibility in choosing among the candidate pool for arrival orbits of Lunar transfers. In response to this, an alternative hybrid manifold construction method which benefits from the flexibility of a baseline CR3BP orbit paired with solar-perturbed departure and arrival motion is developed in Section 3.6.

3.6 Pseudo-manifold Construction

Recent research into the correspondence between frequencies in the HFEM and dynamics of lower-fidelity models has found that solar acceleration on trajectories near the Moon is often over-estimated by the BCR4BP [40]. As a consequence, cislunar BCR4BP periodic orbits are not invalidated, but rather may deviate more significantly from their higher-fidelity representations than their CR3BP counterparts. A compromise is found by using discrete states along a CR3BP periodic orbit as initial conditions for BCR4BP departure and arrival paths; the investigation refers to these passageways as "pseudo-manifolds". These manifold analogs provide the benefit of translation through a continuous family of arrival orbits, allowing for greater flexibility in selecting the arrival state. For each node along the CR3BP baseline trajectory, a variety of sun angles may be implemented and propagated. Because of this, a single state may spawn numerous stable/unstable pseudo-manifold arcs rather than two. In the case of lunar transfer design, this greatly diversifies both the arrival states and epochs available to the spacecraft; a crucial source of flexibility for missions as constrained as secondary payload transfers.

To demonstrate, stable pseudo-manifolds are propagated in reverse time from a CR3BP L_2 2:1 synodic-resonant Lyapunov, as shown in Figure 3.21. Comparison with Figure 3.20(a) highlights the similarities in departing behavior along pseudo-manifolds and their traditional counterparts. To visualize the variation in both ending state and the corresponding epoch, consider the propagation of stable pseudo manifolds from a 9:2 synodic-resonant NRHO.

These arcs are then propagated until crossing a cylindrical hyperplane of 100,000 km radius about the Moon, where the end location is plotted as a point and colored by the terminal sun angle, as shown in Figure 3.22.

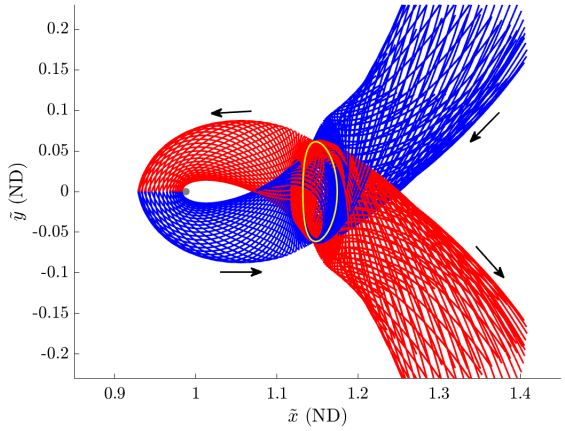

Figure 3.21. Departing (red) and arriving (blue) pseudo-manifolds from L_2 2:1 synodic resonant Lyapunov. Arrows indicate motion in forward time, baseline orbit in yellow. Motion shown in the Earth-Moon frame.

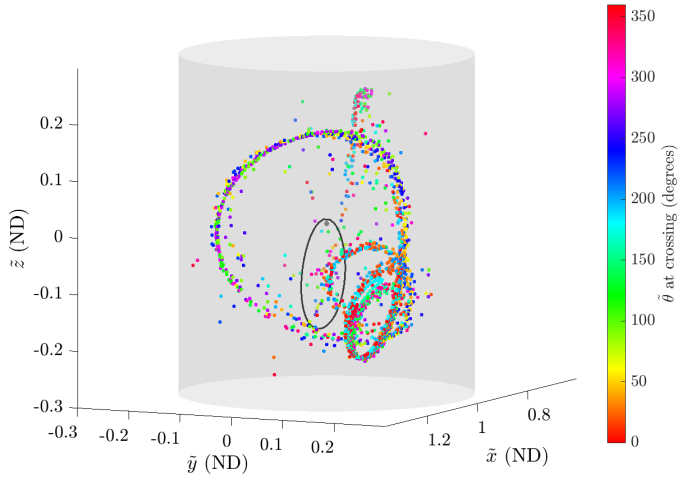

Figure 3.22. Pseudo-manifold locations at cylindrical hyperplane crossing. Baseline orbit (9:2 synodic-resonant NRHO) plotted in black for reference. Behavior depicted in the Earth-Moon frame.

The thorough mixture of sun angles is more accommodating for a spacecraft arriving to the cylinder from the outside, especially in scenarios where time of flight is less flexible. Moreover, solution diversity is easily scalable as now variations in both the number of manifold nodes as well as the number of initial sun angles (and thus the number of pseudo-manifolds per node) may be increased. Within the investigation, the usage of pseudo-manifolds allows for a more thorough and accommodating initial guess generation scheme for arrival arcs. The diversified outbound states and epochs grants a greater opportunity to more closely match an incoming trajectory, further ensuring convergence of a continuous end-to-end lunar transfer in the BCR4BP.

4. BALLISTIC LUNAR TRANSFER DESIGN FOR PRIMARY PAYLOAD MISSIONS

Following the success of the Hiten mission in the early 1990's, lunar transfers leveraging solar gravity have been a common consideration for unmanned missions to the Moon's vicinity. If constructed properly, a ballistic lunar transfer (BLT) exploits the Sun's perturbing acceleration to greatly reduce lunar orbital insertion (LOI) costs as compared to a direct transfer. A BLT is a trajectory which extends beyond the radius of the Moon's orbit such that solar gravity may be exploited to alter its lunar arrival path, rather than using on-board thrust. The transfer is initialized with a trans-lunar injection maneuver (TLI), thus the term "ballistic" refers to the thrust-less transitional portion of the arc following the TLI and prior to any necessary LOI. Since launch proceedings are often centered about the primary payload, initial transfer conditions may be dictated by mission specifications, with particular flexibility being allotted to the starting epoch. This section begins with a summary of solar-perturbation effects, then details the BLT initial-guess generation process using perigee maps. Following this, methods for targeting individual BLTs are outlined for transfers to circular lunar orbits, as well as to libration-point periodic structures using both traditional BCR4BP manifolds and pseudo-manifolds. The flexibility granted to a primary payload is further exploited as families of lunar transfers are formed from the converged individual transfers. Lastly, individual cases which leverage lunar encounters along their ascent are examined.

4.1 Solar Perturbation Analysis

Previous analysis in Section 2.3.6 found that the Sun's influence on the Earth-Moon Hamiltonian may be separated into distinct quadrants. Interestingly, these divisions into separate quadrant effects extend to more than just $\dot{\tilde{H}}$, as the Sun's net acceleration also influences the downstream behavior when viewed through the lens of conic sections. First,

consider the motion of the Moon about the Earth, with the Sun as a perturbation. This may be modelled by adapting (2.4) as such:

$$\vec{R}''_{EM} - \tilde{G}\frac{M_E + M_M}{R^3_{EM}}\vec{R}_{EM} = \tilde{G}M_S\left(\frac{\vec{R}_{MS}}{R^3_{MS}} - \frac{\vec{R}_{ES}}{R^3_{ES}}\right) \tag{4.1}$$

The net solar acceleration on the Moon is represented by the quantity on the right-hand side of the equation. This value is comprised of a direct term representing the attraction acting on the Moon toward the Sun, as well as the indirect acceleration where the Sun's pull on the Earth influences the Earth's gravitational effect on the Moon. Since the indirect and direct terms may oppose one another, both the direction and magnitude of the net solar effect may significantly deviate from the solar acceleration acting solely on the Moon. By fixing the Moon to a circular track about the Earth and modelling the net solar acceleration acting upon it at discrete points along this path, a visualization of the solar effects on the Moon is provided in Figure 4.1.

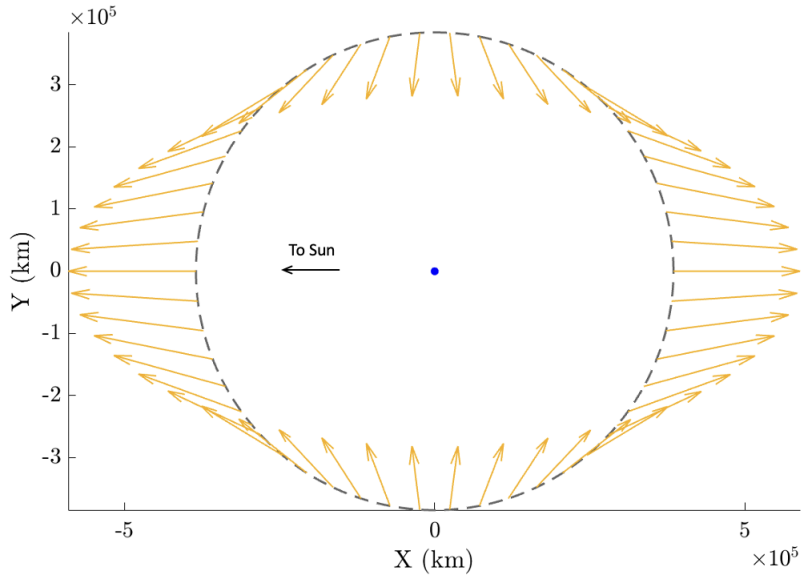

Figure 4.1. Direction of net solar perturbation acting on discrete points along Moon's orbit (in grey). Viewed in an arbitrary inertial reference frame where the Sun is to the left for each individual evaluation.

Where the Sun is located directly to the left at each evaluation. While the accelerations differ between each location, their overall behavior may be grouped into quadrants. A modification of Figure 4.1 to demonstrate these quadrant trends is provided in Figure 4.2.

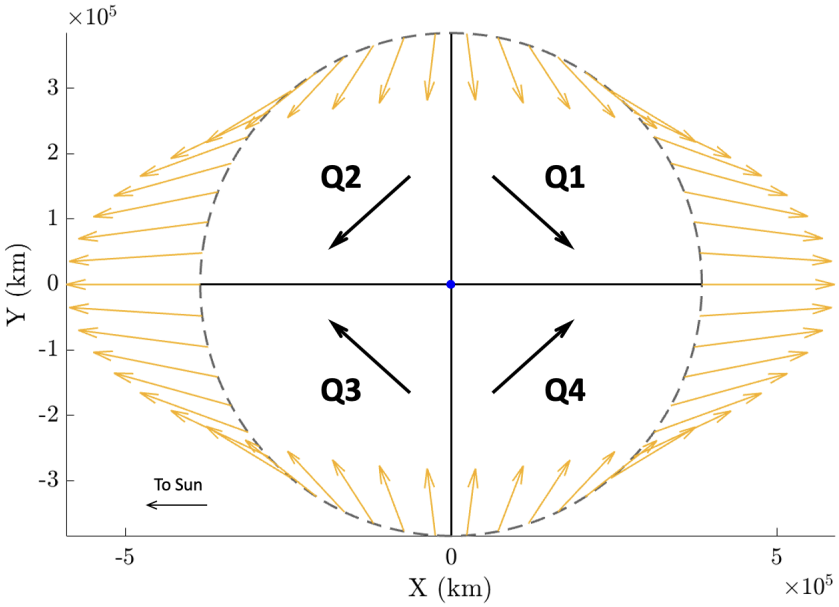

Figure 4.2. Generalization of solar net acceleration directions shown in Figure 4.1.

Since the Moon orbits the Earth in a prograde fashion (counter-clockwise in this view), the solar perturbation generally act along the lunar velocity in quadrants 2 and 4, and contrary in quadrants 1 and 3. Insights into the effect on downstream behavior may be granted by inspecting instantaneous changes to the conic orbital elements of the Moon's motion at each discrete state. Equations for the instantaneous specific energy and specific angular momentum are given in (4.2) and (4.3) respectively. Note that $\vec{V}$ and $\vec{R}$ are the dimensional, inertial velocity and position of the Moon with respect to the Earth, while V and R are their respective magnitudes.

$$\varepsilon = \frac{V^2}{2} - \frac{\tilde{G}M_E}{R} \tag{4.2}$$

$$h = ||\vec{R} \times \vec{V}|| \tag{4.3}$$

By extension, the instantaneous semi-major axis, eccentricity and periapsis radius may be determined, as given by (4.4) through (4.6) respectively.

$$a = -\frac{\tilde{G}M_E}{2\varepsilon} \tag{4.4}$$

$$\mathrm{e} = \sqrt{1 + \frac{2\varepsilon h^2}{(\tilde{G}M_E)^2}} \tag{4.5}$$

$$r_p = a(1 - \mathrm{e}) \tag{4.6}$$

For an instant in time, if the Moon's speed were to instantaneously increase while its position remained the same, this would correspond to an increase in both ε and h. Assuming that the orbit remains a closed conic, then the Moon's semi-major axis about the Earth would subsequently increase, while its eccentricity would decrease; the perigee radius grows as a result of these changes. In the case of a lunar speed reduction, the opposite effect would be observed, where the semi-major axis and perigee radius would both diminish, and the closed conic would grow more elliptic. By pairing these effects with the general alignment between the prograde lunar velocity and solar acceleration vectors for each quadrant, a recreation of Table 3.1 from Davis' dissertation [15] is provided by Table 4.1.

Table 4.1. General changes for osculating elements of prograde motion by quadrant

Orbital Element	Quadrants 1 & 3	Quadrants 2 & 4
a	Decreases	Increases
e	Increases	Decreases
r_p	Decreases	Increases

In the case of a retrograde orbit, since the velocity is reversed, so are the solar perturbing effects, as shown in Table 4.2.

Table 4.2. General changes for osculating elements of retrograde motion by quadrant

Orbital Element	Quadrants 1 & 3	Quadrants 2 & 4
a	Increases	Decreases
e	Decreases	Increases
r_p	Increases	Decreases

In contrast to the quadrant effects on the Earth-Moon Hamiltonian, the changes to the instantaneous orbital elements are dependent upon both location and motion of the spacecraft. The Moon's motion about the Earth acts as a straightforward example of circular motion, though these effects apply to more complex arcs as well. In the case of BLTs, the impact of the solar perturbation is greatest at apogee for both the changes in Hamiltonian and orbital elements. Since the Sun's perturbation is assumed to be planar, alignment between a spatial velocity vector and the solar acceleration is avoided. In other words, cost-reducing quadrant effects experienced by BLTs will be most pronounced for those which have relatively planar motion that reaches far into either quadrant 2 or 4. The prograde motion following the apogee will then be circularized where, for appropriately designed lunar transfers, arrival costs are significantly reduced.

4.2 Perigee Mapping

Consider a scenario where a spacecraft is to to traverse a BLT from an initial parking orbit about the Earth to a destination lunar or cislunar orbit. In this situation, arrival conditions may be particularly specific, while the departure state only requires an initial altitude with respect to the Earth. To reduce complexity of the initial trajectory design procedure, an effective technique is to propagate in reverse time from the more constrained arrival states to be compared with the relatively few departure requirements. This concept is the basis for the implementation of perigee mapping to generate initial guesses for ballistic lunar transfers.

For a spacecraft to most efficiently alter its energy, it must thrust in-line with its velocity (along $\vec{v}$ to increase energy, opposed to decrease). Any component of the $\Delta\vec{v}$ vector which is not parallel with the velocity is instead dedicated toward changing the direction of the spacecraft's motion. For the purposes of minimizing the total transfer cost of a BLT, maneuvers departing from and arriving to circular parking orbits are to be tangential. As a consequence, an additional perigee constraint is imposed on the Earth departure state of the BLT. A periapsis is a local minimum of the spacecraft's distance with respect to a desired body or location; "perigee" and "perilune" are the closest approaches to the Earth and

Moon respectively. On the other hand, local maxima with respect to a body are referred to as apoases, with suffixes mirroring their periapse counterparts. A physical property of a periapse is that the spacecraft position vector with respect to the body is normal to its own velocity, as expressed in terms of a dot product in (4.7). The vectors $\vec{r}$ and $\vec{v}$ are the position and velocity of the spacecraft respectively, while $\vec{r}_B$ is the position vector of the attracting body.

$$(\vec{r} - \vec{r}_B) \bullet \vec{v} = 0 \tag{4.7}$$

Orthogonality between the relative position and velocity vectors is indicative of an apse, though a periapse additionally requires the time rate of change of expression (4.7) to be positive, or:

$$\frac{\partial}{\partial t} \left((\vec{r} - \vec{r}_B) \bullet \vec{v} \right) > 0 \tag{4.8}$$

For BLT construction, necessary perigee maps may be formed through the following procedure:

1. Sample n states along the arrival orbit.
2. At a particular state make any necessary modifications to accommodate arrival circumstances.
   (a) Example alterations are increasing speed, changing epoch, or stepping onto an associated manifold arc.
3. Propagate the state (post-modification if any are made) in reverse time until a perigee occurs.
   (a) An additional terminal condition may be defined such that the perigee is within a specified distance of the attracting body to filter results.
   (b) A reverse-propagation duration must be established as well. A maximum time of flight commonly used in this investigation is 200 days.
4. Store the state and time of flight associated with the perigee, should the event occur.
5. Repeat for the remainder of the n sampled arrival conditions.

Perigee maps produced by this procedure generally have more abundant results when n increases, though this is met with an additional increase in computational intensity. As alluded to in step 2(a), stable manifold arcs may also be used as the means for populating the perigee map, leading to results which, when propagated in forward time, transfer from a perigee directly into the periodic orbit with negligible insertion cost. Consider the BCR4BP L_2 2:1 synodic-resonant Lyapunov orbit (from Figure 3.17). Selecting $n = 25000$ individual states about the periodic trajectory and propagating both directions of the associated stable manifolds at each point, a perigee map is constructed, shown in Figure 4.3. Each black dot corresponds to the location of an individual manifold's closest approach to Earth. As an example mission, consider the departure from a 1000-km altitude LEO parking orbit. Perigee locations relatively close to this radius (shown in red) are of particular focus when analyzing the map, thus a zoomed-in view is provided in Figure 4.4.

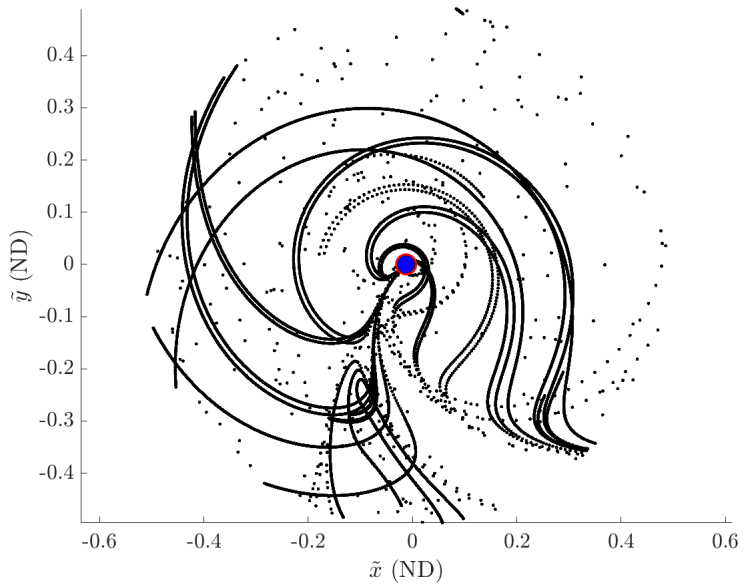

Figure 4.3. Perigee map formed by 50000 stable manifold arcs from the BCR4BP L_2 2:1 synodic-resonant Lyapunov orbit. Shown in Earth-Moon frame.

Additional filtration may be included into the mapping procedure as well. For instance, each perigee may be colored by its associated Earth-Moon Hamiltonian value (Figure 4.5(a)), or the time of flight necessary to insert into the Lyapunov (Figure 4.5(b)).

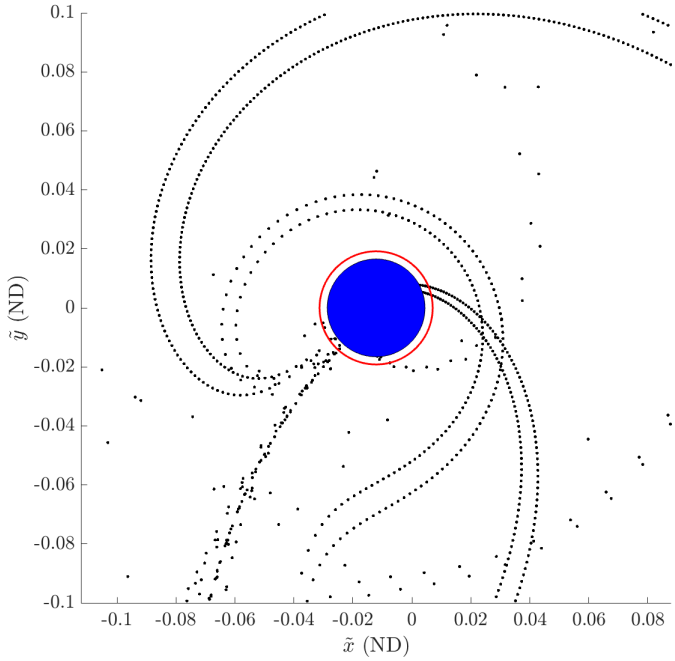

Figure 4.4. Near-Earth portion of Figure 4.3. Desired Earth parking orbit in red.

As a closed conic near the Earth, the parking orbit naturally has a lower energy and thus higher $\tilde{H}$ than any of the incident trajectories. As such, the Hamiltonian mapping enlightens lower-cost choices, as perigees with the highest Earth-Moon Hamiltonian will require less propellant to perform the TLI. The flight duration mapping in Figure 4.5(b) may aid in further filtration should a mission require a narrow window for time of flight.

A more flexible alternative to using BCR4BP manifolds arcs is the usage of pseudo-manifolds. Consider the CR3BP L_2 2:1 synodic-resonant Lyapunov, also depicted in Figure 3.17, along which 500 unique states are selected. At each point, the motion is evaluated in the BCR4BP by propagating in reverse time using 100 evenly-spaced Sun angle values between 0 and 2π. In other words, for each of the 500 CR3BP arrival states, there are 100 arcs constructed using the associated state and a varying epoch value. The resulting perigee map is displayed in Figure 4.6, focused near the Earth and colored by Earth-Moon Hamiltonian.

Much like the large disparity between the CR3BP and BCR4BP 2:1 synodic-resonant Lyapunov orbits, the general structures of the perigee maps differ substantially as well.

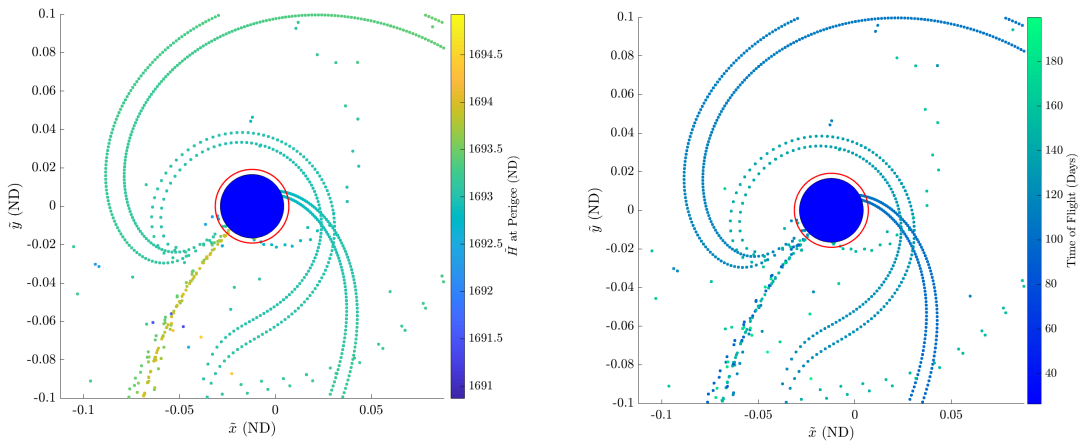

(a) (b)

Figure 4.5. Perigee map formed by 50000 stable manifold arcs from the BCR4BP L_2 2:1 synodic-resonant Lyapunov orbit.

Moreover, The variations in initial epoch for the pseudo-manifold propagation further scatters the mapped points.

An increased variety of terminal perigee states may also be achieved by incorporating differing arrival maneuvers. For instance, much like how the Earth parking orbit has definitively less energy than the outbound trajectory candidates, the same is true for a circular lunar orbit and the inbound arcs. As such, an arrival maneuver is required, though its magnitude may be minimized by design. Consider BLTs from the same initial Earth parking orbit to a destination lunar orbit of constant altitude equal to 1000 kilometers. Construction of an initial-guess perigee map again requires n state samples about the lunar orbit itself, though at each point, m different in-line maneuver magnitudes are examined. Scheuerle notes that an LOI burn for a direct transfer to a lunar orbit may be expected to be about 950 meters per second [20]; this will become the upper-limit for the maneuver costs explored. As an example, let $n = 500$ and $m = 100$ magnitudes evenly distributed among a range from 500 to 950 m/s. Additionally, the destination orbit is prograde about the Moon, though a retrograde example may just as easily be evaluated. At each sampled state, all of the m burn magnitudes are executed, then the resulting state is propagated backward time until its closest encounter with the Earth. Repeating for each state, the perigee map may be

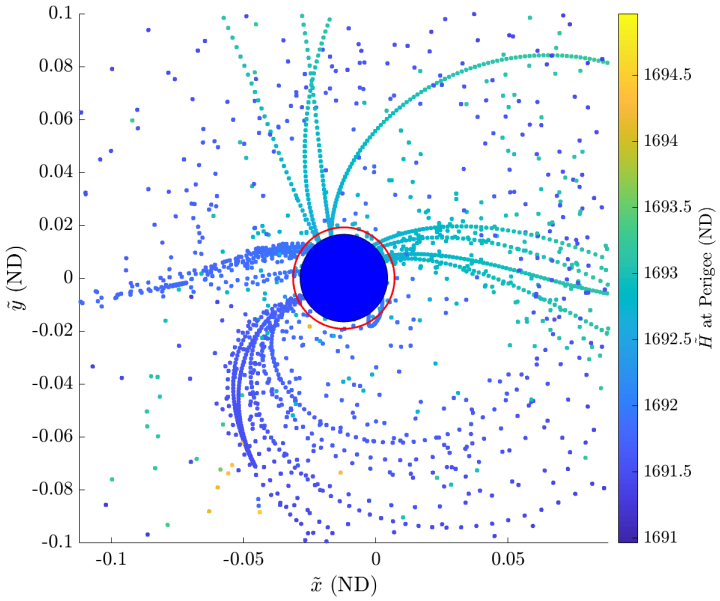

Figure 4.6. Perigee map formed by stable pseudo-manifolds from the CR3BP L_2 2:1 synodic-resonant Lyapunov orbit.

formed, as shown in Figure 4.7. Since the epoch for each backward-propagated arc is chosen arbitrarily, a third dimension to the search may be incorporated to step through k differing initial $\tilde{\theta}$ values. Disregarding this step leads to BLTs which each intercept the Moon at a specific location in the Sun-Barycenter frame.

4.3 Targeting BLTs in the BCR4BP

Following the initial-guess generation process using perigee maps, sufficiently well-suited conditions may be applied to a differential corrections algorithm to produce a BLT. In this section, methods for converging BLTs featuring BCR4BP manifolds, pseudo-manifolds, as well as non-zero LOI maneuvers are explored.

4.3.1 Transfers to BCR4BP Periodic Orbits

To create a lunar transfer to a BCR4BP periodic orbit, the associated manifold arcs may be leveraged. Consider a mission to go from a 1000-kilometer altitude Earth parking orbit to an L_2 2:1 synodic-resonant Lyapunov orbit as modelled in the BCR4BP, an initial

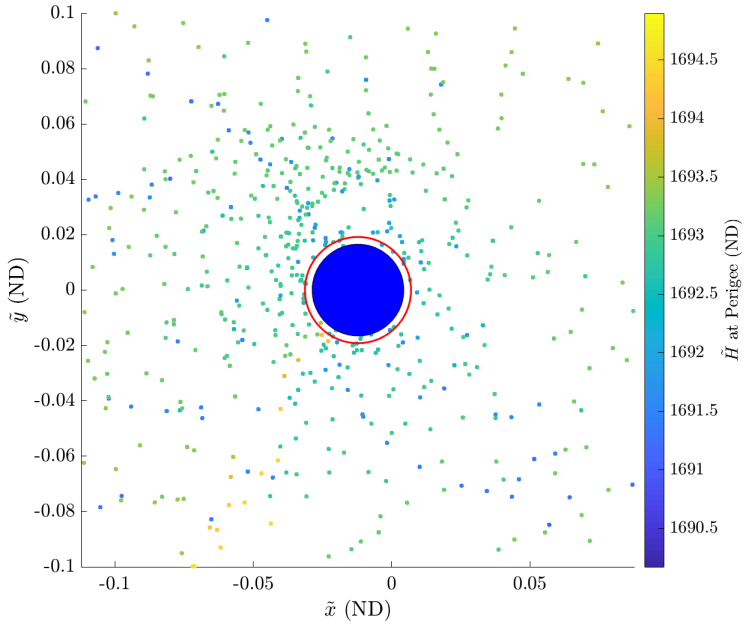

Figure 4.7. Perigee map formed by various maneuvers from a 1000-km altitude circular prograde lunar orbit.

guess generation would require a perigee map such as that depicted by Figure 4.6. After any necessary filtration, the closest perigee to the 1000-km altitude ring is to be selected as the initial guess. There are often multiple considerations when selecting the initial conditions, including proximity to the desired altitude as well as the necessary cost. In general, the best initial guess is that which minimizes TLI costs while remaining close enough in altitude to converge, though considering mission specifications often aids in isolating the best candidate. Once the initial condition is decided, the differential corrections process begins.

In order to minimize the TLI magnitude, the departing state is constrained to be perigee. Moreover, successful insertion into the periodic orbit requires the end of the transfer to match the motion of a point along the periodic orbit. For this to occur, there must be both full-state and Sun/Moon angle continuity upon arrival, as motion along repeating trajectories in the BCR4BP is epoch-dependent. A simple approach is to fix the arrival state along the Lyapunov, though this further constrains an already narrow window for design leniency. Instead, a more flexible approach is to be adopted, where the periodic orbit state $\tilde{\vec{x}}_f^P$ is determined by propagating from the periodic orbit initial state $\tilde{\vec{x}}_o^P$ by time τ. With each

iteration, the terminal state of the incoming BLT arc, $\tilde{\vec{x}}_f^n$ iteratively shortens the disparity between itself and its moving target, $\tilde{\vec{x}}_1$. A diagram is provided in Figure 4.8 to demonstrate the relationship between each of the parameters.

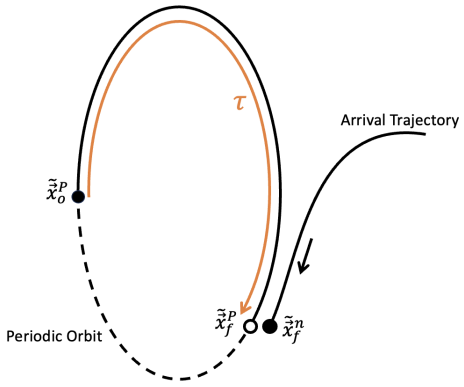

Figure 4.8. Diagram demonstrating approach for altering BCR4BP periodic orbit arrival state.

As an aside, moving-target scenarios may introduce sensitivity into the differential corrections process, thus an attenuation factor f_a may be introduced to further smooth convergence. Attenuation factors are typically positive constants of value less than one which may be applied to the update equation to prevent over-correction.

$$\vec{X}_{\mathrm{i}+1} = \vec{X}_{\mathrm{i}} - f_a(DF)^{-1}\vec{F}(\vec{X}_{\mathrm{i}}) \tag{4.9}$$

An attenuation factor of one has no effect, and the update equation returns to its original form given in (3.20). As the magnitude of the attenuation factor approaches zero, the number of iterations required for convergence typically increases markedly. Therefore the value for f_a should be sufficiently small to converge a solution, though large enough to reduce computation time.

By allowing the target arrival state to vary, the time τ becomes a design variable, while the initial periodic orbit state $\vec{x}_o^P$ remains constant. The insertion constraint may be expressed as:

$$\vec{F}_{ins} = \tilde{\vec{x}}_f^n - \tilde{\vec{x}}_f^P \tag{4.10}$$

Since BLT trajectories span lengthy durations and often traverse sensitive regions of space, a multiple shooter is recommended. For the n arcs chosen to fit together into a continuous transfer, $n-1$ continuity constraints are required, while the terminal connection is covered by F_{ins}. The continuity constraint between the terminal state of arbitrary arc i and initial state of arc i + 1 is given in (4.11).

$$\vec{F}_{con}^{\mathrm{i}} = \tilde{\vec{x}}_f^{\mathrm{i}} - \tilde{\vec{x}}_o^{\mathrm{i}+1} \tag{4.11}$$

Where the superscript denotes the arc number, and the subscript distinguishes between initial state (o) and final state (f). For continuous transfers in the BCR4BP, each continuity constraint vector is 7-dimensional, comprised of position, velocity and epoch components. The time of flight must also be able to change to accommodate for the arrival epoch, thus the duration of the final arc, T_n is designated as a design variable.

Lastly, representations for the initial altitude and perigee constraints are defined by (4.12) and (4.13) respectively, while the "E" denotes the Earth as the reference body for the requirements. The desired initial orbital radius as measured from the Earth's center is represented as r_o, and $\left[\tilde{x}_o^1, \tilde{y}_o^1, \tilde{z}_o^1\right]$ are the position components of the Earth departure state.

$$F_{alt}^E = (\tilde{x}_o^1 + \tilde{\mu})^2 + (\tilde{y}_o^1)^2 + (\tilde{z}_o^1)^2 - (r_o)^2 \tag{4.12}$$

$$F_{\mathrm{peri}}^E = (\tilde{x}_o^1 + \tilde{\mu})\dot{\tilde{x}}_o^1 + \tilde{y}_o^1\dot{\tilde{y}}_o^1 + \tilde{z}_o^1\dot{\tilde{z}}_o^1 \tag{4.13}$$

The constraint and free-variable vectors ($\vec{F}(\vec{X}_{\mathrm{i}})$ and $\vec{X}_{\mathrm{i}}$ respectively) are defined such that:

$$\vec{F}(\vec{X}_{\mathrm{i}}) = \begin{bmatrix} \vec{F}_{con}^1 \\ \vec{F}_{con}^2 \\ \vdots \\ \vec{F}_{con}^{n-1} \\ \vec{F}_{ins} \\ F_{alt}^E \\ F_{\mathrm{peri}}^E \end{bmatrix} \qquad \vec{X}_{\mathrm{i}} = \begin{bmatrix} \tilde{\vec{x}}_o^1 \\ \tilde{\vec{x}}_o^2 \\ \vdots \\ \tilde{\vec{x}}_o^n \\ T_n \\ \tau \end{bmatrix} \tag{4.14}$$

Regardless of the number of arcs chosen, the DF matrix is square with this framework. Various initial guesses may be selected from the perigee map to be converged to continuous BLT transfers, as shown in Figure 4.9. The LTI costs and times of flight for each transfer in Figure 4.9 are provided by Table 4.3.

Table 4.3. Maneuver costs and flight times for BLTs shown in Figure 4.9

Trajectory	(a)	(b)	(c)	(d)	(e)
TLI Cost (m/s)	2941.32	2933.93	2997.50	3016.57	2992.89
TOF (Days)	113.61	168.97	169.69	138.96	128.33

Noting that the two least costly transfers are (a) and (b), both of which leverage a close lunar passage outbound from their Earth departures. In both cases, the Moon's gravity serves to propel the spacecraft further into space such that the solar gravity sufficiently guides the arrival, saving the otherwise necessary additional propellant at TLI. While transfer (b) is slightly cheaper than (a), it is over 50 days longer in duration due to its additional revolution about the Earth; a likely unfavorable tradeoff. The BLTs presented in Figure 4.9 are not an exhaustive list of possible candidates, as various other options exist, extending into both quadrants 2 and 4. Moreover, modifications to the mission requirements may lead to significant differences in results.

For instance, consider a transfer to the same destination orbit, but allowing the initial starting altitude of the Earth orbit to be any value between 100 and 2000 km. A sample result is plotted in Figure 4.10, where the associated TLI magnitude is 2794.43 m/s, time of flight is 113.45 days, and initial altitude is 1738.38 km. The reduced cost may be attributed to both the initial altitude being greater, as well as the lunar encounter along the spacecraft's ascent. The same transfer is represented in the Earth-Moon rotating frame in Figure 4.11(a), accompanied by plots of the behavior near the Earth (Figure 4.11(b)) and Moon (Figure 4.11(c)).

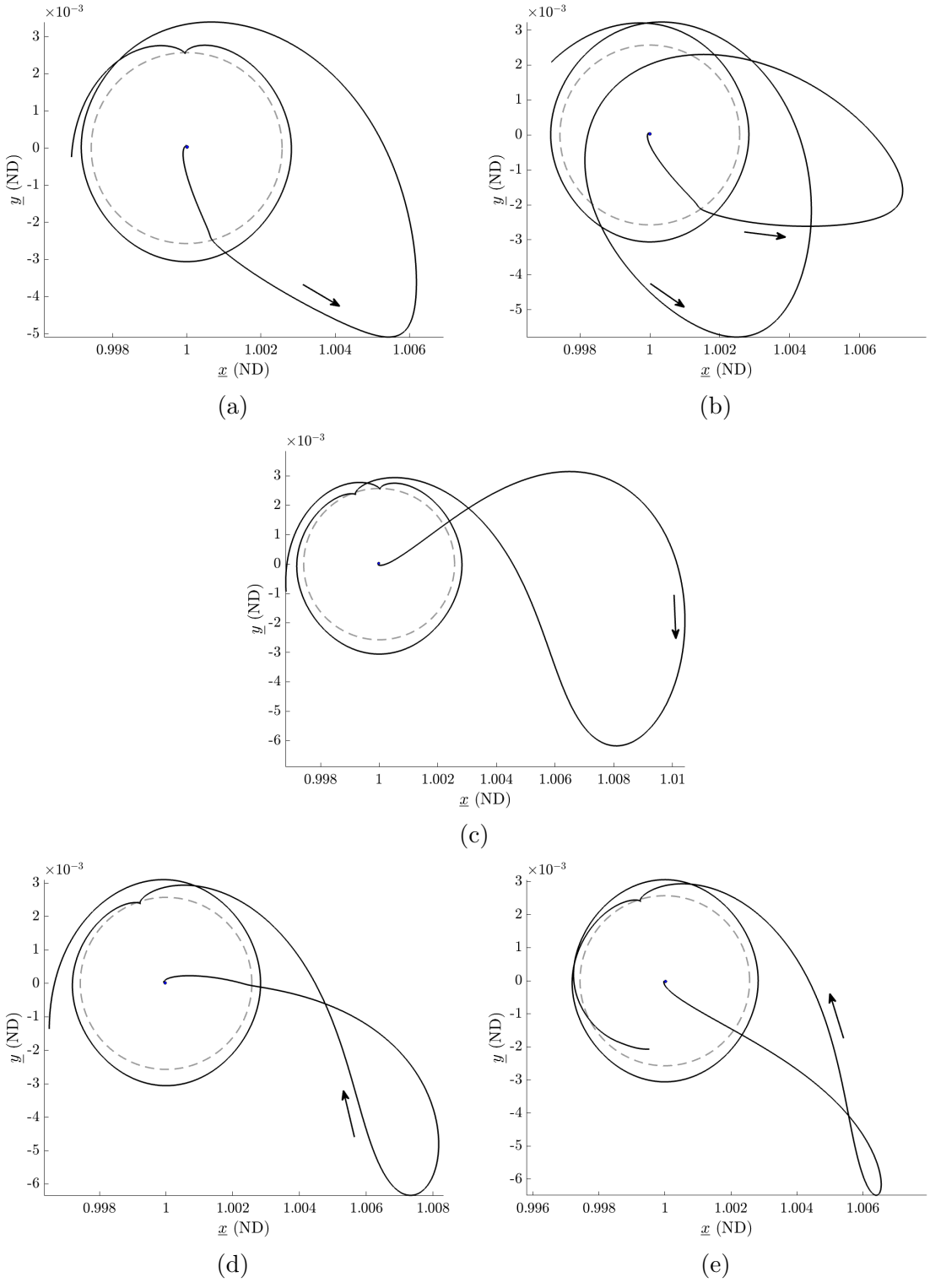

Figure 4.9. Various BLTs inserting into a BCR4BP L_2 2:1 synodic-resonant Lyapunov orbit. Motion for each in the Sun-B_1 frame. Lunar orbit in grey.

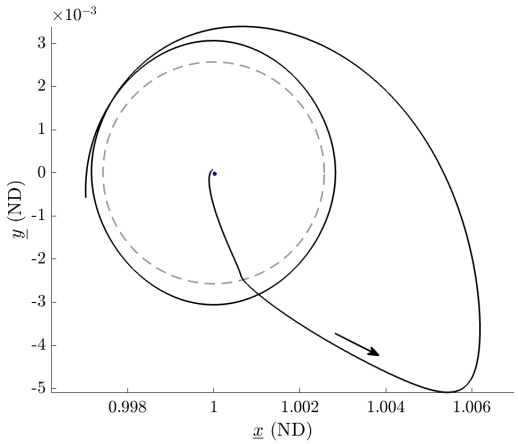

Figure 4.10. BLT to BCR4BP 2:1 Lyapunov with higher starting altitude. Motion in the Sun-B_1 reference frame.

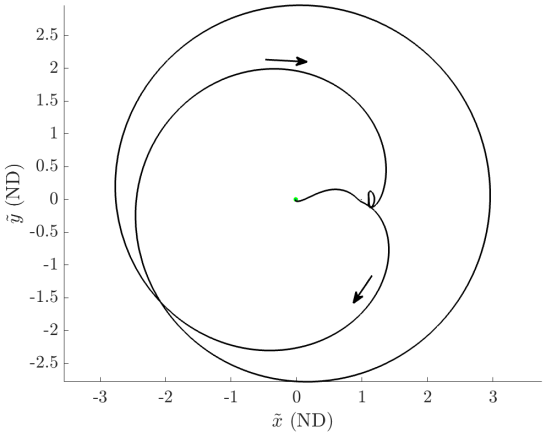

(a) Overview

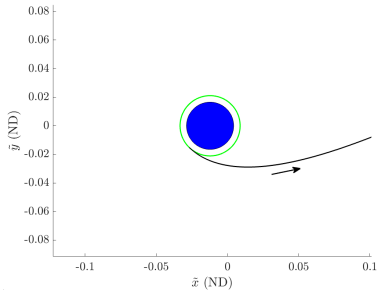

(b) Near Earth

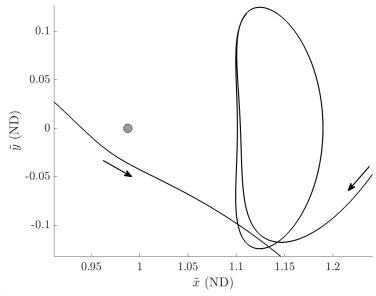

(c) Near Moon

Figure 4.11. BLT from Figure 4.10 represented in the Earth-Moon rotating frame. Green circle is initial Earth parking orbit.

While the convergence of lunar transfers to BCR4BP periodic orbits is certainly possible, the arrival epoch constraint serves to restrict the differential corrections process. Through the usage of pseudo-manifolds, BLT targeting algorithms gain an additional dimension of flexibility when converging upon the arrival state.

4.3.2 Transfers using Pseudo-manifolds

Pseudo-manifolds provide a more lenient means of generating transfers into and out of a CR3BP periodic orbit. Flexibility is increased for both the arrival constraint as well as the choice of host orbit, since a resonant BCR4BP trajectory is no longer required. The general process for correcting a ballistic lunar transfer about a pseudo-manifold is similar to that explored in Section 4.3.1. As such, the lunar transfer itself is maintained in the four-body problem, while the host trajectory is modelled by the CR3BP. As the transition of various CR3BP periodic orbits directly into ephemeris has been thoroughly explored and verified, the lack of solar influence on the destination orbit should not discredit of this method.

Much like the case in Section 4.3.1, a variable-time arrival state is explored by varying the target motion by time τ, as shown by Figure 4.8. The primary difference is that the orbit is in the CR3BP, thus there is no epoch associated with the motion. For targeting transfers to BCR4BP periodic orbits, the state and epoch continuity constraint effectively reduced the targeting process to determining the proper value of τ such that the corresponding state's stable manifold has a perigee at the desired altitude. In the case of pseudo-manifolds, there are two dimensions to the search, as the corrections process is finding a combination of τ and $\tilde{\theta}$ which tangentially encounters the Earth's parking orbit. Since the propagation of the transfer arc itself remains in the BCR4BP, the continuity constraints $\vec{F}^{\mathrm{i}}_{con}$ for $\mathrm{i} = 1, 2, \cdots, n-1$ must remain 7-dimensional. Moreover, the perigee and initial altitude constraint formulations remain unchanged.

Consider the scenario of a BLT transfer from a 1000-km altitude low Earth orbit (LEO) to a CR3BP L_2 2:1 synodic-resonant Halo orbit using pseudo-manifolds. Following the necessary perigee mapping, a differential corrections algorithm may be constructed about the following constraint and free-variable vectors, as shown in (4.15).

$$\vec{F}(\vec{X}_{\mathrm{i}}) = \begin{bmatrix} \vec{F}_{con}^{1} \\ \vec{F}_{con}^{2} \\ \vdots \\ \vec{F}_{con}^{n-1} \\ \vec{F}_{ins} \\ F_{alt}^{E} \\ F_{\mathrm{peri}}^{E} \end{bmatrix} \qquad \vec{X}_{\mathrm{i}} = \begin{bmatrix} \tilde{\vec{x}}_{o}^{1} \\ \tilde{\vec{x}}_{o}^{2} \\ \vdots \\ \tilde{\vec{x}}_{o}^{n} \\ T_n \\ \tau \end{bmatrix} \tag{4.15}$$

While seemingly the same as the formulation in (4.14), recall that $\vec{F}_{ins}$ omits the epoch constraint, meaning that this constraint vector has dimension one less than $\vec{X}_{\mathrm{i}}$.

Construction of a spatial transfer uses the same framework as that for a planar BLT, though it is assumed that the initial Earth parking orbit is of the same inclination as the departing initial state. By constructing a differential corrections algorithm around $\vec{F}(\vec{X}_{\mathrm{i}})$ and $\vec{X}_{\mathrm{i}}$, five sample BLTs are provided in Figure 4.12, while their associated costs and flight durations are given in Table 4.4. Additionally, the maximum spatial dispersion from the Sun-Barycenter plane is provided in Table 4.4.

Table 4.4. Maneuver costs and flight times for BLTs shown in Figure 4.12

Trajectory	(a)	(b)	(c)	(d)	(e)
TLI Cost (m/s)	3001.86	2992.22	3037.37	2996.22	3033.87
TOF (Days)	98.95	104.47	136.32	142.96	110.57
Maximum z-amplitude (km)	68533.41	57049.69	45203.16	52764.07	47863.58

While the circularizing quadrant effects are most pronounced when motion is completely planar, its applicability still extends to slightly inclined orbits as well. As seen in the previous section, lunar encounters have the potential to reduce the TLI cost necessary to reach deeply into a circularizing quadrant. In the case of the Halo transfers, inclined initial conditions drive the subsequent motion away from the Earth-Moon plane. As a result, encounters with the Moon during the ascending portion of the BLT are exceedingly rare. Despite this, an initially near-planar transfer which meets the Moon to then be inclined by the flyby is possible, as investigated later in Chapter 5.

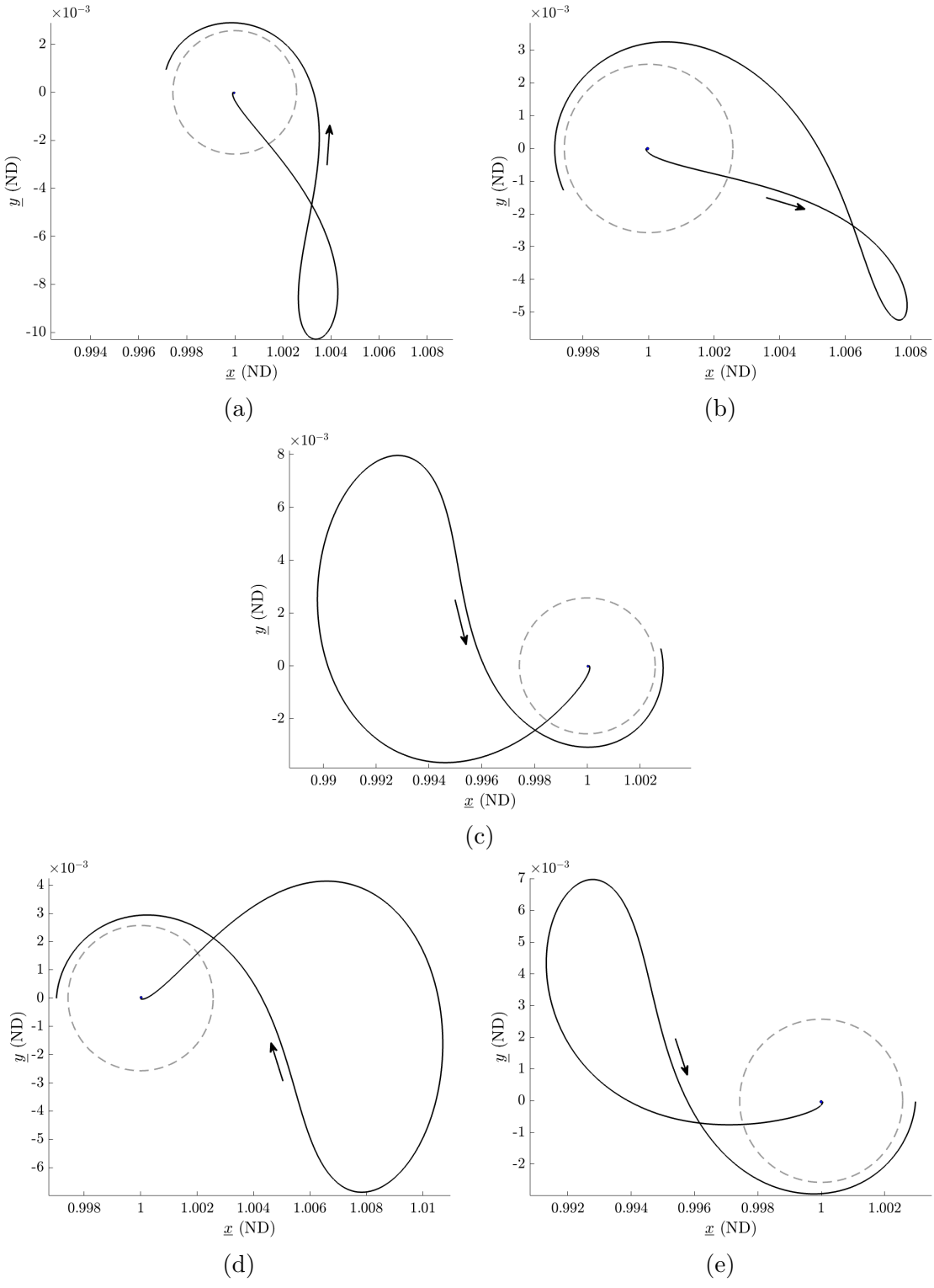

Figure 4.12. Various BLTs inserting into a CR3BP L_2 2:1 synodic-resonant Halo orbit. Motion in the Sun-B_1 frame, lunar orbit in grey.

4.3.3 Transfers to Circular Lunar Orbits

Much like the case for transfers to cislunar periodic trajectories, BLTs to circular lunar orbits may also reduce overall propellant expenditure. Since lower-altitude circular orbits are non-departing, their energies with respect to the host body are always lower than the incident hyperbolic trajectories necessary to arrive. As a result, a second lunar orbital insertion (LOI) maneuver is required in order to match the desired motion. The inclusion of this burn is the primary difference between BLTs to circular lunar orbits and those explored in Sections 4.3.1 and 4.3.2.

To construct a targeter for such a transfer, first define radii for the initial and final circular orbits as r_o and r_f respectively. In order to minimize costs, the Earth-departure state along the BLT is again a perigee, while the Moon-arrival state at the end of the transfer is to be a perilune. Constraints for perigee and altitude above Earth are defined in equations (4.12) and (4.13), while their lunar counterparts are as follows:

$$F_{alt}^{M} = (\tilde{x}_f^n - (1-\tilde{\mu}))^2 + (\tilde{y}_f^n)^2 + (\tilde{z}_f^n)^2 - (r_f)^2 \tag{4.16}$$

$$F_{\text{peri}}^{M} = (\tilde{x}_f^n - (1-\tilde{\mu}))\dot{\tilde{x}}_f^n + \tilde{y}_f^n\dot{\tilde{y}}_f^n + \tilde{z}_f^n\dot{\tilde{z}}_f^n \tag{4.17}$$

Recalling that the superscript for the individual components represents the associated arc they belong to, and the subscript "f" denotes the terminal state of the arc. The lunar altitude constraint governs the terminal position of the spacecraft, while it in tandem with the perigee constraint establish the arriving velocity direction, though the associated speed is allowed to vary. onsntial corrections scheme are given in (4.18).

$$\vec{F}(\vec{X}_{\text{i}}) = \begin{bmatrix} F_{con}^1 \\ F_{con}^2 \\ \vdots \\ F_{con}^{n-1} \\ F_{alt}^E \\ F_{alt}^M \\ F_{\text{peri}}^E \\ F_{\text{peri}}^M \end{bmatrix} \qquad \vec{X}_{\text{i}} = \begin{bmatrix} \vec{x}_{\text{i}}^1 \\ \vec{x}_{\text{i}}^2 \\ \vdots \\ \vec{x}_{\text{i}}^n \\ T_n \end{bmatrix} \tag{4.18}$$

As an example, consider a mission from a 1000-km parking orbit above the Earth's surface to a circular lunar orbit of the same altitude. By generating a perigee map using the method outlined at the end of Section 4.2 for various arrival epochs, example BLT trajectories are shown in Figure 4.13. A breakdown of the costs and times of flight for each of the sampled trajectories is provided in Table 4.5.

Table 4.5. Maneuver costs and flight times for BLTs shown in Figure 4.13

Trajectory	(a)	(b)	(c)	(d)	(e)
TLI Cost (m/s)	3010.40	2929.17	3045.43	2992.58	2994.47
LOI Cost (m/s)	569.64	588.83	589.04	663.49	949.97
Total Cost (m/s)	3580.04	3518.00	3634.46	3656.07	3944.71
Time of Flight (Days)	124.14	106.47	107.04	101.11	100.49

It may be noted that the least costly TLI again belongs to a transfer which encounters the Moon as it approaches apogee. Moreover, due to the presence of insertion maneuvers, additional leniency is allotted for BLTs to venture more deeply into quadrants 1 and 3. As an example, the BLT shown in Figure 4.13(e) has a near-equal amount of presence in quadrant 1 as it does in quadrant 4, diminishing the overall circularization of the orbit. Resulting from this is a trajectory with a near-perpendicular encounter with the lunar orbit, requiring significant propellant to arrive at the destination. Combined with the 100-day time of flight, this option provides little benefit over a direct transfer. Scheuerle demonstrates that the theoretical minimum LOI cost for a 1000-km altitude orbit about the Moon is roughly 500 m/s [20], a magnitude reasonably close to those demonstrated by BLTs (a) through (c). To further reduce costs, additional maneuver magnitude constraints may be applied, though another alternative is to continue a family of BLT trajectories from a converged arc.

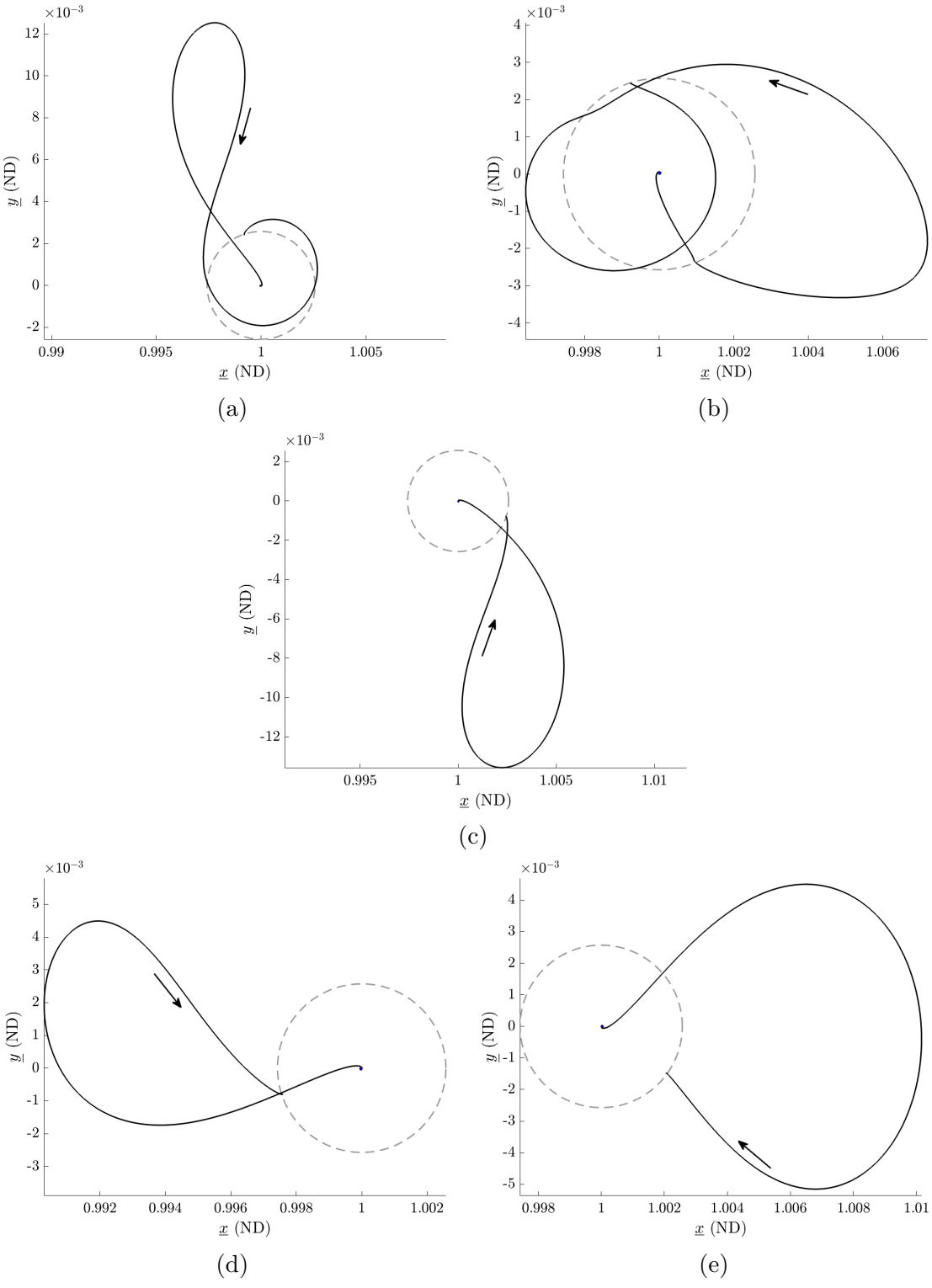

Figure 4.13. Sample BLTs from LEO to a 1000-km altitude lunar orbit. Motion in the Sun-B_1 frame, lunar orbit in grey.

4.4 Continuation of BLT Families

Selection of differing initial conditions leads to a greater variety of BTL trajectory options, though the primary means for increasing the population of the transfer candidate pool is through continuation. Moreover, by scanning through characteristics of each family member, more ideal transfers may be uncovered. While various methods for continuation may be applied, this section focuses on the application of natural parameter continuation (NPC) about select transfer elements. The utility of any continuation method hinges on the flexibility of the associated scenario. For instance, when considering transfers for a maneuver-less insertion into a BCR4BP periodic orbit, the initial targeting process is effectively the determination of the location on the trajectory which has a stable manifold that has a perigee at a desired altitude above the Earth. An adjacent value of τ will likely not correspond to a perigee which also fulfills the departure requirements, thus either another degree of freedom must be created. As such, continuation of families of solutions that ballistically insert into BCR4BP periodic orbits typically fails. Pseudo-manifolds, on the other hand, remove the arrival epoch constraint and impart additional flexibility to the continuation algorithm.

Recall that for transfers using pseudo-manifolds, the dimensionality of the constraint vector is less than that of the free-variables by one, meaning that pseudo-arclength continuation may be applied. While convenient, PALC deprives the user of control through the family traversal, thus a more intuitive NPC method is explored. For example, consider the targeted transfer from a 1000-km altitude Earth parking orbit to a CR3BP L_2 2:1 synodic-resonant Halo orbit shown in Figure 4.12(a). By fixing the time of flight for the n-th segment, a natural parameter continuation scheme may be subsequently defined using the transfer duration. From the initially converged result, T_n may be incrementally increased as well as decreased, forming two subsets of the BLT family. Combining the two subsets, the resultant BLT family is shown in Figure 4.14(b), where each member is colored by the associated TLI magnitude. For clarity in visualization, a majority of the intermediate members of the family are not plotted.

In this case, as the time of flight continually decreases, the TLI maneuver cost is reduced as well. This relationship is explicitly depicted in Figure 4.15.

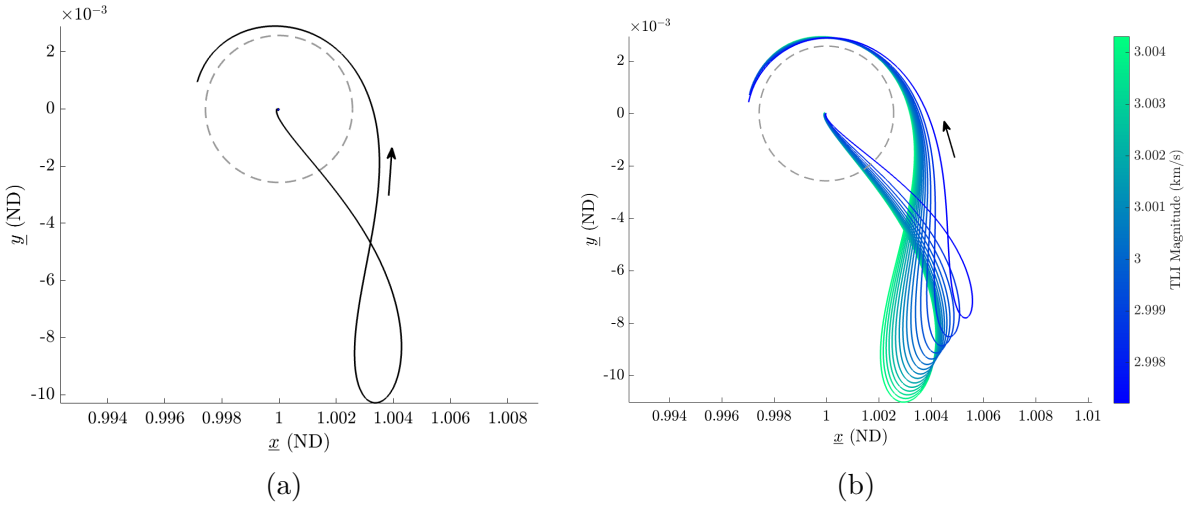

Figure 4.14. Sample BLT family to a L_2 2:1 synodic-resonant Halo orbit (b) compared with the initially converged transfer (a). Motion in the Sun-B_1 frame, lunar orbit in grey.

Continuation of a single BLT family may find the lowest cost among a set of like geometries, though this does not guarantee the cheapest possible transfer for the scenario. Separate families may provide additional options, though it is difficult to predict the extent by which the TLI cost may be reduced through continuation. As a result, the general BLT design process focuses on finding select transfers which accomplish the mission objectives, rather than pursuing the single most optimal result possible.

Removing the arrival epoch constraint creates the flexibility necessary to construct families of BLTs as informed by pseudo-manifolds. Despite this, six dimensions of the arrival state are still governed by the destination orbit, leading to a relatively narrow BLT solution space. In the case of transfers to circular lunar orbits, greater leniency may be exploited, as position along the circular orbit, epoch as well as speed at perilune are all unenforced. Consider an arbitrary BLT transfer from a 1000-km altitude LEO to a circular orbit of the same distance above the Moon, as shown in Figure 4.16(a). Instead of fixing and stepping along time of flight, the NPC scheme may be shifted to the Sun angle value at departure. The resultant family is presented in Figure 4.16(b), noting that the color-scale applied to the family is for the TLI cost alone. A more thorough breakdown of the costs as a function of the continuation parameter is given in Figure 4.17.

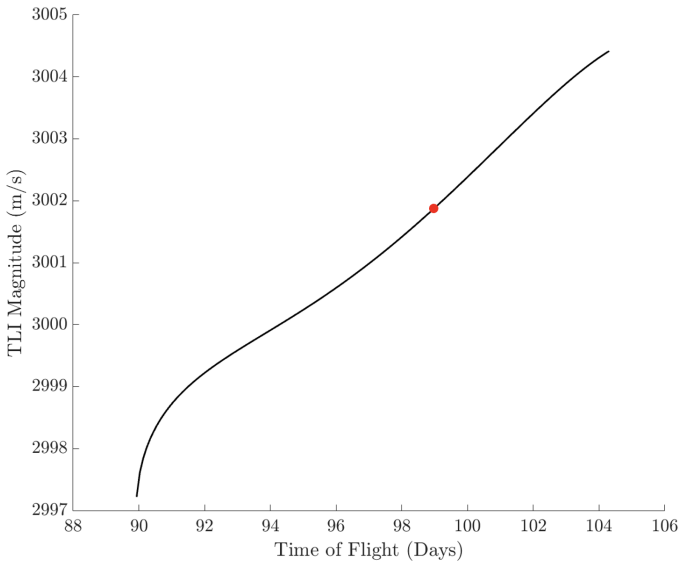

Figure 4.15. Departure cost as a function of flight duration. Red point corresponds to initially converged solution shown in Figure 4.14(a).

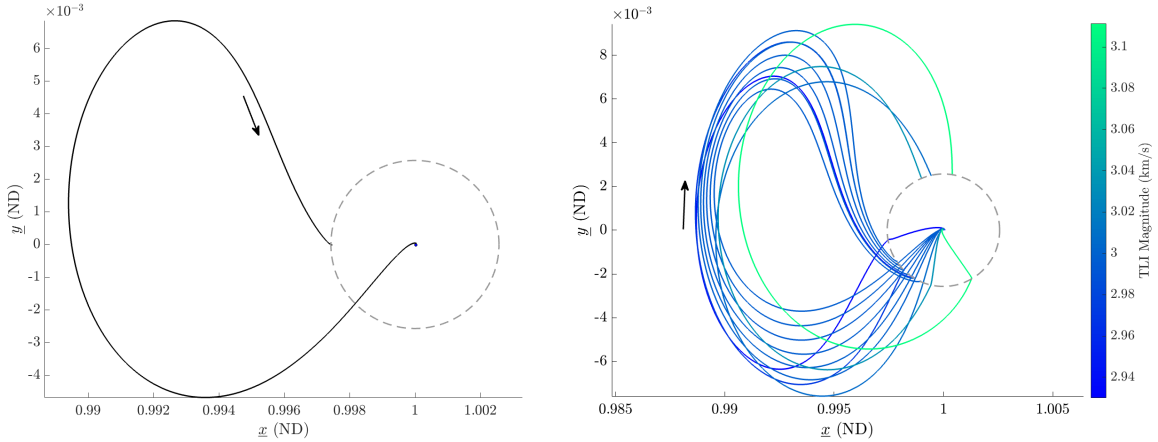

Figure 4.16. Continuation of converged BLT (a) about departure $\tilde{\theta}$ to form a family of transfers (b). Motion in the Sun-B_1 frame, lunar orbit in grey.

The family is bounded in configuration space by two transfers which encounter the Moon at differing epochs. These two members in particular are at opposite extremes in TLI cost for the family, as highlighted in Figure 4.17. While LOI and TLI magnitudes are not independent of one another, there are other influential factors present as well. In particular, tidal perturbations from the Sun and lunar encounters both play critical roles in cost-reduction.

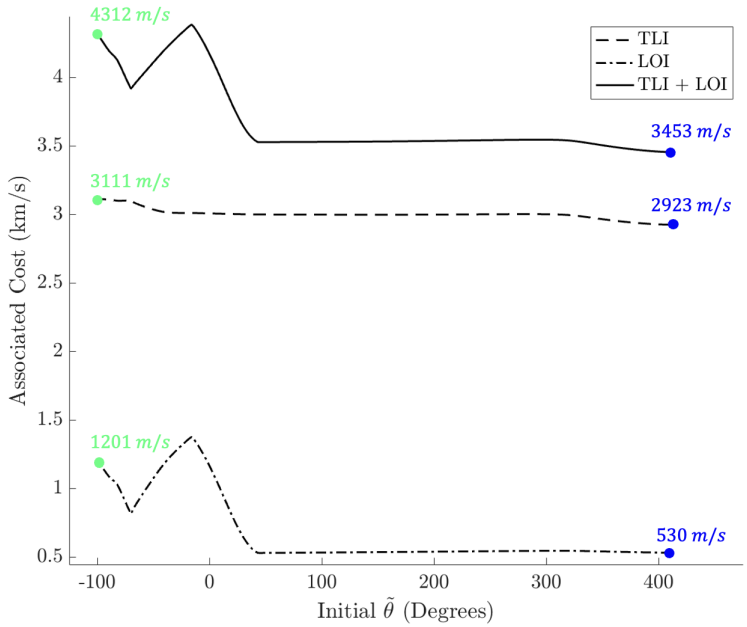

Figure 4.17. Breakdown of maneuver magnitudes across BLT family shown in Figure 4.16(b).

A significant TLI maneuver may indeed send a spacecraft far beyond the Moon's orbital radius about the Earth, but this only cheapens the arrival maneuver if the apogee is located properly to properly circularize the downstream motion. Moreover, several previous examples have demonstrated that lunar encounters have the potential to reduce TLI cost, though the outbound direction of motion is thus altered by the flyby. Should the ascending leg of the BLT be bent by a close Moon-passage such that the subsequent motion is sent into an energizing quadrant, the LOI may be inadvertently inflated. Lunar encounters are not guaranteed to decrease the departure maneuver cost either, as both the most and least expensive TLIs within the family in Figure 4.16(b) belong to transfers with close Moon passages. Further analysis into the impact of flybys within the context of BLT design is conducted in Section 4.5.

4.5 Lunar Encounters along BLTs

The term "gravity assist" is often used within the context of the relative two-body problem for scenarios where a spacecraft proceeds through a relatively close passage by an attracting

body. The effect of such a maneuver is twofold: the acceleration stemming from the body steers the spacecraft in a new direction, and an energy change may result from the encounter. These effects grow increasingly exaggerated as the periapse radius decreases, thus careful planning is recommended for missions featuring relatively close flybys. Despite its name, a gravity assist is only beneficial if constructed properly.

In the previous section, a family of BLTs leading from LEO to a circular lunar orbit featured two members that encounter the Moon during their ascent, as shown in Figure 4.16. While both transfers successfully deliver the spacecraft to its destination, the associated costs radically differed, as labelled in Figure 4.17. Evidently, one benefitted from the lunar encounter, while the other was hindered by it. Reiterating a previous assertion, the presence of a lunar encounter may decrease the necessary TLI cost as the flyby may aid in sending the spacecraft further into space. Section 2.3.7 establishes that the Hamiltonian of a spacecraft when viewed in the Sun-Barycenter frame is perturbed by relatively close encounters with the Earth and Moon. The evolution of the $\underline{H}$ value for both BLTs is provided in Figure 4.18, where the spikes in either curve occur during their respective lunar passages.

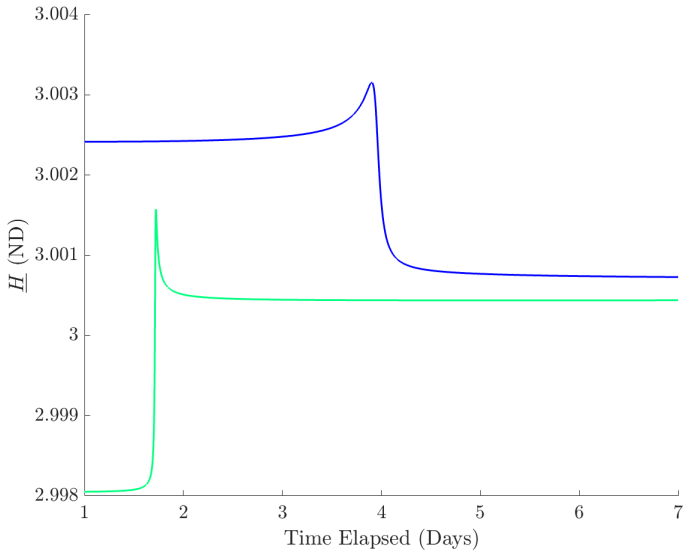

Figure 4.18. Evolution of Sun-Barycenter Hamiltonian value for both BLTs from Figure 4.16(b) with lunar encounters. Curves colored correspondingly.

Recalling the negative relationship between Hamiltonian and spacecraft kinetic energy, the results support the previous conclusion. The high-cost transfer was effectively slowed by its lunar encounter, while the opposite occurred for the cheaper option. In the case of the green curve, the extra fuel consumed to create such a high-energy post-launch state was quickly counteracted by the Moon's gravity, while less of a maneuver was necessary in the case of the blue plot due to the flyby's assistance.

Within the context of gravity assists, the outbound energy of a spacecraft is only increased if the component of its velocity vector along the direction of the body's velocity is positive; the inverse scenario leads to a decrease in energy. In other words, the inbound and outbound hyperbolic speeds relative to a body are the same, thus the inertial spacecraft velocity only increases in magnitude when the relative velocity is in the same general direction as the body's motion. Typically, flybys behind a body's motion, or lagging passages, result in increases in outbound energy, while the opposite is true for flybys in front of a body's motion, or leading passages. When examining the motion of the two investigated BLTs in the Moon-centered Earth-Moon frame (shown in Figure 4.19), it becomes evident that the cheap transfer employed a lagging passage, while the costly BLT used the alternative.

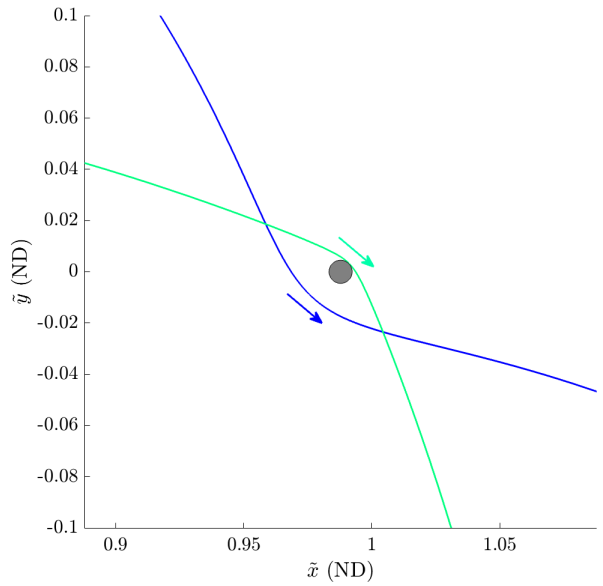

Figure 4.19. Near-Moon motion of both BLTs in the Earth-Moon rotating frame. Arcs colored correspondingly.

While the Moon is motionless in this frame, the $+\tilde{\hat{y}}$ axis corresponds to the Moon's direction of motion in an inertial view, indicating that the green curve crosses into the lunar path, while the other remains behind it.

Lagging passages may certainly reduce the departing maneuver cost, though the minimization of necessary arrival maneuvers hinges more on the resultant directional change. The costliest arc in Figure 4.16(b) is initially heading toward quadrant 4, though is immediately steered into the third quadrant by the lunar encounter, where it receives insufficient circularization and intersects the lunar orbit at a near-perpendicular angle. While the other BLT featuring a flyby also begins in quadrant 3, its subsequent motion tracks deep enough into quadrant 2 in order to raise perigee and approach the Moon at a tangent.

The combination of considerations for flyby altitude as well as for epoch and energy create a non-trivial BLT design process. Dynamical and numerical sensitivities are exaggerated when nearing a gravitational body, further challenging differential corrections. Despite this, lunar flybys present a compelling opportunity to reduce total mission costs for primary payloads. In the case of secondary payload missions, where fuel is more significantly limited and the initial jettison is inflexible, the inclusion of these Moon passages may be vital.

5. SECONDARY PAYLOAD TRANSFERS FEATURING A LUNAR FLYBY

The previous chapter discussed ballistic lunar transfer design with a variable initial state and epoch to reasonably accommodate the mission requirements. This leniency may be leveraged by assuming the launch vehicle will conform to the mission path, a common occurrence for primary payloads. At the same time, the launch vehicle may be carrying additional spacecraft, a practice referred to as a "rideshare". These secondary payloads have little influence on the jettison condition of the launch vehicle, thus their initial state and epoch is constrained. Moreover, rideshare spacecraft are often compact, and as such may be limited in the amount of fuel carried along. In the event the secondary payload is ejected from the launch vehicle on a path to the Moon, direct insertion into a cislunar orbit would be costly or even infeasible. Despite this, a flight path utilizing a lunar flyby may allow for the necessary re-orientation of the outbound trajectory, as well as reduce the required mission Δv.

The investigation is centered about the construction of transfers to cislunar trajectories using a lunar flyby, as well as the minimization of any necessary costs. The framework which accomplishes this is also designed to accommodate most starting epochs and states which correspond to an initial trajectory which coasts to a relatively low-altitude perilune. To this end, analysis into the correlation between perilune condition and the subsequent apogee location in the Sun-Barycenter frame is detailed. Then, two-body dynamics are used to enlighten the design of the post-flyby portion of the transfer's ascending leg, followed by a translation to the Sun-Barycenter CR3BP to account for perturbation effects and phasing. A bridging arc between the pre and post-flyby sections of the transfer's ascent is then constructed using B-Plane targeting. Lastly, a differential corrections algorithm is defined alongside associated methods for relieving computational sensitivity. From this, the lunar gravity may be exploited to develop viable transfers to Halo, Butterfly and Lyapunov orbits.

5.1 Transfer Construction Framework

In Chapter 4, the explored BLT construction process focused primarily on the convergence of a single transfer leg satisfying departure and arrival constraints. As such, propagation of the reference arc is conducted in a single segment, which is then converged using a multiple shooter. Large geometric deviations caused by lunar encounters often challenged the continuation of BLTs, hence why many of the families were bounded by lunar transfers with outbound flybys. Close passages by the Moon will naturally increase the dynamical sensitivity of the transfer, though this is especially prominent when modelling the reference trajectory using a single forward propagation from departure. In this section, the reference transfer is broken into three primary phases, numbered in order from departure to arrival. Moreover, two interfaces Σ_1 and Σ_2 are constructed about the Moon, though they correspond to differing portions of the transfer. The first boundary is a spherical shell of a defined radius fixed about the Moon, while the second is a cylindrical tube of another given radius, extending indefinitely along the $\pm\tilde{\hat{z}}$ direction. These boundaries serve as transitional regions between the phases, as Phase 1 begins at the commissioning maneuver (CM) of the spacecraft and ends when the motion intersects Σ_1. Phase 2 begins when the spacecraft subsequently crosses Σ_1 again from the inside and finishes when encountering Σ_2, where Phase 3 immediately begins. The construction of the lunar flyby which connects Phases 1 and 2 within the first interface requires its own procedure, as detailed in Section 5.3. A visualization of the transfer framework is provided in Figure 5.1 for an arbitrary arrival orbit (in black).

While depicted in Figure 5.1, the transfer segment departing an Earth parking orbit (black dashed line) is not included in the transfer construction. Rather, the commissioning maneuver will be viewed as the beginning of the mission, as this is the assumed location where the secondary payload is then allowed to influence its own motion.

5.1.1 Phase 1 Departure Leg Construction

A secondary objective of the investigation is to create a robust process which can converge lunar transfers for a wide variety of starting epochs and states. While the investigation

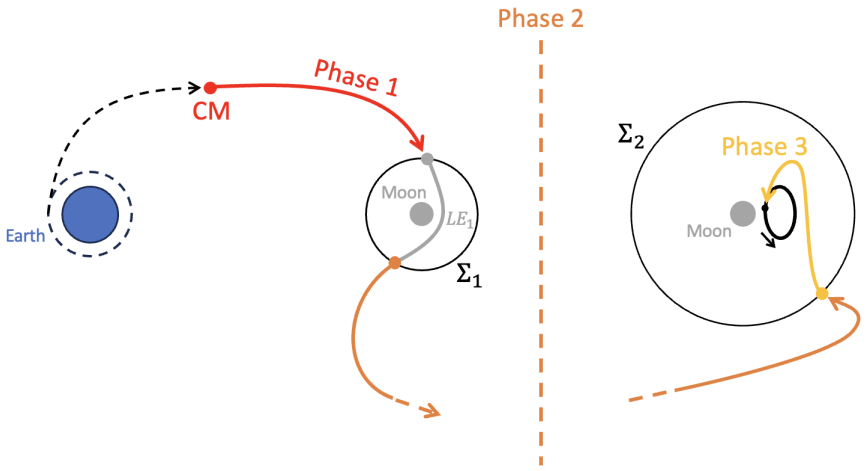

Figure 5.1. Visualization of overall transfer construction framework.

focuses on the transfer of a spacecraft from an inflexible starting state within the design of an individual mission, various different CM states may be utilized between missions. As such, less importance is placed on the precise determination of the CM state itself, rather the focus is centered on maintaining this starting location and epoch during the corrections process. The commissioning maneuver itself represents the first firing of the secondary payload's thrusters following its jettison from the launch vehicle, though this maneuver is situated about a specified initial state. For the purposes of simplicity in the investigation, it is assumed that the launch vehicle provides the necessary thrust to situate the spacecraft into its defined CM state. In general, this state is found by generating a direct transfer to the Moon from a circular Earth orbit, where the CM state is chosen to be along this trajectory following about 1 day from the initial Earth departure. This definition allows for a variety of realistic commissioning maneuver states to be explored by the investigation, moreover a similar process is employed by other publications into lunar transfers for secondary payloads [2] [23]. Additional constraints may be imposed onto the sample direct transfer depending on the mission specifications, though a more general means for determining the beginning state is maintained in this investigation.

Once the location of the commissioning maneuver has been selected, the first iteration of the Phase 1 trajectory is constructed by propagating forwards until perilune. This simulation

is performed within the HFEM in order to avoid potential difficulties the pulsation of the Moon's orbit may impose on convergence in a higher-order model. The Phase 1 reference trajectory is the segment prior to the encounter with Σ_1, though the epoch associated with the flyby may be conveniently determined by continuing to perilune. A sample Phase 1 reference trajectory is rotated to the Earth-Moon frame, as shown in Figure 5.2. The associated baseline CM state is $\vec{x}_{CM} = \begin{bmatrix} 0.345 & 0.276 & 0.007 & 1.224 & 0.887 & 0.023 & 4.521 \end{bmatrix}^T$, where the values are in the Earth-Moon rotating frame and non-dimensionalized as such, while the seventh parameter is the Sun angle, in radians.

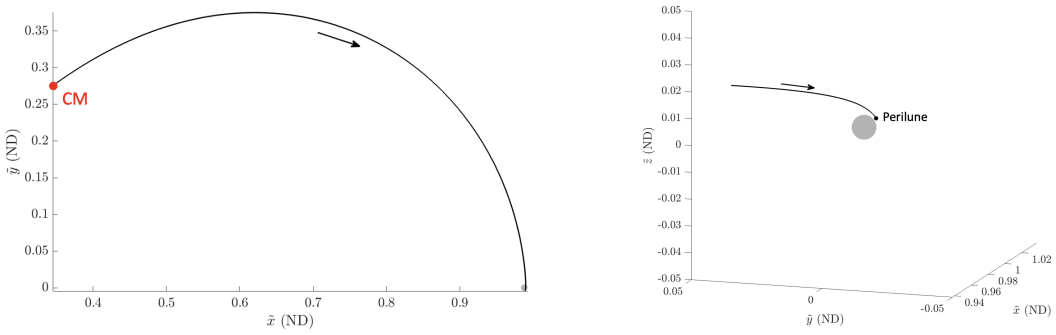

(a) Trajectory overview (b) Near-Moon

Figure 5.2. Sample Phase 1 reference trajectory resulting from $\vec{x}_{CM}$. Propagation in HFEM, motion shown in the Earth-Moon rotating frame.

It is assumed that the CM is instantaneous and may occur in any direction. In reality, many secondary payloads utilize low-thrust engines that require significant time to generate an equivalent thrust, though the instantaneous case serves as a simplified baseline. A benefit to this assumption is that the transfer arc is only required to begin at the time and place associated with the CM state, while the corresponding velocity is unconstrained.

5.1.2 Phase 3 Arrival Leg Construction

While the first interface acts as a bubble in which the bridging arc between Phases 1 and 2 is constructed, Σ_2 is serves as a direct interface between Phases 2 and 3. Since the investigation seeks to define a transfer construction process to various destination orbits, the second boundary must be defined to accommodate this. For modelling natural arrival

behavior into a select science orbit, pathways may be propagated in reverse-time from the destination to their intersection with Σ_2. It is assumed that any arrival manifold is equally welcome, thus the greater variation in arrival conditions provided by stable pseudo-manifolds leads to their usage in the Phase 3 transfer determination process. As mentioned before, the second boundary is a cylinder whose axis is aligned along the $\tilde{\hat{z}}$ direction. This is to surround large, highly inclined science orbits should they be desired. The choice in interface geometry is only for organizing the manifold intersection locations; it does not have any impact on the relevant dynamics. As an example, the Σ_2 crossings of the stable pseudo-manifolds propagated from a southern butterfly orbit with a Jacobi Constant $JC \approx 3.084$ are shown in Figure 5.3. The boundary shown is a cylinder with a 100000 kilometer radius about the Moon.

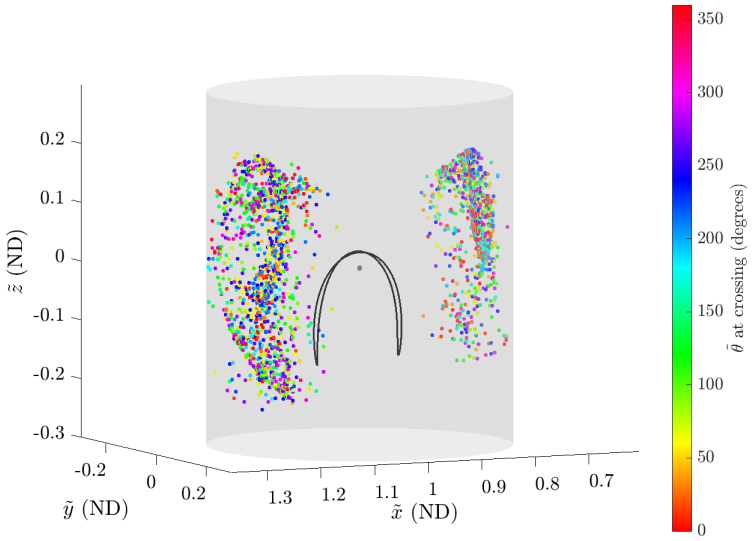

Figure 5.3. Intersections of pseudo-manifolds from a sample Butterfly orbit (in black) with a cylindrical interface (in grey). Intersecting states colored by encounter epoch, figure presented in the Earth-Moon frame.

Each pseudo-manifold state and epoch at their intersection with Σ_2 is then stored as the collection of candidate arrival arcs. The Phase 2 analysis results in a variety of candidate trajectories which intersect Σ_2 from the outside, further discussed in Section 5.2. In order to select an appropriate candidate from either set of Phase 2 and 3 arcs, a nearest-neighbor

algorithm is necessary. Each terminal Phase 2 state at the second interface interaction is denoted ${}^{2}\vec{x}_{\mathrm{j}}$, where j is the index distinguishing between differing arcs. At the same time, each Σ_2-crossing Phase 3 state is similarly cataloged and represented as ${}^{3}\vec{x}_{\mathrm{i}}$. It is to be noted that the state vectors are seven-dimensional, as their respective Sun angles are included. To perform the nearest-neighbor search to determine the most compatible transfer segments on either side of the second interface, a K-D tree is used. This algorithm simultaneously determines the appropriate pseudo-manifold (i) and Phase 2 trajectory (j) which satisfies expression (5.1). Effectively, it finds the individual trajectory from Phase 2 and that from Phase 3 which align the closest, while allowing flexibility for weighting individual components.

$$\min_{[\mathrm{i},\ \mathrm{j}]} \Delta x = \left|\left| {}^{2}\tilde{\vec{x}}_{\mathrm{j}} - {}^{3}\tilde{\vec{x}}_{\mathrm{i}} \right|\right| \tag{5.1}$$

Where:

$$ {}^{2}\tilde{\vec{x}}_{\mathrm{j}} = \begin{bmatrix} {}^{2}x_{\mathrm{j}} \\ {}^{2}y_{\mathrm{j}} \\ {}^{2}z_{\mathrm{j}} \\ c \cdot {}^{2}\dot{x}_{\mathrm{j}} \\ c \cdot {}^{2}\dot{y}_{\mathrm{j}} \\ c \cdot {}^{2}\dot{z}_{\mathrm{j}} \\ {}^{2}\tilde{\theta}_{\mathrm{j}} \end{bmatrix} \qquad {}^{3}\tilde{\vec{x}}_{\mathrm{i}} = \begin{bmatrix} {}^{3}x_{\mathrm{i}} \\ {}^{3}y_{\mathrm{i}} \\ {}^{3}z_{\mathrm{i}} \\ c \cdot {}^{3}\dot{x}_{\mathrm{i}} \\ c \cdot {}^{3}\dot{y}_{\mathrm{i}} \\ c \cdot {}^{3}\dot{z}_{\mathrm{i}} \\ {}^{3}\tilde{\theta}_{\mathrm{i}} \end{bmatrix} \tag{5.2}$$

The scaling factor c allows the user to bias the search with regard to insertion cost, though it possesses the other property of influencing convergence probability. The value $c = 1$ is a more traditional K-D tree state filtration setup that weighs each non-dimensional component equally, though this may not be favorable from a transfer construction standpoint. A velocity discontinuity is allowed at the interface between Phases 2 and 3, though position and epoch must match between the two arcs. As such, the importance placed on velocity components matching is less than that for the others, hence the scaling factor is only applied to $\dot{x}$, $\dot{y}$ and $\dot{z}$. For a given transfer, various c values are tested, providing different initial guesses and thus alternative convergence basins to explore. A line-search may also be used to determine the value of c, where great emphasis is initially placed on velocity and the position discontinuity

is evaluated iteratively for declining values of c until the Phase 2 and 3 intersection locations are deemed close enough. Pritchett explores an alternative approach of appending the Earth-Moon Hamiltonian and velocity directions to the search in order to focus the results toward cost reduction [41].

Following the nearest neighbor search, the pseudo-manifold which satisfies (5.1) becomes the reference trajectory for Phase 3, while simultaneously choosing the Phase 2 candidate. While it is ideal to have no velocity disparity between the two phases, initial guesses often predict significant costs; this may be softened by later convergence and continuation strategies. However, the most important means of reducing necessary maneuver costs is designing Phase 2 trajectories which appropriately leverage solar perturbations.

5.2 Phase 2 Transfer Leg Construction

As shown in Figure 5.1, Phase 2 is defined to exist between the two interfaces, beginning at Σ_1 and finishing at Σ_2. Between these encounters is the largely heliocentric leg where the majority of the solar perturbation effects take hold. As such, it is critical that the farthest excursion of Phase 2 largely lies in either quadrant 2 or 4. In Chapter 4, it is noted that the presence of a lunar encounter may significantly steer the direction of the subsequent BLT, thus understanding general trends between a flyby state and the subsequent behavior is fundamental.

5.2.1 Spacecraft Behavior Following Lunar Encounter

Naturally, the manner by which a spacecraft passes by the Moon determines the downstream direction. For instance, a highly inclined passage by the Moon will significantly shift the following apogee out of the Sun-Barycenter plane. Of course, greater complexities exist when designing a lunar transfer, as the radius of the flyby governs both the energy change and the turning angle caused by the Moon. When designing the heliocentric leg of a lunar transfer, two key factors are at play: the apogee distance and the argument of apoapsis. The former is the magnitude of the position vector from Earth to the farthest excursion of the

lunar transfer. The argument of apoapsis (ω_a) is the angle of the projection of apogee onto the $\hat{\underline{x}}$-$\hat{\underline{y}}$ plane, as measured along $\hat{\underline{z}}$ starting from $\hat{\underline{x}}$, as demonstrated in Figure 5.4

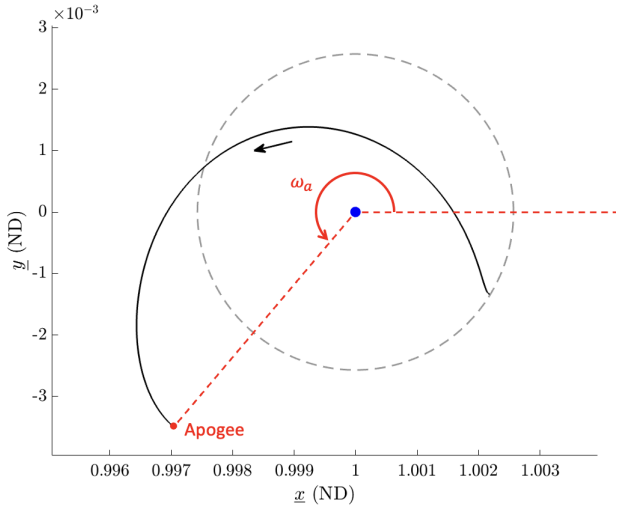

Figure 5.4. Example argument of apoapsis measurement. Motion shown in the Sun-B_1 frame.

To better understand the correlation between a flyby and the ensuing argument of apoapsis, consider a dispersion analysis centered about the CM state shown in Figure 5.2. A uniform spherical distribution of 500 unit vectors is used to construct the directions for the maneuver dispersions, while each direction is to be evaluated at magnitudes ranging from 10 to 100 m/s in increments of 10 m/s. Should a perilune occur when propagating the perturbed state in the Earth-Moon BCR4BP, the behavior at the flyby is then rotated to the Sun-Barycenter BCR4BP and propagated until apogee (if it occurs). At each apogee, the argument of apoapsis is recorded alongside the corresponding distance from the Earth. As an initial demonstration, each of the recorded flybys are projected onto the $\tilde{\hat{x}}$-$\tilde{\hat{z}}$ plane, colored by their subsequent argument of apoapsis angle, as shown in Figure 5.5.

It is noted that $\tilde{\hat{x}}$-$\tilde{\hat{y}}$ plane symmetry is avoided due to the underlying trajectory from the CM state having a small spatial component. The clear majority of the apogees lie within quadrant 4, though this is due to the Moon angle at perilune being approximately -30 degrees. In terms of lunar transfer design, only transfers which have apogees relatively distant from Earth-Moon neighborhood have the opportunity to exploit solar gravity. Filtering out

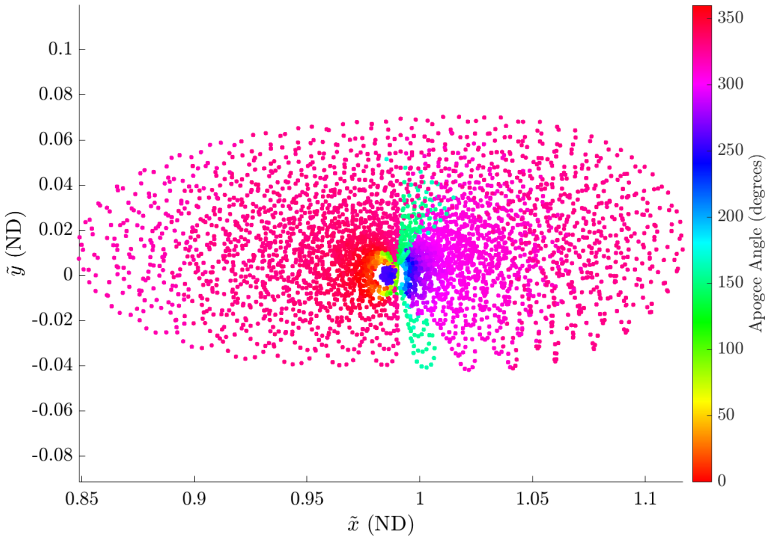

Figure 5.5. Perilune locations in the Earth-Moon frame as a function of subsequent apoapsis angles.

flybys with apogee radii less than 600000 km (above 1.5 times the Moon's orbital radius about the Earth) as well as arguments of apoapsis outside of quadrants 2 and 4, the flyby space may be reduced as shown in Figure 5.6. Moreover, the passages corresponding to the argument of apoapsis values closest to the centers of quadrants 2 and 4 are labelled.

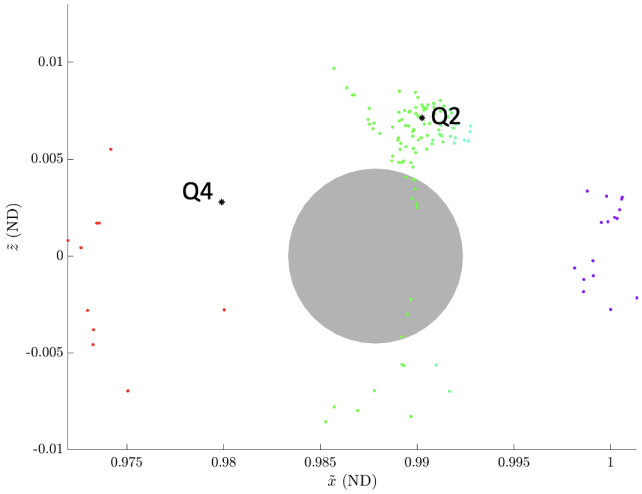

Figure 5.6. Filtered perilune states from Figure 5.5, as shown in the Earth-Moon frame.

The location of the flyby tells half of the story, as the velocity at each point is just as influential in determining the outbound motion. Direct transfers often lie roughly along the $\tilde{\hat{x}}$-$\tilde{\hat{y}}$ plane, meaning that flybys roughly aligned with the $\tilde{z}$ axis above or below the Moon will have a significantly inclined passage. Moreover, spatial flybys near the Moon, such as those shown in Figure 5.6 have an increased likelihood of being steered significantly out of plane, as the turning angle is significant. It may be intuited that the starred second-quadrant trajectory is largely spatial, though this is the case for the selected quadrant-4 example as well. Top and side views of the subsequent motion leading to apogee for both examples are provided in Figure 5.7.

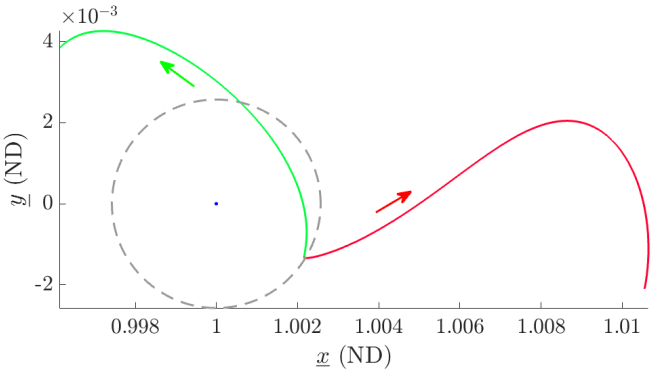

(a) $\underline{\hat{x}}$-$\underline{\hat{y}}$ projection

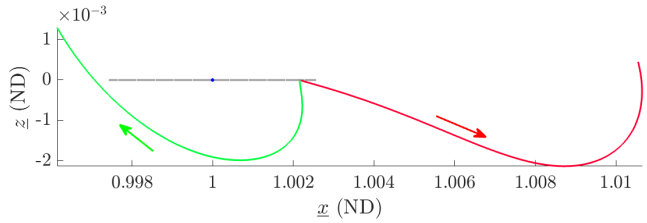

(b) $\underline{\hat{x}}$-$\underline{\hat{z}}$ projection

Figure 5.7. Propagation of starred flybys from Figure 5.6 in the BCR4BP. Motion shown in the Sun-Barycenter frame.

Examining Figure 5.6, the vast majority of transfers which enter the appropriate quadrant at an acceptable distance are inclined. This does not indicate an non-existence of feasible planar trajectories, but rather a highly limited selection to choose from. A primary factor is the epoch of the flyby, as changing the location of the Moon also affects the location of

the subsequent apoapses. To demonstrate, the same CM dispersion is evaluated, though the starting Sun angle ($\tilde{\theta}_o$) is shifted by various values, effectively relocating the lunar encounter to various positions about the Earth. Following the same filtration method as before with a dispersion along 400 uniformly distributed directions evaluated at the same magnitudes, The flybys for each epoch are shown in Figure 5.8.

As the epoch changes, the Phase 1 trajectory is relatively unaffected. Consequently, the geometric location of the unfiltered flybys remains nearly the same. However, as the location where these flybys occur shifts within the Sun-Barycenter frame, so does the resulting directions of the outbound trajectories. Motion with an apogee of appropriate radius but in an energizing quadrant in Figure 5.5 may be rotated such that they are no longer filtered out. As a result, planar options may be far more abundant for some epochs, while others have the majority of their viable outbound arcs highly inclined; another consequence of having an inflexible jettison date. Clearly, a primary contributor to the behavior between the first lunar encounter (LE_1) and apogee is the location of the Moon itself. By further reducing the relevant dynamics, an analytical estimation of the argument of apoapsis may be crafted using relative two-body dynamics.

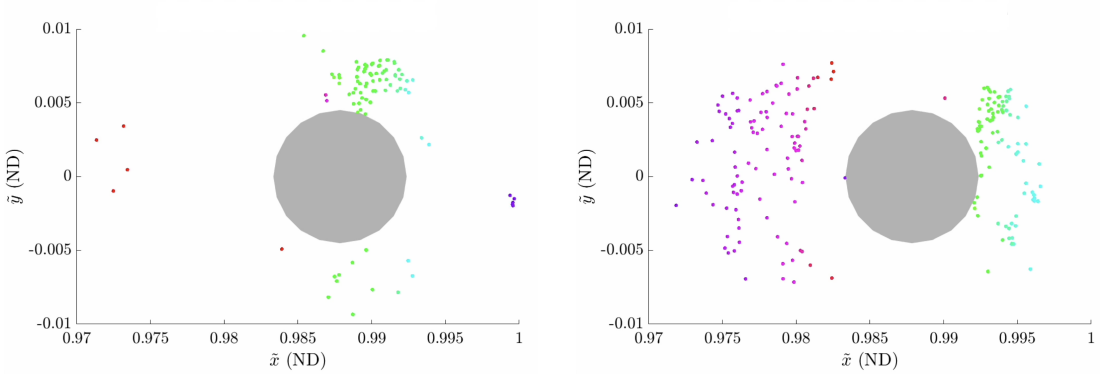

(a) Sun angle: $\tilde{\theta}_o$

(b) Sun angle: $\tilde{\theta}_o + 1.3\ rad$

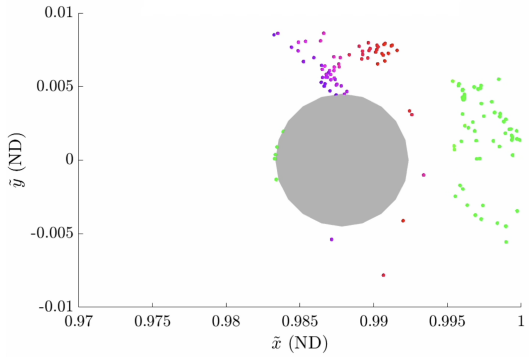

(c) Sun angle: $\tilde{\theta}_o + 2.6\ rad$

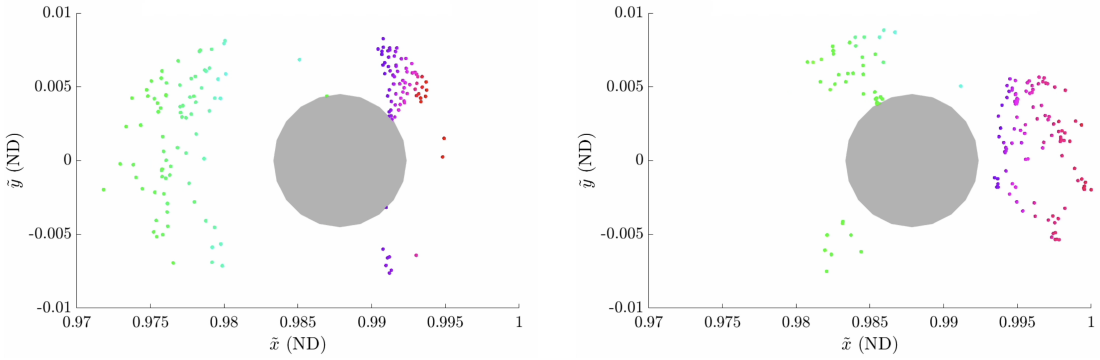

(d) Sun angle: $\tilde{\theta}_o + 3.9\ rad$

(e) Sun angle: $\tilde{\theta}_o + 5.2\ rad$

Figure 5.8. Filtered Flybys resulting from various starting epochs. Colors match the scale shown in Figure 5.6, motion in the Earth-Moon frame.

5.2.2 Apogee Angle Estimation via Relative Two-Body Dynamics

During Phase 1, the Earth serves as a dominant gravitational force acting upon the spacecraft until it approaches the Moon. As the spacecraft goes through its first lunar passage, the Moon assumes the role of the primary accelerator as the spacecraft is steered into a new direction. Along the outbound flight following the flyby, the solar gravitational effects only begin to significantly take root as the spacecraft begins to near its apogee. As such, the location of the apogee is relatively unaffected by the Sun, as its primary effect on the motion is showcased after the most distant excursion from the Earth. From this, it may be assumed that the Sun does not significantly affect the argument of apoapsis. Moreover, once the spacecraft leaves the Moon's sphere of influence, its gravitational pull on the spacecraft significantly weakens, meaning that the outbound portion of Phase 2 is dominantly governed by the Earth's gravity alone. Consequently, the usage of relative two-body dynamics with respect to the Earth may prove beneficial in approximating the location of apogee within the Sun-Barycenter frame.

First, consider an arbitrary inertial reference frame where, for a moment in time, the axes of the inertial and Earth-Moon coordinate frames are aligned. Furthermore, in this moment in time, consider the spacecraft state as it is exiting Σ_1. Another reason for defining the first interface about the Moon is that this boundary may also act as a marker for the Moon's sphere of influence (SOI). While definitions for an SOI radius vary, the analysis assumes it to be 30000 km, as this distance is great enough to model the hyperbolic departure from the Moon, but not far enough to be significantly perturbed by the other bodies. So long as these characteristics are maintained, the radius of Σ_1 is relatively arbitrary. With this, it is also assumed that the state when leaving the boundary is departing the Moon's sphere of influence, with an associated velocity $\vec{v}_\infty^+$.

The components of the hyperbolic departure vector may be represented in terms of spherical coordinates. Define an in-plane angle, α which is measured along $+\tilde{\hat{z}}$ from $\tilde{\hat{x}}$ to the projection of the velocity vector onto the $\tilde{\hat{x}}$-$\tilde{\hat{y}}$ plane. A complimentary out-of-plane angle, β is situated between the relative velocity vector and the $\tilde{\hat{x}}$-$\tilde{\hat{y}}$ plane; a visualization of both

angles is provided in Figure 5.9. The third component is also displayed, being the magnitude of the relative velocity vector, or $||\vec{v}_\infty^+||$.

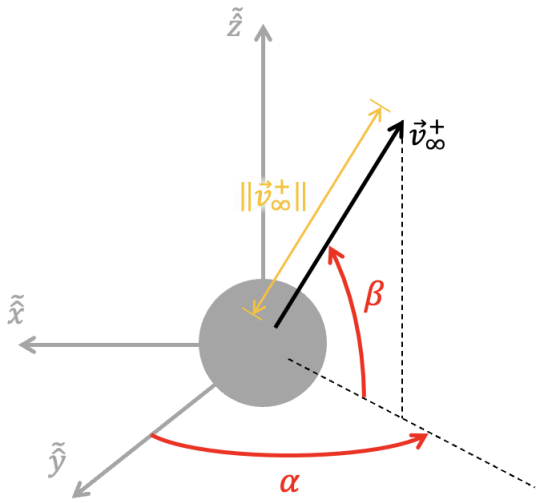

Figure 5.9. Visualization of a spherical coordinate representation for $\vec{v}_\infty^+$ within the Earth-Moon rotating frame.

Mathematically, their representation in the departing velocity vector is as follows:

$$\vec{v}_\infty^+ = ||\vec{v}_\infty^+|| \left[-\sin\alpha\cos\beta\ \tilde{\hat{x}} + \cos\alpha\cos\beta\ \tilde{\hat{y}} + \sin\beta\ \tilde{\hat{z}} \right] \tag{5.3}$$

Due to the assumptions made, $\vec{v}_\infty^+$ is equivalently represented in inertial coordinates. Moreover, since the inertial frame itself is arbitrarily defined, this much can be repeated for the spacecraft's Σ_1 departure state at any epoch. Within the scope of the Sun-Barycenter frame, the position of the spacecraft is roughly equivalent to that of the Moon with respect to the Earth, or $\vec{r}_\infty^+ = \vec{r}_M$. Furthermore, the position of the Moon is along the $\hat{X}$ axis by a magnitude $\tilde{\ell}^*$, a characteristic shared by any initial epoch. With the dimensional gravitational parameter of the Earth defined as μ_E, the velocity of the spacecraft as viewed in the inertial frame may be defined as shown in (5.4).

$$\vec{v}^+ = \vec{v}_\infty^+ + \sqrt{\frac{\mu_E}{\tilde{\ell}^*}}\ \hat{Y} \tag{5.4}$$

The full six-dimensional state of the spacecraft is consequently defined within the Earth relative two-body problem, thus the ensuing orbit may be analytically characterized. The semi-major axis and eccentricity vector of the resultant trajectory are found using (5.5) and (5.6) respectively.

$$a = \frac{\mu_E \ \tilde{\ell}^*}{2\mu_E - \tilde{\ell}^* \ ||\vec{v}^+||^2} \tag{5.5}$$

$$\vec{\mathrm{e}} = \vec{r}_M \left(\tilde{\ell}^* ||\vec{v}^+||^2 - \mu_E\right) - \frac{(\vec{r}_M \bullet \vec{v}^+)\, \vec{v}^+}{\mu_E} \tag{5.6}$$

If the magnitude of the eccentricity vector (e) is close to (but less than) 1, the orbit is likely to become hyperbolic with respect to the Earth when including the solar influence. To avoid this, initial conditions leading to an eccentricity of value $\mathrm{e} \geq 0.95$ are discarded from consideration. Additional constraints such a perigee and apogee radius constraint are also imposed to further filter potentially undesirable candidates. Conditions with instantaneous apogee distances of less than 130% and greater than 400% the Moon's orbital radius about the Earth are excluded.

Aside from its distance, the apogee location may also be determined within the arbitrary inertial frame, though its argument with in the Sun-B_1 rotating frame is desired. While the assumption that the two frames are aligned in the beginning moment is valid, it is unable to be maintained following the time elapsed while coasting to apogee. As such, the time of flight from the location to its farthest excursion must be determined to inform the rotation into the Sun-Barycenter frame. First, the eccentric anomaly is determined:

$$E = \begin{cases} \arccos\left(\frac{a-\tilde{\ell}^*}{a\mathrm{e}}\right) & \text{if} : (\vec{r}_M \bullet \vec{v}^+)\,/\tilde{\ell}^* \geq 0 \\ -\arccos\left(\frac{a-\tilde{\ell}^*}{a\mathrm{e}}\right) & \text{otherwise} \end{cases} \tag{5.7}$$

Noting that the eccentric anomaly is measured in radians. The flight time from the Moon departure to apogee is then calculated using (5.8).

$$T = \sqrt{\frac{a^3}{\mu_E}}\,(\boldsymbol{\pi} + \mathrm{e}\sin E - E) \tag{5.8}$$

Since the lunar encounter epoch is variable, an adaptive quantity may be created by accounting for the Moon's initial position in the rotating frame. Define the relative argument of apoapsis, γ as the angle between the argument of apoapsis and the initial Moon angle, as measured in the Sun-Barycenter frame. A sample visualization is provided in Figure 5.10.

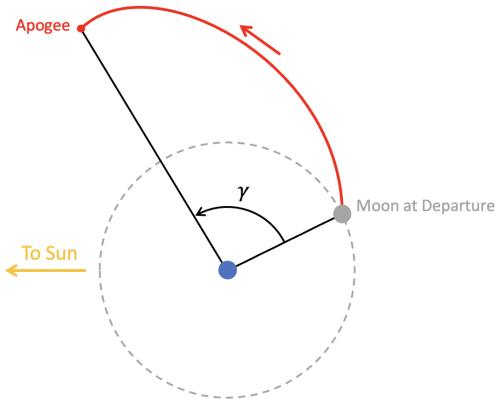

Figure 5.10. Sample measurement of γ. Visualization depicting motion in the Sun-B_1 frame.

Considering that the Moon is assumed to be along $\hat{X}$, the argument of apoapsis as viewed in the inertial reference frame is its angle measured about the $+\hat{Z}$ direction from $\hat{X}$ to $-\vec{e}$. Defining this inertial angle as θ, its value may be corrected to incorporate the rotation of the Sun-B_1 frame during the flight duration via equation (5.9). The value n_E is the mean motion of the Earth about the Sun, $n_E \approx 1.991 \times 10^{-7}\ rad/s$.

$$\gamma = \theta + n_E T \tag{5.9}$$

Since circularizing effects are both position and velocity-dependent, the precise value of ω_a is of lesser concern than the approximate location of apogee within the quadrants. As witnessed in Chapter 4, BLTs with apogees centered in quadrants 2 and 4 were occasionally outperformed by those adjacent; this much is especially true for particularly inclined lunar transfers. Consequently, allowance of error on the order of several degrees is acceptable, especially for an initial guess to be later corrected. Since the reverse evaluation of the expression for flight time is transcendental, the framework may only analytically find values

of γ given α, β and $||\vec{v}_\infty^+||$. As such, surfaces for γ as a function of the relative velocity angles may be evaluated for specified values of $||\vec{v}_\infty^+||$, as demonstrated in Figure 5.11.

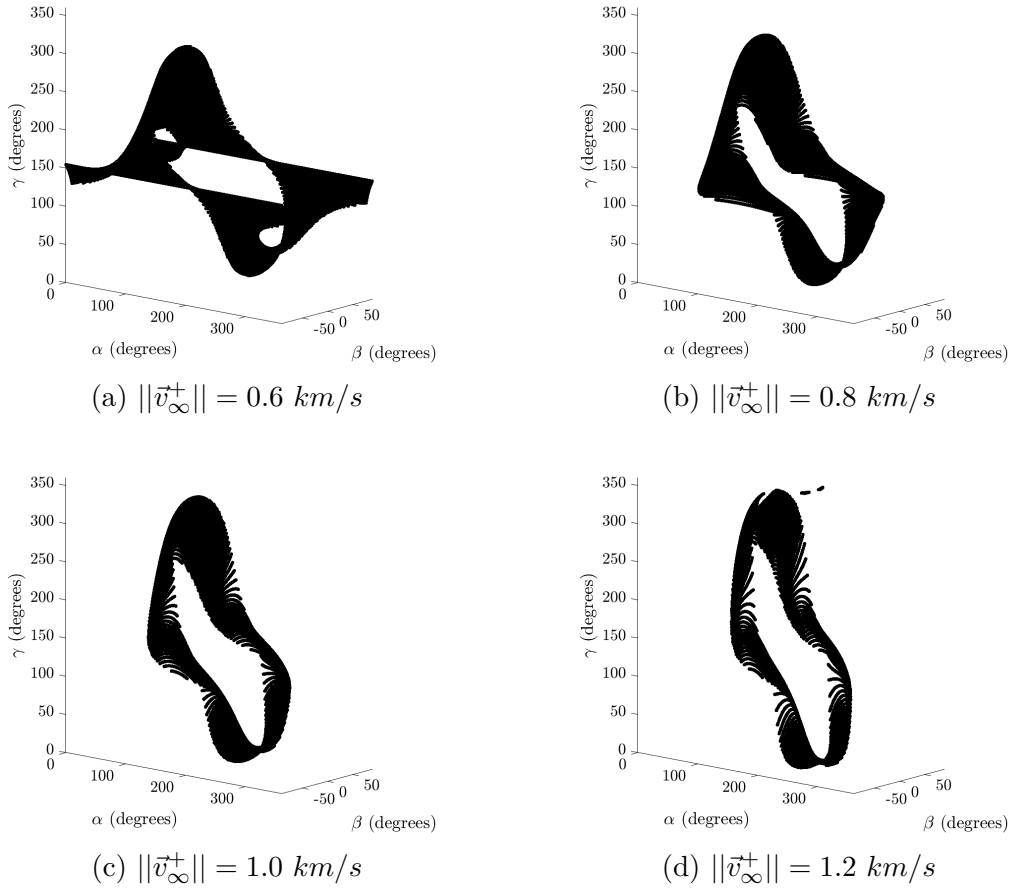

(a) $||\vec{v}_\infty^+|| = 0.6\ km/s$ (b) $||\vec{v}_\infty^+|| = 0.8\ km/s$

(c) $||\vec{v}_\infty^+|| = 1.0\ km/s$ (d) $||\vec{v}_\infty^+|| = 1.2\ km/s$

Figure 5.11. Surfaces for γ evaluated at discrete α and β values, separated by $\vec{v}_\infty^+$ magnitude.

Moreover, the construction of the surface is epoch-independent, meaning that it may be applied to any lunar flyby. For a specified LE_1 epoch, the difference between the Moon angle and the centers of quadrants 2 and 4 may be calculated.

$$\begin{aligned} \theta_2 &= \frac{3\pi}{4} - \underline{\theta} \\ \theta_4 &= \frac{7\pi}{4} - \underline{\theta} \end{aligned} \tag{5.10}$$

Two regions (Γ_2 and Γ_4) may be defined with angular separation ($\Delta\gamma$) from their respective centerlines, where:

$$\begin{aligned} \Gamma_2 &= [\theta_2 - \Delta\gamma, \theta_2 + \Delta\gamma] \\ \Gamma_4 &= [\theta_4 - \Delta\gamma, \theta_4 + \Delta\gamma] \end{aligned} \tag{5.11}$$

Informed initial guess loci may be isolated by examining the solution surface within these regions of its γ-axis. Equating $\Delta\gamma$ to 45 degrees will incorporate all of the initial guesses within quadrants 2 and 4. As an example, consider a spacecraft ending Phase 1 with $||\vec{v}_\infty^+|| = 1\ km/s$ at a time such that the ensuing perilune occurs at a Moon angle of 45 degrees. Moreover, an initial guess sample range of $\Delta\gamma = 60$ degrees is desired in order to accommodate potentially viable initial guesses in the neighboring portions of quadrants 1 and 3. The angles between the initial Moon location and the centerlines of quadrants 2 and 4 are $\theta_2 = 90$ degrees and $\theta_4 = 270$ degrees, respectively. Initial guess loci may be formed by isolating the portions of the $||\vec{v}_\infty^+|| = 1\ km/s$ surface where γ lies between either $\Gamma_2 = [30,\ 150]$ degrees or $\Gamma_4 = [210,\ 330]$ degrees. The resulting sections of the surface are shown in Figure 5.12.

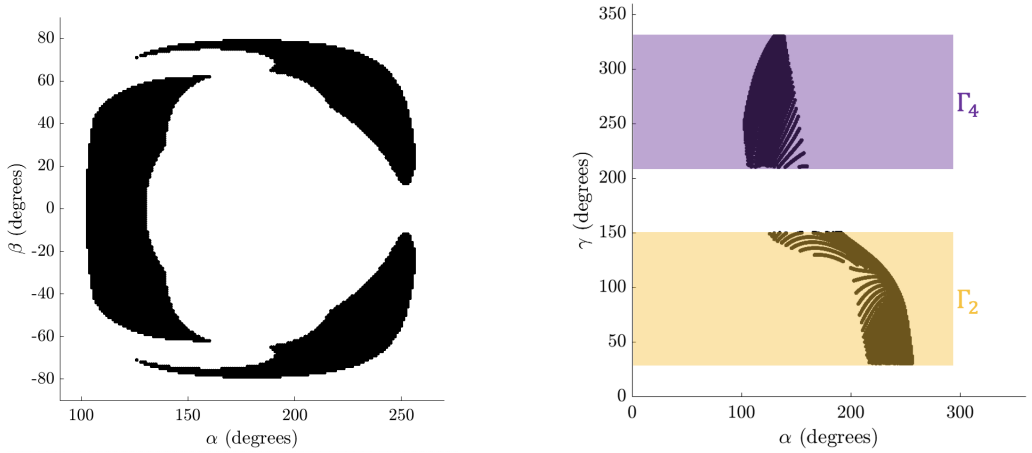

(a) Applicable α and β values

(b) Sections corresponding to Γ_2 and Γ_4

Figure 5.12. Portions of $||\vec{v}_\infty^+|| = 1\ km/s$ surface isolated when $\underline{\theta}_o = 45$ degrees and $\Delta\gamma = 60$ degrees.

While each discrete value evaluated within the filtered surfaces represents a trajectory which likely has an apogee either within or nearby the desired quadrant, no information is known about the solar perturbation effects on the motion following apogee, as well as

its phasing with the Moon. To rectify this, selected discrete solutions within the isolated portions of the surface are then translated to the Sun-B_1 CR3BP. This may be accomplished by first appending the desired lunar encounter Sun angle found during Phase 1 analysis ($\tilde{\theta}_o$) to the Earth-Moon departure state vector for a select $[\alpha, \beta]$ pair.

$$\tilde{\vec{x}} = \left[1-\tilde{\mu},\ 0,\ 0,\ -||\vec{v}_\infty^+||\sin\alpha\cos\beta,\ ||\vec{v}_\infty^+||\cos\alpha\cos\beta,\ ||\vec{v}_\infty^+||\sin\beta,\ \tilde{\theta}_o\right]^T \tag{5.12}$$

The state is then rotated to the Sun-Barycenter frame and propagated until until either contact with Σ_2 occurs or the maximum allowable transfer time expires. Position of the Moon during the simulation is critical for determining whether the second interface is intersected. The Moon angle at a moment along the propagation, $\underline{\theta}_\mathrm{i}$, may be calculated by applying (5.13) to the corresponding time since departure, t_i.

$$\underline{\theta}_\mathrm{i} = \underline{n}_{EM} t_\mathrm{i} + \underline{\theta}_o \tag{5.13}$$

Where $\underline{\theta}_o$ is the initial Moon angle resulting from the rotation of the departing state into the Sun-B_1 frame. Combinations of $[\alpha, \beta, ||\vec{v}_\infty^+||]$ which encounter the second interface make up the pool of candidate trajectories for Phase 2. This set of incident trajectories is then compared with each of the arrival pseudo-manifolds determined in Phase 3, where the K-D tree algorithm determines the most closely aligned Phase 2 and Phase 3 arcs. While the nearest-neighbor search finds the two most suitable candidates to create a seamless transition between Phases 2 and 3, a more applied method is necessary for bridging the gap between Phases 1 and 2.

To further address the accuracy of the determined value for γ, a simulation may be conducted to compare the relative argument of apoapsis as determined using the Earth relative 2-body problem with that found using the Sun-B_1 CR3BP. A uniform distribution of α and β values are sampled and converted to over 1000 combinations of initial outbound states, where $||\vec{v}_\infty^+|| = 1\ km/s$ as a baseline. These are then propagated until apogee (should it occur, discarded otherwise) in both the Earth relative 2-body model as well as in the Sun-Barycenter CR3BP. Following this, the argument of apoapsis is then measured for either

propagation for each sampled state, where then the difference between two arguments for all samples are evaluated as an error metric. For one arbitrarily evaluated starting epoch, 90 percent of the differences were less than 13.0°, while 95% fell below 15.6 degrees. Repeating this process across 100 different starting epochs, the angle associated with the 90-percent confidence interval may be evaluated for each epoch. By doing so, it is found that the mean angle is 19.7° with a standard deviation of ±6.1° and a set maximum of 36.5 degrees. In other words, at any given epoch, there is a 90 percent likelihood that the difference between the argument of apoapsis as modeled in the 2-body problem is within 20 degrees of its Sun-B_1 counterpart. The least favorable epoch tested only increases this angle by about 17 degrees, though the majority of the tests deviate significantly less from the mean. Recall that the precise location of the apogee is of less importance than the general quadrant in which it lies, thus these differences are often quite reasonable. As seen in the previous chapter, ballistic lunar transfers with their most distant excursions in the center of Quadrants 2 or 4 are often out-performed by adjacent members of the same family. Moreover, the two-body model is being used within the context of initial guess generation, meaning that further corrections are to be applied later.

5.3 B-Plane Targeting

While the Phase 2 reference trajectory begins at the Moon's location, propagation of this trajectory is ineffective in the BCR4BP, as this position is coincident with the lunar center of mass. As a result, the portion of the arc that resides within Σ_1 is dismissed, leaving the effective starting state for Phase 2 being that when it departs the Moon's vicinity. Due to this, a gap between the two trajectories is formed within the sphere. To best connect them, B-Plane targeting is employed, where Moon-relative two-body analysis is used to construct a hyperbola whose endpoints most closely align with the incident states. With this, Σ_1 is used for two purposes: to separate Phases 1 and 2, as well as to provide a dynamical boundary encircling the region where Moon two-body dynamics are assumed to be best employed. It is noted that the sphere must be large enough to accommodate various incoming arcs from Phase 1, but not to such a degree that the gravitational accelerations of the Earth and Sun

are non-negligible near its outer reaches. So long as these considerations are met, the choice of the interface radius is relatively arbitrary; in the case of this investigation, it is 30000 km. A visualization is provided in Figure 5.13, noting that the B-Plane method often does not perfectly bridge the incident and departing trajectories. These disparities are to be corrected in the targeting procedure.

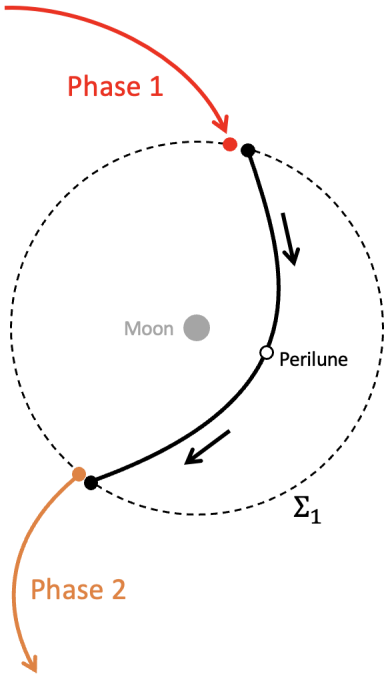

Figure 5.13. Visualization of bridging arc construction.

To construct the bridging arc, the velocity for the ending state of Phase 1, as well as that for the beginning of Phase 2 are necessary. Since B-Plane analysis is conducted in the relative two-body problem, the velocities must be rotated to a Moon-centered inertial reference frame; Zimovan Spreen offers an in-depth walkthrough of such a transformation [42]. These velocity vectors, when evaluated relative to the Moon's motion, describe the hyperbolic incoming and departing velocities of the flyby arc, where the Phase 1 ending velocity is $\vec{v}_\infty^-$, and that at the beginning of Phase 2 is $\vec{v}_\infty^+$. The two vectors span a plane within the inertial reference frame which houses the motion of the flyby arc. The direction

of the plane may be described by the specific angular momentum unit vector of the flyby, determined using (5.14).

$$\hat{h} = \frac{\vec{v}_\infty^- \times \vec{v}_\infty^+}{||\vec{v}_\infty^- \times \vec{v}_\infty^+||} \tag{5.14}$$

Furthermore, the direction of the hyperbola's eccentricity vector bisects the incoming velocity direction and that of $-\vec{v}_\infty^+$, as demonstrated by Figure 5.14. This relationship may be leveraged to determine the direction of the eccentricity vector, $\hat{e}$, given in (5.15).

$$\hat{e} = \frac{\vec{v}_\infty^- - \vec{v}_\infty^+}{||\vec{v}_\infty^- - \vec{v}_\infty^+||} \tag{5.15}$$

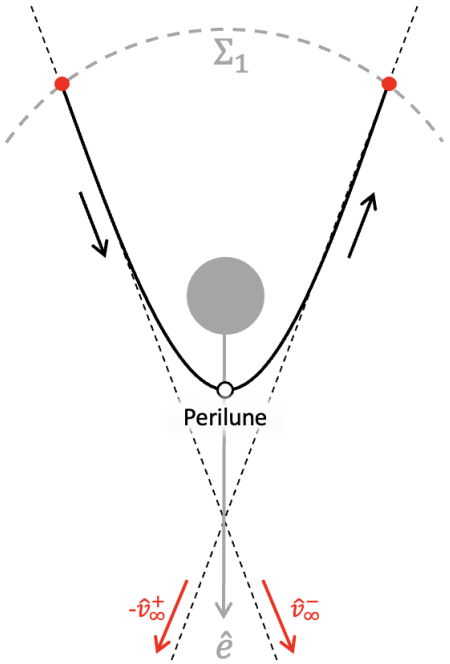

Figure 5.14. Relationship between the eccentricity vector direction and hyperbolic velocities.

To complete the orthonormal triad, the direction toward the aim-point is defined as:

$$\hat{p} = \frac{\hat{h} \times \hat{e}}{||\hat{h} \times \hat{e}||} \tag{5.16}$$

The turning angle associated with the hyperbolic flyby, δ may be found using (5.17).

$$\delta = \arccos\left(\frac{\vec{v}_\infty^- \bullet \vec{v}_\infty^+}{||\vec{v}_\infty^+|| \cdot ||\vec{v}_\infty^-||}\right) \tag{5.17}$$

If μ_M is the dimensional gravitational parameter of the Moon, then the specific energy, semi-major axis and eccentricity of the flyby orbit may be found using equations (5.18) through (5.20), respectively. The sphere of influence radius chosen for the investigation is represented as r_{SOI}. Moreover, the B-Plane analysis assumes that the magnitudes of $\vec{v}_\infty^-$ and $\vec{v}_\infty^+$ are equivalent.

$$\varepsilon = \frac{(v_\infty^-)^2}{2} - \frac{\mu_M}{r_{SOI}} \tag{5.18}$$

$$a = -\frac{\mu_M}{2\varepsilon} \tag{5.19}$$

$$\mathrm{e} = \sin^{-1}\left(\frac{\delta}{2}\right) \tag{5.20}$$

With the semi-major axis and eccentricity determined, the position of the flyby may be determined. As a preventative measure, should the perilune distance be less than the radius of the Moon, the flyby may be forced to a low altitude above the lunar surface. The inertial perilune state may be constructed by noting that the flyby location is along $\hat{\mathrm{e}}$, while its velocity is aligned with $\hat{p}$, thus:

$$\begin{aligned} \vec{r}_p &= a(1-\mathrm{e})\ \hat{\mathrm{e}} \\ \vec{v}_p &= \sqrt{\mu_M\left(\frac{2}{r_p} - \frac{1}{a}\right)}\ \hat{p} \end{aligned} \tag{5.21}$$

Inserting expressions (5.15) and (5.16) into (5.21) may convert the vectors to the inertial coordinate basis. Lastly, the time of flight needed to travel from perilune to the sphere of influence must be determined. First, the distance to the aim-point is found:

$$p = |a|(\mathrm{e}^2 - 1) \tag{5.22}$$

With this, the true anomaly corresponding to the point along the hyperbola which exits the SOI may be determined using (5.23).

$$\theta^*_{SOI} = \arccos\left(\frac{p}{\mathrm{e} \cdot r_{SOI}} - \frac{1}{\mathrm{e}}\right) \tag{5.23}$$

The associated hyperbolic anomaly, H_{SOI} may be calculated using the inverse hyperbolic tangent function.

$$H_{SOI} = 2 \cdot \operatorname{arctanh}\left(\sqrt{\frac{\mathrm{e}-1}{\mathrm{e}+1}} \tan\left(\frac{-\theta^*_{SOI}}{2}\right)\right) \tag{5.24}$$

The time of flight from perilune to intersection with the SOI is determined using (5.25).

$$T_{SOI} = \sqrt{\frac{|a|^3}{\mu_M}} \left(H - \mathrm{e} \cdot \sinh(H)\right) \tag{5.25}$$

The perilune state as expressed in the inertial reference frame may be transformed to the Earth-Moon rotating frame by the inverse method, also detailed by Zimovan Spreen [42]. For this transformation, the epoch associated with the flyby is determined by adding T_{SOI} to the time of flight of Phase 1. Once the perilune motion in the Earth-Moon frame is determined, the bridging arc is constructed by propagating the flyby state in both positive and negative time for T_{SOI} in the BCR4BP. Target states along the Phase 1 and Phase 2 reference trajectories are defined as those corresponding to time T_{SOI} before and after perilune, respectively. As an example, a bridging arc is compared with the incoming and outbound reference trajectories in Figure 5.15, where the flyby altitude is 436.31 kilometers.

The constructed flyby trajectory is also an initial guess to be converged for continuity within the differential corrections process. Since this passage is numerically sensitive due to its proximity to the Moon, special considerations may be necessary for ensuring convergence of continuous transfers.

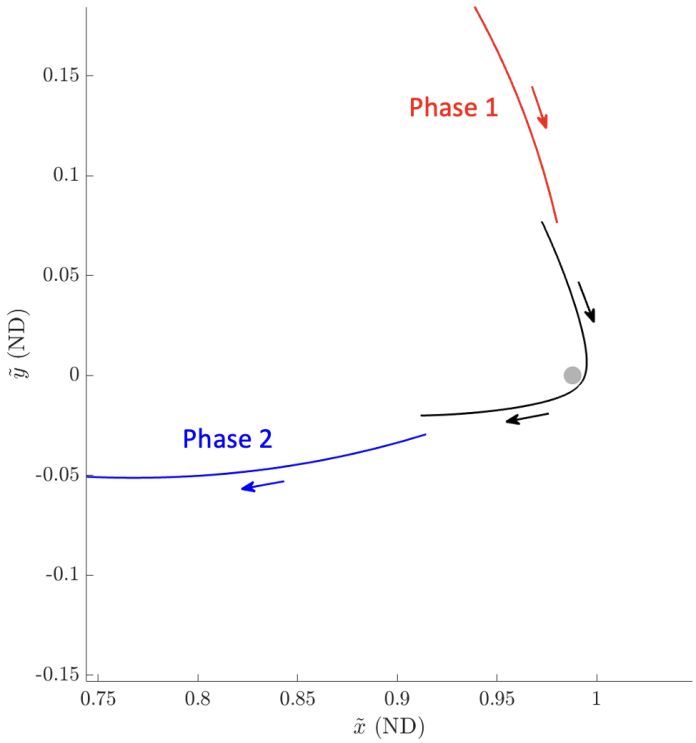

(a) $\tilde{\hat{x}}$-$\tilde{\hat{y}}$ projection

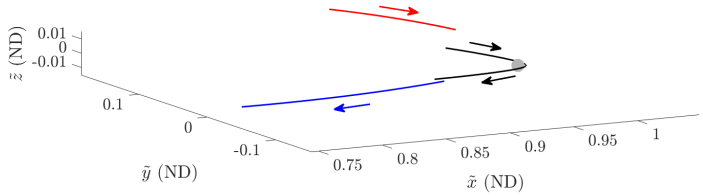

(b) Three-dimensional view

Figure 5.15. Sample bridging arc (in black) as compared to the corresponding Phase 1 and Phase 2 trajectories. Motion shown in the Earth-Moon frame.

5.4 Lunar Transfer Corrections & Continuation

Following the procedure outlined in Sections 5.1 through 5.3, the initial iterations for each segment of a candidate lunar transfer are constructed. The division between reference arc generation for each stage of the transfer leads to minor state and epoch discontinuities between phases. As such, a differential corrections framework is established to converge a continuous BCR4BP transfer from the CM location to a state along the science orbit. The

transfer features a close lunar flyby alongside extensive propagation time, a fixed departure location and epoch, as well arrival states limited to the science orbit. These characteristics culminate in a dynamically and numerically sensitive corrections procedure, thus special considerations are made toward pacifying convergence and continuation. A region of particular focus is the hyperbolic lunar passage within the Σ_1 shell, to which an isolated corrections process known as "priming" is applied.

5.4.1 Flyby Priming

Close alignment of the transfer legs for each lunar transfer phase aids in the potential convergence of a continuous flight path, though this is not guaranteed. Two primary challenges are present in the differential corrections process for such a trajectory: dynamical sensitivities due to the relatively close passage by the Moon, and lack of flexibility to be leveraged. As noted, secondary payloads have little influence in the manner by which they are deployed, effectively constraining their beginning state and epoch. Moreover, insertion into a science orbit though either manifolds or pseudo-manifolds restricts the manner by which arrival is traversed. Many inflexible aspects of the mission design may be loosened by the incorporation of thrust maneuvers, though secondary payloads are often small spacecraft with limited propellant. Impulsive maneuvers are incorporated into the analysis with an additional goal to minimize their cumulative magnitude. A lunar flyby is employed to aid in this endeavor, as it provides a cost-free mode by which the outbound leg of the trajectory may be altered. This is the cornerstone to the transfer construction framework, though it also imparts significant dynamical sensitivity to the corrections process. While targeting a swing-by arc which matches in the inbound and outbound trajectories is possible within a multiple shooting algorithm, the process may be aided by separately correcting the hyperbolic passage prior.

The study defines this isolated targeting as "flyby priming", which is effectively the search for a perilune state which matches the incoming and departing velocity vectors when propagated forward and backward in time. Since the presence of two independent states may over-constrain the targeter, a maneuver is allowed at perilune. The geometries of the Phase 1

and Phase 2 transfer legs change with each iteration of the end-to-end continuity targeter in an attempt to conform to the imposed requirements. As such, closing position discontinuities is generally less challenging than patching together arcs in velocity space, thus the priming method neglects arrival and departure location continuity constraints. The governing constraint and free variable vectors for the priming algorithm are provided in (5.26), where they are evaluated using the Earth-Moon frame BCR4BP. The flyby arc is composed of two segments, both beginning at the perilune location with one propagated forward in time, the other backward. For consistency, the propagation time is fixed to duration determined via (5.25). In defining relevant nomenclature, subscripts "o" and "f" represent the initial and final conditions along the arc respectively, while "T" represents the target velocity. The superscript distinguishes the arcs from one another, with "+" for the forward propagated trajectory, and "−" for that moving in reverse time.

$$\vec{F}(\vec{X}_{\mathrm{i}}) = \begin{bmatrix} \tilde{\vec{v}}_f^{+} - \tilde{\vec{v}}_T^{+} \\ \tilde{\vec{v}}_f^{-} - \tilde{\vec{v}}_T^{-} \\ \tilde{\vec{r}}_o^{+} - \tilde{\vec{r}}_o^{-} \\ \tilde{\theta}_o^{+} - \tilde{\theta}_o^{-} \end{bmatrix} \qquad \vec{X}_{\mathrm{i}} = \begin{bmatrix} \tilde{\vec{x}}_o^{+} \\ \tilde{\vec{x}}_o^{-} \end{bmatrix} \tag{5.26}$$

Where the initial states $\vec{x}_o^{+}$ and $\vec{x}_o^{-}$ include their respective Sun angles. The example flyby arc generated using the B-Plane method is compared to its counterpart following the priming algorithm in Figure 5.16.

While the initial guess is ballistic, the trajectory following the corrections process requires a 589.68 m/s maneuver at a flyby altitude of about 630 km. In general, changes in geometry for hyperbolic flybys are relatively resilient to alterations in velocity, thus a significant Δv is often required at perilune. A $\Delta\vec{v}$ magnitude constraint may be imposed during priming, though the benefit of its inclusion is diminished during the subsequent corrections process. Instead, continuation methods are imposed on the end-to-end trajectory to incrementally reduce the overall cost. The transfer legs before and after the lunar encounter may have differing energies, requiring a maneuver to create full-state continuity. Since energy is a function of v^2, it is most effectively increased or decreased when the speed of the spacecraft

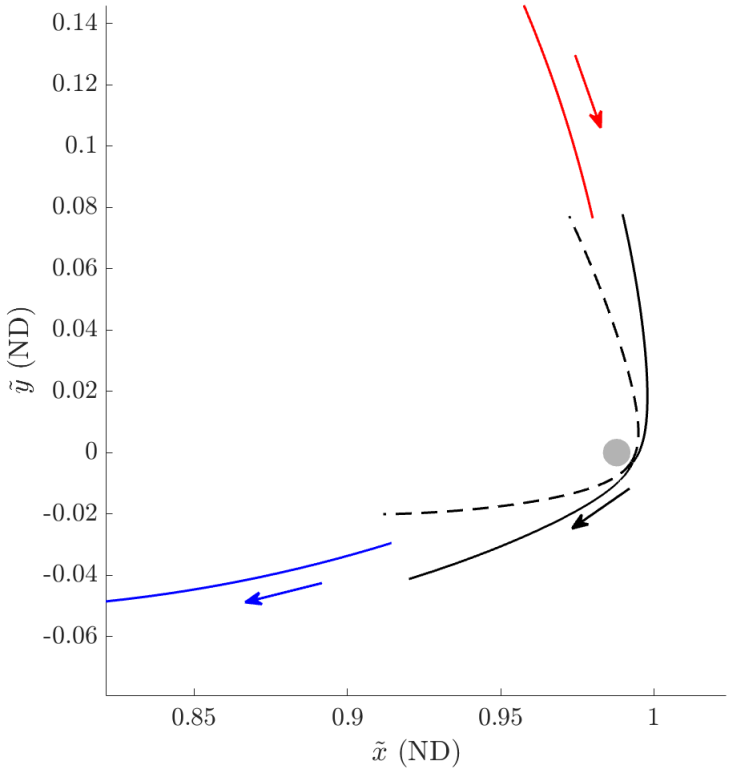

Figure 5.16. Initial iteration of flyby arc (dashed line) compared with its counterpart following the priming corrections process (solid line). Motion shown in the Earth-Moon frame.

is greatest. Because of this, placing an impulsive maneuver at perilune provides both an intuitive node for connecting Phases 1 and 2, as well the most cost-effective means for altering Hamiltonian if necessary.

Following the priming procedure, the individual segments of the lunar transfer are gathered into the end-to-end differential corrections algorithm. While optional, flyby priming lessens the discontinuity between the hyperbolic passage and the surrounding trajectories, reducing initial error within the multiple shooter.

5.4.2 Differential Corrections Framework

While the investigation seeks to converge transfers to different science orbits, the general structure of the targeter remains the same. The division between phases creates separated

trajectories which are to be patched together. Since the reference trajectory for Phase 2 is propagated within the Sun-B_1 CR3BP and rotated to the Earth-Moon frame, significant deviation may occur when transitioning to the BCR4BP. In response to this, the initial state at departure from Σ_1 is propagated in the four-body model until the magnitude of its six-dimensional isochronous difference with the reference exceeds a threshold value, e_T. Define the BCR4BP state at an instance in time as $\tilde{\vec{x}}_i$, where its associated epoch is neglected, and the state along the CR3BP reference evaluated at the same time as $\tilde{\vec{x}}_i^*$. Once $||\tilde{\vec{x}}_i^* - \tilde{\vec{x}}_i|| \geq e_T$, the propagation in the BCR4BP is re-initialized by setting $\tilde{\vec{x}}_i = \tilde{\vec{x}}_i^*$ and appending the corresponding Sun angle. This process is repeated until $\tilde{\vec{x}}_i$ reaches the isochronous CR3BP state that encounters Σ_2. A configuration-space visualization of the Phase 2 segmentation procedure is provided in Figure 5.17.

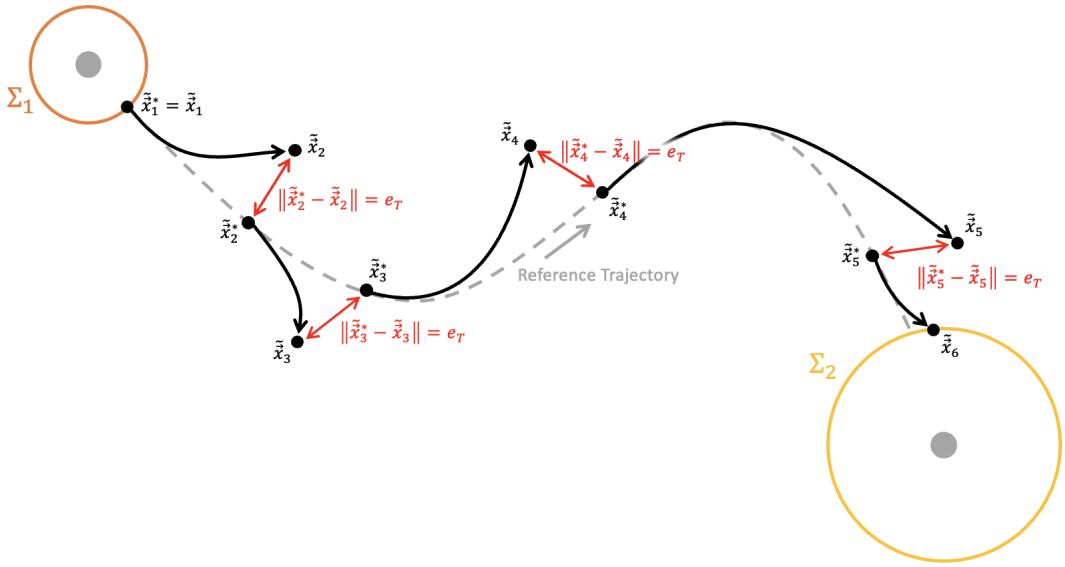

Figure 5.17. Visualization of Phase 2 segmentation method.

Assigning an e_T value which leads to too many segments may inflate the dimensions of the DF matrix, potentially introducing numerical error to the corrections algorithm. On the other hand, a threshold value too great may lead to divergence in the first iterations of the multiple shooter. As a reference, $e_T = 0.2$ non-dimensional units is commonly used in the study, though as long as the previous two considerations are satisfied, the particular number

is arbitrary. A benefit to dividing the Phase 2 leg in this manner is its adaptability to rapid changes in dynamics. Propagating the reference state at Σ_1 departure in the BCR4BP has the potential to remain closely bounded to the reference trajectory, though this likelihood is greatly reduced during passages through the Earth-Moon region. Because of this, adherence to a reference trajectory with more than one lobe about the Earth becomes difficult with a single BCR4BP arc, while the described method populates dynamically-variant regions with more segments.

Each segment within the set of n_2 arcs that make up the Phase 2 transfer must be corrected for full-state continuity. The constraint which enforces this is provided in (5.27), where ${}^2\tilde{\vec{x}}_o^{\,i}$ is the initial state for the i-th arc of the set, and ${}^2\tilde{\vec{x}}_f^{\,i}$ is the terminal motion of the same segment. The numbered superscript on the left of the vector indicates the phase that hosts the grouping of segments.

$$\vec{F}_2 = \begin{bmatrix} {}^2\tilde{\vec{x}}_f^{\,1} - {}^2\tilde{\vec{x}}_o^{\,2} \\ {}^2\tilde{\vec{x}}_f^{\,2} - {}^2\tilde{\vec{x}}_o^{\,3} \\ \vdots \\ {}^2\tilde{\vec{x}}_f^{\,n_2-1} - {}^2\tilde{\vec{x}}_o^{\,n_2} \end{bmatrix} \tag{5.27}$$

For simplicity, the forward-propagated leg of the lunar passage within Σ_1 is added to the grouping of Phase 2 segments, thus its perilune initial condition is denoted ${}^2\tilde{\vec{x}}_o^{\,1}$. A separate requirement is imposed upon this state, as it must be continuous in both position and epoch with its backward-propagated counterpart (${}^1\tilde{\vec{x}}_o^{\,1}$). Moreover, this location is constrained to remain perilune to maximize the energy-changing effect of the maneuver. To prevent a collision with the Moon itself, an altitude inequality constraint is included such that the perilune state remains at a distance greater than or equal to a defined minimum radius, r_{min}. For such a requirement, the slack variable (η_{alt}) is introduced to the free-variable vector. LaFarge provides an excellent guide for the implementation of inequality constraints and slack variables to a differential corrections process [43]. The requirements for the lunar encounter are compiled into $\vec{F}_{LE}$, as shown in (5.28).

$$\vec{F}_{LE} = \begin{bmatrix} {}^{2}\tilde{\vec{r}}_o^1 - {}^{1}\tilde{\vec{r}}_o^1 \\ {}^{2}\tilde{\theta}_o^1 - {}^{1}\tilde{\theta}_o^1 \\ ({}^{2}\tilde{x}_o^1 - (1-\tilde{\mu})) \cdot {}^{2}\dot{\tilde{x}}_o^1 + {}^{2}\tilde{y}_o^1 \cdot {}^{2}\dot{\tilde{y}}_o^1 + {}^{2}\tilde{z}_o^1 \cdot {}^{2}\dot{\tilde{z}}_o^1 \\ ({}^{2}\tilde{x}_o^1 - (1-\tilde{\mu}))^2 + ({}^{2}\tilde{y}_o^1)^2 + ({}^{2}\tilde{z}_o^1)^2 - r_{min}^2 - \eta_{alt}^2 \end{bmatrix} \tag{5.28}$$

If:

$$r_{\text{peri}} = \sqrt{({}^{2}\tilde{x}_o^1 - (1-\tilde{\mu}))^2 + ({}^{2}\tilde{y}_o^1)^2 + ({}^{2}\tilde{z}_o^1)^2} \tag{5.29}$$

then the initial value of the slack variable may be determined using (5.30).

$$\eta_{alt} = \sqrt{r_{\text{peri}}^2 - r_{min}^2} \tag{5.30}$$

Where the quantities evaluated in (5.30) are solely the initial values before the differential corrections process, as the slack variable also iteratively updates with the algorithm.

The segmentation method showcased by Figure 5.17 is also applied to the Phase 1 reference trajectory, which is now evaluated in backward time away from the lunar encounter to reduce targeting sensitivity. For consistency, the nomenclature for states in the Phase 1 grouping mirrors that used for Phase 2, now with a left-superscript of 1. Moreover, the reverse-propagated half of the lunar flyby arc is included in the set of Phase 1 trajectories, represented as ${}^{1}\tilde{\vec{x}}_o^1$. In the case of segments evaluated in negative time, the initial and final states ("o" and "f" respectively) refer to the manner by which propagation is executed rather than the motion in forward time. Continuity is required between the set of n_1 segments, while the final position and epoch must equal that of the CM state. These constraints governing the motion of Phase 1 are collected in $\vec{F}_1$, as shown in (5.31).

$$\vec{F}_1 = \begin{bmatrix} {}^{1}\tilde{\vec{x}}_f^1 - {}^{1}\tilde{\vec{x}}_o^2 \\ {}^{1}\tilde{\vec{x}}_f^2 - {}^{1}\tilde{\vec{x}}_o^3 \\ \vdots \\ {}^{1}\tilde{\vec{x}}_f^{n_1-1} - {}^{1}\tilde{\vec{x}}_o^{n_1} \\ {}^{1}\tilde{\vec{r}}_f^{n_1} - \tilde{\vec{r}}_{CM} \\ {}^{1}\tilde{\theta}_f^{n_1} - \tilde{\theta}_{CM} \end{bmatrix} \tag{5.31}$$

As for the science orbit arrival, a modification to the pseudo-manifold targeting method previously shown in Figure 4.8 is introduced. Since the epoch tied to the commissioning maneuver state is rigid, arrival date flexibility is paramount for allowing a variable time of flight. Following the K-D tree filtration, the selected stable pseudo-manifold becomes the first iteration of the arrival arc. This segment is propagated in negative time for a duration of τ_2, while its initial motion $({}^{3}\tilde{\vec{x}}_o)$ is constrained to be continuous with a state along the orbit $({}^{P}\tilde{\vec{x}}_f)$, determined using τ_1. On the other end, time of flight along the last Phase 2 segment, τ_3, is targeted such that the positions and epochs of ${}^{3}\tilde{\vec{x}}_f$ and ${}^{2}\tilde{\vec{x}}_f^{n_2}$ align. In doing so, the opportunity for a third maneuver for manifold insertion is created. A diagram is provided in Figure 5.18 to highlight the relationship between each of these quantities.

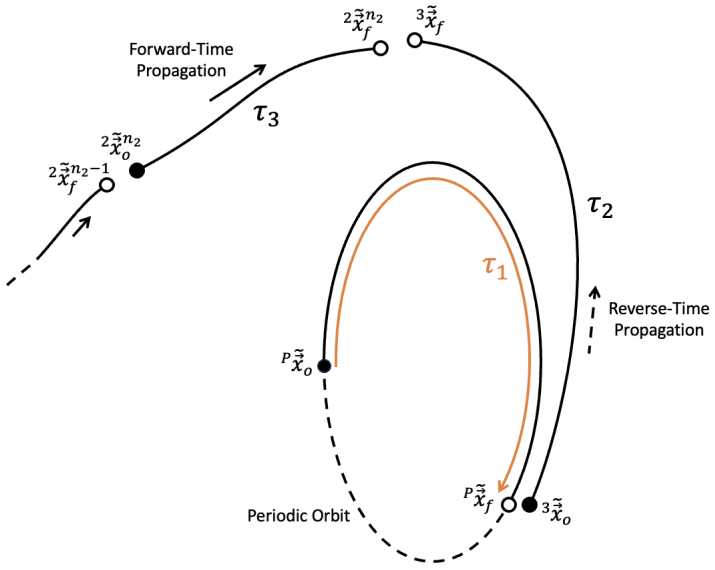

Figure 5.18. Illustration of parameters governing arrival constraints.

In the case of Phase 3, further segmentation is neglected in the investigation, though it may prove beneficial for pseudo-manifolds which closely encounter the Moon. The continuity constraints surrounding arrival into the science orbit are summarized in (5.32), noting that Sun angle is not considered when evaluating the difference between ${}^{P}\tilde{\vec{x}}_f$ and ${}^{3}\tilde{\vec{x}}_o$.

$$\vec{F}_3 = \begin{bmatrix} {}^3\tilde{\vec{r}}_f - {}^2\tilde{\vec{r}}_f^{n_2} \\ {}^3\tilde{\theta}_f - {}^2\tilde{\theta}_f^{n_2} \\ {}^3\tilde{\vec{x}}_o - {}^P\tilde{\vec{x}}_f \end{bmatrix} \tag{5.32}$$

Lastly, the overall cost of the transfer may be constrained as well. An inequality constraint may be defined such that the sum of the flyby and manifold insertion maneuver magnitudes are less than or equal to a maximum desireable value, Δv_{max}. If:

$$\Delta v_2 = \left|\left| {}^2\tilde{\vec{v}}_o^1 - {}^1\tilde{\vec{v}}_o^1 \right|\right| \qquad \Delta v_3 = \left|\left| {}^3\tilde{\vec{v}}_f - {}^2\tilde{\vec{v}}_f^{n_2} \right|\right| \tag{5.33}$$

then:

$$F_{\Delta v} = \Delta v_2^2 + \Delta v_3^2 - \Delta v_{max}^2 + \eta_{\Delta v}^2 \tag{5.34}$$

The initial value of the associated slack variable may be found using (5.35).

$$\eta_{\Delta v} = \sqrt{\Delta v_{max}^2 - \Delta v_2^2 - \Delta v_3^2} \tag{5.35}$$

Equation (5.35) is only used to calculate the initial value of the slack variable prior to targeting.

Since the commissioning maneuver state is defined to place the spacecraft along a direct trajectory to the Moon, the magnitude of the CM is often not the most costly burn. Moreover, during the targeting and continuation process, only minor alterations are made to the flyby state, leading to a Phase 1 trajectory which is highly resilient to change. Should the targeter attempt to significantly alter the velocity departing from the CM state, large deviations may cascade throughout the trajectory and cause divergence. To prevent this, the magnitude of the first maneuver is excluded from the total Δv inequality constraint.

The constraint and free-variable vectors which govern the convergence of an end-to-end lunar transfer in the BCR4BP are defined in (5.36).

$$\vec{F}(\vec{X}_{\mathrm{i}}) = \begin{bmatrix} \vec{F}_1 \\ \vec{F}_2 \\ \vec{F}_3 \\ \vec{F}_{LE} \\ F_{\Delta v} \end{bmatrix} \qquad \vec{X}_{\mathrm{i}} = \begin{bmatrix} {}^1\vec{X} \\ {}^2\vec{X} \\ {}^3\tilde{\vec{x}}_o \\ \tau_1 \\ \tau_2 \\ \tau_3 \\ \eta_{alt} \\ \eta\Delta v \end{bmatrix} \tag{5.36}$$

Where:

$${}^1\vec{X} = \begin{bmatrix} {}^1\tilde{\vec{x}}_o^1 \\ {}^1\tilde{\vec{x}}_o^2 \\ \vdots \\ {}^1\tilde{\vec{x}}_o^{n_1} \end{bmatrix} \qquad {}^2\vec{X} = \begin{bmatrix} {}^2\tilde{\vec{x}}_o^1 \\ {}^2\tilde{\vec{x}}_o^2 \\ \vdots \\ {}^2\tilde{\vec{x}}_o^{n_2} \end{bmatrix} \tag{5.37}$$

The corrections algorithm is often most significantly challenged by the imposed Δv constraint. For ease of satisfying the continuity constraints, the value of Δv_{max} is set relatively high (for example, 1.5 km/s). After the convergence of an end-to-end trajectory, a family of solutions is created via natural parameter continuation along a descending value of Δv_{max}. Individual trajectories showcased in the following sections are the family member at the end of the continuation scheme.

5.4.3 Halo Orbit Insertion

Consider the transfer of a secondary payload from an arbitrary CM state to the L_2 9:2 synodic-resonant Halo orbit. The framework outlined in Section 5.4.2 may be applied to a set of pseudo-manifolds generated for the designated orbit, where a visualization of this Phase 3 candidate pool is provided in Figure 3.22. Since such a science orbit is relatively stable, the implementation of pseudo-manifolds allows for an expedited arrival, further reducing

sensitivity in the corrections algorithm. To demonstrate versatility of the framework, three sample CM states are provided with varying epochs in Table 5.1.

Table 5.1. Commissioning maneuver states sampled for transfers to the L_2 9:2 NRHO

CM Date	$\tilde{x}$ (ND)	$\tilde{y}$ (ND)	$\tilde{z}$ (ND)	$\dot{\tilde{x}}$ (ND)	$\dot{\tilde{y}}$ (ND)	$\dot{\tilde{z}}$ (ND)	$\tilde{\theta}$ (rad)
October 15, 2024	0.280	0.366	−0.009	0.994	1.116	−0.021	3.709
August 02, 2023	0.489	0.252	0.009	1.237	0.353	0.016	2.671
June 07, 2023	0.437	0.307	0.009	1.161	0.546	0.018	1.801

As a starting example, consider the October transfer, where the baseline CM state as provided in Table 5.1 is propagated until perilune, from which the lunar encounter epoch, $||\vec{v}_\infty^-||$, and reference Phase 1 trajectory may be collected. Independently, the candidate Phase 3 arrival trajectories are produced using by generating various stable pseudo-manifolds from the 9:2 NRHO. Since the production of the orbital insertion arcs is epoch independent, this process does not need to be repeated for the other CM states. Given the Moon angle of the lunar encounter, initial guesses for Phase 2 trajectories centered about quadrants 2 and 4 are generated by isolating appropriate sections of the γ surface. The K-D tree algorithm is then applied to determine the best-aligned Phase 2 and 3 candidates. The flyby trajectory is first estimated using the B-Plane formulation and corrected using the priming algorithm. Lastly, the arcs for each phase are then applied to the corrections algorithm as detailed in Section 5.4.2, then continued in total cost constraint (Δv_{max}) to produce the family of lunar transfers shown in Figure 5.19.

A notable aspect of this lunar transfer family is the visible re-direction from Phases 2 to 3 due to Δv_3. The total cost diminishes along with the inclination of the Phase 2 trajectory, as the spatial component of the third maneuver decreases. A visualization of the maneuver locations with respect to the cheapest member of the family is provided in Figure 5.20, while a more thorough breakdown is provided for the representative transfer of each tested CM state in Table 5.2. The total cost for the transfer shown in Figure 5.20 is 472.11 meters per second, paired with a total time of flight of about 103 days. As seen in Tables 5.2 and 5.3, the majority of this value is dedicated to the manifold insertion, while the flyby maneuver required very little thrust.

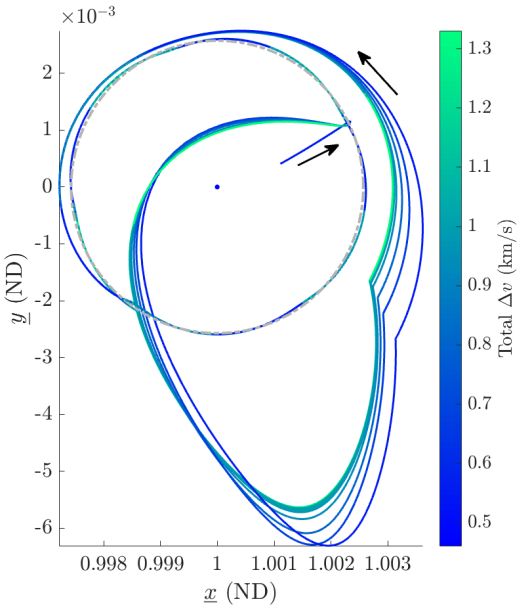

(a) $\hat{\underline{x}}$-$\hat{\underline{y}}$ projection

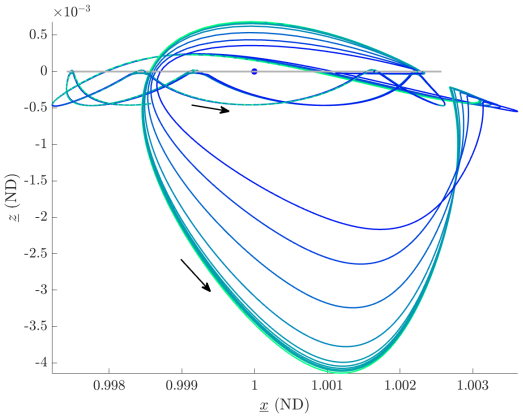

(b) $\hat{\underline{x}}$-$\hat{\underline{z}}$ projection

Figure 5.19. Lunar transfer family for October 15 CM state. Behavior shown in the Sun-B_1 rotating frame.

Previous investigations utilize dispersions of CM magnitudes up to 60 m/s [2], thus the magnitude of Δv_1 on the select October 15 trajectory may exceed mission preferences. Despite this, gradually reproducing the same effect with low-thrust may likely reduce the Phase 1 costs, making the commissioning burn feasible. Alternatively, the cheapest transfer in the family generated for the August CM state reduces the magnitude of Δv_1 by increasing

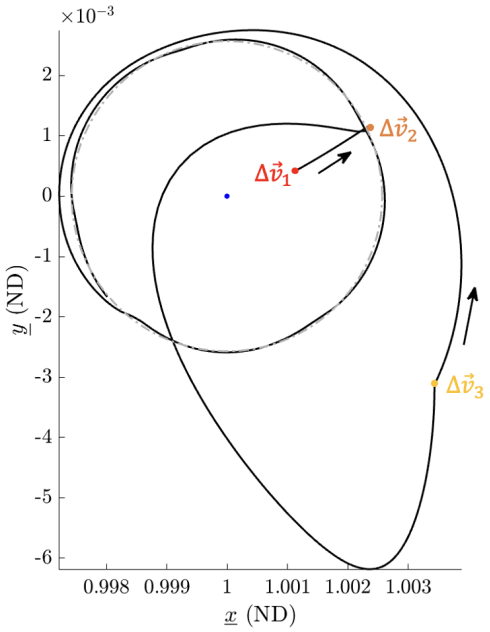

(a) $\hat{\underline{x}}$-$\hat{\underline{y}}$ projection

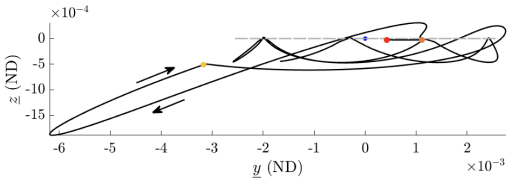

(b) $\hat{\underline{y}}$-$\hat{\underline{z}}$ projection

Figure 5.20. Maneuver locations along cheapest member of the transfer family depicted in Figure 5.19. Motion represented in the Sun-Barycenter frame.

the strength of the flyby maneuver. The resultant trajectory is shown in the Sun-Barycenter frame in Figure 5.21 and the corresponding Earth-Moon behavior in Figure 5.22.
By focusing on the near-Moon motion in the Earth-Moon frame, the insertion into the science orbit may be visualized, as given by Figure 5.23.

While the August transfer is about 4 days shorter than its October counterpart, its total cost is approximately the same, and its flyby altitude is significantly closer, allowing less flexibility for error. On the other hand, the cheapest transfer belongs to the family generated from the June CM state, shown in Figure 5.24. In this case, two lobes about

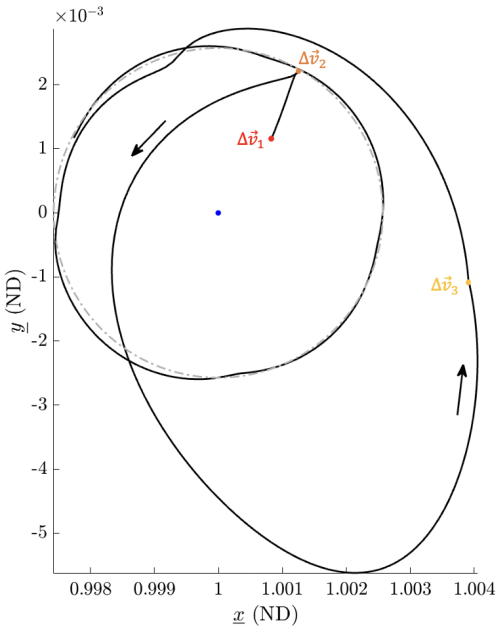

(a) $\hat{x}$-$\hat{y}$ projection

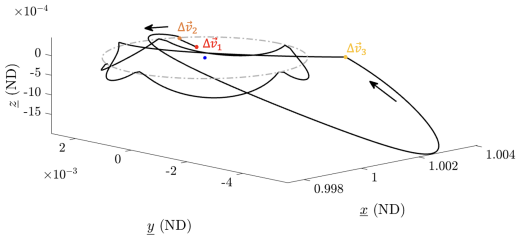

(b) Three-dimensional view

Figure 5.21. Maneuver locations along cheapest member of the transfer family beginning on August 02, 2023. Motion represented in the Sun-Barycenter frame.

the Earth are featured in in the Phase 2 trajectory, better aligning the incoming state to significantly reduce the manifold insertion cost. The evolution of each manuever cost across the family shown in Figure 5.24 is provided in Figure 5.25 as the family is continued from right to left.

The initial guess for the Phase 2 and 3 reference trajectories is determined by the chosen weighting applied to the components of the K-D tree search. As such, the amount of potentially converged trajectories (and families continued from the solution) is equal to the number of combinations possible between the Phase 2 and Phase 3 candidate pools. While

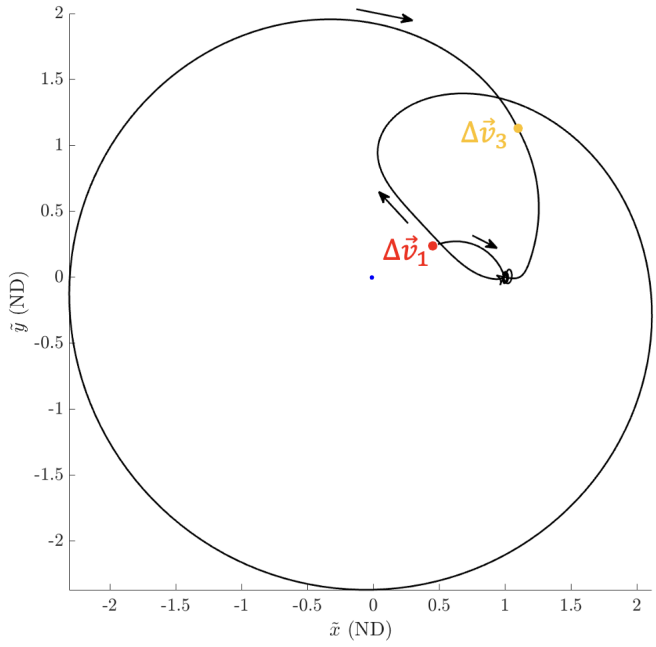

Figure 5.22. Representation of the transfer shown in Figure 5.21(a) in the Earth-Moon frame.

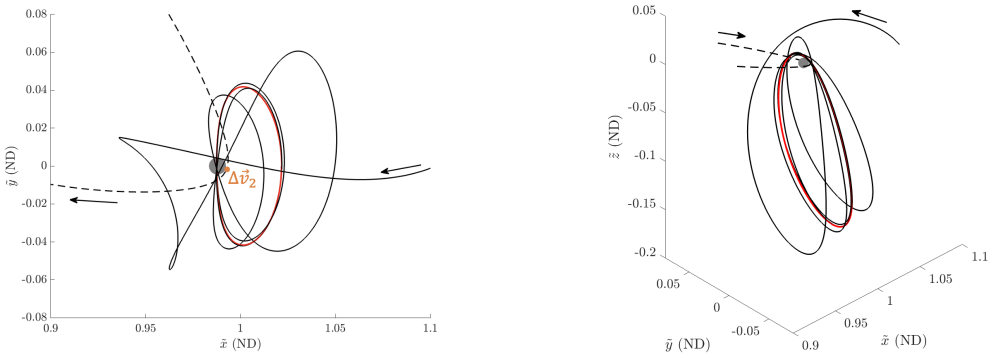

(a) $\tilde{\hat{x}}$-$\tilde{\hat{y}}$ projection (b) Three-dimensional view

Figure 5.23. Insertion into the 9:2 NRHO science orbit (in red). Earlier lunar swing-by distinguished using a dashed curve. Behavior rotated into the Earth-Moon reference frame.

the overall cost for each trajectory may be roughly approximated, the cheapest member of the associated family of solutions is completely unknown a priori. Because of this, there is remarkable potential that for a given solution, a cheaper transfer exists under the same constraints. It is entirely possible for an October transfer to be constructed using a small

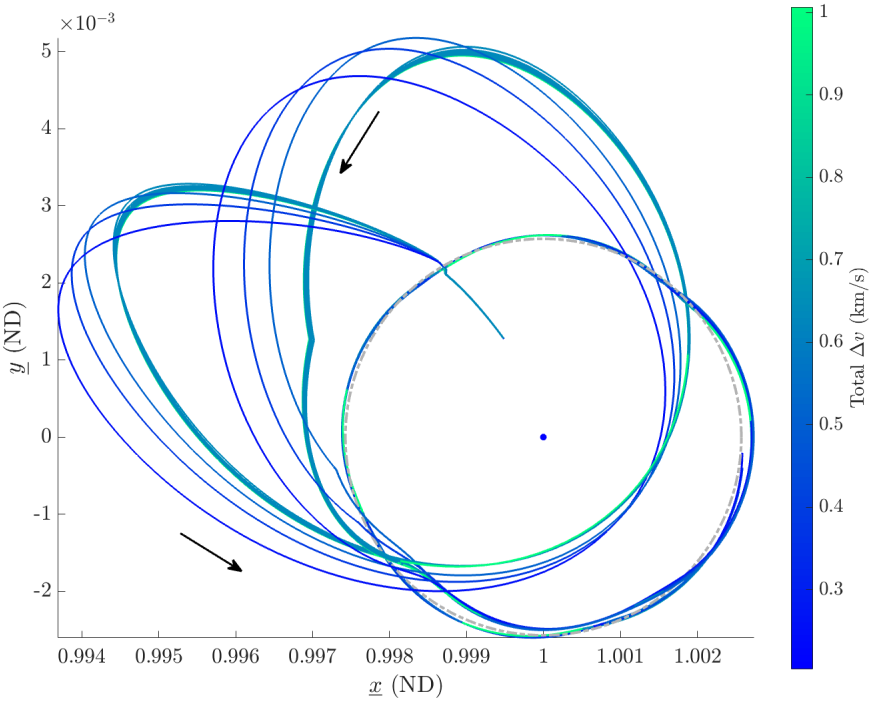

Figure 5.24. Family of solutions stemming from the June 07, 2023 commissioning maneuver. Motion in the Sun-B_1 frame.

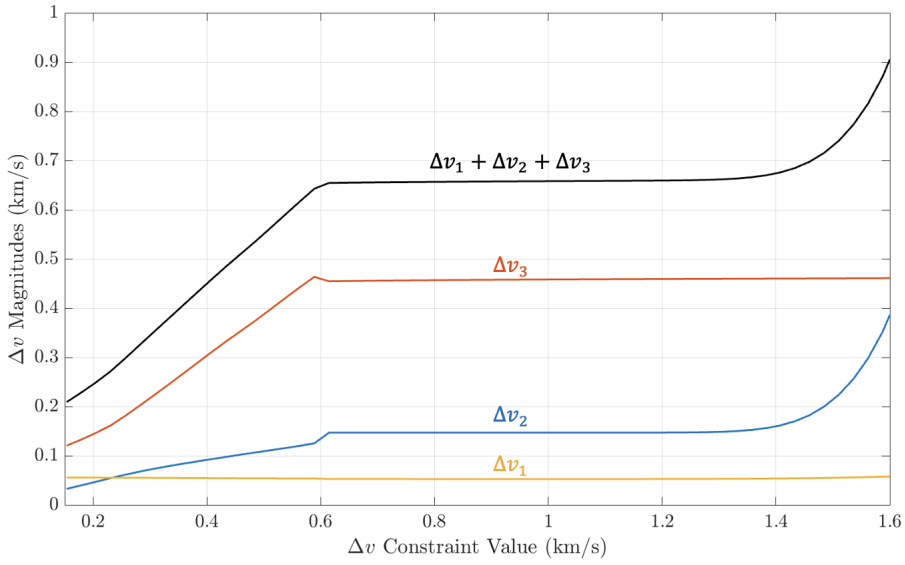

Figure 5.25. Evolution of individual maneuver magnitudes along the cost continuation algorithm.

Table 5.2. Cost breakdown for cheapest members from explored 9:2 NRHO transfer families

CM Date	Δv_1 (m/s)	Δv_2 (m/s)	Δv_3 (m/s)	$\sum_{i=1}^{3} \Delta v_i$ (m/s)
October 15, 2024	88.08	0.20	383.82	472.11
August 02, 2023	37.84	55.02	380.22	473.08
June 07, 2023	54.38	32.02	117.83	204.23

Table 5.3. Additional characteristics of cheapest members from explored 9:2 NRHO transfer families

CM Date	TOF (Days)	Flyby Altitude (km)
October 15, 2024	102.85	2776.66
August 02, 2023	98.88	289.88
June 07, 2023	141.40	3475.06

alteration to the filtration algorithm which is significantly cheaper than the explored June solution, though intuitively location such a solution is non-trivial. Therefore, it is unreasonable for the trajectory designer to be responsible for finding the cheapest possible transfer using this algorithm, rather, their focus should lie on uncovering one that sufficiently satisfies the mission constraints. Transfers to Butterfly orbits of similar Jacobi Constant values may also provide opportunities for re-phasing arrival to a Halo orbit, or even potentially reducing the total cost.

5.4.4 Butterfly Orbit Insertion

At the time of writing, the Butterfly orbit family is an increasingly popular means of transferring into and out of select Halo orbits. Bucchioni et al. investigate re-phasing strategies for the 9:2 NRHO using an intermediate $P2HO_1$ [44]. Waldecker and Howell expand upon this by formulating an autonomous means for determining low-cost transfers between select southern Halo orbits and northern Butterflies of similar JC value [45]. By departing a host orbit, loitering within a separate staging orbit for a designated period, and re-converging onto the original trajectory, a re-phasing transfer may be executed. Using a similar principle, should the cost or epoch for the lunar transfer to a target Halo orbit be

undesirable, an initial insertion into a Butterfly may be a viable option for improving the mission design. Creating the transition arc between the two periodic orbits is beyond the scope of the investigation, as the main focus is relegated to the creation of the initial transfer from the CM state to a specified Butterfly orbit.

As a point of comparison, the August and October CM states are explored with a new mission objective of inserting into a northern Butterfly of the same Jacobi Constant as the 9:2 synodic-resonant NRHO. Choosing a CR3BP northern butterfly with $JC \approx 3.047$, various stable pseudo-manifolds are propagated, populating the group of Phase 3 candidate arcs. Following the remainder of the trajectory design framework outlined in Section 5.4.2, families of varying-cost lunar transfers to the Butterfly staging orbit are determined. First, for the CM on October 15, the collection of transfers resulting from the Δv NPC are shown in Figure 5.26.

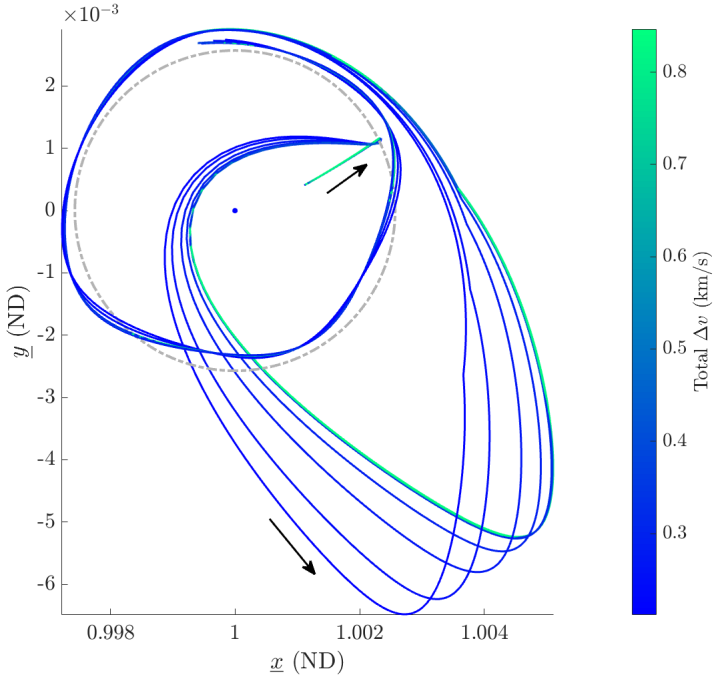

Figure 5.26. Family of transfers from October 15 CM state to a northern Butterfly. Motion in the Sun-B_1 frame.

A portion of the Phase 3 arc which inserts into the Butterfly is viewed in Figure 5.27

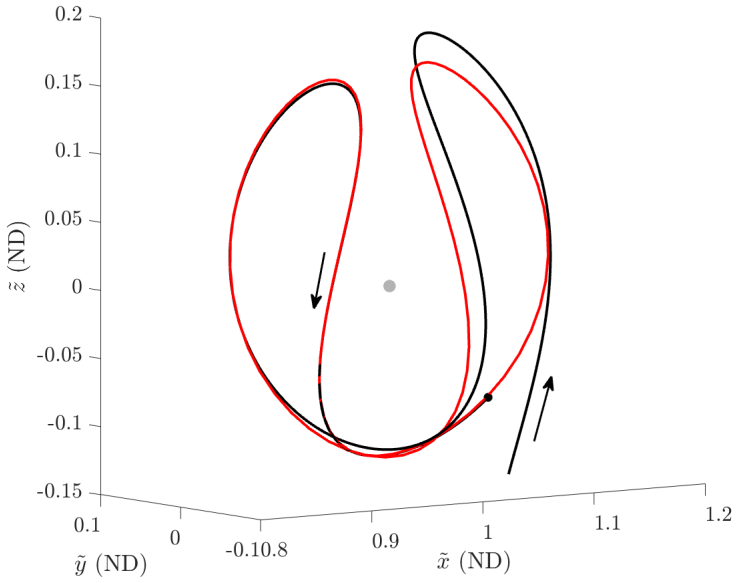

Figure 5.27. Phase 3 arrival arc inserting into science orbit (red). Forward-time motion shown in the Earth-Moon frame.

The cheapest member of the family has a total cost of 212.52 m/s, a value less than half of its NRHO counterpart. According to the results from Bucchioni's investigation, a multitude of transfer options from the Butterfly back to the NRHO are available for less than 100 m/s [44]. This in combination with the used transfer leads to a properly phased insertion into the science orbit for less cost than the direct alternative.

A transfer to the same northern Butterfly using the August 02 CM state is also found using the same strategy. The path resulting from the cost continuation scheme is plotted in the Sun-Barycenter frame as provided in Figure 5.28. Relevant attributes for the cheapest Butterfly transfer arcs from either family are compared in Tables 5.4 and 5.5.

Table 5.4. Cost breakdown for cheapest members of explored Butterfly transfer families

CM Date	Δv_1 (m/s)	Δv_2 (m/s)	Δv_3 (m/s)	$\sum_{i=1}^{3} \Delta v_i$ (m/s)
October 15, 2024	87.52	1.19	123.81	212.52
August 02, 2023	42.96	60.00	349.00	447.96

In this case, the total required cost is comparable to that of its direct NRHO counterpart, being 447.96 meters per second. As a result, the route shown in Figure 5.28 provides a

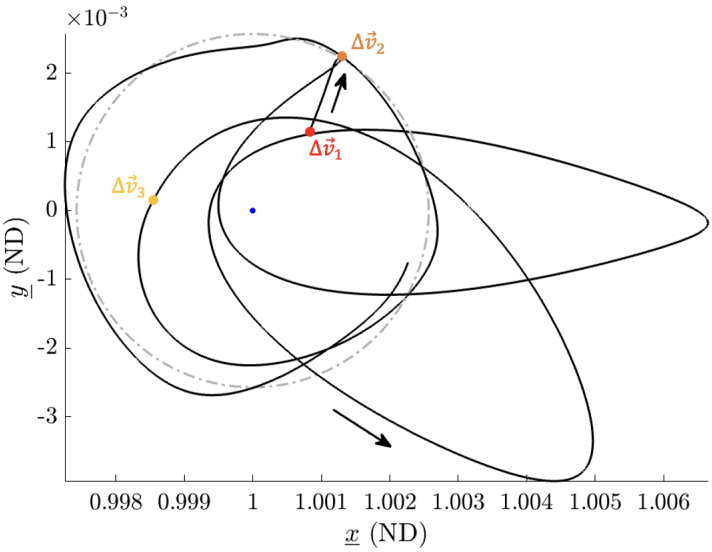

Figure 5.28. Lowest cost transfer from family of solutions generated for August 2 CM state. Motion in Sun-B_1 frame.

Table 5.5. Additional characteristics of cheapest members from explored Butterfly transfer families

CM Date	TOF (Days)	Flyby Altitude (km)
October 15, 2024	104.91	2721.64
August 02, 2023	137.26	725.56

means for traversing from the CM state to an appropriately phased destination NRHO, with possibly little to no additional cost than the direct transfer. Of course, the primary drawback to this scenario would be the increased flight duration introduced by the interaction with the staging orbit.

In both this section and the previous, the families of transfers generated often had significant spatial excursions. Reduction in the magnitude of the pseudo-manifold insertion maneuver often required a decrease in transfer inclination with respect to the Sun-Barycenter plane. Both Halo and Butterfly orbits have ballistic arrival arcs which traverse three-dimensional space, though transfers to a designated planar Lyapunov orbit are explored as well.

5.4.5 Lyapunov Orbit Insertion

Planar science orbits are equally accepted into the design framework, though a significant reduction in arrival arc diversity is to be expected. In this section, transfers to two distinct L_2 Lyapunov orbits are explored alongside two new CM states. The details surrounding either CM state explored are outlined in Table 5.6.

Table 5.6. Commissioning maneuver states sampled for transfers to the L_2 9:2 NRHO

CM Date	$\tilde{x}$ (ND)	$\tilde{y}$ (ND)	$\tilde{z}$ (ND)	$\dot{\tilde{x}}$ (ND)	$\dot{\tilde{y}}$ (ND)	$\dot{\tilde{z}}$ (ND)	$\tilde{\theta}$ (rad)
December 18, 2023	0.378	0.376	0.008	1.055	0.742	0.019	4.827
November 12, 2024	0.345	0.276	0.007	1.224	0.887	0.023	4.521

Consider two separate missions, where the November launch date is to insert into the L_2 Lyapunov of Jacobi Constant value $JC \approx 3.05$, while the December state is set to arrive into the $JC \approx 3.10$ member of the same family. Various stable pseudo-manifolds are propagated for either orbit, populating their respective candidate arrival arc groupings. Following this, the procedure outlined in Section 5.4.2 is then applied to both sets of conditions, where following the Δv cost continuation algorithm, resultant trajectories are provided in Figure 5.29 and Figure 5.30.

The motion shown in either figure is planar and requires a significant amount of thrust to insert into the pseudo-manifold. Despite the lack of spatial component to be mitigated, the transfers do not reach far enough into the center of Quadrants 2 or 4 to sufficiently circularize the downstream motion. For the associated lunar encounter epochs, the majority of Phase 2 outbound legs which venture into the de-energizing quadrants require a significantly inclined passage over the Moon. Consequently, most of the transfers which may have their energy diminished by solar perturbations likely have a non-negligible spatial velocity component to be nullified by Δv_3. On the other hand, the departure options with a near-zero value for β primarily lead to the energizing quadrants, thus intuitively determining a low-cost initial guess is further challenged. A more thorough breakdown of both transfers' characteristics is presented in Tables 5.7 and 5.8.

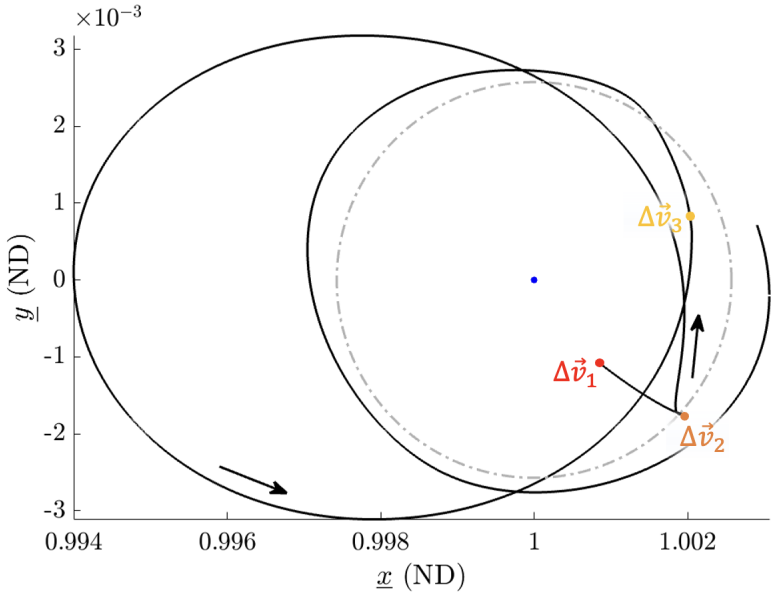

Figure 5.29. Transfer from the December 18 CM state to an L_2 Lyapunov with $JC \approx 3.10$. Motion represented in the Sun-Barycenter frame.

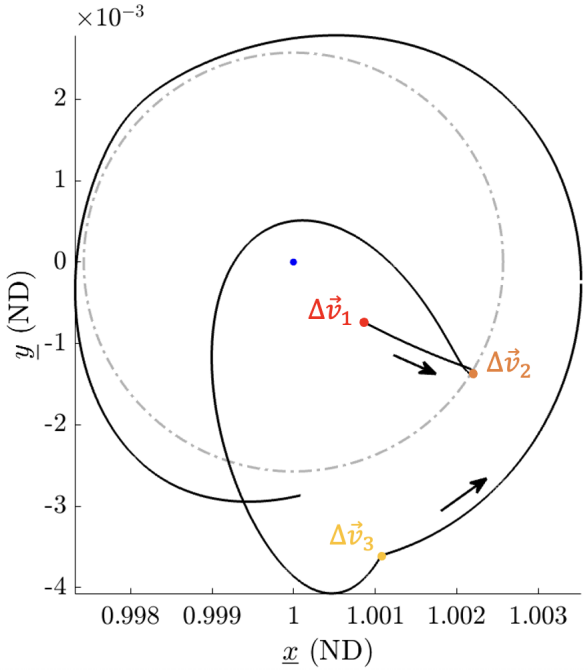

Figure 5.30. Transfer from the November 12 CM state to an L_2 Lyapunov with $JC \approx 3.05$. Motion represented in the Sun-Barycenter frame.

Table 5.7. Maneuver breakdown for cheapest members of explored L_2 Lyapunov transfer families

CM Date	Δv_1 (m/s)	Δv_2 (m/s)	Δv_3 (m/s)	$\sum_{i=1}^{3} \Delta v_i$ (m/s)
December 18, 2023	36.99	138.26	381.57	556.83
November 12, 2024	27.79	6.46	473.54	507.79

Table 5.8. Additional characteristics of cheapest members from explored L_2 Lyapunov transfer families

CM Date	TOF (Days)	Flyby Altitude (km)
December 18, 2023	98.37	1995.65
November 12, 2024	52.77	3877.52

Despite the presented results, there are likely numerous low-cost transfers that exist for either epoch, though the primary challenge lies in uncovering them. A drawback of the presented framework is that the user is allotted little flexibility to intuitively scan for more desireable transfer options. Moreover, the jettison epoch, such as those evaluated in this section, may create an abundance of undesirable candidate trajectories. The modularity of the design framework investigated has the benefit of combining favorable segments into a complete transfer, though it also allows the addition of entirely new Phases. In Section 5.4.4, an intermediate staging orbit may be leveraged to soften necessary costs, provide a staging orbit for re-phasing the arrival into the science orbit, and diversify the catalog of potential transfers. A secondary lunar encounter may be introduced into the framework to provide these same benefits, as well as an opportunity to change the geometry of Phase 2 for potentially negligible cost. Chapter 6 provides a case study to exemplify how the modularity of the presented lunar transfer construction method may adapt to accommodate a secondary flyby. This example seeks exploit the flexibility provided by a subsequent lunar encounter to intuitively design a passage from the December 18 CM state to the assigned destination Lyapunov orbit.

6. CASE STUDY: INCORPORATION OF A SECONDARY LUNAR FLYBY INTO THE LUNAR TRANSFER

In Chapter 4, methods for constructing BLTs are explored for scenarios where the epoch of departure is allowed complete freedom. This is juxtaposed in the following chapter with a lunar transfer scheme constrained by an initial state and time. As a result, trajectory options are created and filtered to determine viable pathways for a secondary payload to insert into a designated science orbit. One conclusion which may be drawn from Chapter 5 is that the candidate pool for Phase 2 is largely affected by the lunar encounter epoch. Moreover, due to the constrained initial CM state and timing, a high degree of inflexibility is exhibited by the Moon angle at the flyby. In Figure 5.8, it is demonstrated that the inclination of lunar passages that lead to distant Quadrant 2/4 apogees evolve as the Moon traverses it's orbit about the Earth. For example, the majority of the points in Figure 5.8(a) correspond to a near-vertical traversal above the Moon, leading to inclined departures. Using the same CM dispersion but evaluated 6 days later, near-planar flybys are abundant, as shown in Figure 5.8(b).

The relationship between viable flyby groupings and epoch indicates that the general inclination of Phase 2 legs outbound to circularizing quadrants is tied to the inflexible jettison date. For dates like that explored in Figure 5.8(a), the majority of outbound lunar transfers are highly inclined, each leading to costly insertions into the arrival pseudo-manifold. While viable near-planar transfers likely exist for such a scenario, their determination is non-trivial. In response to this, a secondary lunar passage may be leveraged at a more favorable Moon angle in order to diversify the pool of near-planar Phase 2 candidates.

6.1 Transfer Construction Overview

The modularity of the lunar transfer design framework introduced in Chapter 5 allows for the inclusion of additional segments and events. By appending a second flyby, the previous design strategy for Phase 2 is effectively repeated. To accommodate this, the terminology surrounding a lunar transfer with two Moon passages is altered slightly.

- **Phase 1:** Arc from CM to outside Σ_{1a} intersection.
- **Phase 2a:** Path outbound from Σ_{1a}, terminating at the encounter with Σ_{1b}.
- **Phase 2b:** Transfer leg departing Σ_{1b}, leading to the interaction with Σ_2.
- **Phase 3:** Arrival segment leading into science orbit from Σ_2 entrance.

To correspond with the separation of Phase 2 into sections "a" and "b", the first interface Σ_1 is provided an additional subscript "a" for the first lunar encounter, and "b" for the second. A visualization of the phases for a double-flyby transfer is provided in Figure 6.1.

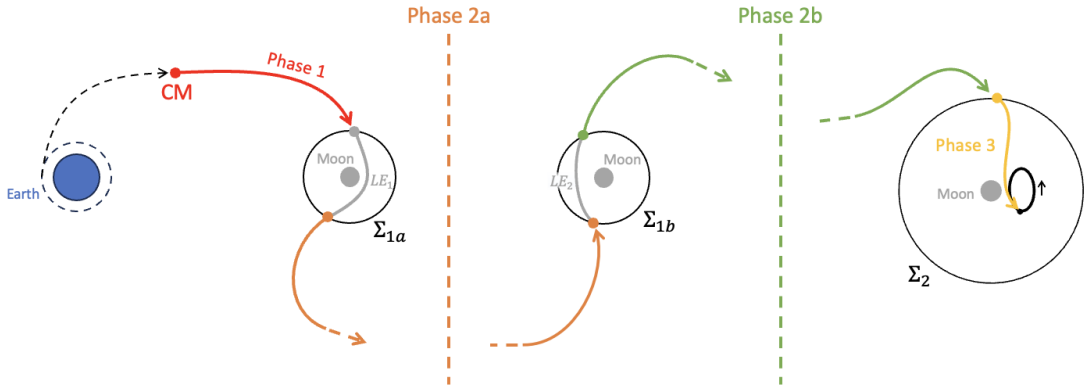

Figure 6.1. Relationship between individual phases and boundaries for a two flyby lunar transfer.

To bridge together the first two sections, as well as both legs of Phase 2, hyperbolic lunar passages are constructed. The first lunar encounter (between Phases 1 and 2a) is denoted LE_1, occurring within Σ_{1a}, while the second flyby (LE_2) seeks to merge Phases 2a and 2b together. The construction of interfaces Σ_{1a} and Σ_{1b} mirrors that done for Σ_1 in the previous chapter.

Particular consideration is paid toward the selection of the epoch associated with LE_2. The relationship between the relative argument of apoapsis, γ and the Moon departure characteristics α, β and $||\vec{v}_\infty^+||$ is leveraged to provide insight toward this decision. Moreover, narrowing the scope of this initial guess surface allows for a focus on Phase 2b transfer arcs

that remain relatively planar, allowing for greater alignment between the end of Phase 2 and the beginning of the science orbit arrival arc.

6.2 Trajectory Planarization

The term "planarization" refers to the event where a highly-inclined orbit is then diverted to motion which travels nearly parallel to the x-y plane. While a maneuver may accomplish this, a course-diverting lunar passage may be leveraged to provide a similar effect. Moreover, the flyby may be used to alter the spacecraft's energy, should this be necessary. In this investigation, the relative two-body γ function models motion outbound from a lunar encounter in terms of in-plane and out-of-plane angles, α and β respectively. As such, there is a direct connection between the value of β and the inclination of the ascending leg of the transfer, where planar pathways are found by evaluating the function at $\beta = 0$. This property is the means by which planarization is modelled in the investigation.

Consider the scenario established in Section 6.1, where a lunar transfer is to be designed for a secondary payload, leading from its assigned CM state to an L_2 Lyapunov with $JC \approx 3.10$. As LE_2 establishes the arrival behavior, the location of its apogee is crucial. Since this motion is desired to be near-planar, the γ surface may be limited to β values closely surrounding nill. For $\beta = 0$, the γ surface is reduced to a curve of non-inclined initial conditions. These initial conditions are not the only means for determining planar transfers, as continuation may be leveraged to flatten a spatial arc. Because of this, the LE_2 departure leg search is diversified by incorporating neighboring out-of-plane angle values. In the investigation, the range of out-of-plane angles values tested is limited to $[-10, 10]$ degrees, though the particular limits are arbitrarily chosen. These surfaces are then evaluated for differing values of $||\vec{v}_\infty^+||$ as shown in Figure 6.2, noting that the incident motion to the second lunar encounter has greater variation in speed. The curves associated with $||\vec{v}_\infty^+|| = 1.0\ km/s$ span the majority of γ angles present for higher departure speeds, thus it is chosen as the benchmark value for the following analysis.

Following the choice of $||\vec{v}_\infty^+|| = 1.0\ km/s$ as the speed governing the reference γ surface, the ranges of the relative argument of apoapsis values tied to the isolated curves may be

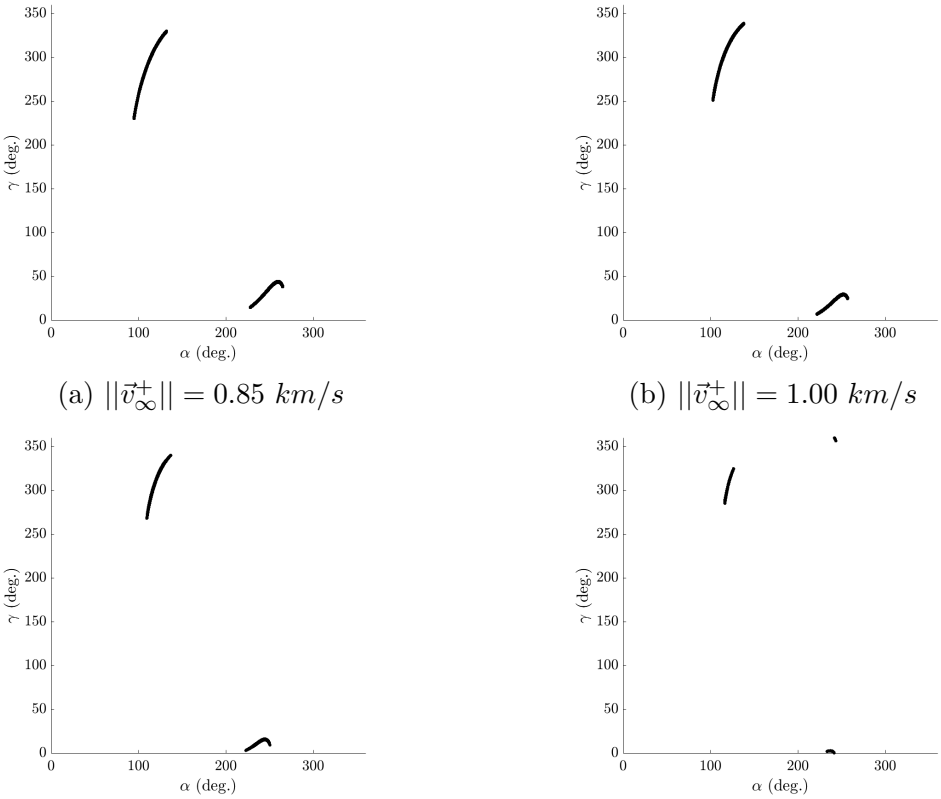

(a) $||\vec{v}_\infty^+|| = 0.85\ km/s$ (b) $||\vec{v}_\infty^+|| = 1.00\ km/s$

(c) $||\vec{v}_\infty^+|| = 1.15\ km/s$ (d) $||\vec{v}_\infty^+|| = 1.30\ km/s$

Figure 6.2. Portions of γ surface limited to $\beta = [-10, 10]$ degrees, evaluated at differing values of $||\vec{v}_\infty^+||$.

examined. In the case of the reference plot given in Figure 6.2(b), there exist two distinct curves, meaning that there are two sections of Moon angles which may provide near-planar trajectories that satisfy a selected ω_a value. The γ values bounding these curves may be represented as two distinct groups, R_1 and R_2, where in the case of $||\vec{v}_\infty^+|| = 1.0\ km/s$:

$$R_1 \approx [251, 343] \text{ degrees}$$

$$R_2 \approx [6, 38] \text{ degrees}$$

A visualization of the boundaries is provided by Figure 6.3. While effective lunar transfers feature a variety of ω_a values, they are often centered about the centerlines of either Quadrants 2 or 4, especially in the case of planar motion. As such, desired arguments of apoapsis are assigned values of ${}^2\omega_a = 135$ degrees, and ${}^4\omega_a = 315$ degrees, where the left superscript

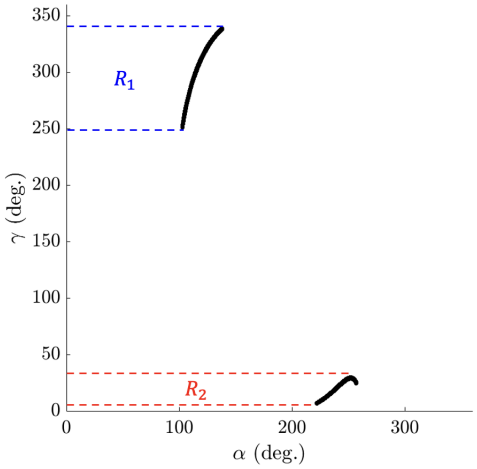

Figure 6.3. Relationship between γ and R_1, R_2 groupings visualized.

indicates the corresponding quadrant. First consider transfers which seek utilize a planar arc outbound from the secondary flyby to have an apogee near ${}^2\omega_a$. The ranges R_1 and R_2 host the Moon angles for such a secondary flyby are most likely accomplish this goal. For example, R_2 states that the flyby should occur at a Moon angle 6 to 38 degrees prior (or clockwise) to ${}^2\omega_a$, corresponding to a Moon angle range of $\underline{\theta} = [97, 129]$ degrees. The other set of Moon angles to accomplish the same goal are between $\underline{\theta} = [152, 244]$ degrees, according to R_1. These groupings may be visualized by the orange arcs in Figure 6.4, while the ranges for ${}^4\omega_a$ may be calculated in the same manner, shown in green.

To summarize, the chart shown in Figure 6.4 maps the Moon angles where the second lunar encounter would best occur to produce a favorable near-planar transfer. In contrast to LE_1 which is highly constrained due to the CM epoch, the second lunar encounter is free to occur anywhere within the highlighted portions of Figure 6.4, introducing significant flexibility for choosing LE_2. The following section exploits this by introducing a reference arc continuation algorithm which allows the location of the second lunar encounter to vary.

6.3 Phase 2 Reference Trajectory

As shown in Figure 6.1, Phase 2 is sub-divided into sections "a" and "b" by a secondary lunar flyby. While the CM state strictly governs the epoch of the first lunar flyby, the second

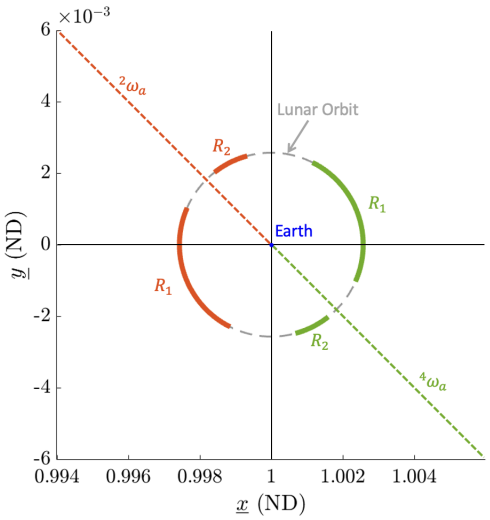

Figure 6.4. Ranges of Moon angles most likely to provide planar transfers to apogees at ${}^{2}\omega_a$ (orange) and ${}^{4}\omega_a$ (green). Plotted in the Sun-B_1 frame.

may occur anywhere. Further analysis leveraging the Earth relative two-body problem refines this Moon encounter to designated regions of Moon angles, though any flyby within these windows has the potential to produce a viable transfer. A line search may be conducted by propagating a Phase 2 dispersion similar to that done in Section 5.2.2 at various $\underline{\theta}$ values, though the approach is extremely computationally expensive. Instead, a single Moon angle may be selected within the ranges designated in Figure 6.4, then the epoch flexibility of LE_2 may be leveraged in a corrections algorithm to refine the Phase 2 candidate trajectory. This process may be divided into two main steps, the first generates the Phase 2b leg using the γ surface applied to the selected Moon angle, then lowers the manifold insertion cost using continuation. The second pairs the appropriate Phase 2a leg that connects the two flybys, then employs differential corrections to lower the associated costs.

6.3.1 Phase 2b Leg Generation & Corrections

Consider the regions of $\underline{\theta}$ values shown in Figure 6.4. As noted before, lunar encounters anywhere within these highlighted sections are viable for generating transfers, thus discerning the optimal location is non-trivial. Rather, a single Moon angle for LE_2 is chosen arbitrarily within the highlighted sections, then corrections are applied while allowing the associated

encounter $\underline{\theta}$ to vary. For this case study, the sampled epoch is the angle which lies in the middle of the orange R_1 section shown in Figure 6.4, or a Moon angle of $\underline{\theta} \approx 200$ degrees. Recall the particular value of the initial Moon angle is of lesser importance, as it is later inserted into a corrections algorithm. Following the selection of the epoch for LE_2, candidate Phase 2b trajectories may be generated by using the same procedure detailed in Section 5.2.2. As a point of note, since Lunar encounters within either R_1 set shown in Figure 6.4 are in front of their respective target apogee locations, passages within the Earth-Moon region are expected.

Following the generation of Phase 2b candidate segments, the ending states are compared with the arrival arcs at Σ_2 and filtered using a K-D tree algorithm, as detailed in Section 5.1.2. Doing so creates the initial guess for the second half of Phase 2, a trajectory which may be isolated and corrected to allow for a cheaper insertion into the pseudo-manifold. To construct such a targeter, first consider the conditions necessary to construct the free-variable vector. Effectively, the entire Phase 2b arc is allowed to change in order to conform to Phase 3, so long as it begins with a lunar encounter and its ending point is appropriately phased. This means that the initial departure speed, direction and epoch are allowed to vary, as well as the time of flight. The investigation uses departure angles and speed to govern the beginning motion, though alternative approaches are also valid. The corrections algorithm is constrained by the ending position and epoch being coincident with one of the Phase 3 arrival states at Σ_2. Moreover, a maneuver magnitude constraint may be imposed and iteratively decreased to more closely approach full-state continuity. If ${}^{2b}\underline{\vec{r}}_f$ is the ending position of the Phase 2 arc in the Sun-B_1 frame, ${}^{3}\underline{\vec{r}}_f$ is the Phase 3 state at Σ_2 in the same frame, ${}^{2b}\underline{\vec{v}}_f$ and ${}^{3}\underline{\vec{v}}_f$ are their respective velocities, and Δv_{max} is the maneuver magnitude constraint, then:

$$\vec{F}(\vec{X}_{\text{i}}) = \begin{bmatrix} {}^{2b}\underline{\vec{r}}_f - {}^{3}\underline{\vec{r}}_f \\ {}^{2b}\underline{\theta}_f - {}^{3}\underline{\theta}_f \\ ||{}^{2b}\underline{\vec{v}}_f - {}^{3}\underline{\vec{v}}_f||^2 - \Delta v_{max}^2 \end{bmatrix} \qquad \vec{X}_{\text{i}} = \begin{bmatrix} \alpha_{2b} \\ \beta_{2b} \\ ||\vec{v}_{\infty}^{+}||_{2b} \\ {}^{2b}\underline{\theta}_o \\ T_{2b} \end{bmatrix} \tag{6.1}$$

Where the first three variables within $\vec{X}_{\text{i}}$ are departure states from LE_2, ${}^{2b}\underline{\theta}_o$ is the Moon angle of LE_2, and T_{2b} is the time of flight for the trajectory until its encounter with Phase 3. It may be noted that α_{2b}, β_{2b} and $||\vec{v}_{\infty}^{+}||_{2b}$ all govern the departing behavior as viewed in the Earth-Moon frame, though the reference trajectory is propagated in the Sun-Barycenter CR3BP. As such, the derivatives must account for the frame change, exemplified for each component by the chain rule expansions given in Equation (6.2).

$$\begin{aligned}
\frac{\partial \underline{\vec{x}}_f}{\partial \alpha} &= \frac{\partial \underline{\vec{x}}_f}{\partial \underline{\vec{v}}_{\text{i}}} \cdot \frac{\partial \underline{\vec{v}}_{\text{i}}}{\partial \tilde{\vec{v}}_{\text{i}}} \cdot \frac{\partial \tilde{\vec{v}}_{\text{i}}}{\partial \alpha} \\
\frac{\partial \underline{\vec{x}}_f}{\partial \beta} &= \frac{\partial \underline{\vec{x}}_f}{\partial \underline{\vec{v}}_{\text{i}}} \cdot \frac{\partial \underline{\vec{v}}_{\text{i}}}{\partial \tilde{\vec{v}}_{\text{i}}} \cdot \frac{\partial \tilde{\vec{v}}_{\text{i}}}{\partial \beta} \\
\frac{\partial \underline{\vec{x}}_f}{\partial ||\vec{v}_{\infty}^{+}||} &= \frac{\partial \underline{\vec{x}}_f}{\partial \underline{\vec{v}}_{\text{i}}} \cdot \frac{\partial \underline{\vec{v}}_{\text{i}}}{\partial \tilde{\vec{v}}_{\text{i}}} \cdot \frac{\partial \tilde{\vec{v}}_{\text{i}}}{\partial ||\vec{v}_{\infty}^{+}||}
\end{aligned} \tag{6.2}$$

Where for an STM of the Sun-B_1 CR3BP trajectory, Φ_v may be found by isolating the last three columns of its host matrix Φ. The equations in Equation (6.2) may be equivalently expressed as shown in Equation (6.3).

$$\begin{aligned}
\frac{\partial\ {}^{2b}\underline{\vec{x}}_f}{\partial \alpha_{2b}} &= q||\vec{v}_{\infty}^{+}||_{2b} \cdot \Phi_v \cdot C \cdot \begin{bmatrix} -\cos\alpha_{2b}\cos\beta_{2b} & -\sin\alpha_{2b}\cos\beta_{2b} & 0 \end{bmatrix}^T \\
\frac{\partial\ {}^{2b}\underline{\vec{x}}_f}{\partial \beta_{2b}} &= q||\vec{v}_{\infty}^{+}||_{2b} \cdot \Phi_v \cdot C \cdot \begin{bmatrix} \sin\alpha_{2b}\sin\beta_{2b} & -\cos\alpha_{2b}\sin\beta_{2b} & \cos\beta_{2b} \end{bmatrix}^T \\
\frac{\partial\ {}^{2b}\underline{\vec{x}}_f}{\partial ||\vec{v}_{\infty}^{+}||_{2b}} &= q \cdot \Phi_v \cdot C \cdot \begin{bmatrix} -\sin\alpha_{2b}\cos\beta_{2b} & \cos\alpha_{2b}\cos\beta_{2b} & \sin\beta_{2b} \end{bmatrix}^T
\end{aligned} \tag{6.3}$$

Where for the Moon angle associated with the end of the Phase 2b arc, ${}^{2b}\underline{\theta}_f$:

$$C = \begin{bmatrix} \cos {}^{2b}\underline{\theta}_f & -\sin {}^{2b}\underline{\theta}_f & 0 \\ \sin {}^{2b}\underline{\theta}_f & \cos {}^{2b}\underline{\theta}_f & 0 \\ 0 & 0 & 1 \end{bmatrix} \tag{6.4}$$

$$q = \sqrt{\frac{a_s}{(\tilde{m}_s + 1)}} \tag{6.5}$$

The first and second time-derivatives for the rotation matrix, C may be leveraged for determining the change in the six-dimensional state ${}^{2b}\underline{\vec{x}}_f$ resulting from alterations to ${}^{2b}\underline{\theta}_o$.

$$\frac{\partial\ {}^{2b}\vec{\underline{x}}_f}{\partial\ {}^{2b}\underline{\theta}_o} = \begin{bmatrix} \frac{\tilde{\ell}^*}{\underline{\ell}^*}\dot{C}\cdot {}^3\vec{\underline{r}}_f \\ \frac{q(n-1)}{n}\ddot{C}\cdot {}^3\vec{\underline{r}}_f + \dot{C}\cdot {}^3\vec{\underline{v}}_f \end{bmatrix} \tag{6.6}$$

While other equivalent variables may be used in $\vec{X}_{\text{i}}$, the benefit to the implementation of the departure angles and speed is in the case of isolating solution families. For instance, departing states may be limited to planar motion by fixing $\beta_{2b} = 0$, or families where the speed at which the spacecraft leaves the Moon's vicinity may be isolated by removing $||\vec{v}_\infty^+||_{2b}$ from $\vec{X}_{\text{i}}$. In this case, however, each variable is maintained in the expression for increased flexibility. By employing the targeting algorithm and incrementally decreasing the value of Δv_{max}, a family of Phase 2b reference trajectories may be spawned from a single initial guess, as shown in Figure 6.5. The more costly members of the family are shown to have significantly inclined motion in Figure 6.5(b) as a result of their passages by the Earth.

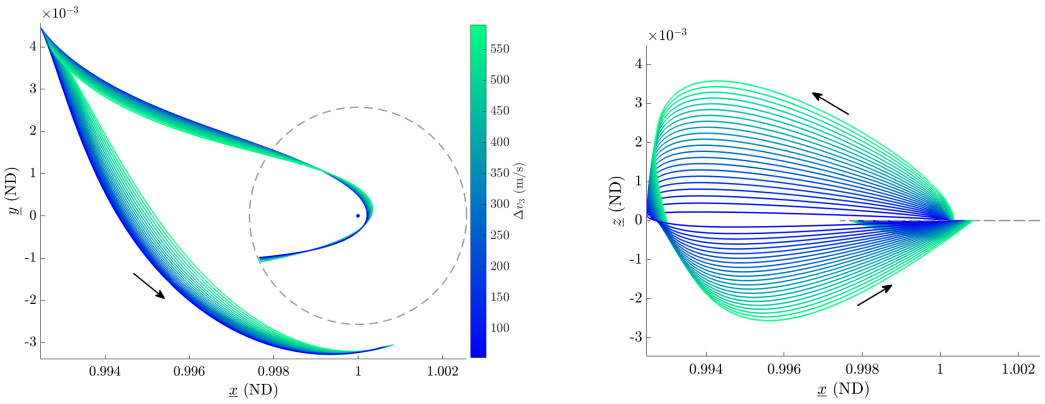

(a) $\hat{\underline{x}}$-$\hat{\underline{y}}$ projection (b) $\hat{\underline{x}}$-$\hat{\underline{z}}$ projection

Figure 6.5. Family of Phase 2b Sun-B_1 CR3BP reference arcs continued along pseudo-manifold insertion cost, Δv_3. Motion shown in the Sun-Barycenter frame. Lunar orbit in grey.

The Earth may be beneficial in diverting the spacecraft to an appropriate quadrant, though relatively close perigees are generally avoided as they pose an impact risk, as well as further introduce numerical sensitivity to the BCR4BP targeting algorithm. Aside from the insertion cost being reduced for the reference trajectory, the Phase 2 and 3 ending states

have continuity in four of the seven state components, reducing the stress imposed on the BCR4BP targeter.

With a candidate Phase 2b reference arc determined, an appropriate Phase 2a leg must be selected to connect the two lunar encounters. Moreover, a corrections strategy similar to that explored in this section may be implemented to refine differences between the Phase 2 reference arc segments.

6.3.2 Continuous Phase 2 Reference Trajectory Design

To find the Phase 2a arc which links the first flyby with the value of ${}^{2b}\underline{\theta}_o$ found from the continuation process in Section 6.3.1, various trajectories may be propagated from the location of LE_1 in the Sun-B_1 CR3BP. The difference between this procedure and that outlined in Section 5.2.2 is that the initial guess surface γ does not need to be limited to specific values for the relative argument of apoapsis. This is because the quadrant in which the Phase 2a's apogee lies is of little concern, as the primary objective of this leg is to connect the two flybys. By removing any limits (or Γ regions) imposed onto the initial guess surface, a large variety of phasing arcs may be examined. In the case of this search, discrete [α,β] pairs with solutions on the γ surface are propagated in the Sun-Barycenter CR3BP until an encounter with Σ_{1b}. While the Moon angle associated with Σ_{1b} is determined using the procedure from the previous section, storing each interface encounter at various locations aids in discerning alternative Phase 2 reference trajectories. Results which encounter Σ_{1b} at the value of $\underline{\theta}$ nearest that determined for ${}^{2b}\underline{\theta}_o$ make up the primary candidate arcs for Phase 2a. Additional filtration may then be applied to remove options from the Phase 2a set which exhibit unfavorable characteristics, including close or multiple passages by the Earth as well as significant differences between the arriving and departing LE_2 speeds, $||\vec{v}_\infty^-||_{2a}$ and $||\vec{v}_\infty^+||_{2b}$ respectively. This magnitude difference is measured in the Earth-Moon frame, and generally correlates to the burn necessary for transitioning between the two sections of Phase 2.

Once the candidate Phase 2a reference arc is selected, a multiple-shooting algorithm may be employed to create a continuous trajectory in the Sun-Barycenter CR3BP. To this end, initial conditions departing LE_1 and LE_2 are examined, constraining the epoch associated

with the first flyby. Continuity between the position and epoch at the end of Phase 2a and the beginning of 2b is enforced, along with that between the end of Phase 2b and the pseudo-manifold insertion state at Σ_2. The targeting requirements and free-variables are summarized in expression (6.7), where the times of flight for Phases 2a and 2b are denoted T_{2a} and T_{2b} respectively.

$$\vec{F}(\vec{X}_{\mathrm{i}}) = \begin{bmatrix} {}^{2a}\underline{\vec{r}}_f - {}^{2b}\underline{\vec{r}}_o \\ {}^{2a}\underline{\theta}_f - {}^{2b}\underline{\theta}_o \\ {}^{2b}\underline{\vec{r}}_f - {}^{3}\underline{\vec{r}}_f \\ {}^{2b}\underline{\theta}_f - {}^{3}\underline{\theta}_f \end{bmatrix} \qquad \vec{X}_{\mathrm{i}} = \begin{bmatrix} \alpha_{2a} \\ \beta_{2a} \\ ||\vec{v}_\infty^+||_{2a} \\ T_{2a} \\ \alpha_{2b} \\ \beta_{2b} \\ ||\vec{v}_\infty^+||_{2b} \\ T_{2b} \\ {}^{2b}\underline{\theta}_o \end{bmatrix} \tag{6.7}$$

Optionally, the Earth-Moon speed difference, $||\vec{v}_\infty^-||_{2a} - ||\vec{v}_\infty^+||_{2b}$ may be appended to the constraint vector and governed by a threshold value, though this is neglected for the case study. Using the described targeter, a continuous reference path for Phase 2 is generated, as shown in Figure 6.6. The first lobe's excursion into the third quadrant increases its eccentricity with respect to the Earth, having a near-perpendicular approach to the Moon's orbit. Moreover, the inclination change between Phases 2a and 2b is a desired byproduct of the secondary flyby. The same paths may be represented in the Earth-Moon frame, as plotted in Figure 6.7.

As is the case with the targeting algorithm shown in Section 6.3.1, the corrections provide a trajectory which is continuous with the Phase 3 arrival position and epoch. Due to the presence of two lunar passages, the BCR4BP corrections process becomes dynamically and numerically sensitive, thus minimization of initial error is crucial for ensuring convergence.

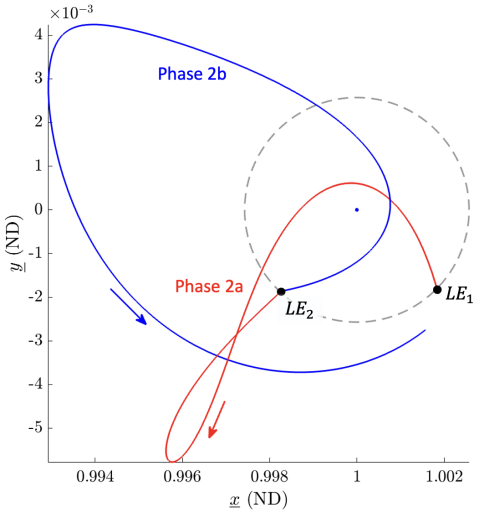

(a) $\hat{\underline{x}}$-$\hat{\underline{y}}$ projection

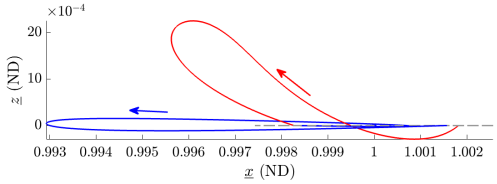

(b) $\hat{\underline{x}}$-$\hat{\underline{z}}$ projection

Figure 6.6. Converged CR3BP reference arcs for Phase 2. Behavior shown in the Sun-Barycenter frame. Lunar orbit in grey. Blue arc ends at pseudo-manifold insertion location.

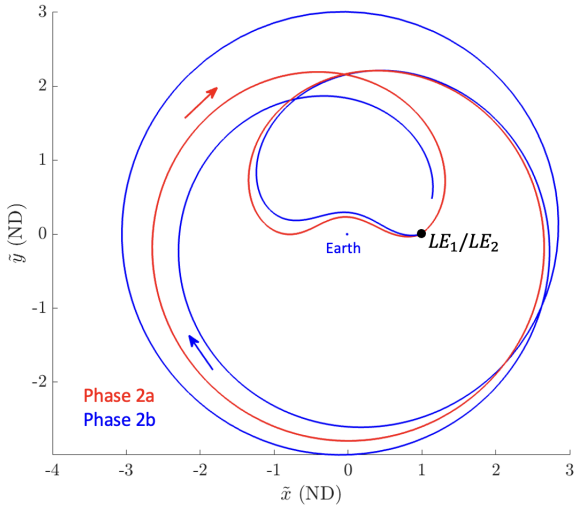

Figure 6.7. Trajectories for Phases 2a and 2b represented in the Earth-Moon rotating frame. Blue arc ends at pseudo-manifold insertion location.

6.4 Construction of a Double-Flyby Lunar Transfer in the BCR4BP

Due to the presence of two close lunar passages, the differential corrections algorithm is particularly sensitive, thus many measures are taken to prevent divergence. Much like in Chapter 5, flyby priming is used to better match the ends of the hyperbolic flybys, generated using B-Plane targeting, to their desired states. Following this, the targeter is constructed. The requirements for the first Phase are the same as in the case of the single flyby transfer, with the segmentation process summarized by Figure 5.17 being applied to the Phase 1 reference trajectory, propagated in reverse-time. The Phase 3 arrival arc is also propagated in reverse time as a single trajectory, initially informed by the pseudo-manifold selected from the K-D tree algorithm. To add flexibility to the corrections process, the arrival state may be varied along the destination orbit by time τ_1, just as done for the trajectories in Chapter 5. The primary difference for the double-flyby trajectory is in the constraints governing the intermediate transfer stage, Phase 2a.

Sensitivity may be reduced by dividing Phase 2a into two portions at its apogee, propagating the earlier section in forward time, while the latter may be evaluated in backward time, both away from their respective Moon encounters. For clarity, segments within the forward-propagated portion of Phase 2a are denoted "$2f$" while those in reverse-time are marked with "$2r$". As an example, the Earth-Moon ending state of the third segment in the reverse-time portion of Phase 2a is represented as ${}^{2r}\tilde{\vec{x}}_f^3$. Phase 2b, much like Phase 2 from the single-flyby design strategy, is propagated in positive time until its encounter with the ending state of Phase 3. The segmentation method applied to Phase 1 is also used for both portions of Phase 2a as well as Phase 2b, leading to a continuity requirement for each leg. Moreover, both forward and backward-propagated legs of Phase 2a are to be joined at apogee. The continuity constraints governing Phases 2a and 2b are given in (6.8), where the number of segments in the positive-time and negative-time portions of Phase 2a are represented with n_{2f} and n_{2r}, and that for Phase 2b is denoted n_{2b}.

$$\vec{F}_{2a} = \begin{bmatrix} {}^{2f}\tilde{\vec{x}}_f^1 - {}^{2f}\tilde{\vec{x}}_o^2 \\ {}^{2f}\tilde{\vec{x}}_f^2 - {}^{2f}\tilde{\vec{x}}_o^3 \\ \vdots \\ {}^{2f}\tilde{\vec{x}}_f^{(n_{2f}-1)} - {}^{2f}\tilde{\vec{x}}_o^{n_{2f}} \\ {}^{2r}\tilde{\vec{x}}_f^1 - {}^{2r}\tilde{\vec{x}}_o^2 \\ {}^{2r}\tilde{\vec{x}}_f^2 - {}^{2r}\tilde{\vec{x}}_o^3 \\ \vdots \\ {}^{2r}\tilde{\vec{x}}_f^{(n_{2r}-1)} - {}^{2r}\tilde{\vec{x}}_o^{n_{2r}} \\ {}^{2f}\tilde{\vec{x}}_f^{n_{2f}} - {}^{2r}\tilde{\vec{x}}_f^{n_{2r}} \end{bmatrix} \qquad \vec{F}_{2b} = \begin{bmatrix} {}^{2b}\tilde{\vec{x}}_f^1 - {}^{2b}\tilde{\vec{x}}_o^2 \\ {}^{2b}\tilde{\vec{x}}_f^2 - {}^{2b}\tilde{\vec{x}}_o^3 \\ \vdots \\ {}^{2b}\tilde{\vec{x}}_f^{(n_{2b}-1)} - {}^{2b}\tilde{\vec{x}}_o^{n_{2b}} \end{bmatrix} \tag{6.8}$$

The continuity between the end of Phases 2b and 3 is maintained by the constraint vector given in Equation (6.9). Similar to the framework outlined for Phase 3 in Section 5.4.2, the initial state along the pseudo-manifold, ${}^3\tilde{\vec{x}}_o$ is constrained to be continuous with motion along the host periodic orbit, ${}^P\tilde{\vec{x}}_f$, as dictated by time τ_1.

$$\vec{F}_3 = \begin{bmatrix} {}^3\tilde{\vec{r}}_f - {}^{2b}\tilde{\vec{r}}_f^{n_{2b}} \\ {}^3\tilde{\theta}_f - {}^{2b}\tilde{\theta}_f^{n_{2b}} \\ {}^3\tilde{\vec{x}}_o - {}^P\tilde{\vec{x}}_f \end{bmatrix} \tag{6.9}$$

The constraints surrounding the flybys are similar to those enforced for the single-flyby transfers, but are now applied to both passages as shown by (6.10).

$$\vec{F}_{LE_1} = \begin{bmatrix} {}^{2f}\tilde{\vec{r}}_o^1 - {}^1\tilde{\vec{r}}_o^1 \\ {}^{2f}\tilde{\theta}_o^1 - {}^1\tilde{\theta}_o^1 \\ ({}^{2f}\tilde{x}_o^1 - (1-\tilde{\mu})) \cdot {}^{2f}\dot{\tilde{x}}_o^1 + {}^{2f}\tilde{y}_o^1 \cdot {}^{2f}\dot{\tilde{y}}_o^1 + {}^{2f}\tilde{z}_o^1 \cdot {}^{2f}\dot{\tilde{z}}_o^1 \\ ({}^{2f}\tilde{x}_o^1 - (1-\tilde{\mu}))^2 + ({}^{2f}\tilde{y}_o^1)^2 + ({}^{2f}\tilde{z}_o^1)^2 - r_{min}^2 - \eta_{alt_1}^2 \end{bmatrix}$$
$$\vec{F}_{LE_2} = \begin{bmatrix} {}^{2b}\tilde{\vec{r}}_o^1 - {}^{2r}\tilde{\vec{r}}_o^1 \\ {}^{2b}\tilde{\theta}_o^1 - {}^{2r}\tilde{\theta}_o^1 \\ ({}^{2b}\tilde{x}_o^1 - (1-\tilde{\mu})) \cdot {}^{2b}\dot{\tilde{x}}_o^1 + {}^{2b}\tilde{y}_o^1 \cdot {}^{2b}\dot{\tilde{y}}_o^1 + {}^{2b}\tilde{z}_o^1 \cdot {}^{2b}\dot{\tilde{z}}_o^1 \\ ({}^{2b}\tilde{x}_o^1 - (1-\tilde{\mu}))^2 + ({}^{2b}\tilde{y}_o^1)^2 + ({}^{2b}\tilde{z}_o^1)^2 - r_{min}^2 - \eta_{alt_2}^2 \end{bmatrix} \tag{6.10}$$

Where initial values for the slack variables η_{alt_1} and η_{alt_2} are found using the same method detailed in Section 5.4.2. Continuity between each of the backward-propagated Phase 1 segments is enforced while the ending position and epoch are to coincide with that of the CM state, all captured by $\vec{F}_1$.

$$\vec{F}_1 = \begin{bmatrix} {}^1\tilde{\vec{x}}_f^1 - {}^1\tilde{\vec{x}}_o^2 \\ {}^1\tilde{\vec{x}}_f^2 - {}^1\tilde{\vec{x}}_o^3 \\ \vdots \\ {}^1\tilde{\vec{x}}_f^{n_1-1} - {}^1\tilde{\vec{x}}_o^{n_1} \\ {}^1\tilde{\vec{r}}_f^{n_1} - \tilde{\vec{r}}_{CM} \\ {}^1\tilde{\theta}_f^{n_1} - \tilde{\theta}_{CM} \end{bmatrix} \tag{6.11}$$

Lastly, an inequality constraint allows for the total cost of the transfer (excluding the CM maneuver) to be maintained under a user-provided value. If:

$$\Delta v_2 = \left\| {}^{2f}\tilde{\vec{v}}_o^1 - {}^1\tilde{\vec{v}}_o^1 \right\| \qquad \Delta v_3 = \left\| {}^{2b}\tilde{\vec{v}}_o^1 - {}^{2r}\tilde{\vec{v}}_o^1 \right\| \qquad \Delta v_4 = \left\| {}^3\tilde{\vec{v}}_f - {}^{2b}\tilde{\vec{v}}_f^{n_{2b}} \right\| \tag{6.12}$$

then:

$$F_{\Delta v} = \Delta v_2^2 + \Delta v_3^2 + \Delta v_4^2 - \Delta v_{max}^2 + \eta_{\Delta v}^2 \tag{6.13}$$

The initial value of the slack variable η_{Deltav} may be found to be:

$$\eta_{\Delta v} = \sqrt{\Delta v_{max}^2 - \Delta v_2^2 - \Delta v_3^2 - \Delta v_4^2} \tag{6.14}$$

The BCR4BP targeter is governed by the culmination of these constraints, as shown by $\vec{F}(\vec{X}_\mathrm{i})$ in equation (6.15).

$$\vec{F}(\vec{X}_\mathrm{i}) = \begin{bmatrix} \vec{F}_1 \\ \vec{F}_{2a} \\ \vec{F}_{2b} \\ \vec{F}_3 \\ \vec{F}_{LE_1} \\ \vec{F}_{LE_2} \\ F_{\Delta v} \end{bmatrix} \qquad \vec{X}_\mathrm{i} = \begin{bmatrix} {}^1\vec{X} \\ {}^{2f}\vec{X} \\ {}^{2r}\vec{X} \\ {}^{2b}\vec{X} \\ {}^3\tilde{\vec{x}}_o \\ \tau_1 \\ \tau_2 \\ \tau_3 \\ \eta_{alt_1} \\ \eta_{alt_2} \\ \eta\Delta v \end{bmatrix} \tag{6.15}$$

Where:

$$ {}^{1}\vec{X} = \begin{bmatrix} {}^{1}\tilde{\vec{x}}_o^{1} \\ {}^{1}\tilde{\vec{x}}_o^{2} \\ \vdots \\ {}^{1}\tilde{\vec{x}}_o^{n_1} \end{bmatrix} \quad {}^{2f}\vec{X} = \begin{bmatrix} {}^{2f}\tilde{\vec{x}}_o^{1} \\ {}^{2f}\tilde{\vec{x}}_o^{2} \\ \vdots \\ {}^{2f}\tilde{\vec{x}}_o^{n_{2f}} \end{bmatrix} \quad {}^{2r}\vec{X} = \begin{bmatrix} {}^{2r}\tilde{\vec{x}}_o^{1} \\ {}^{2r}\tilde{\vec{x}}_o^{2} \\ \vdots \\ {}^{2r}\tilde{\vec{x}}_o^{n_{2r}} \end{bmatrix} \quad {}^{2b}\vec{X} = \begin{bmatrix} {}^{2b}\tilde{\vec{x}}_o^{1} \\ {}^{2b}\tilde{\vec{x}}_o^{2} \\ \vdots \\ {}^{2b}\tilde{\vec{x}}_o^{n_{2b}} \end{bmatrix} \tag{6.16} $$

By applying (6.15) to the generated reference trajectories and lunar swing-by arcs, as well as selecting $\Delta v_{max} = 0.35$ non-dimensional units, a continuous trajectory is converged in the BCR4BP, as shown in Figure 6.8. A small family may be produced by iteratively decreasing the value of Δv_{max}, plotted in Figure 6.10. For the cheapest transfer, a breakdown of each maneuver cost is provided in Table 6.1, while additional data is provided in Table 6.2. The pattern that the individual costs follow along the continuation of the family is given in Figure 6.11.

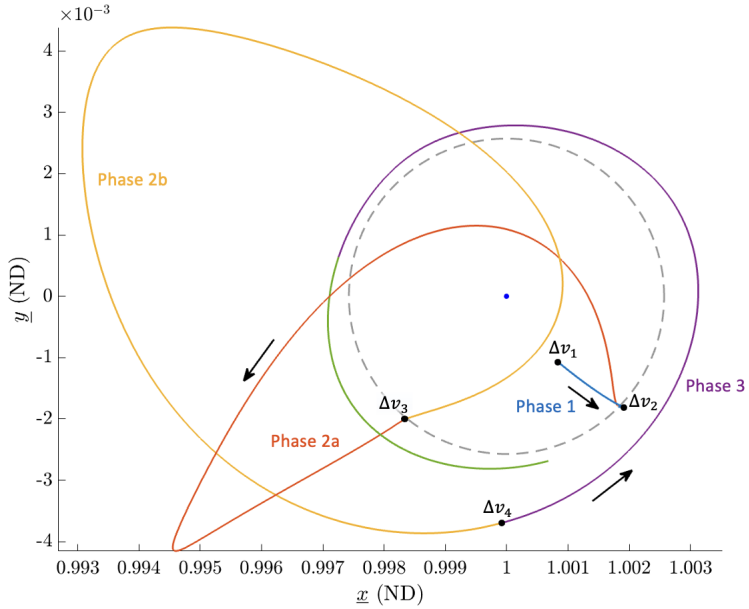

Figure 6.8. Each phase and maneuver of the converged BCR4BP transfer labelled. Motion represented in the Sun-B_1 frame.

The motion near the Moon as viewed in the Earth-Moon rotating frame is depicted in Figure 6.9, showcasing both flybys as well as the insertion into science orbit (in black).

In the case of the December 18 single-flyby transfer, the largest cost belonged to the pseudo-manifold insertion maneuver, chiefly dedicated toward changing the spacecraft's di-

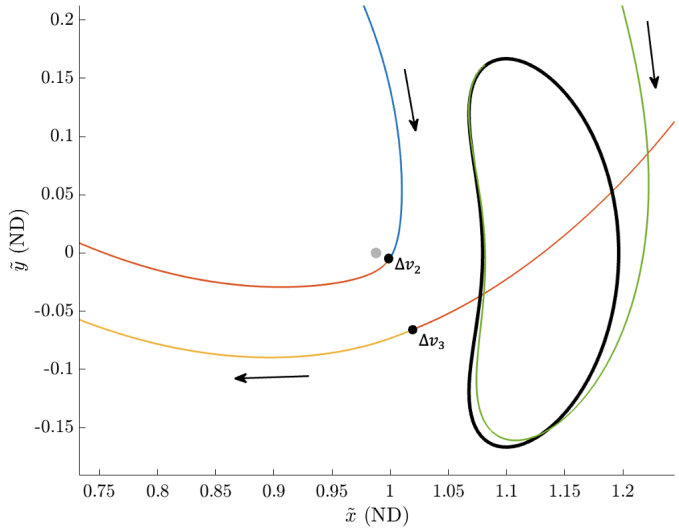

Figure 6.9. Near-Moon motion as viewed in the Earth-Moon frame. Colored correspondingly to phases as labelled in Figure 6.8.

Table 6.1. Maneuver Costs of cheapest member from produced double-flyby family

	Δv_1	Δv_2	Δv_3	Δv_4	$\sum_{\mathrm{i}=1}^{4} \Delta v_{\mathrm{i}}$
Cost (m/s)	21.56	29.65	277.47	0.41	329.09

Table 6.2. Additional characteristics of cheapest member from produced double-flyby family

	Time of Flight (Days)	LE_1 Altitude (km)	LE_2 Altitude (km)
Value	168.64	3014.27	26252.46

rection of motion. In this scenario, most of the cost is needed at the second lunar passage, though this is primarily to change the energy of the spacecraft as the velocity vectors are aligned. While additional interactions with the Moon are incorporated, the altitudes for either flyby ensure little collision risk, especially in the case of LE_2, which barely enters the 30000-km radius Σ_{1b} interface. The primary drawback of the double-flyby mission is the increased flight time, which is approximately 70 days longer than its single-flyby counterpart.

Much like how the diversion to a Butterfly orbit allows for the re-phasing of a single-flyby transfer to the 9:2 NRHO, a secondary lunar encounter grants additional freedom to do the

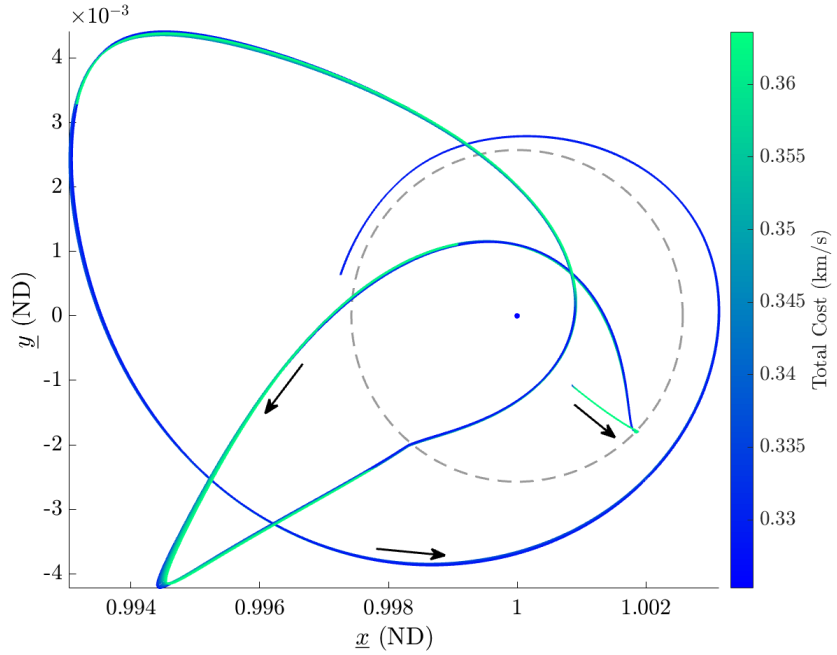

(a) $\hat{\underline{x}}$-$\hat{\underline{y}}$ projection

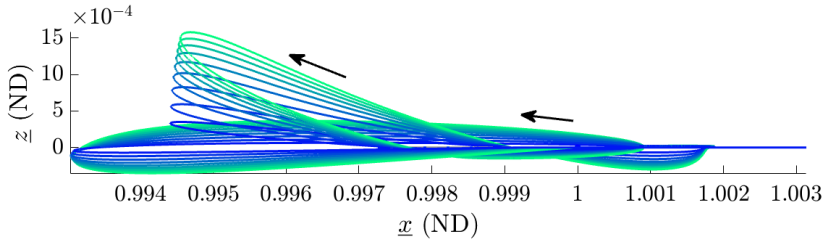

(b) $\hat{\underline{x}}$-$\hat{\underline{z}}$ projection

Figure 6.10. Family of double-flyby lunar transfers from Dec. 18 2023 CM state to $JC \approx 3.10$ L_2 Lyapunov orbit. Motion in Sun-B_1 frame. Lunar orbit in grey.

same for the transfer to a Lyapunov. By extending the time of flight, the secondary lunar passage effectively re-phases the transfer to the science orbit. In this case, the secondary lunar passage enables greater modularity for changing the candidate trajectories, where choosing between each option governs the general arrival date, while family continuation may be leveraged to fine-tune the insertion epoch and cost, if necessary.

Recall that the single flyby transfer between the same CM state and destination orbit had a total cost of 556.83 meters per second, thus the cheapest member of the double-flyby

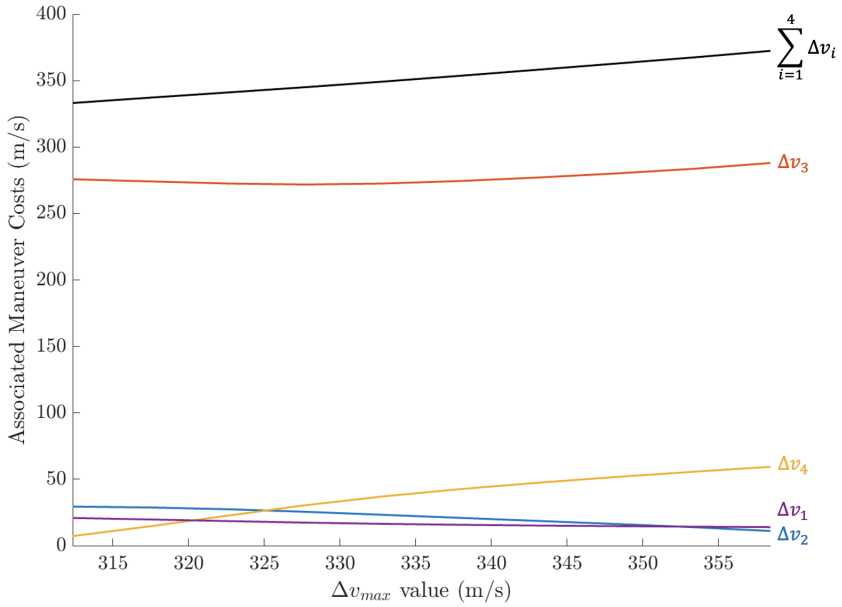

Figure 6.11. Evolution of each maneuver cost along continuation of family.

family is about 57% the cost of its Chapter 5 counterpart. Despite this reduction, it is entirely possible that cheaper transfers using a single flyby exist for this scenario. With the number of variables increased by the inclusion of a second passage, the possibility of a still cheaper transfer is especially high for a double-flyby transfer. For the case study, the transfer is constructed from a single, arbitrarily chosen epoch for LE_2, thus an entirely different pathway may be found by focusing on a different Moon angle. In light of this, the true benefit of the inclusion of a secondary lunar flyby is the vast diversification of transfer options. In the case of the single flyby transfer, only a single method is available for changing the transfer geometry: re-weighting the components of the K-D tree algorithm. By doing so, production of viable results is heavily reliant on trial-and-error, as little feedback is provided before convergence of the initial trajectory. The modularity of the double-flyby framework provides the user a more intuitive transfer design process, as they may select Phase 2a and 2b trajectories independently, then match them together using the corrections algorithm. With this, the mission designer is more greatly enabled to craft a transfer from a constrained initial state and epoch to the destination cislunar orbit while meeting mission specifications.

7. CONCLUDING REMARKS

7.1 Summary of Investigation

With the increasing interest for missions set in cislunar space comes a growing need of viable pathways to these science orbits. Primary payloads often benefit from flexibility granted to the determination of their departure state and epoch. Rideshare spacecraft, or secondary payloads, have little influence in their jettison condition, limiting the available flight paths. Furthermore, these spacecraft are often relatively small and thus unable to carry a significant amount of fuel, imposing additional maneuver restrictions to the mission design. The investigation seeks to provide a design framework centered around the exploitation of lunar flybys to aid in the construction of viable lunar transfers for secondary payloads to cislunar periodic orbits. Sample converged trajectories are provided, with motion modelled in the Bi-Circular Restricted 4-Body Problem.

A cornerstone of the analysis is the dynamical models used. The Earth-Moon CR3BP is utilized to generate periodic orbit families from which candidate science orbits are chosen, while its Sun-B_1 counterpart is used to screen for properly-phased lunar transfer candidates. Reference trajectories generated in the Sun-Barycenter CR3BP are then transitioned to the BCR4BP to model the presented continuous transfer results.

Numerical methods and dynamical systems theory are applied to both the CR3BP and BCR4BP to gain additional insight into the latent behavior in such gravitational regimes. The state transition matrix is formulated for either dynamical model, then used within a differential corrections scheme to iteratively refine trajectories such as periodic orbits and transfer arcs. Continuation methods are defined such that families of transfers may be spawned from a single solution, varying about a select mission parameter, such as total cost or time of flight. The eigenspace of CR3BP and BCR4BP periodic orbits is evaluated to produce invariant manifolds, enlightening low-cost arrival pathways into target science orbits. A flexible alternative in pseudo-manifolds is also presented, creating a diverse arrival arc candidate pool that is lenient with destination epoch.

To gain intuition on the construction of pathways for rideshare spacecraft, four-body BLT construction techniques are explored for primary payload missions. To this end, quadrant

effects on the spacecraft Hamiltonian and osculating orbital characteristics are outlined, enlightening desirable outbound directions for lunar transfers. BLTs to cislunar trajectories are produced using both invariant manifolds and pseudo-manifolds, while pathways to circular lunar orbits are formed with select examples feature outbound Moon-encounters. The effects of leading and lagging lunar flybys on spacecraft Hamiltonian are analyzed, validating the utility of a Moon flyby for secondary payload transfers.

Focusing on rideshare spacecraft, transfers are constructed centered about the outbound Lunar encounter, separated into Phases to accommodate its inclusion. Analytical expressions for generating initial guess loci are formulated using Earth relative two-body dynamics. The produced surface for departing states is then limited to send spacecraft to circularizing quadrants, where further filtration is introduced via the Sun-B_1 CR3BP to exclude improperly phased arcs. The first two trajectory phases are then patched together via B-Plane targeting, while a K-D tree algorithm selects the best-aligned reference trajectories to insert into the science orbit. Lastly, transfers from various sample CM states to Halo, Butterfly and Lyapunov orbits are converged, then continued to reduce total mission cost.

The modularity of the transfer design framework also admits the inclusion of intermediate events, such as a secondary lunar encounter. To demonstrate this, a case study for a double-flyby transfer from a specific CM state to a designated Lyapunov orbit is examined. Following an applied Phase 2 selection, matching and continuation process, a candidate solution is converged. The introduction of the secondary lunar passage showcases the flexibility of the modular framework presented, while introducing an intuitive design strategy to better enable the construction of viable cislunar transfers for secondary payloads.

7.2 Recommendations for Future Work

Various research directions may expand upon the methodology presented in the investigation. Example extensions include:

- **Improvement of candidate arc initial guess evaluation:** Each combination between the Phase 2 and Phase 3 candidate pools provides a set of candidate trajectories to be evaluated. The disparity between each of the pairs is evaluated using the exist-

ing framework, where this value is then used to gage the cost of the pseudo-manifold insertion maneuver, though this quantity will change following convergence. Furthermore, the cost following continuation is completely unknown a priori, where some pairs initially seen as more expensive may reduce to one of the cheapest options during the continuation process. As a result, it is difficult to determine the candidates most likely to ultimately have lower cost transfers, thus a metric which provides insight into this would prove highly valuable to the existing framework.

- **The Transition to a higher-fidelity dynamical model:** The results provided in the text are converged in the BCR4BP. In doing so, the corresponding real-world motion likely exists, but has yet to be verified in the HFEM. Transitioning sets of motion from the BCR4BP to Ephemeris has been extensively performed [20] [34] [39], though the presence of close Moon passages may conflict with the variable lunar orbit about the Earth. In events where the Moon's pulsating orbit destroys BCR4BP reference trajectories, an alternative four-body model which incorporates a non-circular lunar track may prove beneficial. Following this, additional considerations, such as solar radiation pressure, lunar J2 effects, etcetera may be appended to better represent real-world circumstances.

- **Inclusion of low-thrust:** The investigation modelled maneuvers as impulsive burns to occur in any direction. Typically, smaller secondary payloads feature low-thrust engines with limited output. For such cases, the instantaneous maneuvers employed in the presented results must be converted to sustained burns over a non-negligible period of time. Moreover, additional thrusting arcs may be employed to significantly alter the geometry of outbound trajectories, better aligning the spacecraft with the arrival manifold for potentially less cost overall.

- **Alternative flyby applications:** The inclusion of flybys in trajectory design extends far beyond lunar transfer design. As such, the implementation of a segmented trajectory construction framework centered about a body's passage may extend to a diverse set of scenarios. For instance, consider transfers between two cislunar orbits where

little to no manifold intersections exist. Alternatively, passageways between cislunar and heliocentric periodic orbits have been examined within the BCR4BP [34], though additional revolutions about the Earth paired with strategic lunar encounters may allow for a flexible strategy to appropriately phase the departure into heliocentric space. The insightful application of appropriate dynamical models within a segmented corrections scheme can lead to a robust transfer design tool to be used for a vast amount of scenarios.

REFERENCES

[1] A. L. Batcha, J. Williams, T. F. Dawn, *et al.*, "Artemis I Trajectory Design and Optimization," NTRS Author Affiliations: Johnson Space Center, Jacobs (United States) NTRS Report/Patent Number: AAS 20-649 NTRS Document ID: 20205005150 NTRS Research Center: Johnson Space Center (JSC), Virtual, Jul. 2020. [Online]. Available: https://ntrs.nasa.gov/citations/20205005150.

[2] A. Hoffman, B. Park, T. Roorda, S. Stewart, and K. Howell, "Trajectory Design for a Secondary Payload within a Complex Gravitational Environment: The Khon-1 Spacecraft," Charlotte, NC, Aug. 2022.

[3] N. Bosanac, A. D. Cox, K. C. Howell, and D. C. Folta, "Trajectory design for a cislunar CubeSat leveraging dynamical systems techniques: The Lunar IceCube mission," *Acta Astronautica*, vol. 144, pp. 283–296, Mar. 2018, ISSN: 0094-5765. DOI: 10.1016/j.actaastro.2017.12.025. [Online]. Available: https://www.sciencedirect.com/science/article/pii/S0094576517307725.

[4] P. C. Lai, D. C. Sternberg, R. J. Haw, E. D. Gustafson, P. C. Adell, and J. D. Baker, "Lunar Flashlight CubeSat GNC system development," *Acta Astronautica*, vol. 173, pp. 425–441, Aug. 2020, ISSN: 0094-5765. DOI: 10.1016/j.actaastro.2020.01.022. [Online]. Available: https://www.sciencedirect.com/science/article/pii/S0094576520300333.

[5] A. P. Zucherman, K. Jawork, A. Buchwald, *et al.*, "Cislunar Explorers: Lessons Learned from the Development of an Interplanetary CubeSat," 2020. [Online]. Available: https://www.semanticscholar.org/paper/Cislunar-Explorers%3A-Lessons-Learned-from-the-of-an-Zucherman-Jawork/cbef61bb4eeb5d609dc38a662d802dad79f01dbd.

[6] A. L. Genova and D. W. Dunham, "Trajectory Design for the Lunar Polar Hydrogen Mapper Mission," NTRS Author Affiliations: NASA Ames Research Center, KinetX Aerospace, Inc. NTRS Report/Patent Number: ARC-E-DAA-TN39796 NTRS Document ID: 20170009830 NTRS Research Center: Ames Research Center (ARC), San Antonio, TX, Feb. 2017. [Online]. Available: https://ntrs.nasa.gov/citations/20170009830.

[7] K. Oguri, K. Oshima, S. Campagnola, *et al.*, "EQUULEUS Trajectory Design," en, *The Journal of the Astronautical Sciences*, vol. 67, no. 3, pp. 950–976, Sep. 2020, ISSN: 2195-0571. DOI: 10.1007/s40295-019-00206-y. [Online]. Available: https://doi.org/10.1007/s40295-019-00206-y.

[8] A. Mickelwait and R. Booton, "Analytical and Numerical Studies of Three-Dimensional Trajectories to the Moon," *JOURNAL OF THE AEROSPACE SCIENCES*, vol. 27, no. 8, pp. 561–573, Aug. 1960.

[9] A. J. Schwaniger, "Lunar Flight Study Series: Volume 5. Trajectories in the Earth-Moon Space with Symmetrical Free Return Properties," Tech. Rep. NASA-TN-D-1833, Jun. 1963, NTRS Author Affiliations: Marshall Space Flight Center NTRS Document ID: 19630007117 NTRS Research Center: Marshall Space Flight Center (MSFC). [Online]. Available: https://ntrs.nasa.gov/citations/19630007117.

[10] D. Lozier, K. Galal, D. Folta, and M. Beckman, "Lunar prospector mission design and trajectory support," vol. 100, Jun. 1998.

[11] N. Vighnesam, A. Sonney, B. Subramanian, and N. Gopinath, "India's first lunar mission: Chandrayaan-1 launch and early orbit phase orbit determination," *60th International Astronautical Congress 2009, IAC 2009*, vol. 6, pp. 4560–4568, Jan. 2009.

[12] M. Beckman, "Mission Design for the Lunar Reconnaissance Orbiter," en, Breckenridge, CO, Feb. 2006.

[13] K. Uesugi, "Results of the MUSES-A HITEN mission," *Advances in Space Research*, Missions to the Moon and Exploring the Cold Universe, vol. 18, no. 11, pp. 69–72, Jan. 1996, ISSN: 0273-1177. DOI: 10.1016/0273-1177(96)00090-7. [Online]. Available: https://www.sciencedirect.com/science/article/pii/0273117796000907.

[14] W. S. Koon, M. W. Lo, J. E. Marsden, and S. D. Ross, "Low Energy Transfer to the Moon," en, *Celestial Mechanics and Dynamical Astronomy*, vol. 81, no. 1, pp. 63–73, Sep. 2001, ISSN: 1572-9478. DOI: 10.1023/A:1013359120468. [Online]. Available: https://doi.org/10.1023/A:1013359120468.

[15] D. Davis, "Multi-body trajectory design strategies based on periapsis Poincare maps," Dissertation, Purdue University, West Lafayette, IN, Jan. 2011.

[16] R. Roncoli and K. Fujii, "Mission Design Overview for the Gravity Recovery and Interior Laboratory (GRAIL) Mission," in *AIAA/AAS Astrodynamics Specialist Conference*, ser. Guidance, Navigation, and Control and Co-located Conferences, Toronto, ON: American Institute of Aeronautics and Astronautics, Aug. 2010. DOI: 10.2514/6.2010-8383. [Online]. Available: https://arc.aiaa.org/doi/10.2514/6.2010-8383.

[17] K. K. Boudad, D. C. Davis, and K. C. Howell, "Disposal Trajectories from Near Rectilinear Halo Orbits," NTRS Author Affiliations: Purdue Univ., AI Solutions, Inc. NTRS Report/Patent Number: JSC-E-DAA-TN60056 NTRS Document ID: 20180006805 NTRS Research Center: Johnson Space Center (JSC), Snowbird, UT, Aug. 2018. [Online]. Available: https://ntrs.nasa.gov/citations/20180006805.

[18] R. Pritchett, K. Howell, and D. Folta, "Low-Thrust Trajectory Design for a Cislunar CubeSat Leveraging Structures from the Bicircular Restricted Four-Body Problem," Washington D.C., Oct. 2019.

[19] S. Scheuerle, "Construction of Ballistic Lunar Transfers in the Earth-Moon-Sun System," English, ISBN: 9798379830809, M.S. thesis, Purdue University, United States – Indiana, 2021. [Online]. Available: https://www.proquest.com/docview/2838330319/abstract/32F4780341CF4859PQ/1.

[20] S. Scheuerle, "Low-Energy Lunar Transfers in the Bicircular Restricted Four-body Problem," en, Dissertation, Purdue University Graduate School, Apr. 2024. DOI: 10.25394/PGS.25670040.v1. [Online]. Available: https://hammer.purdue.edu/articles/thesis/Low-Energy_Lunar_Transfers_in_the_Bicircular_Restricted_Four-body_Problem/25670040/1.

[21] M. Thompson, E. Kayser, J. Parker, *et al.*, "Navigation Design of the CAPSTONE Mission Near NRHO Insertion," Big Sky, MT, Aug. 2021.

[22] D. E. Lee, *White Paper: Gateway Destination Orbit Model: A Continuous 15 Year NRHO Reference Trajectory*, NTRS Author Affiliations: NASA Johnson Space Center NTRS Report/Patent Number: JSC-E-DAA-TN72594 NTRS Document ID: 20190030294 NTRS Research Center: Johnson Space Center (JSC), Aug. 2019.

[23] A. E. Hoffman, "Design of lunar transfer trajectories for secondary payload missions," en, thesis, Purdue University Graduate School, Apr. 2023. DOI: 10.25394/PGS.22695991.v1.

[24] V. Egorov, *Three-Dimensional Lunar Trajectories* (Mechanics of Space Flight). Israel Progral for Scientific Translations, 1969.

[25] R. W. Farquhar and D. W. Dunham, "A new trajectory concept for exploring the earth's geomagnetic tail," *Journal of Guidance and Control*, vol. 4, no. 2, pp. 192–196, 1981, Publisher: American Institute of Aeronautics and Astronautics _eprint: https://doi.org/10.2514/3.19733, ISSN: 0162-3192. DOI: 10.2514/3.19733. [Online]. Available: https://doi.org/10.2514/3.19733.

[26] D. Muhonen, S. Davis, and D. Dunham, "Alternative gravity-assist sequences for the ISEE-3 escape trajectory," in *Astrodynamics Conference*, ser. Guidance, Navigation, and Control and Co-located Conferences, Seattle, WA: American Institute of Aeronautics and Astronautics, Aug. 1984. DOI: 10.2514/6.1984-1977. [Online]. Available: https://arc.aiaa.org/doi/10.2514/6.1984-1977.

[27] K. Galal, T. Colaprete, S. Cooley, B. Kennedy, and T. McElrath, "Trajectory Design and Orbit Determination for the Lunar CRater Observation and Sensing Satellite (LCROSS)," NTRS Author Affiliations: NASA Ames Research Center, NASA Goddard Space Flight Center, Jet Propulsion Lab., California Inst. of Tech. NTRS Document ID: 20080012691 NTRS Research Center: Goddard Space Flight Center (GSFC), Annapolis, MD, Sep. 2007. [Online]. Available: https://ntrs.nasa.gov/citations/20080012691.

[28] D. J. Dichmann, J. J. K. Parker, T. W. Williams, and C. R. Mendelsohn, "Trajectory Design for the Transiting Exoplanet Survey Satellite," NTRS Author Affiliations: NASA Goddard Space Flight Center NTRS Report/Patent Number: GSFC-E-DAA-TN14089 NTRS Document ID: 20140007518 NTRS Research Center: Goddard Space Flight Center (GSFC), Laurel, MD, May 2014. [Online]. Available: https://ntrs.nasa.gov/citations/20140007518.

[29] I. Newton, *Philosophiae naturalis principia mathematica*, Latin, 3rd ed. Cambridge, MA: Harvard University Press, 1726, ISBN: 0-674-66475-2.

[30] J. Lagrange, *Essai sur le Probléme des Trois Corps* (Prix de lAcadémie Royale des Sciences de Paris), French. 1772, vol. tome IX.

[31] A. E. Roy and M. W. Ovenden, "On the Occurrence of Commensurable Mean Motions in the Solar System: The Mirror Theorem," *Monthly Notices of the Royal Astronomical Society*, vol. 115, no. 3, pp. 296–309, Jun. 1955, ISSN: 0035-8711. DOI: 10.1093/mnras/115.3.296. [Online]. Available: https://doi.org/10.1093/mnras/115.3.296.

[32] E. W. Brown, *An Introductory Treatise on the Lunar Theory*. The Cambridge University Press, 1896.

[33] B. Park and K. C. Howell, "Assessment of dynamical models for transitioning from the Circular Restricted Three-Body Problem to an ephemeris model with applications," *Celestial Mechanics and Dynamical Astronomy*, vol. 136, no. 1, p. 6, Feb. 2024, ISSN: 1572-9478. DOI: 10.1007/s10569-023-10178-9. [Online]. Available: https://doi.org/10.1007/s10569-023-10178-9.

[34] K. K. Boudad, "Trajectory Design Between Cislunar Space and Sun-Earth Libration Points in a Four-Body Model," en, thesis, Purdue University Graduate School, Apr. 2022. DOI: 10.25394/PGS.19669632.v1.

[35] K. K. Boudad, "Disposal Dynamics from the Vicinity of Near Rectilinear Halo Orbits in the Earth-Moon-Sun System," en, thesis, Purdue University Graduate School, Dec. 2018. DOI: 10.25394/PGS.7413359.v1.

[36] D. A. P. Williams, "Dynamics of Long-Term Orbit Maintenance Strategies in the Circular Restricted Three Body Problem," en, thesis, Purdue University Graduate School, West Lafayette, IN., Apr. 2024. DOI: 10.25394/PGS.25639269.v1. [Online]. Available: https://hammer.purdue.edu/articles/thesis/Dynamics_of_Long-Term_Orbit_Maintenance_Strategies_in_the_Circular_Restricted_Three_Body_Problem/25639269/1.

[37] V. Yakubovich and V. Starzhinskii, *Linear Differential Equations with Periodic Coefficients*. New York, NY: John Wiley and Sons, 1975, vol. 1.

[38] B. A. Steves, A. J. Maciejewski, and M. Hendry, Eds., *Chaotic Worlds: From Order to Disorder in Gravitational N-Body Dynamical Systems*, en. Springer Netherlands, 2006, ISBN: 978-1-4020-4704-6. DOI: 10.1007/978-1-4020-4706-0. [Online]. Available: http://link.springer.com/10.1007/978-1-4020-4706-0.

[39] B. P. McCarthy, "Cislunar Trajectory Design Methodologies Incorporating Quasi-Periodic Structures With Applications," en, thesis, Purdue University Graduate School, West Lafayette, IN., Apr. 2022. DOI: 10.25394/PGS.19678857.v1. [Online]. Available: https://hammer.purdue.edu/articles/thesis/Cislunar_Trajectory_Design_Methodologies_Incorporating_Quasi-Periodic_Structures_With_Applications/19678857/1.

[40] B. Park, R. R. Sanaga, and K. C. Howell, *A Frequency-Based Hierarchy of Dynamical Models in Cislunar Space: Leveraging Periodically and Quasi-Periodically Perturbed Models*, ISSN: 2693-5015, Aug. 2024. DOI: 10.21203/rs.3.rs-4822764/v1. [Online]. Available: https://www.researchsquare.com/article/rs-4822764/v1.

[41] R. E. Pritchett, "Strategies for Low-Thrust Transfer Design Based on Direct Collocation Techniques," en, thesis, Purdue University Graduate School, Aug. 2020. DOI: 10.25394/PGS.12739775.v1. [Online]. Available: https://hammer.purdue.edu/articles/thesis/Strategies_for_Low-Thrust_Transfer_Design_Based_on_Direct_Collocation_Techniques/12739775/1.

[42] E. M. Spreen, "Trajectory Design and Targeting For Applications to the Exploration Program in Cislunar Space," en, thesis, Purdue University Graduate School, May 2021. DOI: 10.25394/PGS.14445717.v1. [Online]. Available: https://hammer.purdue.edu/articles/thesis/Trajectory_Design_and_Targeting_For_Applications_to_the_Exploration_Program_in_Cislunar_Space/14445717/1.

[43] N. B. LaFarge, "Reinforcement Learning Approaches for Autonomous Guidance and Control in a Low-Thrust, Multi-Body Dynamical Environment," en, thesis, Purdue University Graduate School, Apr. 2023. DOI: 10.25394/PGS.22696261.v1. [Online]. Available: https://hammer.purdue.edu/articles/thesis/Reinforcement_Learning_Approaches_for_Autonomous_Guidance_and_Control_in_a_Low-Thrust_Multi-Body_Dynamical_Environment/22696261/1.

[44] G. Bucchioni, S. Lizy-Destrez, T. Vaujour, V. Thoraval, L. Rouverand, and C. Silva, "Phasing with near rectilinear Halo orbits: Design and comparison," *Advances in Space Research*, vol. 71, pp. 2449–2466, Mar. 2023, ADS Bibcode: 2023AdSpR..71.2449B, ISSN: 0273-1177. DOI: 10.1016/j.asr.2022.10.036. [Online]. Available: https://ui.adsabs.harvard.edu/abs/2023AdSpR..71.2449B.

[45] C. Waldecker and K. Howell, "A Design Approach for Cislunar On-Orbit Servicing Networks," Broomfield, CO, Aug. 2024. [Online]. Available: https://engineering.purdue.edu/people/kathleen.howell.1/Publications/Conferences/2024_AAS_WalHow.pdf.